PHYSICS AND APPLICATIONS OF SEMICONDUCTOR HETEROSTRUCTURES:

I. MEASUREMENT OF BAND OFFSETS IN SEMICONDUCTOR HETEROJUNCTIONS

II. THEORETICAL AND EXPERIMENTAL STUDIES OF TUNNELING IN SEMICONDUCTOR HETEROSTRUCTURE DEVICES

Thesis by

Edward Tsu-Wei Yu

In Partial Fulfillment of the Requirements

for the Degree of

Doctor of Philosophy

California Institute of Technology

Pasadena, California

1991

(Submitted April 12, 1991)

To my parents

Acknowledgements

It is a pleasure to acknowledge my advisor, Professor Thomas C. McGill, for providing a consistently stimulating and supportive atmosphere in which to conduct research. His dedication, insight into the process of scientific research, and ability to keep his laboratories well equipped have contributed immensely to my scientific development; of at least equal value to me have been his sound and perceptive advice, on matters scientific and otherwise, and his concern for my personal well-being. I am grateful for having had the privilege of working in Professor McGill's research group.

I have enjoyed many interactions with Professor James O. McCaldin, whose knowledge and understanding of semiconductor materials and solid-state chemistry have significantly influenced my own thinking on these subjects. Dr. Ron Grant of the Rockwell International Science Center provided valuable advice regarding the measurement of band offsets by x-ray photoelectron spectroscopy; the benefit of his knowledge and experience contributed substantially to the success of the band offset studies reported in this thesis. I have benefited from many interesting conversations with Mr. Ogden Marsh of the Hughes Research Laboratories. I am also grateful to Professor Amnon Yariv for his hospitality during my first year at Caltech.

The everyday operation of the McGill group would rapidly deteriorate were it not for the untiring efforts of the administrative and secretarial staff. Marcia Hudson has coordinated the myriad aspects of the group's administration with superlative talent and skill; her competence, patience, and friendly and cheerful manner have made my time at Caltech much more enjoyable. In addition, Carol McCollum and, more recently, Sandy Brooks have consistently provided excellent support on administrative and secretarial matters.

My experience as a graduate student has been enriched by my interactions with many current and former members of the McGill group. It has been a pleasure to work with Dr. David Ting on a number of the tunneling projects described in this thesis. I have learned a great deal from Dave about a variety of subjects, and his good sense, patience, and friendliness have made our interactions extremely enjoyable. I am also grateful to Dave for his reading of Chapter 1 of this thesis. I have enjoyed working with Dr. David Chow on numerous research projects over the years, and appreciate his sound physical insights, generosity, and good nature. I have benefited from numerous discussions with Drs. Bob Hauenstein, Matthew Johnson, and Richard Miles; I am particularly grateful to Matthew for his role in designing and purchasing the clean-room, MBE, and ESCA facilities, and to Richard for performing the x-ray diffraction measurements required for the Si/Ge band offset measurement. I would also like to acknowledge interesting discussions with Drs. Ted Woodward, Wesley Boudville, and George Wu.

I have had a number of fascinating conversations with Dr. Yasantha Rajakarunanayake, from which I extracted considerable physical insight into and knowledge about many aspects of solid-state physics. I have enjoyed my collaborations with Dr. Michael Jackson on various aspects of tunneling, and appreciate his rigorous approach to problems and his consistently sound, well-considered opinions. It has been a pleasure to interact with Ed Croke, my contemporary in the McGill group; I especially appreciated his willingness to grow the multitude of samples required for the Si/Ge band offset measurements. Among my other classmates, I have enjoyed immensely my interactions, both scientific and recreational, with Pete Zampardi. My friendship with Pete and his wife Valerie has often provided a much-needed respite from life at Caltech. Finally, I have learned a great deal from my interactions with Rex Burington, whose outlook

and opinions were, in my experience, truly unique.

I have had a number of fruitful collaborations with Doug Collins, and am especially grateful to Doug for his recent patience and generosity in teaching me about III-V MBE. I have enjoyed working with Mark Phillips on the projects involving II-VI semiconductors, and have found our interactions to be quite stimulating. I profited from many conversations with Dr. Jan Söderström during the year he spent as a student at Caltech. Brian Cole contributed significantly to the initial installation and maintenance of the MBE, ESCA, and clean-room facilities. I have had many interesting conversations with Ron Marquardt, and Ron's extensive and occasionally herculean efforts in recent months to upgrade and maintain the numerous computer workstations in our group, without which the writing of this thesis would have been extremely difficult, are appreciated. I have enjoyed working recently with Mike Wang on a number of projects; Mike performed several of the recent XPS measurements in our studies of III-V/II-VI heterojunctions. I have profited from numerous discussions with my officemates Harold Levy and Robert Miles. I have also benefited from conversations with Tracy Fu, Yixin Liu, Todd Rossi, Johanes Swenberg, and Shaun Kirby.

I would like to acknowledge graduate fellowship support from the National Science Foundation, the AT&T Foundation, and the California Institute of Technology, and additional financial support via research grants to Professor McGill from the Office of Naval Research, the Defense Advanced Research Projects Agency, and the Air Force Office of Scientific Research.

Finally, I would like to thank my parents and my brother for their encouragement and support. My parents have always encouraged me to define worthwhile goals and to pursue them with vigor, and placed special emphasis on the value of education. Without my parents none of this work would have been possible, and it is to them that I have chosen to dedicate this thesis.

List of Publications

Parts of this thesis have been, or will be, published under the following titles:

Part I

Commutativity of the GaAs/AlAs (100) Valence Band Offset,
E. T. Yu, D. H. Chow, and T. C. McGill, *Phys. Rev. B* **38**, 12764 (1988).

Commutativity of the GaAs/AlAs (100) Valence Band Offset,
E. T. Yu, D. H. Chow, and T. C. McGill, *J. Vac. Sci. Technol. B* **7**, 391 (1989).

Measurement of the Valence Band Offset in Strained Si/Ge (100) Heterojunctions by X-Ray Photoelectron Spectroscopy,
E. T. Yu, E. T. Croke, T. C. McGill, and R. H. Miles, *Appl. Phys. Lett.* **56**, 569 (1990).

Measurement of the Strain Dependence of the Si/Ge (100) Valence Band Offset,
E. T. Yu, E. T. Croke, T. C. McGill, and R. H. Miles, presented at the SPIE Symposium on Advances in Semiconductors and Superconductors: Physics Toward Device Applications, San Diego, CA (1990).

Measurement of the Valence Band Offset in Novel Heterojunction Systems: Si/Ge (100) and AlSb/ZnTe (100),
E. T. Yu, E. T. Croke, D. H. Chow, D. A. Collins, M. C. Phillips, T. C. McGill, J. O. McCaldin, and R. H. Miles, *J. Vac. Sci. Technol. B* **8**, 908 (1990).

Measurement of Band Offsets in III–V/II–VI Semiconductor Heterostructures,
E. T. Yu, M. C. Phillips, D. H. Chow, D. A. Collins, and T. C. McGill, *Bull. Am. Phys. Soc.* **35**, 416 (1990).

Heterojunction Approaches to Light Emitters: The Role of Band Offsets,
E. T. Yu, Y. Rajakarunanayake, M. C. Phillips, J. O. McCaldin, and T. C. McGill, presented at the 1990 International Conference on Solid State Devices and Materials, Sendai, Japan (1990).

Characterization of CdSe/ZnTe Heterojunctions,
M. C. Phillips, E. T. Yu, Y. Rajakarunanayake, J. O. McCaldin, D. A. Collins, and T. C. McGill, presented at the Sixth International Conference on Molecular Beam Epitaxy, San Diego, CA (1990).

Measurement of the CdSe/ZnTe Valence Band Offset by XPS,
E. T. Yu, M. C. Phillips, J. O. McCaldin, and T. C. McGill, presented at the Eighteenth Conference on the Physics and Chemistry of Semiconductor Interfaces (1991).

Interfacial Reactions and Non-transitivity of Band Offsets in the AlSb/GaSb/ZnTe Material System,
E. T. Yu, M. C. Phillips, D. H. Chow, D. A. Collins, M. W. Wang, J. O. McCaldin, and T. C. McGill, submitted to *Phys. Rev. B* (1991).

Band Offsets in ZnTe Heterojunctions for Visible Light Emitters,
E. T. Yu, M. C. Phillips, M. W. Wang, D. A. Collins, D. H. Chow, J. O. McCaldin, and T. C. McGill, submitted to the 1991 Electronic Materials Conference, Boulder CO (1991).

Band Offsets in Semiconductor Heterojunctions,

E. T. Yu, J. O. McCaldin, and T. C. McGill, to appear in *Solid State Phys.* (1991).

Part II

III-V/II-VI Double-Barrier Resonant Tunneling Structures,

E. T. Yu and T. C. McGill, *Appl. Phys. Lett.* **53**, 60 (1988).

Hole Tunneling Times in GaAs/AlAs Double-Barrier Structures,

E. T. Yu, M. K. Jackson, and T. C. McGill, *Appl. Phys. Lett.* **55**, 744 (1989).

Two-Band Modeling of Narrow Bandgap and Interband Tunneling Devices,

J. R. Söderström, E. T. Yu, M. K. Jackson, Y. Rajakarunanayake, and T. C. McGill, *J. Appl. Phys.* **68**, 1372 (1990).

Novel InAs/GaSb/AlSb Tunnel Structures,

D. H. Chow, J. R. Söderström, D. A. Collins, D. Z.-Y. Ting, E. T. Yu, and T. C. McGill, presented at the SPIE Symposium on Advances in Semiconductors and Superconductors: Physics Toward Device Applications, San Diego, CA (1990).

Modeling of Novel Heterojunction Tunnel Structures,

D. Z.-Y. Ting, E. T. Yu, D. A. Collins, D. H. Chow, and T. C. McGill, *J. Vac. Sci. Technol. B* **8**, 810 (1990).

Experimental Observation of Negative Differential Resistance from an InAs/GaSb Interface,

D. A. Collins, E. T. Yu, Y. Rajakarunanayake, J. R. Söderström, D. Z.-Y. Ting, D. H. Chow, and T. C. McGill, *Appl. Phys. Lett.* **57**, 683 (1990).

InAs/GaSb/AlSb: The Material System of Choice for Novel Tunneling Devices,

D. A. Collins, D. H. Chow, E. T. Yu, D. Z.-Y. Ting, J. R. Söderström, Y. Rajakarunanayake, and T. C. McGill, presented at the 1990 NATO Workshop on Resonant Tunneling, El Escorial, Spain (1990).

Large Peak Current Densities in Novel Resonant Interband Tunneling Heterostructures,

D. Z.-Y. Ting, D. A. Collins, E. T. Yu, D. H. Chow, and T. C. McGill, *Appl. Phys. Lett.* **57**, 1257 (1990).

Modeling InAs/GaSb/AlSb Interband Tunnel Structures,

D. Z.-Y. Ting, E. T. Yu, D. A. Collins, D. H. Chow, and T. C. McGill, presented at the Workshop on Computational Electronics, Urbana, IL (1990).

Interband Tunneling in InAs/GaSb/AlSb Heterostructures,

D. A. Collins, D. Z.-Y. Ting, D. H. Chow, E. T. Yu, J. R. Söderström, Y. Rajakarunanayake, and T. C. McGill, presented at the Sixth International Conference on Molecular Beam Epitaxy, San Diego, CA (1990).

The Role of Heavy–Hole States in Interband Tunnel Structures,

D. Z.-Y. Ting, E. T. Yu, and T. C. McGill, *Appl. Phys. Lett.* **58** 292 (1991).

Theoretical Studies of Current Transport in Interband Tunnel Structures Using the Effective Bond Orbital Model,

D. Z.-Y. Ting, E. T. Yu, and T. C. McGill, presented at the 1990 International Electron Devices Meeting, San Francisco (1990).

Demonstration of Resonant Transmission in InAs/GaSb/InAs Interband Tunneling Devices,

E. T. Yu, D. A. Collins, D. Z.-Y. Ting, D. H. Chow, and T. C. McGill, *Appl. Phys. Lett.* **57**, 2675 (1990).

Band Structure Effects on Interband Tunnel Structures,

D. Z.-Y. Ting, E. T. Yu, and T. C. McGill, presented at the Eighteenth Conference on the Physics and Chemistry of Semiconductor Interfaces (1991).

Effect of Band Mixing on Hole Tunneling Times in GaAs/AlAs Double-Barrier Heterostructures,

D. Z.-Y. Ting, E. T. Yu, and T. C. McGill, submitted to *Phys. Rev. B* (1991).

Effective Bond Orbital Model and Quantum Transport,

D. Z.-Y. Ting, E. T. Yu, and T. C. McGill, submitted to *Phys. Rev. B* (1991).

The following publications discuss work related to, but not included in, the contents of this thesis:

Large Peak-to-Valley Current Ratios in Triple Barrier Heterostructures,

D. A. Collins, D. H. Chow, D. Z.-Y. Ting, E. T. Yu, J. R. Söderström, and T. C. McGill, *Solid–State Electron.* **32**, 1095 (1989).

Negative Differential Resistance Negative Differential Resistance Due to Resonant Interband Tunneling of Holes,

D. H. Chow, E. T. Yu, J. R. Söderström, D. Z.-Y. Ting, and T. C. McGill, *J. Appl. Phys.* **68**, 3744 (1990).

Evidence for Coherent Interaction Between Quantum Well States in AlAs/GaAs Triple Barrier Heterostructures,

D. A. Collins, D. H. Chow, D. Z.-Y. Ting, E. T. Yu, J. R. Söderström, and T. C. McGill, submitted to *Superlattices and Microstructures* (1990).

Abstract

This thesis describes investigations concerning the physics and applications of band edge discontinuities in semiconductor heterojunctions. An historical overview and an assessment of the current experimental and theoretical understanding of band offsets are presented in Chapter 1. The physics and potential device applications of tunneling phenomena in semiconductor heterostructures are also introduced.

Part I of the thesis describes measurements of semiconductor heterojunction valence-band offsets by x-ray photoelectron spectroscopy (XPS). In Chapter 2, the basic physical principles of XPS are discussed, with emphasis on capabilities of the technique that are especially relevant in studies of semiconductor interfaces. The experimental procedures and data analysis techniques required to measure band offsets by XPS are also described. A measurement of the GaAs/AlAs (100) valence-band offset is presented in Chapter 3. Our results are discussed in the context of the recent controversy surrounding the value of the GaAs/AlAs band offset. The relationship between band offset commutativity and interfacial quality as elucidated by our experiments and by previously reported results is also explained. A measurement of the valence band offset for the lattice-mismatched Si/Ge (001) heterojunction system is described in Chapter 4. A method developed to extend the applicability of the XPS technique to the determination of strain-dependent band offsets is presented and applied to the Si/Ge (001) material system. Our results demonstrate the profound influence of strain on band offset values in lattice-mismatched heterojunctions. An interpolation scheme for determining band offset values for $Si_{1-x}Ge_x$ alloy heterojunctions is described, and is used to demonstrate the consistency of our results with $Si/Si_{1-x}Ge_x$ modulation doping experiments that have been reported. Studies of band offsets and

interfacial reactions in III-V/II-VI heterojunction systems are reported in Chapter 5. Specifically, band offsets and interface chemistry have been examined in the AlSb/GaSb/ZnTe material system; the influence of interfacial chemistry on band offset values is demonstrated, and implications of our work for the viability of proposed heterojunction approaches for fabricating visible light emitters are discussed. The measurement of the CdSe/ZnTe (100) valence band offset is described in Chapter 6. Our results are discussed in the context of possible heterojunction approaches for injection of electrons into *p*-ZnTe for fabricating visible light emitters, and implications of our results for the common anion rule are addressed.

Part II of the thesis describes theoretical and experimental studies of tunneling in semiconductor heterostructures. Various theoretical models we have used to simulate the electrical behavior of a wide variety of heterostructure devices are described in Chapter 7. These techniques are applied to the calculation of current-voltage characteristics for double-barrier tunnel structures proposed in the GaAs/ZnSe and InAs/ZnTe material systems. Theoretical and experimental studies of interband transport in the InAs/GaSb/AlSb material system are described in Chapter 8. Band alignments in the InAs/GaSb/AlSb system and material properties of InAs and GaSb are discussed in the context of both fundamental physics and device applications. Attention is then focused on a theoretical and experimental study of transport in the InAs/GaSb/InAs device structure that helped to clarify the basic nature of interband transport and the coupling between conduction-band and valence-band states in different layers of a heterostructure. In Chapter 9, a theoretical study of hole tunneling times in GaAs/AlAs double-barrier heterostructures is presented. The experimental observation of anomalously short hole tunneling times that motivated this work is reviewed, and a phenomenological model explaining this experimental observa-

tion as a consequence of valence-band-mixing is developed.

Contents

Acknowledgements iii

List of Publications vi

Abstract xii

List of Figures xxi

List of Tables xxvi

1 Introduction 1

1.1 Introduction to Thesis 1

1.1.1 Overview 1

1.1.2 Summary of Results 3

1.1.3 Outline of Chapter 8

1.2 Band Offsets in Semiconductor Heterojunctions 9

1.2.1 Motivation 9

1.2.2 Band Offset Theories 12

1.2.2.1 Band Offsets as Bulk Parameters 12

1.2.2.2 Self–Consistent Calculations for Specific Interfaces 26

1.2.3 Measurement of Band Offsets by XPS 32

1.2.4 Other Band Offset Measurement Techniques 37

1.2.5 Overview of Theoretical and Experimental Band Offset Determinations 40

1.3 Tunnel Structures 45

1.3.1 Overview 45

1.3.2 Tunneling Theory and Simulation of Devices 49

1.3.2.1 Band Bending 50

1.3.2.2 Transmission Coefficients and Current-Voltage Characteristics 51

1.3.3 Physics of Interband Tunneling 52

1.3.4 Quantum-Well Band Structure and Tunneling Times for Holes 55

1.4 Outline of Thesis 58

References 64

I Measurement of Band Offsets in Semiconductor Heterojunctions 79

2 Measurement of Band Offsets Using X-Ray Photoelectron Spectroscopy 80

2.1 Introduction 80

2.1.1 Background and Motivation 80

2.1.2 Outline of Chapter 81

2.2 Physical Principles of XPS 82

2.3 Measurement of Band Offsets by XPS 89

2.3.1 Experimental Considerations 89

2.3.2 Data Analysis 96

2.4 Summary of Chapter 102

References 104

3 Commutativity of the GaAs/AlAs (100) Valence-Band Offset 109

3.1 Introduction 109

3.1.1 Background and Motivation 109

3.1.2 Summary of Results 116

3.1.3 Outline of Chapter 117

3.2 Experiment 117

3.2.1 Sample Growth 117

3.2.2 X-ray Photoelectron Spectroscopy Measurements 118

3.3 Results and Discussion 125

3.4 Conclusions 129

References 133

4 Measurement of the Si/Ge (001) Valence-Band Offset: The Role of Strain 138

4.1 Introduction 138

4.1.1 Background and Motivation 138

4.1.2 Summary of Results 152

4.1.3 Outline of Chapter 154

4.2 Experimental Procedure 155

4.3 Sample Growth 157

4.4 XPS Measurements and Data Analysis 162

4.5 X-Ray Diffraction Measurements 173

4.6 Results and Discussion 177

4.7 Band Offsets for Alloy Heterojunctions 181

4.7.1 Interpolation Method for Alloys 181

4.7.2 Comparison with Results for Alloy Heterojunctions 187

4.8 Conclusions 193

References 197

5 III-V/II-VI Heterojunction Systems: The Role of Interfacial Chemistry 204

5.1 Introduction 204

5.1.1 Background and Motivation 204

5.1.2 Summary of Results 210

5.1.3 Outline of Chapter 212

5.2 The AlSb/ZnTe (100) Heterojunction 213

5.2.1 Sample Growth 213

5.2.2 XPS Measurements and Data Analysis 215

5.2.3 Results and Discussion 218

5.3 Transitivity in the AlSb/GaSb/ZnTe Material System 229

5.3.1 The AlSb/GaSb (100) Heterojunction 231

5.3.2 The GaSb/ZnTe (100) Heterojunction 238

5.3.3 Demonstration of Nontransitivity 243

5.4 Direct Observation of Band Offset Variation Arising from Interface Chemistry 248

5.5 Conclusions 253

References 257

6 Measurement of Band Offsets in II-VI Heterojunction Systems: CdSe/ZnTe 263

6.1 Introduction 263

6.1.1 Background and Motivation 263

6.1.2 Summary of Results 267

6.1.3 Outline of Chapter 268

6.2 Experiment 269

6.2.1 Sample Growth 269

6.2.2 XPS Measurements and Data Analysis 270

6.3 Results and Discussion 274

6.4 Conclusions 280

References 282

II Theoretical and Experimental Studies of Tunneling in Semiconductor Heterostructures 286

7 Theoretical Simulation of Novel Semiconductor Tunnel Structures 287

7.1 Introduction 287

7.1.1 Background and Motivation 287

7.1.2 Outline of Chapter 289

7.2 Calculation of Electrostatic Band Bending 290

7.3 Calculation of Transmission Coefficients 297

7.3.1 The One-Band Model 299

7.3.2 Two-Band Models 301

7.3.3 Beyond Two-Band Models 307

7.4 Calculation of Current-Voltage Characteristics 308

7.5 III-V/II-VI Resonant Tunneling Structures 313

7.6 Conclusions 318

References 322

8 Carrier Transport in Two-Terminal Interband Tunnel Structures 325

8.1 Introduction 325

8.1.1 Background and Motivation 325

8.1.2 Summary of Results 328

8.1.3 Outline of Chapter 329

8.2 Overview of Two-Terminal Interband Transport Structures 329

8.3 Interband Transport in InAs/GaSb/InAs Structures 336

8.3.1 Device Structures 337

8.3.2 Calculation of Transmission Coefficients 338

8.3.3 Current-Voltage Characteristics: Theory and Experiment . 345

8.4 Conclusions 347

References 349

9 Calculation of Hole Tunneling Times in GaAs/AlAs Double-Barrier Structures 352

9.1 Introduction 352

9.1.1 Background and Motivation 352

9.1.2 Summary of Results 355

9.1.3 Outline of Chapter 356

9.2 Luttinger-Kohn Valence-Band Hamiltonian 357

9.3 Phenomenological Model for Average Hole Tunneling Times . . . 363

9.4 Comparison with Experimental Results 365

9.5 Transmission Resonances Calculated in the Effective-Bond-Orbital Model 368

9.6 Conclusions 372

References 378

List of Figures

1.1 Possible types of band alignments at a semiconductor interface . . 11

1.2 Band offsets according to the electron affinity rule 14

1.3 Band offsets according to the common anion rule 16

1.4 Band offsets according to the theory of Frensley and Kroemer . . 19

1.5 Band offsets according to the LCAO theory of Harrison 22

1.6 Band offsets according to the theories of Tersoff and of Harrison and Tersoff 25

1.7 Band offsets proposed by Katnani and Margaritondo 27

1.8 Band offsets in the model solid theory of Van de Walle and Martin 30

1.9 Band offsets determined by dielectric midgap energies of Cardona and Christensen 31

1.10 Sample XPS spectrum for GaAs (100) 34

1.11 XPS band-offset measurement technique 36

1.12 The tunnel diode and the double-barrier tunnel structure 47

1.13 Band alignments in the InAs/GaSb/AlSb material system 54

1.14 Transmission coefficient across the InAs/GaSb interface 56

1.15 Valence subband structure in a GaAs/AlAs quantum well 59

2.1 Energy levels in x-ray photoelectron spectroscopy 84

2.2 Sample XPS spectrum for GaAs (100) 86

2.3 Electron mean free path in solids 88

2.4 XPS band-offset measurement technique 90

2.5 Diagram of UHV system 94

2.6 XPS spectrum for Au $4f$ core-level peaks 99

2.7 Representative XPS valence-band spectra 101

3.1 Samples grown for GaAs/AlAs band offset measurement 119

3.2 Schematic energy-band diagram for the GaAs/AlAs heterojunction 121

3.3 XPS spectra for GaAs (100) and AlAs (100) 123

3.4 XPS spectra for GaAs-AlAs (100) and AlAs-GaAs (100) 124

3.5 GaAs/AlAs valence-band offsets reported in the literature 130

3.6 Summary of experimental band offsets for GaAs/AlGaAs 131

4.1 Critical thickness for strain relaxation 150

4.2 Schematic energy-band diagrams for the Si/Ge (100) heterojunction 156

4.3 Samples grown to measure strain-dependent Si $2p$ and Ge $3d$ core-level binding energies 158

4.4 Samples grown to measure strain-dependent Si $2p$ and Ge $3d$ core-level energy separations 159

4.5 XPS spectra for Si (001), Ge (001), and Si/Ge (001) 166

4.6 XPS valence-band spectra for Si (001) and Ge (001) 167

4.7 X-ray rocking-curve spectra for sample with strained Ge film . . . 175

4.8 $\theta/2\theta$ x-ray-diffraction spectrum for Si/Ge superlattice sample . . . 178

4.9 Si $2p$ and Ge $3d$ binding energies and energy separations as functions of strain 179

4.10 Energy band gap in unstrained $Si_{1-x}Ge_x$ alloys 184

4.11 Band offsets for $Si_{1-x}Ge_x/Si_{1-y}Ge_y(001)$ heterojunctions on Si (001) 188

4.12 Band offsets for $Si_{1-x}Ge_x/Si_{1-y}Ge_y$ (001) heterojunctions on Ge (001) 190
4.13 Modulation-doping experiments reported in the literature 194

5.1 Proposed AlSb/ZnTe heterojunction visible LED structure 207
5.2 Proposed AlSb/ZnTe valence-band offset values 208
5.3 Schematic energy-band diagram for the AlSb/ZnTe (100) heterojunction 216
5.4 XPS spectra for AlSb (100), ZnTe (100), and AlSb/ZnTe (100) . . 217
5.5 XPS valence-band spectra for AlSb (100) and ZnTe (100) 219
5.6 Sb 4*d* core-level spectra from bulk AlSb and an AlSb/ZnTe heterojunction 221
5.7 Al 2*p* core-level spectra from bulk AlSb and an AlSb/ZnTe heterojunction 223
5.8 Te 4*d* core-level spectra from bulk AlSb and an AlSb/ZnTe heterojunction 224
5.9 Reaction at the AlSb/ZnTe interface 226
5.10 Proposed AlSb/ZnTe valence-band offset values, and our measured value 228
5.11 Schematic energy-band diagram for the AlSb/GaSb (100) heterojunction 233
5.12 XPS spectra for bulk AlSb (100) and GaSb (100) 234
5.13 XPS valence-band spectrum for GaSb (100) 236
5.14 XPS spectra for AlSb-GaSb and GaSb-AlSb (100) heterojunctions 237
5.15 Schematic energy-band diagram for the GaSb/ZnTe heterojunction 239
5.16 XPS spectra for GaSb (100), ZnTe (100), and GaSb/ZnTe (100) . 242

5.17 Core-level XPS spectra from bulk GaSb, bulk ZnTe, and a GaSb/-ZnTe heterojunction 244

5.18 Nontransitivity in the AlSb/GaSb/ZnTe material system 247

5.19 XPS spectra for GaSb/ZnTe and AlSb/ZnTe heterojunctions grown with initial Zn exposure at the interfaces 250

5.20 Al $2p$ core-level XPS spectra from AlSb/ZnTe samples grown with and without initial exposure to Zn at the interface 252

6.1 Predicted values for the CdSe/ZnTe valence-band offset 266

6.2 Schematic energy-band diagram for the CdSe/ZnTe heterojunction 271

6.3 XPS spectra for cubic CdSe (100), ZnTe (100), and CdSe/ZnTe (100) 273

6.4 XPS valence-band spectra for cubic CdSe (100) and ZnTe (100) . 275

6.5 Predicted CdSe/ZnTe valence-band offset values, and our measured value 278

6.6 Conduction- and valence-band alignments for the CdSe/ZnTe heterojunction 279

7.1 Electron concentration as a function of chemical potential 294

7.2 Band-bending profiles, electric field, and charge density 298

7.3 Transmission coefficients calculated in two-band and eight-band models 309

7.4 InAs/ZnTe double-barrier structure and J–V characteristics . . . 317

7.5 GaAs/ZnSe double-barrier structure and J–V characteristics . . . 319

8.1 Band alignments in the InAs/GaSb/AlSb material system 327

8.2 Energy-band diagrams for RIT and InAs/GaSb/InAs structures . 333

8.3 Schematic energy-band diagrams for InAs/GaSb, InAs/GaSb/-AlSb/GaSb, and InAs/AlSb/InAs/GaSb devices 335
8.4 Current-voltage characteristics for the InAs/GaSb/InAs device . . 339
8.5 Transmission coefficients for InAs/GaSb/InAs devices with varying GaSb layer width 342
8.6 Theoretical and experimental resonant currents for the InAs/-GaSb/InAs structure 346

9.1 Measured tunneling times for GaAs/AlAs double-barrier heterostructures 354
9.2 Valence subband structure in a GaAs/AlAs quantum well 360
9.3 Probability densities for heavy-hole and light-hole components of a quantum-well valence subband 361
9.4 Decomposition of quantum-well subband into zone-center basis components 362
9.5 Hole tunneling time as a function of $k_{||}$ 366
9.6 Calculated hole and electron tunneling times and experimentally measured tunneling times 367
9.7 Temperature dependence of average hole tunneling times 369
9.8 Hole tunneling time as a function of $k_{||}$ in the effective-bond-orbital model 371
9.9 Hole and electron tunneling times calculated in the effective bond orbital model, and experimentally measured tunneling times . . . 373
9.10 Temperature dependence of average hole tunneling times in the effective-bond-orbital model 374

List of Tables

3.1 Core-level to valence-band-edge binding energies for GaAs (100) and AlAs (100) 126

3.2 Core-level energy separations for GaAs/AlAs heterojunctions . . . 127

4.1 Samples grown to measure strain-dependent Si $2p$ and Ge $3d$ core-level binding energies 163

4.2 Samples grown to measure strain-dependent Si $2p$ to Ge $3d$ core-level energy separations 164

4.3 Si and Ge material parameters for alloy band offset interpolation . 183

8.1 Summary of two-terminal interband device performance 331

Chapter 1

Introduction

1.1 Introduction to Thesis

1.1.1 Overview

This thesis describes various investigations concerning the physics and applications of semiconductor heterostructures. In Part I, attention is focused on the issue of band offsets, i.e., the discontinuities in energy of the conduction-band and valence-band edges at a heterojunction interface. Band offset values are of critical importance in determining the performance and even the feasibility of device concepts in a given material system. However, the factors that determine the values of the conduction-band and valence-band offsets at a given interface are not well known; theoretical predictions of band offset values have historically been notoriously unreliable, and band offset values for each material system must therefore be determined experimentally. The work reported in this thesis provides experimental band offset values for a number of semiconductor heterojunctions currently and potentially of interest for various device applications. These measurements also provide valuable data needed to facilitate the development of a

predictive theory of band offsets. In addition, we have investigated the influence on band offset values of effects such as strain and chemical reactivity at certain semiconductor interfaces, and have demonstrated that such effects can exert a very strong influence on band offset values.

Part II of this thesis focuses on tunneling processes in semiconductor heterostructures. Theoretical simulations providing a semiquantitative description of the electrical behavior of various types of tunnel structures have been developed, and are used to design and analyze tunnel structures in various material systems. A material system of particular interest is InAs/GaSb/AlSb; the unusual Type II broken-gap band alignment between InAs and GaSb, in which the conduction band edge of InAs is lower in energy than the valence-band edge of GaSb, permits great flexibility in the design of heterostructure tunnel devices, and contributes to enhanced device performance. A wide variety of tunnel structures exhibiting negative differential resistance have been demonstrated in the McGill group laboratories. The InAs/GaSb band alignment also gives rise to coupling between InAs conduction-band states and GaSb valence-band states; theoretical and experimental studies we have performed provide insight into the basic nature of this interaction. Also of interest in the operation of tunnel structures is the fundamental time scale for the relevant tunneling processes; the issue of tunneling times arises because of the use of double-barrier tunnel devices in high-speed oscillators, and interest in the application of tunnel structures in high-speed electrical circuits. Although tunneling times for electrons, rather than for holes, are the more relevant in most conventional double-barrier structures, tunneling times for holes can be of great importance in studies of tunneling times involving photoexcited carriers and in novel device structures involving tunneling transport through valence-band states. Our studies of hole tunneling times indicate that mixing between light-hole and heavy-hole states, which arises only in realistic,

multiband theoretical models of valence-band structure, is extremely important in determining hole tunneling times; actual tunneling times for holes can differ by orders of magnitude from times calculated using simple band structure models in which light-hole and heavy-hole states do not interact.

1.1.2 Summary of Results

In Part I of this thesis we discuss results of x-ray photoelectron spectroscopy (XPS) measurements of valence-band offsets in a number of semiconductor heterojunction systems. The first system we consider is the GaAs/AlAs (100) heterojunction. Using XPS, we obtain a valence-band offset $\Delta E_v = 0.46 \pm 0.07$ eV for the GaAs/AlAs (100) interface, independent of growth sequence; i.e., the band offset value is the same, within experimental error, for both GaAs grown on AlAs and AlAs grown on GaAs. Our results therefore confirm the commutativity of the GaAs/AlAs (100) band offset, and are consistent with other recent measurements of the GaAs/$Al_xGa_{1-x}As$ band offset. We attribute this confirmation of commutativity to the high quality of our epitaxial growths; our measurements indicate that it is possible to grow GaAs/AlAs (100) heterostructures consistently and reproducibly that do not suffer from the dependence on growth sequence observed by other investigators[1, 2].

Next we investigate the effect of strain on band offset values in the $Si_{1-x}Ge_x$ (001) material system. These measurements represent the first full extension of the XPS technique to the study of band offsets in heavily lattice-mismatched heterojunctions with well-characterized strain configurations. Using novel low-temperature growth techniques, we are able to obtain pure Si, pure Ge, and Si/Ge heterojunctions with varying degrees of strain, from which the strain dependence of the $Si_{1-x}Ge_x$ (001) valence-band offset is determined. Our measurements yield

$\Delta E_v = 0.83 \pm 0.11$ eV for Ge coherently strained to Si ($a_{\|} = 5.431$ Å), and $\Delta E_v = 0.22 \pm 0.13$ eV for Si coherently strained to Ge ($a_{\|} = 5.658$ Å). These results are in good agreement with other theoretical[3, 4] and experimental[5] results that have been reported. In addition, interpolation from our results to obtain band offset values for $Si/Si_{1-x}Ge_x$ interfaces yields band offset values that are consistent with reported observations of modulation doping in $Si/Si_{1-x}Ge_x$ heterojunctions[6, 7].

The feasibility of a proposed AlSb/ZnTe heterojunction LED concept, and the possible influence of interfacial reactions on band offset values, are addressed in our studies of III-V/II-VI heterojunctions. The initial motivation for studying III-V/II-VI material systems was to measure the AlSb/ZnTe (100) valence band offset to determine the feasibility of an AlSb/ZnTe visible LED concept proposed by McCaldin and McGill[8]. Our measurements yield a valence-band offset $\Delta E_v = 0.42 \pm 0.07$ eV, corresponding to a conduction-band offset $\Delta E_c = 0.21 \pm 0.07$ eV. This value for the conduction-band offset indicates that, on the basis of material dopability and band alignments, the proposed LED concept should be feasible. Evidence is also found indicating that an intermediate, chemically reacted layer containing Al and Te, probably forming Al_2Te_3, is present at the AlSb/ZnTe (100) interface. To determine the effect of this interfacial layer on band offset values, transitivity of band offsets is checked for the AlSb/GaSb/-ZnTe system. Our measurements demonstrate a deviation from transitivity of 0.21 ± 0.05 eV; since the transitivity rule is expected to hold for ideal, abrupt interfaces, this result suggests that interfacial reactions at the III-V/II-VI interfaces (AlSb/ZnTe and GaSb/ZnTe) exert a significant influence on band offset values. Additional experiments demonstrate that certain changes in growth conditions induce definite shifts in the AlSb/ZnTe band offset value; a correlation is observed between partial suppression of the reaction at the AlSb/ZnTe interface

and a shift in the valence-band offset that reduces the deviation from transitivity of band offsets.

A valence-band offset value is also determined, using XPS, for the CdSe/ZnTe heterojunction, another material system potentially of interest for application in visible light emitters. Cubic CdSe is closely lattice-matched to ZnTe, and a favorable band alignment might allow injection of electrons from n-CdSe into p-ZnTe. The band offset in this material system is also of interest for the information it might provide about band offsets in other heterojunction systems containing Se and Te, and about the general validity of the common anion rule[9]. We obtain a valence-band offset for CdSe/ZnTe of 0.64 ± 0.07 eV, corresponding to a conduction-band offset $\Delta E_c = 1.22 \pm 0.07$ eV. These values indicate that injection of electrons directly from n-CdSe into p-ZnTe is not feasible; however, electron injection from n-$(CdSe)_{1-x}(ZnTe)_x$ into p-ZnTe remains a possibility, depending on the dopability of n-$(CdSe)_{1-x}(ZnTe)_x$ alloys. Comparison of the CdSe/ZnTe valence-band offset to a value of 0.98 ± 0.10 eV proposed[10] for the ZnSe/ZnTe valence-band offset also casts some doubt upon the general validity of the common anion rule, especially for heavily lattice-mismatched material systems such as ZnSe/ZnTe.

Part II of the thesis concerns theoretical and experimental studies of tunneling in semiconductors. We develop a number of techniques to simulate the electrical behavior of semiconductor heterostructure devices. The initial step in our simulation is to solve Poisson's equation in a device structure to obtain a profile of the electrostatic band bending in a device. Transmission coefficients are then calculated for the resulting device profile, from which current-voltage characteristics can be computed. These simulations yield a semiquantitative description of device behavior, and are shown to be extremely useful in analyzing device behavior and designing new device structures. As an illustration of these techniques,

we calculate current-voltage characteristics for double-barrier tunnel structures realized in the GaAs/ZnSe and InAs/ZnTe material systems, which are expected to yield device performance superior in many respects to that obtained in more conventional GaAs/$Al_xGa_{1-x}As$ devices, and which could also provide a useful method for characterizing growth of these and other III-V/II-VI heterojunction systems.

We have performed a number of studies of device structures in the InAs/-GaSb/AlSb material system. The unusual Type II broken-gap band alignment between InAs and GaSb, in which the InAs conduction-band edge is lower in energy than the GaSb valence-band edge, allows great flexibility in the design of tunnel structures exhibiting negative differential resistance, and contributes to the enhanced device performance exhibited by a number of InAs/GaSb/-AlSb heterostructure devices. A wide variety of interband transport devices, so-called because of the interaction between InAs conduction-band states and GaSb valence-band states that overlap in energy, have been grown, fabricated, and characterized in the McGill group laboratories. In this thesis we focus on one particular theoretical and experimental investigation of current-voltage characteristics in an InAs/GaSb/InAs device structure; this study demonstrates clearly the resonant nature of transport through the GaSb quantum well, despite the absence of classically forbidden barrier regions in the transport path across the device. By examining theoretically calculated and experimentally measured resonant current densities in these devices as a function of the GaSb layer width, we demonstrate that transmission resonances are formed solely because of the imperfect matching of wave functions at the InAs/GaSb interface. Our results also suggest that coupling between InAs conduction-band and GaSb heavy-hole states has relatively little influence on the current-voltage characteristics of these devices; as expected, the resonant current is dominated by the interaction between

the conduction-band and light-hole states.

Finally, we develop a model for calculating tunneling escape times for holes in a double-barrier heterostructure that explains anomalously short hole tunneling times in GaAs/AlAs double-barrier structrures measured by Jackson et al.[11] using photoluminescence excitation correlation spectroscopy. The tunneling time in a double-barrier structure is of great interest from a fundamental physical perspective, and also because it will limit the ultimate performance of high-speed devices, such as high-frequency oscillators, that utilize double-barrier tunnel structures. Our model demonstrates that, because of band-mixing effects, tunneling times for holes are much shorter than one would expect from a simple calculation of heavy-hole tunneling times in a double-barrier structure. A simple model in which band-mixing effects are ignored predicts that hole tunneling times should be much longer than electron tunneling times. The measurements of Ref. [11], however, indicate that tunneling times for electrons and holes are very similar. By including band-mixing effects in a phenomenological model for calculating average tunneling times for a population of holes in the lowest quantum-well valence subband, we obtain average hole tunneling times that are comparable to electron tunneling times and are in good agreement with the experimental results of Ref. [11]. More recent calculations using a more elaborate band-structure model to calculate transmission coefficients for valence-band states in a GaAs/AlAs double-barrier heterostructure confirm the basic validity of our earlier phenomenological model for calculating average hole tunneling times.

1.1.3 Outline of Chapter

An overview of various issues that arise in the study of semiconductor heterojunction band offsets is given in Section 1.2. A summary of several theoretical and semiempirical treatments of band offsets is given in Section 1.2.2. Early treatments of band offsets as characteristics of bulk semiconductors are described, followed by a discussion of more recent calculations that explicitly include properties of specific interfaces. Experimental considerations are addressed in Sections 1.2.3 through 1.2.5. The use of x-ray photoelectron spectroscopy to measure valence-band offsets is described in Section 1.2.3, and some other methods that have been used to measure band offset values are discussed in Section 1.2.4. A brief evaluation of the current state of understanding of band offsets is given in Section 1.2.5.

Section 1.3 describes some issues of interest in our studies of tunneling in semiconductors. An overview of the issues we have addressed is given in Section 1.3.1. The techniques we have used to simulate the electrical behavior of heterostructure devices are discussed in Section 1.3.2, and some studies of interband tunneling in the InAs/GaSb/AlSb material system are summarized in Section 1.3.3. Section 1.3.4 describes some theoretical results we have obtained that explain anomalously short hole tunneling times that were observed in time-resolved photoexcitation experiments on GaAs/AlAs double-barrier structures. Finally, an outline of the thesis is presented in Section 1.4.

1.2 Band Offsets in Semiconductor Heterojunctions

1.2.1 Motivation

The use of heterojunctions in the design and fabrication of semiconductor devices has yielded dramatic improvements in the performance attainable with existing device concepts[12, 13, 14, 15], and has led to the development of a variety of new structures that could not have been realized using simple homojunction technology [16, 17, 18, 19, 20, 21, 22]. Among the most important physical parameters for a given heterojunction system are the conduction-band and valence-band offsets; indeed, the quality and even the feasibility of heterojunction device concepts often depend crucially on the values of these band offsets.

Fig. 1.1 shows the various types of band alignments that can arise in semiconductor interfaces: Type I, Type II staggered, Type II broken-gap, and Type III. A Type I alignment, in which the band gap of one semiconductor lies completely within the band gap of the other, occurs in a large number of heterojunction systems, e.g., GaAs/$Al_xGa_{1-x}As$ and AlSb/GaSb. A Type II staggered alignment occurs when the band gaps of the two materials overlap, but one does not completely enclose the other, and is characteristic of interfaces such as InAs/AlSb and CdSe/ZnTe. A Type II broken-gap alignment occurs when the band gaps of the two materials do not overlap at all in energy, and occurs in the InAs/GaSb heterojunction. A Type III alignment occurs for the HgTe/CdTe heterojunction, and results from the semimetallic nature of HgTe. The device concepts that can be implemented successfully in a given heterojunction system will depend very strongly on the type of band alignment characteristic of that heterojunction, and heterojunction device performance will often depend critically on the exact values

of the band offsets.

One would like to have a reliable yet relatively simple way to obtain band offset values for novel heterojunction systems to help determine their suitability for various device applications. Unfortunately, our current theoretical understanding of electronic structure at semiconductor interfaces is such that reliable predictions of band offset values to the accuracy required for evaluation of device concepts cannot be obtained from any existing theory. To be of use in the quantitative evaluation and design of a device, a band offset must be known to an accuracy of ± 0.1 eV or better; however, predicted band offset values for many heterojunctions of current interest extend over a range of approximately 1 eV or more, rendering them of little use in determining the viability of various device structures in these material systems.

The large discrepancies among theoretically predicted band offset values for many heterojunction systems make apparent the need for reliable experimental determinations of band offset values. A large number of techniques have been used to measure band offsets for various heterojunction systems[10, 23, 24, 25, 26, 27, 28, 29, 30, 31]. However, the technical difficulty and often indirect nature of these measurements have led to sizable discrepancies in measured band offset values. Until very recently, the value of the valence-band offset even for the extensively studied and supposedly well–understood $GaAs/Al_xGa_{1-x}As$ heterojunction system was a subject of considerable controversy[2, 24, 26, 27, 28, 29, 30, 32, 33, 34, 35, 36, 37, 38]. An additional consideration for certain heterojunction systems, particularly those involving II-VI semiconductors, is that many band offset measurement techniques require the growth and fabrication of functional electrical devices. Because processing technologies for many semiconductors are not well developed, band-offset measurement techniques requiring device fabrication are ill-suited to the study of novel

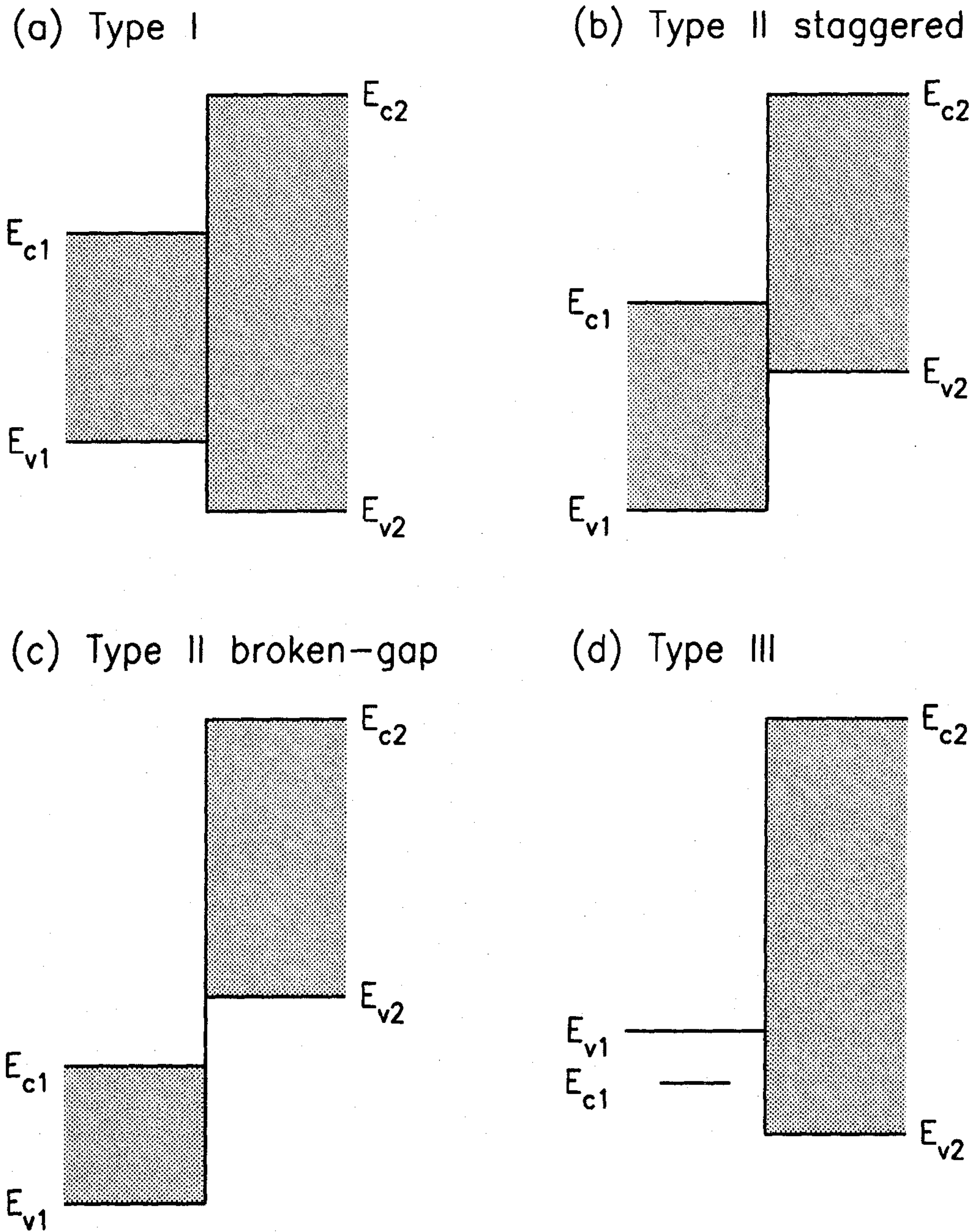

Figure 1.1: Possible types of band alignments at a semiconductor interface. Conduction-band-edge and valence-band-edge positions for each material have been labeled E_c and E_v, respectively, with the shaded regions indicating the forbidden energy gap in each material.

heterojunction systems. In the work presented in this thesis, x-ray photoelectron spectroscopy has been used to measure valence-band offsets for a number of novel semiconductor heterojunction systems. This technique has the advantages that the band offset is measured directly, that the structures required are very simple, and that fabrication of electrical devices is not required.

1.2.2 Band Offset Theories

We have divided theoretical treatments of semiconductor heterojunction band offsets into two categories — those that assume the electronic states in every semiconductor can be placed on a single common energy scale, and therefore inherently treat the band offset as a bulk parameter independent of the detailed structure of a specific interface, and those that include both heterojunction constituents in a single calculation, thereby yielding explicitly the electronic structure of each heterojunction considered, and allowing the influence of variables such as strain and crystal orientation to be studied.

1.2.2.1 Band Offsets as Bulk Parameters

Electron Affinity Rule

The earliest attempts to describe band offsets theoretically assumed that band offset values were determined by the bulklike properties of each individual semiconductor, and therefore attempted to place the electronic levels in every material on a single, absolute energy scale. Band offsets were then determined by the relative positions of each material on this absolute energy scale. The first such model was the so-called "electron affinity rule"[39, 40], which states that the conduction band offset ΔE_c is given simply by the difference in the electron affinities of the

two heterojunction constituents. Experimentally determined electron affinities are used to obtain values for conduction band offsets.

Because the electron affinity is an experimental measure of the energy of the conduction band edge relative to the vacuum level, the essential assumption of the electron affinity rule is that the vacuum level serves as a valid common energy reference for all materials. A major conceptual weakness of this rule is that electron affinities reflect potential shifts arising from surface electronic structure, rather than shifts arising from charge redistribution at an actual interface; a more practical consideration is that large uncertainties in experimental electron-affinity values for many materials produce correspondingly large ambiguities in predicted band offset values.

Fig. 1.2 shows the energy band gaps of several semiconductors plotted on the absolute energy scale given by the electron affinity rule as a function of lattice constant, a data presentation format often referred to as a McCaldin diagram. Electron-affinity data were taken from the compilation in Ref. [40]. The origin of the energy scale is taken to be the valence-band edge of GaAs. For each material, the position of the energy band gap is indicated by a vertical line, with solid lines representing direct band gaps and dashed lines representing indirect gaps. The conduction- and valence-band edges are indicated by horizontal bars. The conduction- and valence-band offsets given by the electron affinity rule can be determined directly from this figure.

Common Anion Rules

A number of other semi-empirical "rules" have been proposed as at least qualitative guides for predicting band offset values. Among the more widely quoted of these have been the so-called "common anion rules," proposed originally by McCaldin, McGill, and Mead[9], with a modified, weaker form later postulated

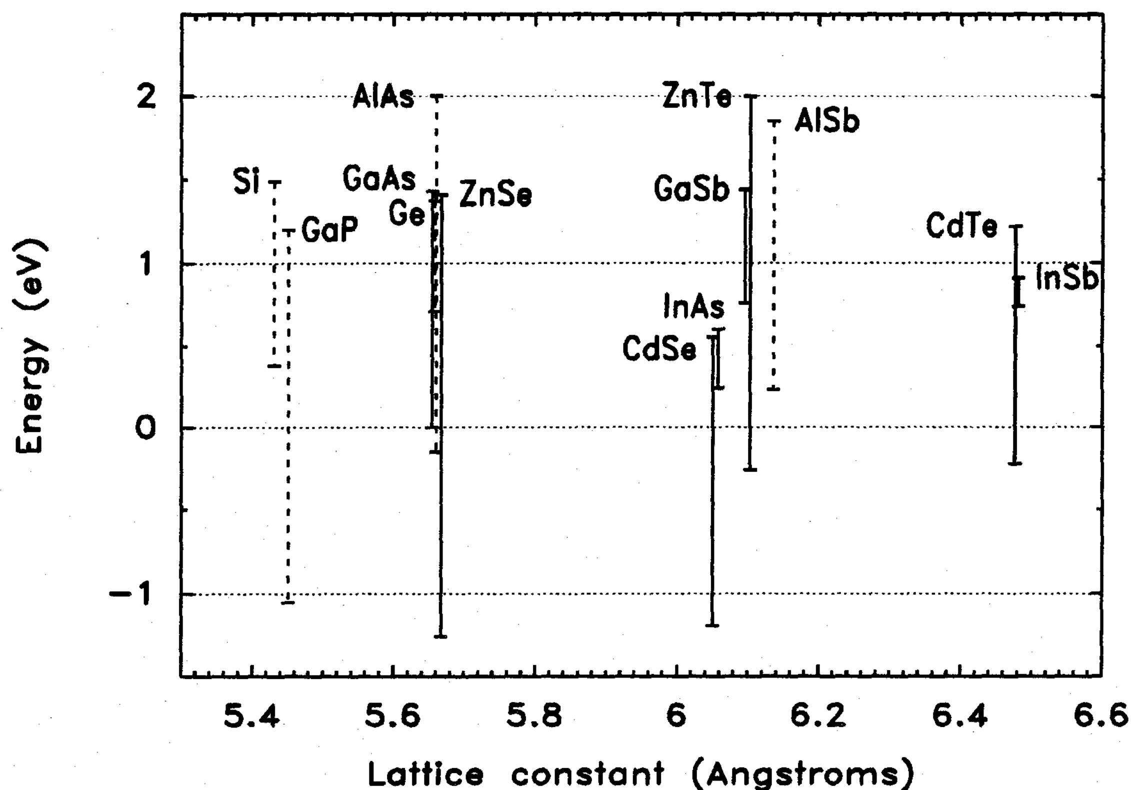

Figure 1.2: Energy band gaps of selected semiconductors plotted as a function of lattice constant on an absolute energy scale as determined by the electron affinity rule. The origin of the energy scale is taken to be the valence-band edge of GaAs. Direct band gaps are indicated by solid vertical lines, indirect gaps by dashed lines. Conduction- and valence-band offsets can be determined directly from the figure.

by Menéndez et al.[41]. The physical motivation for the original common anion rule arises from well-established theoretical evidence that in compound semiconductors, the valence-band states are derived primarily from *p*-like atomic orbitals of the anion[42]. One might then expect that the position of the semiconductor valence-band edge on an absolute energy scale would be determined primarily by the energies of the outermost (valence) electrons of the anion. In their original paper, McCaldin et al. pointed out that the Au Schottky barrier height for a large number of III-V and II-VI semiconductors depended only on the electronegativity of the anion. It was later proposed[44] that this correlation should extend to band offset values as well, leading to the postulate that, for a large number of compound semiconductors (materials containing Al being the most notable exception), the valence-band offset in a heterojunction should depend only on the difference in anion electronegativity for the two constituent materials. Fig. 1.3 shows the energy band gaps of several semiconductors plotted as a function of lattice constant on the absolute energy scale determined by the common anion rule.

The modified version of the common anion rule proposed by Menéndez et al.[41] states that the valence-band offset in a heterojunction system in which the constituents share a common anion is determined primarily by the two cations. This rule was proposed on the basis of experimental evidence from the GaAs/-$Al_xGa_{1-x}As$ and GaSb/$Al_xGa_{1-x}Sb$ heterojunctions and the theoretical predictions of Tersoff[52, 53] for these heterojunctions and for the GaP/InP, GaAs/-InAs, and GaSb/InSb material systems. Unfortunately, considerations of lattice match severely limit the number of heterojunction systems for which this rule can be tested; substituting Al for Ga or Hg for Cd are the only cation changes that preserves the lattice constant. In lattice-mismatched heterojunctions, strain effects will most likely overwhelm any potential deviation from the modified com-

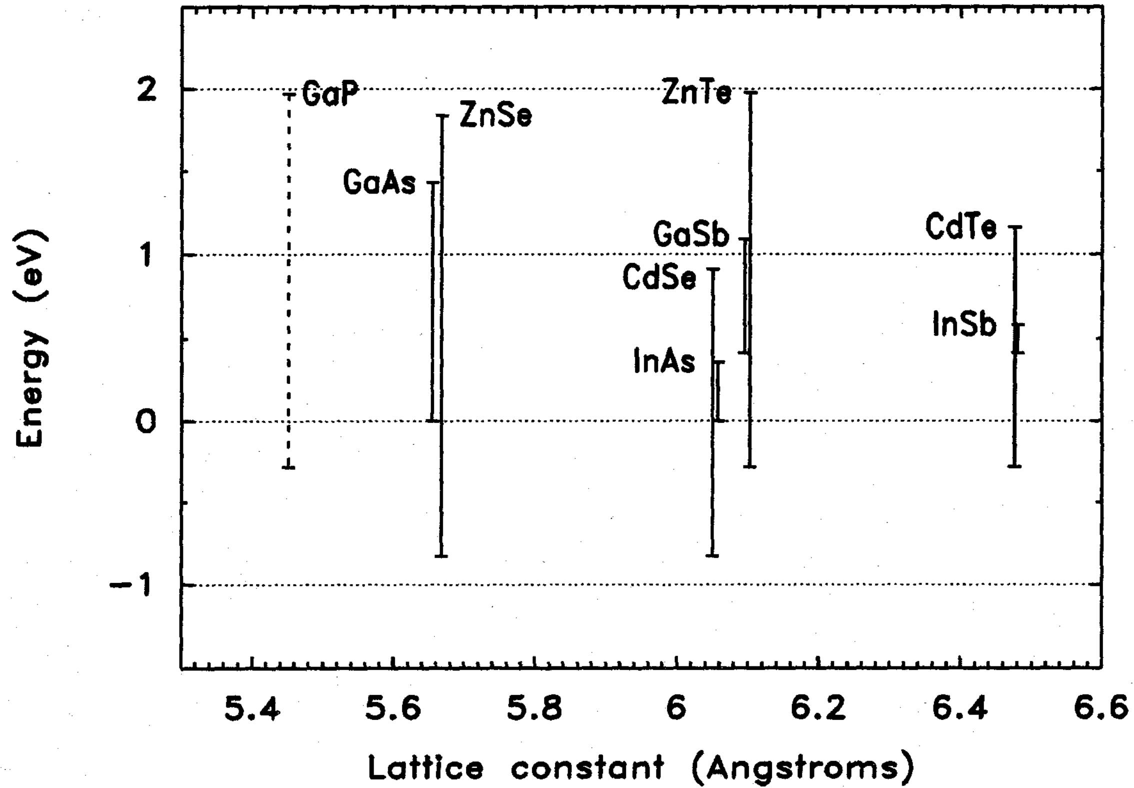

Figure 1.3: Energy band gaps of selected semiconductors plotted as a function of lattice constant on an absolute energy scale determined by anion electronegativity, as postulated by the common anion rule of McCaldin, McGill, and Mead. Compounds containing Al have been omitted from the plot. The origin of the energy scale is taken to be the valence band edge of GaAs. Direct band gaps are indicated by solid vertical lines, indirect gaps by dashed lines. Conduction and valence band offsets can be determined directly from the figure.

mon anion rule of Menéndez. However, the apparent validity of this rule for the $GaAs/Al_xGa_{1-x}As$ and $GaSb/Al_xGa_{1-x}Sb$ heterojunctions might provide some useful insight into the basic physics of band offsets.

Pseudopotential Theory of Frensley and Kroemer

The first attempt to calculate band offset values without the use of experimental data from vacuum–semiconductor or metal–semiconductor interfaces was the pseudopotential theory of Frensley and Kroemer[44, 45]. In this theory, a pseudopotential calculation was used to obtain the bulk band structure of each semiconductor, with a self–consistency condition enforced for the electrostatic potential and the charge density calculated from valence-band wave functions. Once the bulk band structure was obtained for each individual semiconductor, the band offsets at a heterojunction were obtained by matching the energies of the interstitial potentials for the two heterojunction constituents.

This theory was subsequently refined to include an approximate correction arising from heterojunction dipoles induced by charge redistribution near the interface[45]. An approximate calculation of heterojunction dipole effects was made by estimating the effective charge on atoms near the interface, using the electronegativities of each atom and its nearest neighbors. This scheme leads to an effective "electronegativity potential" for each semiconductor. The correction to the band offsets arising from heterojunction dipole effects is then simply the difference in the electronegativity potential for the two heterojunction constituents.

An interesting consequence of this result is that even when corrections arising from heterojunction dipole effects are included, band offset values are still predicted to be transitive; i.e., for three semiconductors labeled A, B, and C, the

following rule should be obeyed:

$$\Delta E_v(A/B) + \Delta E_v(B/C) + \Delta E_v(C/A) = 0. \tag{1.1}$$

While the validity of this rule is obvious for treatments, such as the common anion and electron affinity rules, which do not include any effects specific to a particular interface, it is not obvious that band offsets should be transitive when the detailed properties of each heterojunction interface have been taken into account. The theory of Frensley and Kroemer, and in particular the ability to define an effective electronegativity potential for each material that accounts for interfacial dipole effects, therefore suggests that the concept of band offsets as quantities determined primarily by properties of bulk semiconductors may be physically sound.

Figs. 1.4(a) and 1.4(b) show the band gaps of several semiconductors on absolute energy scales determined by the Frensley-Kroemer pseudopotential theory. Corrections arising from heterojunction dipole effects have been neglected in Fig. 1.4(a), and included in Fig. 1.4(b). In many cases the dipole corrections are extremely large, ranging up to several tenths of an electron volt or greater. In particular, there is a marked decrease in the position of each material on the energy scale with increasing lattice constant; this trend appears to arise from the decrease in electronegativity with increasing atomic number (and therefore increasing lattice constant) for atoms from a single column of the periodic table.

LCAO Theory of Harrison

Another early theory of heterojunction band offsets, one that remains widely quoted, is the LCAO (Linear Combination of Atomic Orbitals) theory of Harrison[46]. In Harrison's approach, the electronic states in a semiconductor

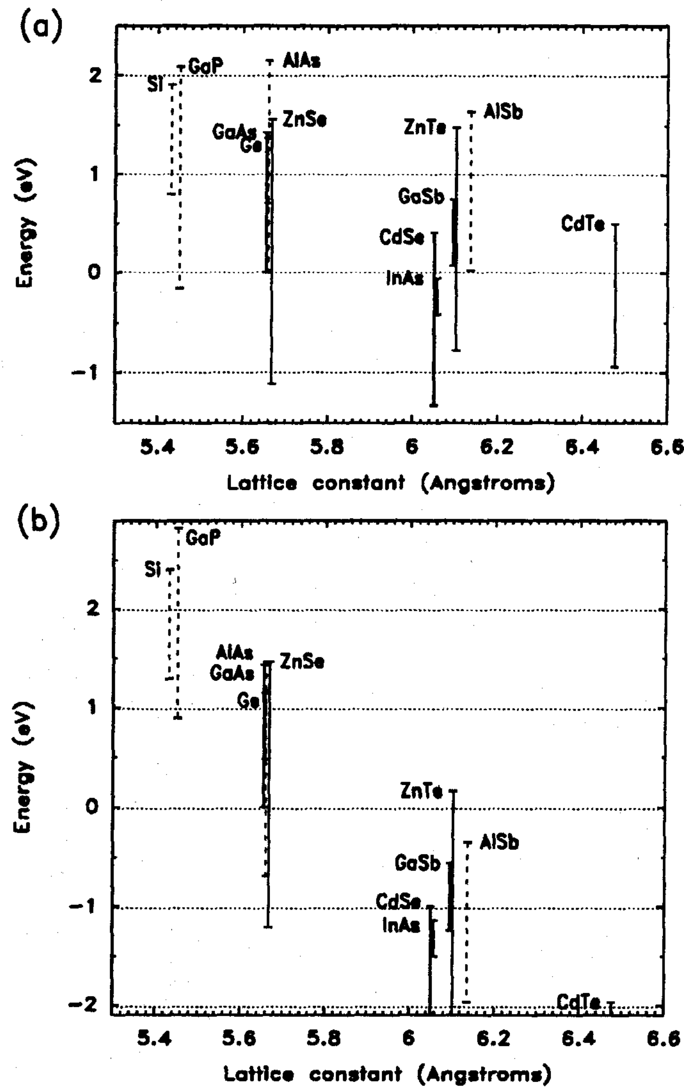

Figure 1.4: Energy band gaps of several selected semiconductors plotted as a function of lattice constant on an absolute energy scale determined by the Frensley-Kroemer pseudopotential theory. The two plots have been constructed (a) neglecting and (b) including the electronegativity potential, which provides an approximate correction for effects arising from the formation of heterojunction dipoles.

are constructed as a superposition of individual atomic orbitals. It is claimed that an adequate description of the relevant electronic structure in each material can be obtained using four orbitals — a single atomic s state and three atomic p states — for each of the two atoms in the zincblende primitive cell. The position of the valence-band edge is then given by[46, 47]

$$E_v = \frac{\epsilon_p^c + \epsilon_p^a}{2} - \left[\left(\frac{\epsilon_p^c - \epsilon_p^a}{2} \right)^2 + V_{xx}^2 \right]^{1/2}, \tag{1.2}$$

where ϵ_p^c is the on-site energy of the cation p state and ϵ_p^a is the on-site energy of the anion p state, both taken from calculated atomic values. V_{xx} is a matrix element between atomic p states for adjacent atoms, and is given approximately by[46]

$$V_{xx} = 2.16\hbar^2/md^2, \tag{1.3}$$

where the numerical coefficient has been chosen to agree with values obtained by Chadi and Cohen[47] to fit the true bands of Si and Ge. The valence-band-edge energies obtained using the LCAO approach are therefore automatically given on the absolute energy scale determined by the individual atomic-state energies, and valence-band offsets are computed simply by taking the difference between valence-band-edge energies on this common energy scale for the two heterojunction materials. Conduction-band offsets can be determined from the valence-band offset and experimental band gaps for each material. As is the case for the early semi–empirical rules and the original theory of Frensley and Kroemer, Harrison's LCAO theory does not include any correction for heterojunction dipole effects.

Fig. 1.5 shows the energy band gaps of several semiconductors plotted as a function of lattice constant on a common energy scale calculated using Harrison's LCAO theory. The values shown in the figure were calculated by Harrison using atomic p-state energies taken from the calculations of Herman and Skillman[48]. Harrison later modified his theory by adding excited s states to his basis set and

adjusting the interatomic matrix elements[49]. These modifications and the use of Hartree-Fock atomic energies yielded a better description of the conduction bands, and allowed both dielectric and elastic properties to be described using a single set of parameters, which had not been possible in the earlier version of his theory. Kraut[50] has recalculated the valence-band-edge energies, using Harrison's LCAO theory of band offsets in conjunction with Hartree-Fock neutral atom ionization energies computed by Mann[51]. However, valence-band offsets obtained in this way were found by Kraut to be in poorer agreement with available experimental results than the original calculations of Harrison using the Herman-Skillman atomic energies.

Interface Dipole Theories

A number of more recent theories, such as those of Tersoff[52, 53] and of Harrison and Tersoff[54], have argued that interfacial dipoles, rather than bulk semiconductor energy levels, are the dominant factor in determining band offset values. The physical principle underlying the theories both of Tersoff and of Harrison and Tersoff is that at a semiconductor heterojunction, the energy gaps will align such that the interface dipole is minimized. It is argued that, by analyzing the band structure of each individual semiconductor, a "midgap," "pinning," or "charge neutrality" reference energy level, at which evanescent states in the band gap are composed equally of conduction-bandlike and valence-bandlike states, can be determined for each material. Band offsets are then determined by aligning the midgap energies of each material at a heterojunction interface, a procedure that effectively minimizes the electrostatic dipole formed at the interface.

The basic concept of a charge neutrality energy level was proposed by Tejedor and Flores[55] for calculating Schottky barrier heights in metal-semiconductor interfaces. This idea was later extended[56, 57] to the calculation of band offsets

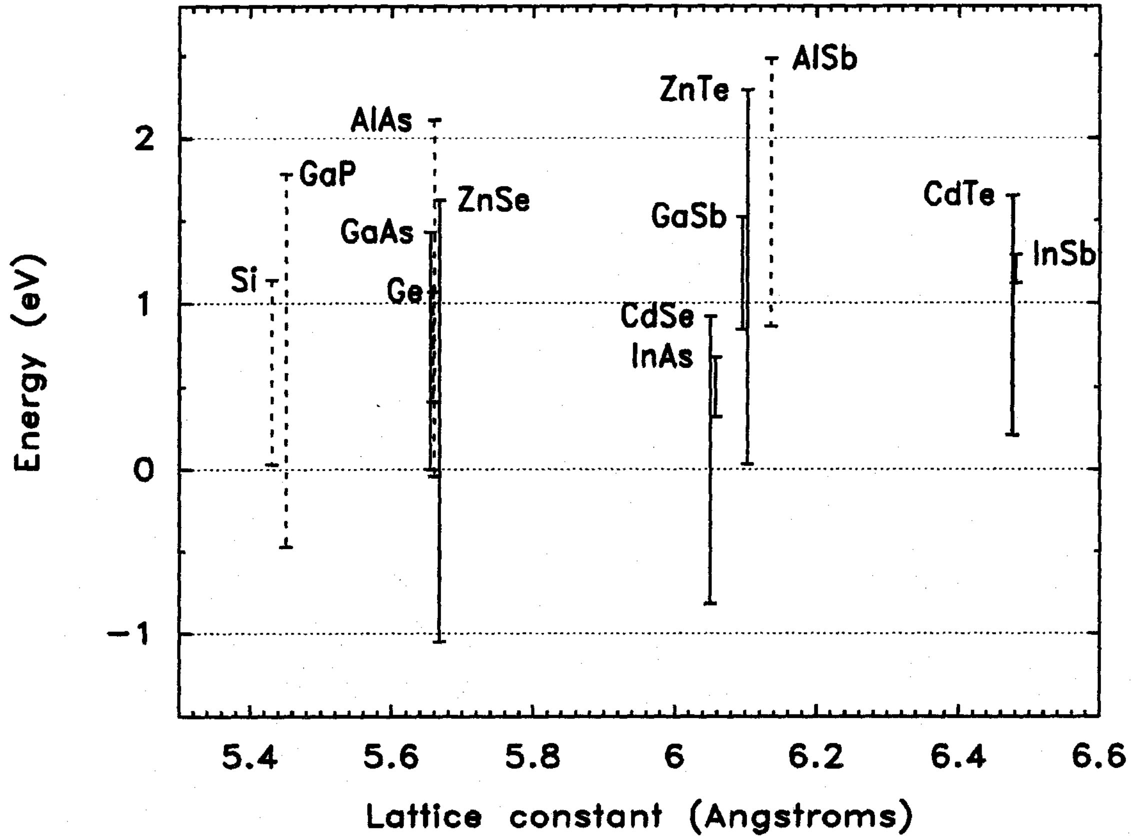

Figure 1.5: Energy band gaps of selected semiconductors plotted as a function of lattice constant on an absolute energy scale calculated using the LCAO theory of Harrison. The origin of the energy scale is taken to be the valence band edge of GaAs. Direct band gaps are indicated by solid vertical lines, indirect gaps by dashed lines. Conduction and valence band offsets can be determined directly from the figure.

in semiconductor heterojunctions. The influence of interfacial dipoles, and the relevance of the charge neutrality level, is perhaps most easily understood by first considering the case of a metal-metal junction[53]. At a metal-metal interface, a misalignment of the work functions, or equivalently of the electronegativities, of the two metals will induce a charge transfer, resulting in the formation of a dipole. However, the essentially infinite dielectric constant of a metal will screen any discontinuity in the electronegativity and yield a simple alignment of the Fermi level across the interface.

For semiconductors, Tersoff[52, 53, 58] argued for the existence of a so-called "midgap" level corresponding to the energy in the band gap at which a surface, interface, or defect state induced in the band gap contains equal conduction- and valence-band character. A discontinuity in the midgap energy would induce charge transfer and the formation of a dipole at the interface; discontinuities in the midgap energy would therefore be screened by the dielectric constant of the semiconductors. The band alignment at a semiconductor heterojunction would therefore be within an energy V/ϵ of the alignment determined by a rigorous alignment of the midgap energies, where V is the discontinuity in the midgap energy corresponding to theories in which interfacial dipoles are neglected. Since typical values of V were on the order of 0.5 eV or less, it was argued that, with dipole effects included, the midgap energies should be aligned to within $\sim$0.05 eV for typical values of semiconductor dielectric constants.

The ability to determine an effective midgap energy for each individual semiconductor, independent of the material with which it is to form an interface, is again equivalent to placing the energy gaps of each material on a single, common energy scale, although the common energy scale in this case is not determined by any external reference energy as was the case, for example, in Harrison's LCAO theory. The theories of Tersoff and of Harrison and Tersoff, which differ princi-

pally in the method used to calculate the midgap energy, therefore provide further theoretical evidence that even when heterojunction dipole effects are taken into account, and in fact are assumed to be the dominant factor in determining band offset values, the transitivity condition given by Eq. (1.1) should remain valid. Figs. 1.6(a) and 1.6(b) show the energy gaps of several selected semiconductors on a common energy scale determined by the theories of Tersoff[53] and of Harrison and Tersoff[54], respectively.

An empirical correlation noted independently by Zunger[59, 60] and by Langer and Heinrich[61] has recently been shown[62] to be related to the concept of the midgap energy alignment. It was pointed out by Zunger and by Langer and Heinrich that alignment of transition-metal impurity levels in compound semiconductors appeared to yield fairly accurate values for valence-band offsets in isovalent (i.e., III-V on III-V or II-VI on II-VI) heterojunctions. Model calculations of Tersoff and Harrison[62] indicate that for cation-substitutional impurities, requiring charge neutrality in the impurity d shell yields a correlation, for a given transition-metal impurity, of the impurity level with a characteristic energy level in the semiconductor very close to the midgap energy. Alignment of the midgap energy at a heterojunction should therefore also produce an approximate alignment of the transition-metal impurity levels across the interface.

Empirical Compilation of Katnani and Margaritondo

Using an approach reminiscent of early attempts to deduce empirical correlations between experimental electron affinities or Schottky barrier heights and band offset values, Katnani and Margaritondo[63, 64] measured band offsets for a large number of heterojunctions formed by depositing various semiconductors on either Si or Ge substrates. It was hoped that these measurements would yield reliable valence-band-edge energies, relative to the Si and Ge valence-band

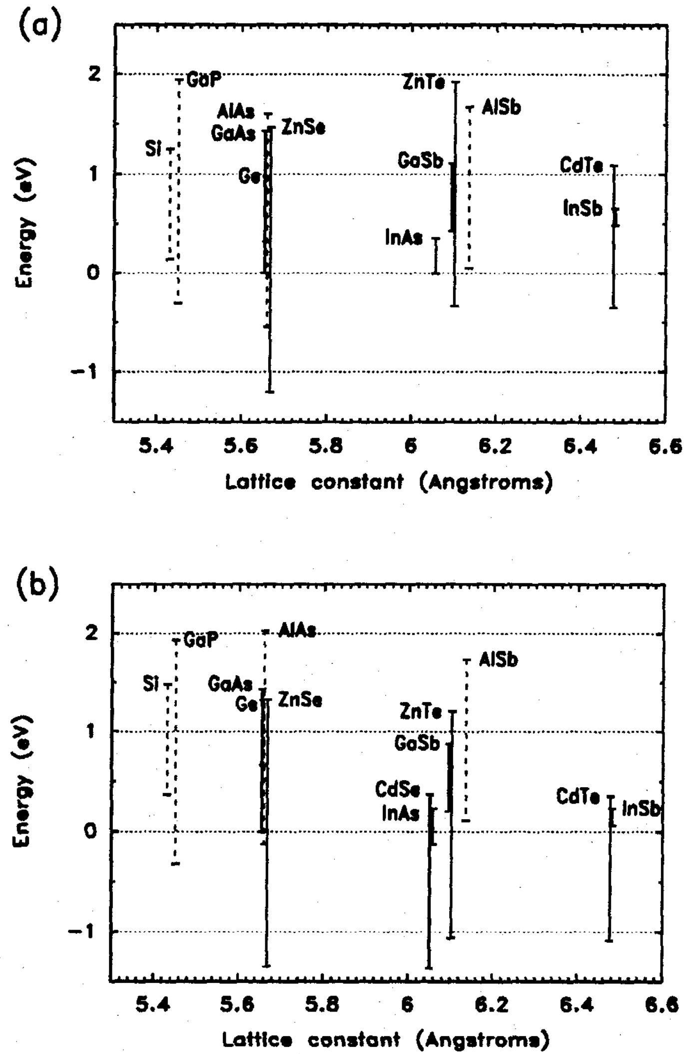

Figure 1.6: Energy band gaps of several selected semiconductors plotted as a function of lattice constant on an absolute energy scale determined by the interface dipole theories of (a) Tersoff[53] and (b) Harrison and Tersoff[54]. The origin of the energy scale is taken to be the valence band edge of GaAs. Direct band gaps are indicated by solid vertical lines, indirect gaps by dashed lines. Conduction and valence band offsets can be determined directly from the figure.

edges, for a large number of semiconductors. The results of these measurements were combined with other available experimental band offset values to produce a set of valence-band-edge energies optimized to yield the best agreement with the available experimental data. This scheme was somewhat analogous to the earlier semi-empirical electron affinity and common anion rules, except that experimental data from semiconductor–semiconductor interfaces, rather than from metal–semiconductor or vacuum–semiconductor interfaces, were used to provide a common energy reference for all materials. As acknowledged by the authors, however, this compilation was obtained merely by optimizing agreement with the experimental data available at the time, and provides little insight into the physical basis responsible for determining band offset values. Fig. 1.7 shows the energy gaps of several selected semiconductors plotted as a function of lattice constant on the common energy scale proposed by Katnani and Margaritondo on the basis of the experimental data available to them.

1.2.2.2 Self–Consistent Calculations for Specific Interfaces

In recent years a number of theories have been developed that include effects arising from the detailed electronic structure of the specific interface under consideration. The typical approach is to calculate the electronic band structure for a so-called "supercell" geometry, essentially a superlattice with a unit cell consisting of n monolayers of one semiconductor followed by n monolayers of the other. Because the electronic structure in each layer becomes bulklike very rapidly as one moves away from the interface[3, 4, 65, 66, 67], it is possible to determine the position of the valence-band edge in each layer, and therefore the value of the valence-band offset, in structures with only 5–10 monolayers of each material in the supercell.

The first approaches of this type were reported by Baraff, Appelbaum, and

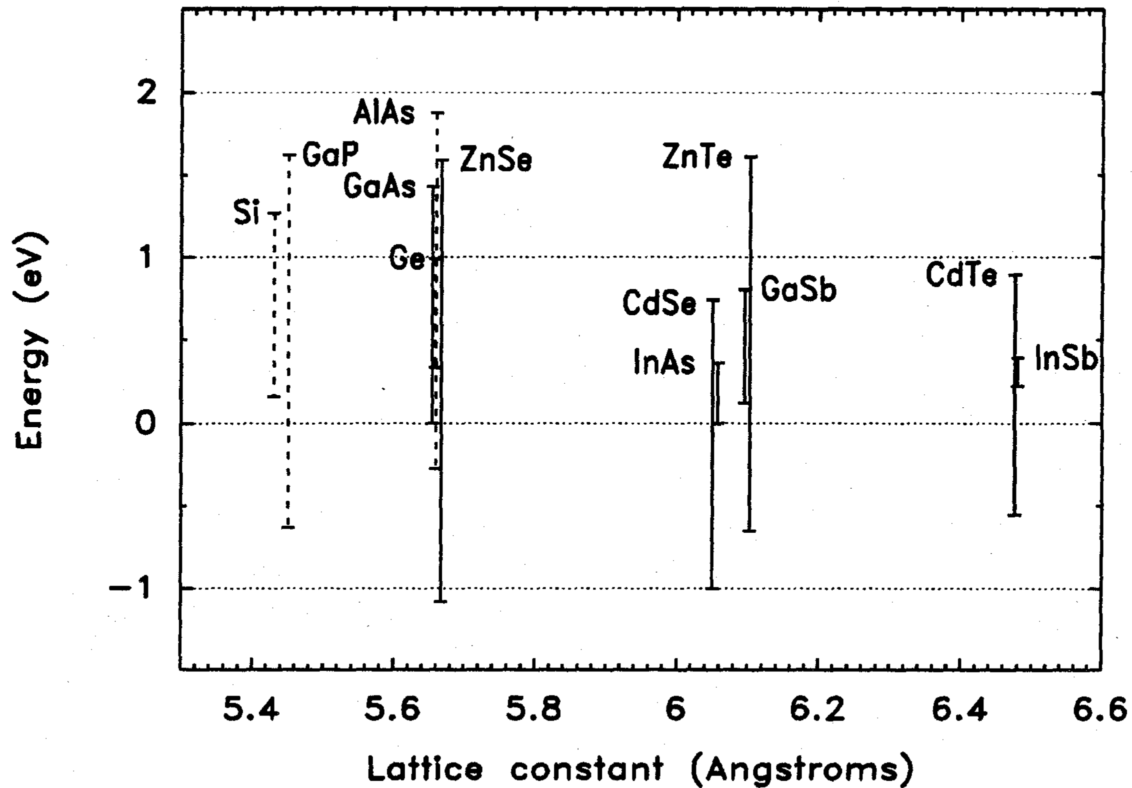

Figure 1.7: Energy band gaps of selected semiconductors plotted as a function of lattice constant on the common energy scale proposed by Katnani and Margaritondo[63, 64]. The origin of the energy scale is taken to be the valence band edge of GaAs. Direct band gaps are indicated by solid vertical lines, indirect gaps by dashed lines. Conduction and valence band offsets can be determined directly from the figure.

Hamann[65, 66] and by Pickett, Louie and Cohen[68]. Baraff et al. and Pickett et al. calculated the electronic structure of the GaAs/Ge interface, and obtained valence-band offsets of ~ 0.9 eV and 0.35 eV, respectively. Presumably because of the prohibitive amount of computation that would have been required, neither group applied their methods to a large number of other heterojunctions.

More recently, Van de Walle and Martin[3, 4, 67, 69, 70] have calculated band offset values by using a self-consistent local density functional theory and *ab initio* pseudopotentials to compute the electronic structure for a superlattice structure. The calculations of Van de Walle and Martin were the first to incorporate the effects of strain in lattice-mismatched heterojunctions, with the Si/Ge heterojunction system being considered as a prototypical lattice-mismatched material system. On the basis of their self-consistent local density functional calculations for Si/Ge and other heterojunction systems, Van de Walle and Martin proposed a "model solid" theory of band offsets[67, 69, 70].

In their model solid theory, an absolute electrostatic potential is computed for each material by constructing the solid as a superposition of neutral atoms. The atomic potentials can be placed on an absolute energy scale common to all materials, and an average electrostatic potential relative to the atomic potentials can be defined in the solid. This procedure was found[67, 69, 70] to yield good agreement with the results of the full self-consistent interface calculation. The bulk band structure relative to the average electrostatic potential within the solid is then calculated using *ab initio* pseudopotentials. It is then possible to define the position of the valence-band edge in each material on the common energy scale given by the atomic potentials and consequently to derive band offset values for various heterojunctions. The relatively good agreement between the results of the model solid theory and the fully self-consistent calculations suggests that band offsets can be considered, at least approximately, to be determined pri-

marily by characteristics of the bulk constituent materials. Van de Walle[70] has also calculated absolute deformation potentials within the model solid approach, allowing band offsets in strained heterojunctions to be predicted. Fig. 1.8 shows the energy gaps of several selected semiconductors on the common energy scale defined by the model solid theory of Van de Walle and Martin.

Cardona and Christensen[71, 72, 73] and Lambrecht et al.[74, 75] have also performed self-consistent calculations of band offsets for superlattice geometries, using a linear-muffin-tin-orbital (LMTO) method rather than *ab initio* pseudopotentials. These calculations have been used to develop and justify simpler theories of band offset values that allow offsets for a large number of heterojunctions to be estimated in a straightforward manner.

Cardona and Christensen[71] have proposed a model in which band offset values are determined by an approximate alignment of dielectric midgap energies calculated for each material; the deviation from an exact alignment of the dielectric midgap energies is due to finite screening with an effective dielectric constant, obtained by averaging the long-wavelength dielectric constants for each material:

$$\Delta E_v(A/B) = E_v^B - E_v^A - \left(E_D^B - E_D^A\right)\left(\frac{\bar{\epsilon}-1}{\bar{\epsilon}}\right), \tag{1.4}$$

where E_v^A and E_v^B are the valence-band-edge energies in materials A and B, respectively, E_D^A and E_D^B are the dielectric midgap energies, and $\bar{\epsilon}$ is the effective dielectric constant. A reasonable approximation to the band offset values obtained in this model can be obtained by assuming $\bar{\epsilon} = 3.5$ for all materials[57, 71]; this approximation then allows a common energy scale to be defined for all materials. Fig. 1.9 shows the energy gaps of several selected semiconductors on the resulting common energy scale.

Lambrecht et al. used the results of their LMTO calculations to develop their "interface bond polarity" model[74, 76]. In their model, the bulk electronic struc-

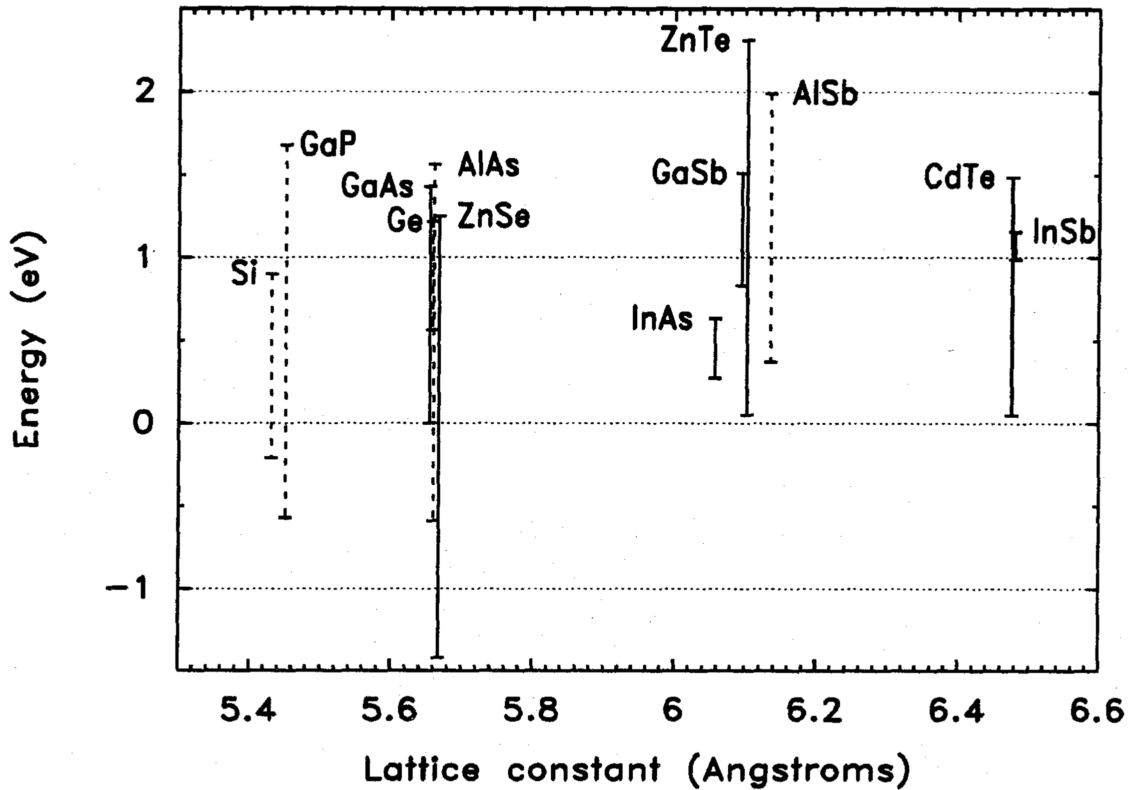

Figure 1.8: Energy band gaps of selected semiconductors plotted as a function of lattice constant on the common energy scale corresponding to the model solid theory of Van de Walle and Martin[67, 69, 70]. The origin of the energy scale is taken to be the valence band edge of GaAs. Direct band gaps are indicated by solid vertical lines, indirect gaps by dashed lines. Conduction and valence band offsets can be determined directly from the figure.

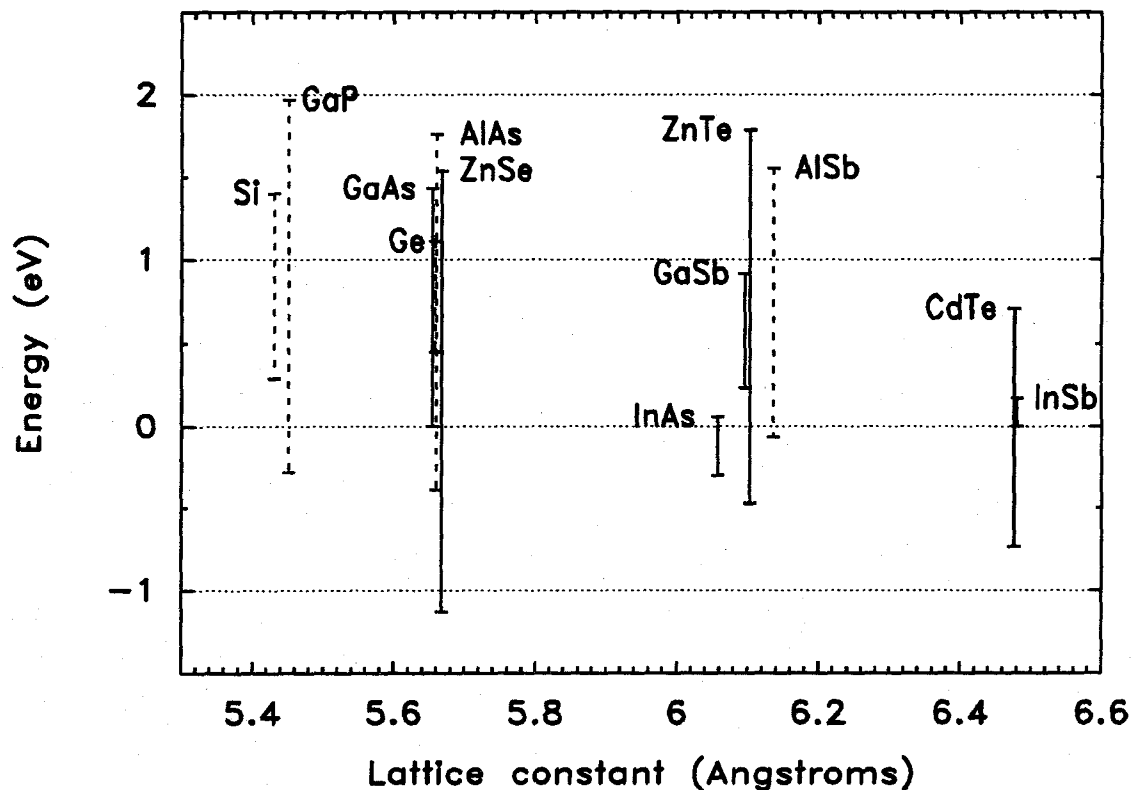

Figure 1.9: Energy band gaps of selected semiconductors plotted as a function of lattice constant on the common energy scale corresponding to the screened dielectric midgap energy alignment proposed by Cardona and Christensen[71]. The origin of the energy scale is taken to be the valence band edge of GaAs. Direct band gaps are indicated by solid vertical lines, indirect gaps by dashed lines. Conduction and valence band offsets can be determined directly from the figure.

ture in each material is first calculated with respect to an average reference potential using LMTO methods. Band offsets are obtained by calculating the difference in the average reference potential for each material, and applying a screened dipole correction arising from bond polarity and charge transfer at the heterojunction interface. An analysis of their fully self-consistent LMTO calculations indicated that a relatively simple and accurate approximation for the screened dipole correction could be obtained by estimating the charge transfer in bonds formed between the two materials from bond polarities, and calculating the resulting dipole potential with screening given by the long-wavelength dielectric constant. The resulting band offset values do not rigorously obey the transitivity relation, Eq. (1.1), and this model therefore does not allow all materials to be placed on a single energy scale. Nevertheless, the interface bond polarity model has been found to agree reasonably well with the fully self-consistent LMTO calculations of Cardona and Christensen and of Lambrecht et al., and therefore with the predictions of the dielectric midgap energy model proposed by Cardona and Christensen[71], shown in Fig. 1.9.

1.2.3 Measurement of Band Offsets by XPS

Despite the extensive theoretical efforts reviewed in Section 1.2.2, band offset values in novel semiconductor heterojunction systems cannot yet be predicted reliably by any existing theory, and must therefore be determined experimentally for each material system of interest. In the work reported in this thesis we have used x-ray photoelectron spectroscopy to measure band offset values for a number of heterojunction systems.

In x-ray photoelectron spectroscopy, a sample is excited using x rays — photons with energies ranging approximately from 100 eV to $\sim 10,000$ eV — and the

energy spectrum of electrons photoexcited from the sample is measured. For our experiments we have used an Al $K\alpha$ x-ray source, yielding photons with energy $h\nu = 1486.6$ eV. The energy spectrum of the photoexcited electrons yields a profile of the electronic density of states in the sample, modulated by a photoelectric cross section. Fig. 1.10 shows a typical XPS spectrum from a GaAs (100) sample; as shown in the figure, the spectrum contains peaks corresponding to atomic core levels in the sample, and a continuous density of states for the valence-band electrons.

Fig. 1.11 illustrates the use of XPS to measure the valence-band offset in a semiconductor heterojunction. From Fig. 1.10 it can be seen that the separation between two core-level peaks and between a core-level peak and the valence-band edge can be measured quite precisely; the relatively high energy resolution available in XPS allows core-level energy separations to be measured to within $\pm 0.02 - 0.03$ eV, and core-level to valence-band-edge binding energies can be obtained to within $\pm 0.04 - 0.05$ eV. To obtain a value for the valence-band offset, reference core-level to valence-band-edge binding energies are measured in each material, as illustrated in Fig. 1.11; to measure the GaAs/AlAs valence-band offset, for example, the Ga $3d$ and Al $2p$ core-level to valence-band-edge binding energies would be measured in pure GaAs and pure AlAs, respectively. The separation between the core-level peaks would then be measured in a heterojunction sample consisting of $\sim$25 Å of one material deposited on a thick layer (typically a few hundred Angstroms or more) of the other; e.g., the Al $2p$ to Ga $3d$ core-level energy separation would be measured in a GaAs/AlAs heterojunction. One can see from Fig. 1.11 that the valence-band offset is then given by

$$\Delta E_v(1/2) = (E_{cl}^1 - E_v^1) + (E_{cl}^2 - E_{cl}^1) - (E_{cl}^2 - E_v^2), \tag{1.5}$$

where $\Delta E_v(1/2)$ is the valence-band offset between semiconductor 1 and semi-

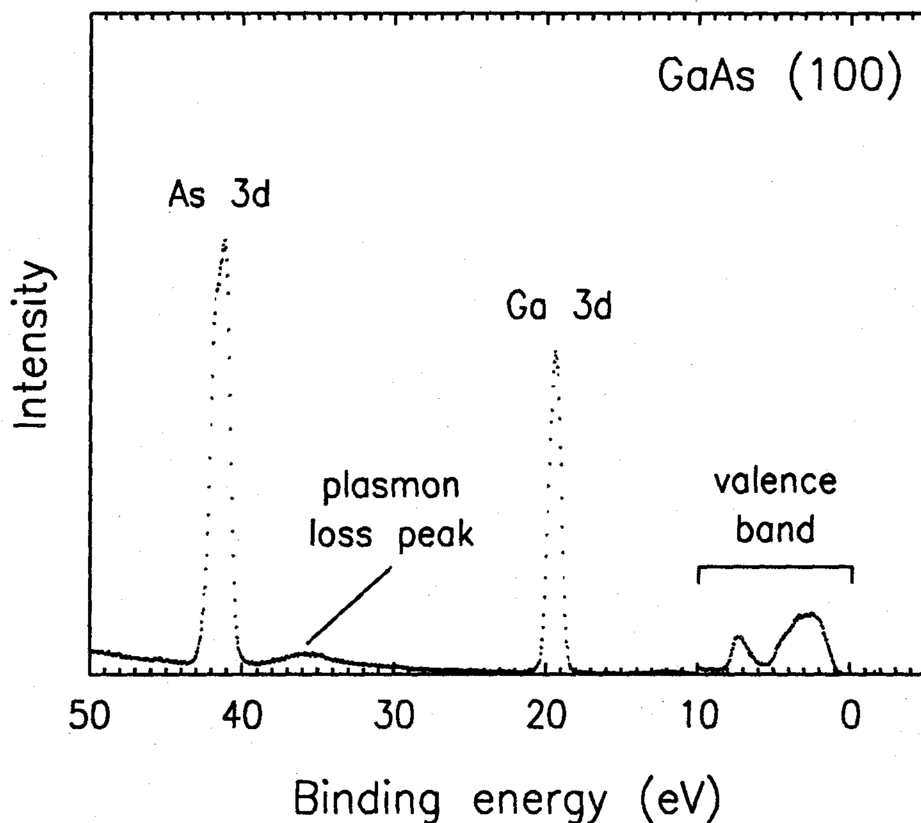

Figure 1.10: A representative XPS electron energy spectrum obtained from GaAs (100). Peaks are observed for the Ga 3*d* and As 3*d* atomic core levels, and a continuous spectrum is observed for the valence band states. A plasmon loss peak, corresponding to excitation of a single plasmon mode by electrons photoexcited from the Ga 3*d* core level, can also be seen. The discontinuity in the spectrum at 10 eV binding energy is due to the longer sampling times used near the valence band edge.

conductor 2, E^i_{cl} is the reference core-level energy of semiconductor i, and E^i_v is the position in energy of the valence-band edge in semiconductor i.

The determination of band offsets by XPS has a number of advantages over other band-offset measurement techniques. Unlike many optical and electrical methods for determining band offsets, the XPS method provides a direct measurement of the band offset, so that interpretation of the experimental results is fairly straightforward. In addition, the XPS technique is well suited to the study of novel material systems, since the structures required are very simple, and fabrication of functional electrical devices is not necessary. The application of the XPS technique can be extended to lattice-mismatched heterojunctions[77, 78, 79], in which effects arising from strain become important, and can also yield information about chemical reactivity at certain semiconductor interfaces[78, 80, 81].

In addition to the work reported in this thesis, XPS has been used by a number of investigators to study band offsets in a wide variety of heterojunction systems; a partial accounting of this work is given here. Kraut, Grant, Waldrop, and Kowalczyk[23, 84] at Rockwell International developed the initial version of the high-precision analysis techniques we have used in our studies, and the Rockwell group pioneered the use of these techniques to study band offsets in heterojunctions such as Ge/GaAs[82, 83], GaAs/AlAs[1, 2], and InAs/-GaAs[85]. In addition, XPS has been used to measure valence-band offsets for the nearly lattice-matched ZnSe/GaAs/Ge material system[86, 87], the InAs/GaSb heterojunction[88], and the GaSb/AlSb heterojunction[89]. Band-offset measurements for the HgTe/CdTe heterojunction[90] and the CdTe/HgTe/ZnTe material system[91] have also been reported, although in the latter work strain effects were neglected despite the large lattice mismatch (6.5%) of CdTe and HgTe with ZnTe. Various other measurements will be discussed in relation to our work at

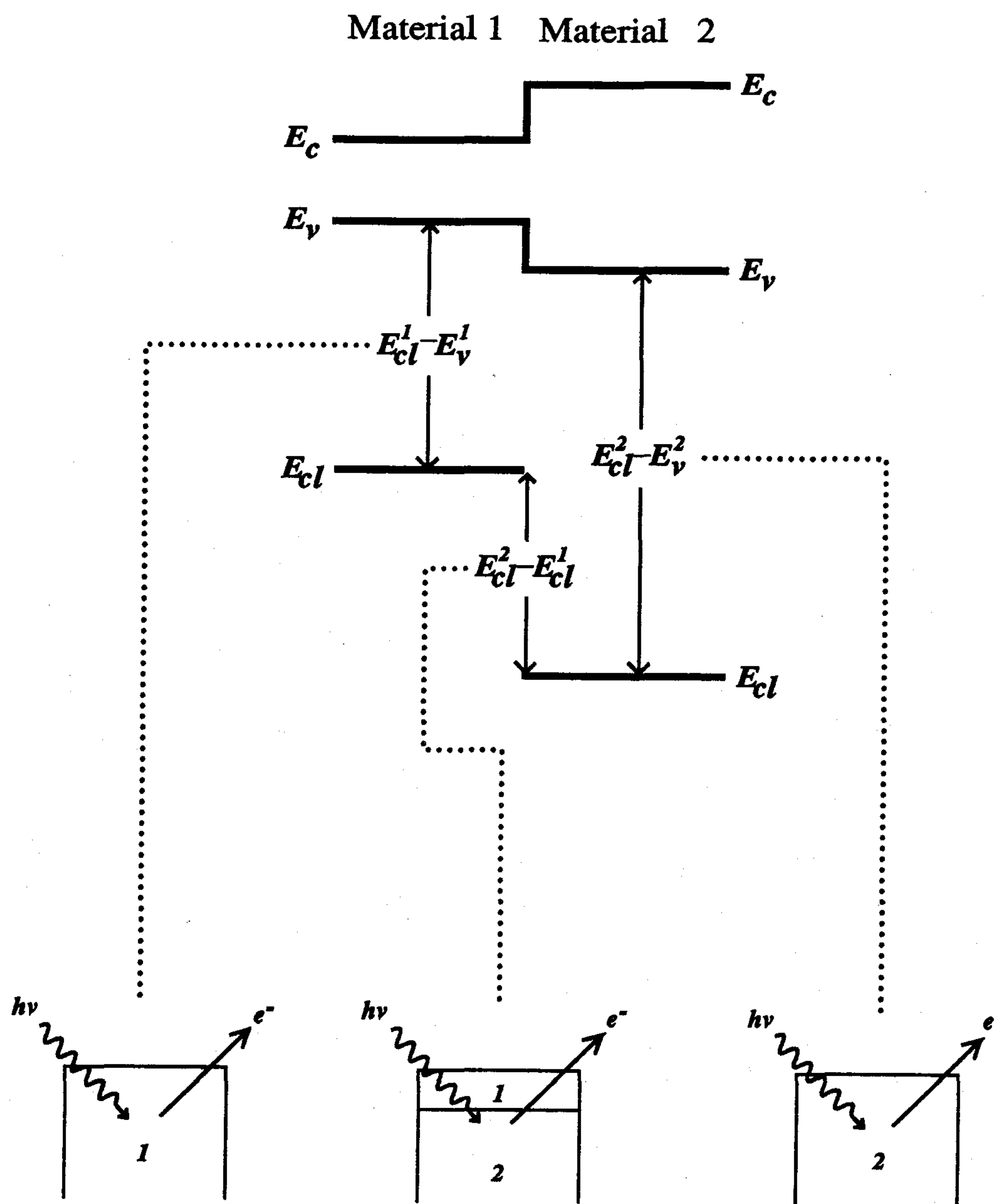

Figure 1.11: A schematic energy-band diagram illustrating the basic principle of the XPS band-offset measurement. Reference core-level binding energies are measured in thick films of each material, and the separation between the two reference core levels is measured in heterojunction samples. These three quantities can then be combined to yield a value for the valence-band offset.

later points in the thesis. A number of investigators have also studied band offsets using related techniques, such as photoemission spectroscopy using synchrotron radiation[63, 64, 92, 93] and the measurment of variations in XPS binding energies with sample doping[94, 95].

1.2.4 Other Band Offset Measurement Techniques

A variety of other techniques have been used to measure band offsets in semiconductor heterojunctions. Most of these techniques can be divided into two categories: optical techniques, in which optical absorption, photoluminescence, or photoluminescence excitation spectra from quantum-well or superlattice structures are analyzed with the band offsets as fitted parameters, and electrical (devicelike) techniques, in which either the conduction or the valence band offset is extracted from measurements, such as C–V or I–V characteristics, on electrical device structures.

Analysis of optical absorption spectra from $Al_xGa_{1-x}As/GaAs/Al_xGa_{1-x}As$ quantum-well heterostructures by Dingle et al.[24] yielded what was until quite recently the most widely accepted value for the $GaAs/Al_xGa_{1-x}As$ band offsets, $\Delta E_c \approx 0.85\Delta E_g$ and $\Delta E_v \approx 0.15\Delta E_g$, where ΔE_g is the difference between the GaAs and $Al_xGa_{1-x}As$ band gaps. In this technique, calculated quantum-well bound-state energies are fitted to the observed structure in the absorption spectrum, with the band offset as an adjustable parameter. Unfortunately, the calculated bound-state energies for these structures depend more strongly on the well width and carrier effective mass than on the band offset. Subsequent photoluminescence experiments on parabolic quantum wells[26, 32], in which the bound-state energies depend more sensitively on the band offset, demonstrated the importance of using accurate material parameters, such as effective masses,

and yielded a conduction-band offset $\Delta E_c \approx 0.57 \Delta E_g$, in closer agreement with the currently accepted values. Optical techniques of this type have also been applied, with somewhat mixed results, to other material systems such as InP/-$In_{0.53}Ga_{0.47}As$[96, 97] and $Ga_{0.47}In_{0.53}As/Al_{0.48}In_{0.52}As$[98].

A related technique, in which a light-scattering method is used to determine conduction band offsets, has been applied to $GaAs/Al_xGa_{1-x}As$[31] and GaSb/-$Al_xGa_{1-x}Sb$[41] heterojunctions. In this method, backscattering spectra obtained from photoexcited carriers in multiple-quantum-well structures were found to contain peaks arising from inelastic light scattering, with energy shifts corresponding to transition energies between bound states in the quantum wells[99]. Values for the conduction-band offset were obtained by fitting these transition energies to a theoretical model for quantum-well bound-state energies, with the conduction-band offset as an adjustable parameter. Band offsets were obtained for the $GaAs/Al_xGa_{1-x}As$ and $GaSb/Al_xGa_{1-x}Sb$ heterojunctions that were in fairly good agreement with other reported results.

The $GaAs/Al_xGa_{1-x}As$ valence band offset has also been measured by studying the pressure dependence of photoluminescence from $GaAs/Al_xGa_{1-x}As$ quantum wells and superlattices[30]. This technique exploited the proximity in energy of the Γ-point and X-point conduction band minima in $Al_xGa_{1-x}As$; by applying hydrostatic pressure to $GaAs/Al_xGa_{1-x}As$ heterostructure samples, the GaAs quantum-well confined states were shifted above the X-point conduction-band minimum in the $Al_xGa_{1-x}As$ barriers, resulting in a sharp reduction in photoluminescence intensity from the Γ-confined quantum-well states. By analyzing the pressure dependence of the $Al_xGa_{1-x}As$ energy band gap and of the photoluminescence energies for pressures $\lesssim$60 kbar, a $GaAs/Al_xGa_{1-x}As$ valence-band offset $\Delta E_v = (0.32 \pm 0.02)\Delta E_g^\Gamma$ was deduced, in good agreement with currently accepted values. A nontrivial assumption of this technique, how-

ever, would appear to be that the valence-band offset is independent of pressure. Magneto-optical studies of InAs/GaSb superlattices[100] indicate that the InAs/-GaSb valence-band offset varies with pressure; the separation between the InAs conduction-band edge and the GaSb valence-band edge was found to decrease at a rate of 5.8 meV/kbar. Given an increase in the InAs energy band gap of 10 meV/kbar[100], this yields a valence-band offset that increases with pressure at a rate of 4.2 meV/kbar.

A number of electrical techniques have also been used to determine band offset values. Thermionic emission current across a single barrier has been used to measure band offsets in a number of heterojunctions[27, 28, 33, 34, 101, 102]. By analyzing the temperature dependence of current-voltage characteristics in single-barrier heterostructures, it is possible to determine the barrier height, and therefore the band offset values. This technique has been applied with considerable success to, among others, the GaAs/$Al_xGa_{1-x}As$[27, 28, 33, 34] and CdTe/HgCdTe[102] material systems.

Capacitance-voltage measurements have also been applied to the measurement of band offset values. Kroemer et al. showed[25] that it is possible, by performing C–V profiling through a heterojunction, to extract a value for the band offset in that heterojunction. This technique has been used to determine band offsets in a number of heterojunction systems, including GaAs/-$Al_xGa_{1-x}As$[25, 35, 36], lattice-matched InGaAsP/InP[103], and $In_xAl_{1-x}As$/-$In_{0.53}Ga_{0.47}As$[104, 105]. A number of investigators have also employed a somewhat simplified version of the C–V profiling technique. For cases in which the doping level is constant in each heterojunction layer, a plot of $(1/C^2)$ as a function of V should yield a straight line. The intercept voltage V_{int} should then yield the total built-in voltage of the heterojunction, and consequently, the band offset value, assuming that the doping level in each layer is known. This technique has

been used to determine band offsets in several heterojunction systems, including InAs/AlSb[106], $InAs_{0.95}Sb_{0.05}$/GaSb[107], and CdS/InP[108].

A charge transfer method has also been used to determine band offset values. In this technique, the sheet density is measured in the two-dimensional carrier gas formed at a heterojunction interface; a method has been developed[29, 109] to estimate the band offset value from the measured sheet carrier density. This method has been used to measure the valence-band offset in GaAs/AlAs (100)[29] and GaAs/$Al_xGa_{1-x}As$ (100)[109] heterojunctions; the orientation dependence of the GaAs/$Al_xGa_{1-x}As$ valence-band offset has also been studied[110], with no measurable difference found between the valence-band offsets in the (100) and (311) orientations.

Finally, internal photoemission measurements have been used to determine band offsets for the GaAs/$Al_xGa_{1-x}As$ material system. In these experiments, threshold photon energies determined from photocurrent measurements in p^+-GaAs/n^--$Al_xGa_{1-x}As$ heterojunctions[111, 112] or in a GaAs/$Al_xGa_{1-x}As$ heterojunction combined with a Mo-GaAs Schottky barrier[113] were used to obtain values for the conduction-band offset. GaAs/$Al_xGa_{1-x}As$ conduction-band offset values have also been derived from measurements of photocurrents[111] and photovoltages[114] arising from internal photoemission from the two-dimensional electron gas in GaAs/$Al_xGa_{1-x}As$ heterostructures.

1.2.5 Overview of Theoretical and Experimental Band Offset Determinations

The research that has been devoted to the issue of band offsets over the past several years has done much to improve our knowledge of band offset values for many heterojunction systems and our understanding of the physics of band

offsets. In this section we present a very brief overview of the current experimental and theoretical understanding of band offsets, and a synopsis of some of the contributions to this understanding presented in this thesis. More thorough and specific reviews of semiconductor heterojunction band offsets have been given by a number of authors[37, 42, 115, 116, 117, 118].

For the technologically important GaAs/$Al_xGa_{1-x}As$ material system, numerous band-offset measurements utilizing a variety of experimental techniques[26, 27, 28, 29, 30, 31, 32, 33, 34, 35, 36, 109, 110, 119] have yielded widely accepted valence-band offset values in the range $0.45 - 0.55$ eV for GaAs/AlAs, with a linear dependence on alloy composition x. For the related $In_{0.52}Al_{0.48}As$/-$In_{0.53}Ga_{0.47}As$ heterojunction, photoluminescence[98, 120], C–V profiling[6, 105], and temperature-dependent I–V characterization[121] have consistently yielded $\Delta E_c \approx 0.70 \Delta E_g$.

Another material system in which band offsets now appear to be well known is the nearly lattice-matched InAs/GaSb/AlSb system. Early studies[122, 123] of GaSb/AlSb heterostructures often erroneously assumed the validity of the common anion rule[9] for this material system, although it was known that the common anion rule should not be valid because of the presence of Al in one of the compounds. More recently, however, measurements have been performed, using various techniques, of the InAs/GaSb[88, 100] and GaSb/AlSb[41, 89] valence-band offsets, and C–V profiling has been used to measure the InAs/AlSb conduction-band offset[106]. Valence-band offsets of 0.51 eV for InAs/GaSb and ~ 0.40 eV for GaSb/AlSb are now quite widely accepted, and the conduction-band offset $\Delta E_c = 1.35 \pm 0.05$ eV obtained in Ref. [106] is consistent with these results. The measured band offset values obey the transitivity rule, Eq. (1.1), to within experimental error, indicating that variations related to growth conditions are not significant. In addition, numerous other experiments have verified both the siz-

able valence-band offset for GaSb/AlSb[124, 125, 126] and the Type II broken-gap band alignment for GaSb/InAs[127, 128, 129, 130].

Considerable effort has also been devoted to the measurement of band offsets in the technologically important $In_{0.53}Ga_{0.47}As/InP$ heterojunction system. The most widely accepted measurements for this band offset[96, 103, 131, 132, 133] typically yield $\Delta E_c \approx 0.4\Delta E_g$, although a substantial number of measurements[97, 134, 135] have yielded a larger conduction-band offset, $\Delta E_c \approx 0.6\Delta E_g$. These results are indicative of the difficulty and complexity of most experimental band-offset determinations, and may also suggest a possible influence of growth conditions on band offset values.

The other material system in which band offsets appear now to be relatively well understood is Si/Ge, a material system potentially of great technological importance. The Si/Ge heterojunction differs from the other material systems previously considered because of the 4.18% lattice mismatch between Si and Ge. This lattice mismatch induces strain in $Si/Si_{1-x}Ge_x$ heterojunctions, which could strongly influence band offset values. Theoretical calculations[3, 4] and experimental measurements[5, 77, 78, 79, 94, 95] of Si/Ge band offset values have confirmed the effect of strain on the valence-band offset. In addition, modulation-doping experiments on $Si/Si_{1-x}Ge_x$ heterojunctions[6, 7] have yielded results consistent with these measured and calculated band offset values, with, in some cases, qualitatively different behavior induced by varying strain configurations.

For other material systems, band offset values are less well understood. One reason for this is that for many novel heterojunction systems, relatively few experimental band-offset studies have been performed; in most of these cases, only XPS has been used to determine the value of the valence-band offset. Another reason, perhaps more significant, is that the optimum growth conditions for many of these heterojunctions have not been determined. Particularly in heterojunc-

tions involving an elemental semiconductor, e.g., Ge, and a III-V or II-VI compound semiconductor, or involving a III-V semiconductor and a II-VI material, band offsets have been found to depend on factors such as structural antiphase disorder[42], e.g., for GaAs deposited on Ge, or interdiffusion and chemical reactivity at the heterojunction interface[78, 83, 136]. Band-offset values have also been found by some investigators to depend on substrate orientation and on growth conditions such as substrate temperature or growth sequence. For the Ge/GaAs heterojunction system, variations in band offset values as large as several tenths of an electron volt have been observed[135, 136, 82]; variations of a few tenths of an electron volt have been measured even for the thoroughly studied GaAs/$Al_xGa_{1-x}As$ heterojunction system[1, 2]. Other investigators, however, have failed to observe any dependence of the GaAs/$Al_xGa_{1-x}As$ band offset on substrate orientation[110, 137] or on growth sequence[38, 93, 137].

Theoretical calculations of band offsets have yielded very mixed results. The early theories and empirical rules, such as the electron affinity rule, the common anion rule, the LCAO theory of Harrison, and the pseudopotential theory of Frensley and Kroemer are somewhat useful for predicting broad trends in lattice-matched heterojunctions, but are not sufficiently accurate to be useful in predicting offset values for previously unstudied heterojunctions. In addition, certain predictions, such as the very small GaAs/AlAs and GaSb/AlSb valence-band offsets predicted by the LCAO theory of Harrison and the pseudopotential theory of Frensley and Kroemer, have been convincingly refuted by experiment, indicating a fundamental deficiency in the physical concepts upon which those theories were based.

More recent theories, such as the interface dipole theories of Tersoff and of Harrison and Tersoff, as well as models developed from self-consistent calculations for specific interfaces by Van de Walle and Martin, by Cardona and Christensen,

and by Lambrecht et al., have met with reasonable success in reproducing experimentally measured band offset values, but the predictive value of these theories remains questionable. In addition, the physical principles underlying these various models are relatively diverse, suggesting that a thorough understanding of the physics of band offsets has yet to be attained. A further complication may be that theories that consider only abrupt, idealized interfaces may in fact be unable to predict band offset values to the precision desired by device physicists. Effects arising from growth conditions and other aspects of interfacial chemistry have been demonstrated to change band offset values by as much as several tenths of an electron volt, and these effects will not be accounted for in any theory treating idealized interfaces. Experimental considerations such as these may ultimately limit the accuracy to which theories will be able to predict band offset values.

In the work described in this thesis, we have used the XPS technique to investigate a number of semiconductor heterojunction systems, with particular attention devoted to systems of current or potential technological significance. Our initial studies focused on the GaAs/AlAs material system, which is the heterojunction of greatest current technological importance, and to which the greatest amount of research has been devoted. Abrupt, high-quality heterojunction interfaces were fabricated using molecular-beam epitaxy (MBE). Band offsets measured in these samples confirmed the commutativity, i.e., independence of growth sequence, of the GaAs/AlAs valence band offset. As discussed above, earlier studies of band offsets in GaAs/AlAs heterojunctions had yielded inconsistent results regarding the dependence of band offset values on growth sequence. Our verification of commutativity was taken to be an indication of the high quality of our MBE-grown heterojunctions, and demonstrated that GaAs/AlAs heterostructures in which band offsets were not affected by growth sequence could be grown consistently and reproducibly.

We have also succeeded in confirming the importance of strain effects in determining band offset values in the technologically important Si/Ge heterojunction system. Until very recently, the influence of strain on band offsets was ignored, both theoretically and in experiments with lattice-mismatched heterojunction systems. Careful theoretical and experimental studies of the Si/Ge system by various investigators, however, have demonstrated that strain exerts an extremely strong influence on band offset values, and must be taken into account in designing, fabricating, and analyzing $Si/Si_{1-x}Ge_x$ heterostructure devices.

Studies we have performed of various III-V/II-VI heterojunction systems have demonstrated the influence of interface chemistry on band offset values. A number of investigators have observed that interfacial reactivity appears to be a generic feature of III-V/II-VI interfaces[78, 138, 139, 140, 141]. Experiments we have performed in the AlSb/GaSb/ZnTe material system and in particular for the AlSb/ZnTe heterojunction have demonstrated that these interfacial reactions can exert a significant influence on band offset values for III-V/II-VI heterojunctions. In addition, we have measured band offset values in other material systems of potential technological interest, such as CdSe/ZnTe, that, while not necessarily elucidating a specific physical issue, provide useful information for testing new and existing theories of band offsets.

1.3 Tunnel Structures

1.3.1 Overview

Tunneling in semiconductors has been a subject of considerable interest since the early work of Leo Esaki in the 1950's[142]. The subsequent proposal by Esaki and co-workers of semiconductor device structures such as superlattices

and multibarrier heterostructrures[143], in which tunneling phenomena are of central importance, and the demonstration of resonant tunneling and negative differential resistance in double-barrier heterostructures[17], eventually led to the development of an entire field of research devoted to the physics and device applications of tunneling phenomena in semiconductor heterostructures. Advances in epitaxial growth techniques such as molecular beam epitaxy (MBE) and metalorganic chemical vapor deposition (MOCVD) have made possible the experimental realization of these structures, whose fabrication requires control of layer thicknesses with resolution close to a single atomic layer.

The key feature of interest in tunnel devices, resonant or otherwise, is negative differential resistance (NDR) in the current-voltage characteristic, i.e., a voltage range over which an increase in voltage applied to the device yields a decrease in the current through the device. This behavior in the current-voltage characteristic can be used in a number of applications, with considerable success having been achieved for high-frequency oscillators. Fig. 1.12 shows schematic band edge diagrams and current-voltage characteristics for two types of tunnel devices, a conventional tunnel diode and a double-barrier heterostructure. A typical tunnel diode might consist of an n-Si/p-Si homojunction, whereas a double-barrier structure might consist of n-GaAs electrodes surrounding an undoped GaAs quantum well with AlAs barrier regions.

In the tunnel diode shown in Fig. 1.12(a), current flows at low voltage from the occupied states (shaded) in the conduction band of the n-type electrode, through the forbidden band gap, into the unoccupied states in the valence band of the p-type electrode. At higher bias, however, current transport is blocked by the forbidden energy gap in the p-type electrode, leading to the region of negative differential resistance. In the double-barrier heterostructure, NDR is produced by the quasi-bound state resonance in the GaAs quantum well. At low

(a) Tunnel diode:

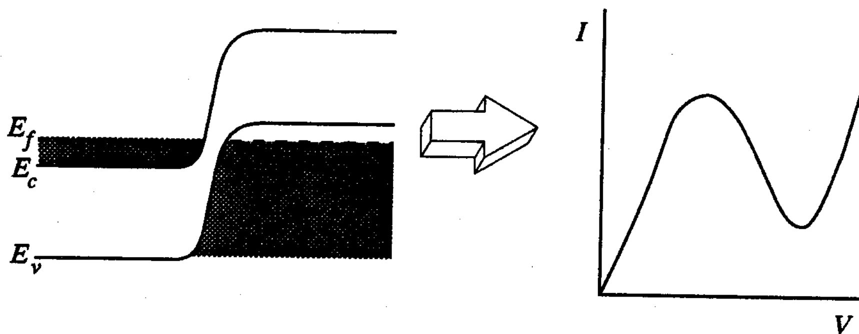

(b) Double-barrier tunnel structure:

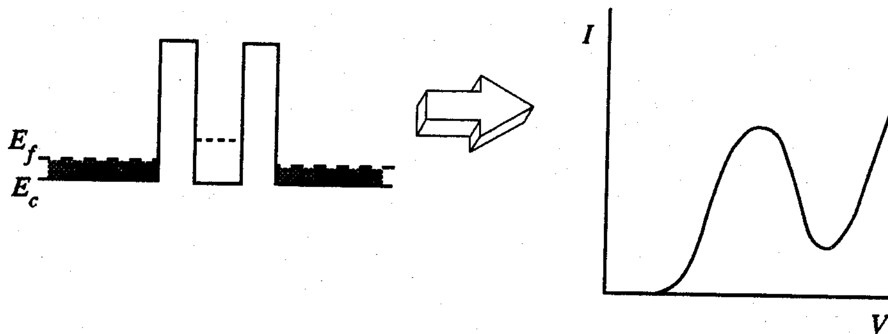

Figure 1.12: Schematic energy-band diagrams and current-voltage characteristics for (a) a conventional tunnel diode, and (b) a double-barrier tunnel structure. The current-voltage characteristics of both devices exhibit a region of negative differential resistance. In each figure, E_c is the conduction band edge, E_v is the valence band edge, and E_f is the Fermi level. For the double-barrier heterostructure, the dashed line in the quantum well indicates the position of the quasi-bound state resonance.

bias, transport through the double-barrier structure is strongly attenuated in the forbidden energy gap of the AlAs barriers. At higher bias, however, the Fermi sea in the emitter electrode is aligned in energy with the resonance, resulting in strongly enhanced transport and an increase in current density. With further applied bias, the resonance moves below the emitter Fermi sea, decreasing the current density and resulting in negative differential resistance.

Much of the interest in tunnel structures arises from their promise for use in high-speed devices, with interest in the double-barrier heterostructure in particular increasing considerably following the observation of high-speed oscillations in GaAs/$Al_xGa_{1-x}As$ double-barriers[144]. In subsequent work, oscillations at frequencies of up to 675 GHz were observed[145] in InAs/AlSb/InAs/AlSb/InAs double-barrier tunnel structures. Tunnel devices have also been investigated for possible use in high-speed electrical circuits, with particular emphasis placed on three-terminal transistor structures utilizing tunneling[146, 147, 148, 149, 150, 151, 152, 153, 154, 155, 156].

An issue of considerable relevance in determining the speed of devices based on tunneling, and of fundamental physical interest as well, is the characteristic time scale of the tunneling process. Brown et al.[157] have shown that the maximum attainable oscillation frequency in a resonant-tunneling diode should depend critically on the tunneling lifetime of the resonance[157]; the speed of other devices based on tunneling should depend strongly on this lifetime as well. A number of investigators have attempted to calculate theoretically[158, 159, 160, 161, 162] or measure experimentally[11, 163, 164] the tunneling time for carriers in the quantum well of a double-barrier heterostructure. Experimentally, it has been found that tunneling times for double-barrier heterostructures depend exponentially on the barrier width, and for typical GaAs/AlAs structures tunneling times as short as 12 ps have been measured[11]. Until recently, however, studies of tunneling

times have focused almost exclusively on electrons, since hole tunneling times were assumed to be extremely long compared to electron tunneling times due to the large heavy-hole effective mass[163, 165]. However, recent calculations we have performed[166, 167] of hole tunneling times in double-barrier heterostructures that include effects arising from valence band mixing, as well as the experiments of Ref. [11], have shown that tunneling times for holes in GaAs/AlAs double-barrier structures are actually much shorter than the heavy-hole tunneling time calculated without band-mixing effects, and comparable in fact to electron tunneling times. These results should affect the interpretation of a number of experiments purporting to study tunneling of electrons[163, 165, 168, 169, 170], and could influence the conception, design, and performance of new device structures involving tunneling of holes.

1.3.2 Tunneling Theory and Simulation of Devices

In conjunction with experimental advances in the fabrication and characterization of tunnel structures, a theoretical framework has been developed to aid in the understanding, analysis, and design of device structures[143, 171, 172, 173, 174, 175, 176]. Realistic theoretical models for simulating device behavior are often critical in obtaining the highest possible performance for a device structure, since such models allow one to explore a large range of design parameters and to investigate new device concepts much more efficiently than would be possible experimentally. In addition, the electrical behavior of many heterostructure devices depends on factors such as quantum-mechanical tunneling times, electron coherence effects, and other basic physical considerations. The fundamentally quantum-mechanical nature of tunneling allows one to use structures such as double barriers, quantum wells, superlattices, and eventually, quantum wires and

dots, to investigate some basic theoretical issues in quantum mechanics.

1.3.2.1 Band Bending

To obtain as realistic a simulation as possible of the electrical behavior of a device, one first needs to calculate the electrostatic band-bending profile for the device structure. Band bending is induced by electrostatic charges distributed across a device structure under a given DC applied bias, with effects that are due to ionized dopants and free electrons and holes typically being included in calculations of a device band edge profile[177]. Because our device simulations treat transport primarily in the direction of growth in a heterostructure, band edge profiles are calculated only in the growth direction, with the potential assumed to be independent of position in the other directions. If one employs the Thomas-Fermi approximation and assumes that the positions of the band edges at a given point in space depend only on the local carrier concentrations at that point, the band-bending profile can be calculated by solving Poisson's equation,

$$\frac{d^2 E_c(z)}{dz^2} = \frac{e\rho(z)}{\epsilon} = -\frac{e^2}{\epsilon}(n(z) - p(z) + N_A(z) - N_D(z)), \tag{1.6}$$

where $E_c(z)$ is the conduction band edge profile, e is the electron charge, ϵ is the dielectric constant, $n(z)$ is the electron concentration, $p(z)$ is the hole concentration, and $N_A(z)$ and $N_D(z)$ are the acceptor and donor densities, respectively. A boundary condition of overall charge neutrality is imposed across the entire device structure. A detailed discussion of band-bending calculations is given in Section 7.2.

Certain effects, such as the formation of localized two-dimensional carrier gases at accumulation regions adjacent to heterojunction interfaces, are not included in this treatment. Effects such as these are critical in the operation of devices such as high-electron-mobility transistors (HEMT's), in which current

transport through a two-dimensional electron gas formed by modulation doping at a heterojunction interface is an essential aspect of device behavior, but are of secondary importance in the structures of interest for this thesis. In the work presented here, the incorporation of electrostatic band bending allows one to calculate parameters such as current densities and resonant voltages with considerably greater accuracy than if one simply assumed that the entire voltage across a device structure dropped linearly over a limited region of the device.

1.3.2.2 Transmission Coefficients and Current-Voltage Characteristics

The transmission coefficient, defined as the probability for a carrier with a given energy E and wave vector $\vec{k}$ to be transmitted across the device structure, yields a great deal of information about transport across a semiconductor heterostructure, and provides the basis for calculating current-voltage characteristics for heterostructure devices. In calculations of transmission coefficients, it is generally assumed that the carrier energy E and the wave-vector component parallel to the direction of propagation $\vec{k}_{||}$ are conserved. Thus, only purely elastic transport processes are included, i.e., effects arising from scattering are neglected. A basic transfer-matrix approach for calculating transmission coefficients for arbitrary potential profiles was developed by Kane[178]; this method has been adapted to account for more realistic band structure models and the resulting interactions at interfaces between carrier states in different materials[174, 175, 176]. These effects have been found to be of central importance in understanding the behavior of devices involving coupling between conduction-band and valence-band states in different layers of a heterostructure device[179, 180].

Once transmission coefficients have been calculated, the electrical current through a structure can be obtained by integrating over the incoming carrier

distribution, with appropriate Fermi factors and carrier velocities included. For a device structure to which a voltage V has been applied, the current density J is given by

$$J = \frac{e}{4\pi^3\hbar}\left(\int T(E_\perp,\vec{k}_\parallel)f(E)[1-f(E+eV)]dE_\perp d^2k_\parallel - \int T(E_\perp,\vec{k}_\parallel)f(E+eV)[1-f(E)]dE_\perp d^2k_\parallel\right) \quad (1.7)$$

$$= \frac{e}{4\pi^3\hbar}\int T(E_\perp,\vec{k}_\parallel)[f(E)-f(E+eV)]dE_\perp d^2k_\parallel, \quad (1.8)$$

where $E_\perp$ is the energy corresponding to the component of the wave vector in the direction of propagation, and $f(E)$ is the Fermi distribution function.

Using Eq. (1.8), DC current-voltage characteristics for a device structure can be calculated. Current-voltage characteristics computed in this manner are generally capable of yielding a semiquantitative description of the actual electrical behavior of heterostructure devices. For typical tunnel devices, one can compute parameters such as peak current densities and often peak (resonant) voltages semiquantitatively; however, nonresonant currents, such as valley currents in double-barrier structures, are not calculated accurately because of the neglect of scattering processes. Detailed explanations of these types of calculations and of the various band structure models we have employed are given in Chapter 7. We have also illustrated the use of these techniques by simulating the behavior of novel III-V/II-VI double-barrier heterostructures.

1.3.3 Physics of Interband Tunneling

Considerable attention has been devoted recently to the study of transport in so-called "interband" transport devices. These devices, realized in the InAs/-GaSb/AlSb material system, exploit the unusual Type II broken-gap band alignment between InAs and GaSb, in which the conduction band of InAs is lower

in energy than the valence band of GaSb, and the flexibility provided by having three nearly lattice-matched materials. Fig. 1.13 shows the conduction- and valence-band alignments for the InAs/GaSb/AlSb material system. We have assumed valence-band offsets of 0.51 eV and 0.40 eV for the GaSb/InAs[88] and GaSb/AlSb[89] interfaces, respectively, and have assumed the validity of the transitivity rule for band offsets in Fig. 1.13. As can be seen from the figure, transport in InAs/GaSb/AlSb heterostructures involves InAs conduction-band states and GaSb valence-band states, with AlSb acting as a barrier in the energy range between the InAs conduction-band edge and the GaSb valence-band edge. In addition, InAs and GaSb possess a number of electrical properties that make them especially attractive for tunneling and other quantum-effect devices. InAs is easily doped n-type, has very high electron mobility ($\sim 33\,000$ cm^2/V·s at 300 K), and naturally forms n-type ohmic contacts. GaSb can be doped p-type and has a small p-type Schottky barrier, facilitating the formation of p-type ohmic contacts. Furthermore, InAs has a very small effective mass compared to that of GaAs ($m^*_{\mathrm{InAs}} = 0.023m_e$ compared to $m^*_{\mathrm{GaAs}} = 0.067m_e$), which enhances quantum effects so that, for example, subband spacings in quantum-confined structures such as quantum wells, wires, and dots will be larger for given feature sizes in InAs than in GaAs; technological limitations such as lithographic resolution should therefore be less restrictive for InAs than for GaAs. These factors have led to the proposal and realization of a number of new device concepts, many of which exhibit electrical properties and capabilities superior to those currently attainable in other material systems[18, 128, 129, 130, 181, 182, 183, 184].

The electrical behavior of interband transport devices is also strongly influenced by the detailed nature of the coupling between InAs conduction-band states and GaSb valence-band states. Because of the imperfect matching of InAs conduction-band and GaSb valence-band wave functions, the transmission coef-

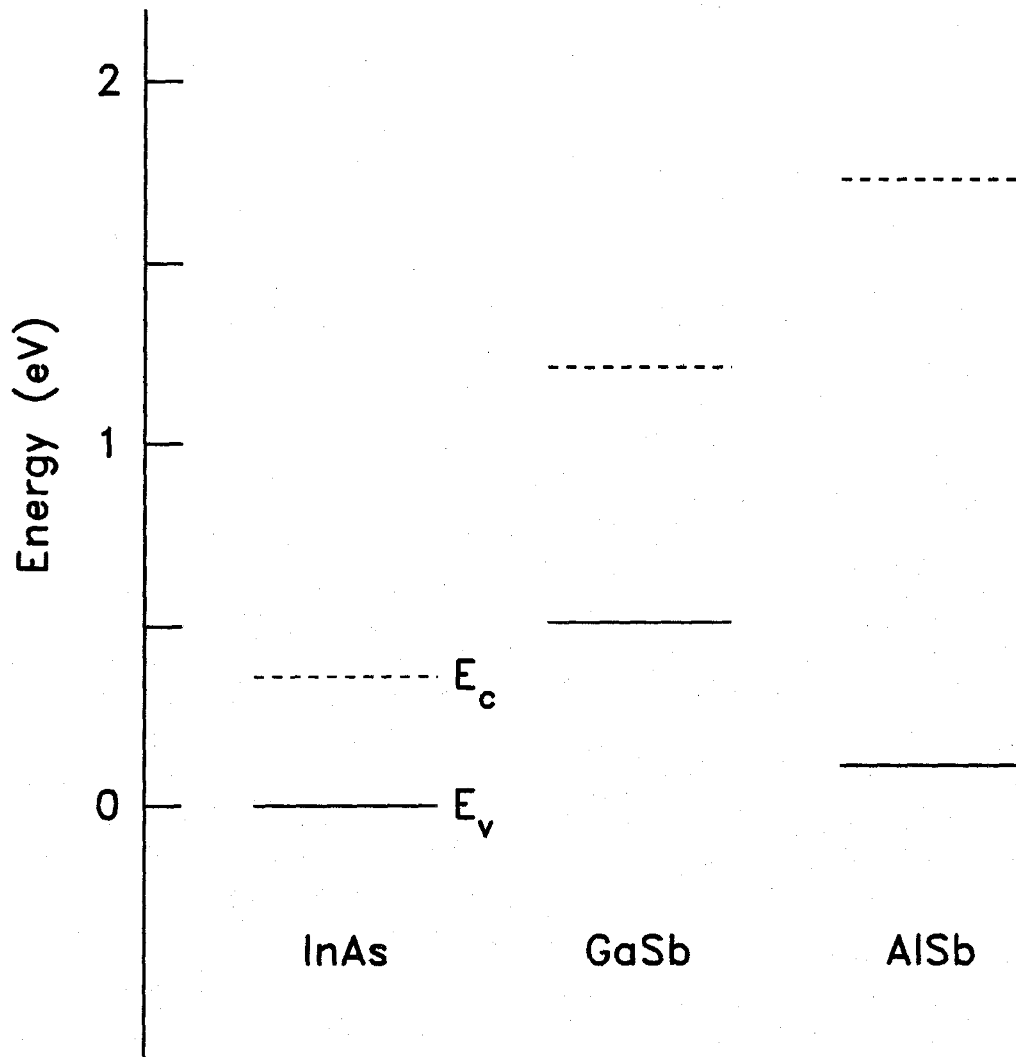

Figure 1.13: Relative positions of the conduction band edges (dashed lines) and valence band edges (solid lines) for InAs, GaSb, and AlSb, as determined from the InAs/GaSb and GaSb/AlSb valence band offsets measured by x-ray photoelectron spectroscopy[88, 89] and assuming transitivity of band offsets. The conduction band edge shown for AlSb is the indirect minimum, in the Δ direction in the Brillouin zone.

ficient across an InAs/GaSb interface is less than unity; this produces carrier confinement at InAs/GaSb interfaces, allowing resonances to form even in the absence of the classically forbidden barrier regions that are responsible for the formation of quasi-bound states in conventional tunnel structures. Fig. 1.14 shows the transmission coefficient calculated for an InAs/GaSb interface, in the energy region between the InAs conduction band edge (0 eV) and the GaSb valence band edge (0.15 eV).

Studies of current-voltage characteristics in InAs/GaSb/InAs heterostructures as a function of GaSb layer width have provided strong confirmation of the existence of these confinement effects at the InAs/GaSb interface. By studying theoretically calculated and experimentally observed peak current densities in these devices as a function of GaSb layer width, we were able to demonstrate that transmission resonances are formed solely because of the imperfect matching of wavefunctions at the InAs/GaSb interfaces[179]. Additional studies have provided further confirmation of these effects[180], and a more detailed theoretical understanding of the full interactions among the light-hole, heavy-hole, and split-off valence bands and the lowest conduction band has also been developed[176].

1.3.4 Quantum-Well Band Structure and Tunneling Times for Holes

As discussed in Section 1.3.1, the characteristic time scale for tunneling processes in semiconductors is an issue of considerable fundamental, physical interest, and is also a major factor in determining the ultimate speed limitations of semiconductor tunnel devices. A number of optical experiments have measured the time for tunneling escape of photoexcited carriers in GaAs/AlAs/GaAs/AlAs/-GaAs double-barrier heterostructures[11, 163]. In these experiments, the electron

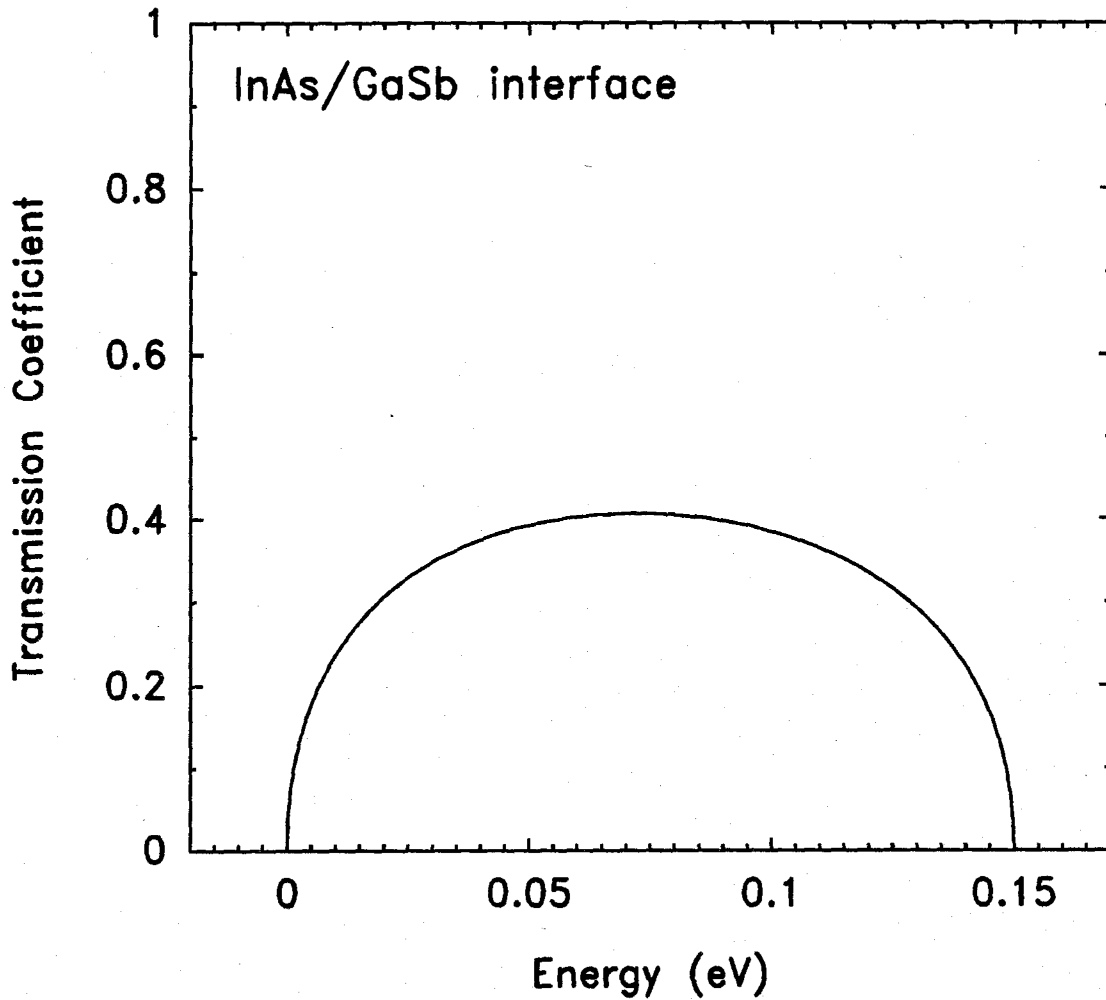

Figure 1.14: Transmission coefficient across the InAs/GaSb interface in the energy range between the InAs conduction-band edge (0 eV) and the GaSb valence-band edge (0.15 eV). The transmission coefficient was calculated using the two-band, tight-binding model discussed in Section 8.3.2.

tunneling times were found to depend exponentially on the barrier width, with good agreement obtained between the experimentally observed times and electron tunneling times calculated from the width of transmission resonances through the lowest quasi-bound state in the double barrier. Similar results were obtained by Norris et al.[170] for tunneling escape of carriers through a single finite barrier. In the experiments of Refs. [163] and [170], tunneling of holes was neglected; hole tunneling times were expected to be much longer than electron times because of the large effective mass of the heavy holes[163]. The work of Ref. [11], however, indicated that tunneling times for holes were much shorter than suggested by a simple calculation using the heavy-hole effective mass, and were actually comparable to electron tunneling times.

An explanation for these anomalously short hole tunneling times has been developed by incorporating band-mixing effects for quantum-well valence-band states. In the very simplest calculations of valence-band structure, the light-hole and heavy-hole bands are assumed to be parabolic, with effective masses m^*_{lh} and m^*_{hh}, respectively, and no interactions between the bands are included. Such a band-structure model would yield the extremely long heavy-hole tunneling times assumed in Refs. [163] and [170]. The heavy-hole tunneling time was assumed to be the more relevant, since the valence subband with the lowest energy in a quantum well should be heavy-holelike.

In reality, however, there is considerable interaction between the light-hole and heavy-hole states. Fig. 1.15 shows the valence subband structure for a 58 Å GaAs quantum well surrounded by AlAs barriers calculated using the 4×4 Luttinger-Kohn Hamiltonian[185], which accounts for interactions between the zone-center light-hole and heavy-hole states. The presence of interactions between bands is apparent from the pronounced nonparabolicity of the individual subbands. At the Brillouin zone center ($k_{\|} = 0$), the quantum-well valence subbands can be

characterized as being entirely heavy-holelike or light-holelike in character; for $k_{\|} \neq 0$, however, each subband is composed of a mixture of heavy-hole and light-hole components. By including this effect in a phenomenological model for calculating average tunneling times for a population of holes in the lowest quantum-well valence subband[166], average hole tunneling times are obtained that are comparable to electron tunneling times and in good agreement with the experimental results of Ref. [11]. The average hole tunneling times are found to depend quite strongly on experimental conditions such as carrier temperature and concentration. Subsequent calculations using the effective-bond-orbital model[186, 187] to compute transmission coefficients for valence-band states in GaAs/AlAs double-barrier heterostructures confirmed the basic validity of the earlier phenomenological model for calculating average hole tunneling times[167].

1.4 Outline of Thesis

Part I of the thesis describes studies of band offsets in semiconductor heterojunctions using XPS. Chapter 2 describes in detail the use of XPS to measure semiconductor heterojunction valence-band offsets. The basic physical principles of the XPS technique are discussed, with emphasis placed on capabilities of the technique that have proven to be especially relevant in our studies of semiconductor interfaces. The specific measurements required to determine a valence-band offset value are described, and data analysis techniques are presented that allow the extraction of band offset values to a typical accuracy of $\pm 0.07 - 0.08$ eV.

Chapter 3 discusses a measurement of the GaAs/AlAs (100) valence-band offset, and a confirmation of the commutativity (independence of growth sequence) of band offset values in the GaAs/AlAs material system. A synopsis of

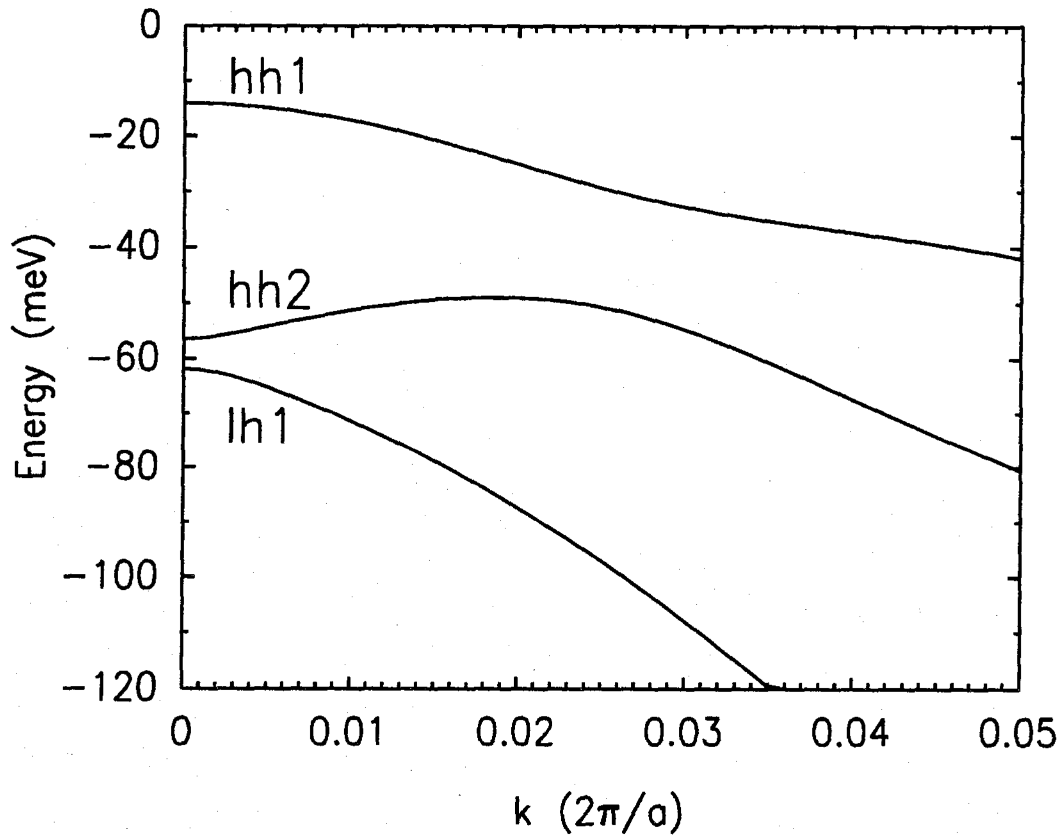

Figure 1.15: Valence subband structure for a 58 Å GaAs quantum well surrounded by AlAs barriers. The quantum-well subband structure was calculated using the 4×4 Luttinger-Kohn Hamiltonian in the spherical approximation. The two lowest subbands (labeled $hh1$ and $hh2$) correspond to pure heavy-hole states at $k = 0$. The third subband (labeled $lh1$) corresponds to a pure light-hole state at $k = 0$.

the controversy surrounding the GaAs/AlAs band offset value, and the eventual resolution of that controversy, is presented, and our measured value is shown to be consistent with the currently accepted band offset values. The relationship between commutativity and interfacial quality as elucidated by our experiments and previously reported results is explained; our demonstration of commutativity is taken as an indication of good interfacial quality.

In Chapter 4 we present a measurement of the valence-band offset for the lattice-mismatched Si/Ge (001) heterojunction system. A discussion of some of the issues arising in the study of strained-layer heterojunctions is given, with particular emphasis placed on the issues of critical thickness for strain relaxation and the influence of strain on electronic structure. A method developed to extend the applicability of the XPS technique described in Chapter 2 to the determination of strain-dependent band offsets is presented and applied to the Si/Ge (001) heterojunction system. Our results are shown to confirm that strain effects exert a profound influence on band offset values, and are compared to other reported experimental and theoretical results for the Si/Ge heterojunction. An interpolation scheme for determining band offset values for $Si_{1-x}Ge_x$ alloy heterojunctions is described, and is used to demonstrate the consistency of our results with Si/-$Si_{1-x}Ge_x$ modulation-doping experiments that have been reported.

Chapter 5 discusses a number of studies of band offsets in III-V/II-VI heterojunction systems. III-V/II-VI heterojunctions are of potential technological interest in the development of II-VI-based LED's, and also allow one to explore the influence of interfacial chemistry on band offset values. A measurement of the AlSb/ZnTe (100) valence-band offset is described, and implications for a proposed AlSb/ZnTe heterojunction light-emitter device concept are discussed. Evidence of an interfacial reaction occurring at the AlSb/ZnTe interface is presented, and approaches for determining the influence of these reactions on band offset values

are discussed. In one approach, band offset transitivity for the AlSb/GaSb/ZnTe material system is tested, the motivation being that a violation of transitivity would suggest that chemical reactivity at the III-V/II-VI interfaces was influencing band offset values. Measurements of the GaSb/AlSb and GaSb/ZnTe valence-band offsets are shown to demonstrate a clear violation of the transitivity rule, suggesting that band offset values are indeed shifted by III-V/II-VI interfacial reactions. Finally, alterations of growth conditions at the GaSb/ZnTe and AlSb/ZnTe interfaces are shown to produce shifts in band offset values, with an apparent correlation observed between partial suppression of the AlSb/ZnTe interface reaction and a shift in the AlSb/ZnTe valence-band offset that reduces the deviation from transitivity in the AlSb/GaSb/ZnTe material system.

Chapter 6 describes the measurement of the valence-band offset for the CdSe/-ZnTe (100) heterojunction. Growth of CdSe in the cubic zincblende form, rather than in its natural wurtzite structure, on nearly lattice-matched ZnTe surfaces is described, and the measurement of the CdSe/ZnTe valence-band offset by XPS, including a confirmation of commutativity, is presented. The results are discussed in the context of possible heterojunction approaches for injection of electrons into *p*-ZnTe for fabricating visible light emitters. In addition, the CdSe/ZnTe valence-band offset is compared to results reported for the ZnSe/ZnTe valence-band offset, and possible implications for the common anion rule are addressed.

Part II of the thesis describes theoretical and experimental studies of tunneling in semiconductor heterostructures. Chapter 7 explains the basic theoretical models we have used to simulate a wide variety of tunnel structures. The calculation of electrostatic band bending in heterostructure devices is described, and methods are developed to treat band bending in a wide range of structures; some numerical issues are also addressed. Calculations of transmission coefficients, using a transfer-matrix method in conjunction with a wide variety of band struc-

ture models, are discussed; implementations of the transfer-matrix method for one-band and two-band models are described in detail. Methods for calculating current-voltage characteristics for heterostructure devices are then presented, and the validity of various quantities, e.g., current densities, resonant voltages, and peak-to-valley current ratios for tunnel structures, extracted from these theoretical calculations is discussed. Finally, these techniques are applied to the calculation of current-voltage characteristics for double-barrier tunnel structures realized in the GaAs/ZnSe and InAs/ZnTe material systems.

Chapter 8 discusses theoretical and experimental studies of interband transport in the InAs/GaSb/AlSb material system. Band alignments in the InAs/-GaSb/AlSb system, and material properties of InAs and GaSb are discussed in the context of both fundamental physics and device applications. Several device structures that have been demonstrated in the McGill group laboratories, and their respective advantages, disadvantages, and novel properties of interest are briefly discussed. We then focus on a study of transport in the InAs/GaSb/-InAs device structure. A theoretical and experimental study of the dependence of the resonant current density on the GaSb layer width in this device is shown to demonstrate the existence of resonances in the GaSb quantum-well layers, despite the absence of classically forbidden barrier layers surrounding the GaSb layer; this result helps to clarify the basic nature of interband transport and the coupling between conduction-band and valence-band states in different layers of a heterostructure.

Finally, in Chapter 9 we present a theoretical study of hole tunneling times in GaAs/AlAs double-barrier heterostructures. The experimental observation of anomalously short hole tunneling times that motivated this work is reviewed, and a phenomenological model explaining this experimental observation as a consequence of valence-band mixing is developed. Average hole tunneling times

calculated for a distribution of holes photoexcited in a quantum well are shown to be in good agreement with experimental observations, and variations in the calculated average hole tunneling times with hole temperature and concentration are discussed. A brief description is then given of more recent calculations of average hole tunneling times derived from transmission coefficients computed using the eight-band effective-bond-orbital model. These results are shown to confirm the basic validity of the earlier phenomenological model.

References

[1] J. R. Waldrop, S. P. Kowalczyk, R. W. Grant, E. A. Kraut, and D. L. Miller, *J. Vac. Sci. Technol.* **19**, 573 (1981).

[2] J. R. Waldrop, R. W. Grant, and E. A. Kraut, *J. Vac. Sci. Technol. B* **5**, 1209 (1987).

[3] C. G. Van de Walle and R. M. Martin, *J. Vac. Sci. Technol. B* **3**, 1256 (1985).

[4] C. G. Van de Walle and R. M. Martin, *Phys. Rev. B* **34**, 5621 (1986).

[5] G. P. Schwartz, M. S. Hybertsen, J. Bevk, R. G. Nuzzo, J. P. Mannaerts, and G. J. Gualtieri, *Phys. Rev. B* **39**, 1235 (1989).

[6] R. People, J. C. Bean, D. V. Lang, A. M. Sergent, H. L. Störmer, K. W. Wecht, R. T. Lynch, and K. Baldwin, *Appl. Phys. Lett.* **45**, 1231 (1984).

[7] G. Abstreiter, H. Brugger, T. Wolf, H. Jorke, and H. J. Herzog, *Phys. Rev. Lett.* **54**, 2441 (1985).

[8] J. O. McCaldin and T. C. McGill, *J. Vac. Sci. Technol. B* **6**, 1360 (1988).

[9] J. O. McCaldin, T. C. McGill, and C. A. Mead, *Phys. Rev. Lett.* **36**, 56 (1976).

[10] Y. Rajakarunanayake, R. H. Miles, G. Y. Wu, and T. C. McGill, *Phys. Rev. B* **37**, 10212 (1988).

[11] M. K. Jackson, M. B. Johnson, D. H. Chow, T. C. McGill, and C. W. Nieh, *Appl. Phys. Lett.* **54**, 552 (1989).

[12] H. Kroemer, *Proc. IRE* **45**, 1535 (1957).

[13] H. Kroemer, *Proc. IEEE* **70**, 13 (1982).

[14] W. P. Dumke, J. M. Woodall, and V. L. Rideout, *Solid-State Electron.* **15**, 1339 (1972).

[15] H. C. Casey and M. B. Panish, *Heterostructure Lasers* (Academic Press, New York, 1978).

[16] R. Tsu and L. Esaki, *Appl. Phys. Lett.* **22**, 562 (1973).

[17] L. L. Chang, L. Esaki, and R. Tsu, *Appl. Phys. Lett.* **24**, 593 (1974).

[18] G. A. Sai-Halasz, R. Tsu, and L. Esaki, *Appl. Phys. Lett.* **30**, 651 (1977).

[19] J. N. Schulman and T. C. McGill, *Appl. Phys. Lett.* **34**, 663 (1979).

[20] D. L. Smith, T. C. McGill, and J. N. Schulman, *Appl. Phys. Lett.* **43**, 180 (1983).

[21] G. C. Osbourn, *J. Appl. Phys.* **53**, 1586 (1982).

[22] D. L. Smith and C. Mailhiot, *J. Appl. Phys.* **62**, 2545 (1987).

[23] E. A. Kraut, R. W. Grant, J. R. Waldrop, and S. P. Kowalczyk, *Phys. Rev. Lett.* **44**, 1620 (1980).

[24] R. Dingle, W. Wiegmann, and C. H. Henry, *Phys. Rev. Lett.* **33**, 827 (1974).

[25] H. Kroemer, W. Y. Chien, J. S. Harris, Jr., and D. D. Edwall, *Appl. Phys. Lett.* **36**, 295 (1980).

[26] R. C. Miller, A. C. Gossard, D. A. Kleinman, and O. Munteanu, *Phys. Rev. B* **29**, 3740 (1984).

[27] J. Batey and S. L. Wright, *J. Appl. Phys.* **59**, 200 (1985).

[28] J. Batey and S. L. Wright, *Surf. Sci.* **174**, 320 (1986).

[29] W. I. Wang and F. Stern, *J. Vac. Sci. Technol. B* **3**, 1280 (1985).

[30] D. J. Wolford, T. F. Kuech, J. A. Bradley, M. A. Gell, D. Ninno, and M. Jaros, *J. Vac. Sci. Technol. B* **4**, 1043 (1986).

[31] J. Menéndez, A. Pinczuk, D. J. Werder, A. C. Gossard, and J. H. English, *Phys. Rev. B* **33**, 8863 (1986).

[32] R. C. Miller, D. A. Kleinman, and A. C. Gossard, *Phys. Rev. B* **29**, 7085 (1984).

[33] T. W. Hickmott, P. M. Solomon, R. Fischer, and H. Morkoç, *J. Appl. Phys.* **57**, 2844 (1985).

[34] D. Arnold, A. Ketterson, T. Henderson, J. Klem, and H. Morkoç, *Appl. Phys. Lett.* **45**, 1237 (1984).

[35] H. Okumura, S. Misawa, S. Yoshida, and S. Gonda, *Appl. Phys. Lett.* **46**, 377 (1985).

[36] M. O. Watanabe, J. Yoshida, M. Mashita, T. Nakanisi, and A. Hojo, *J. Appl. Phys.* **57**, 5340 (1985).

[37] G. Duggan, *J. Vac. Sci. Technol. B* **3**, 1224 (1985).

[38] E. T. Yu, D. H. Chow, and T. C. McGill, *Phys. Rev. B* **38**, 12764 (1988).

[39] R. L. Anderson, *Solid–State Electron.* **5**, 341 (1962).

[40] A. G. Milnes and D. L. Feucht, *Heterojunctions and Metal–Semiconductor Junctions* (Academic Press, New York, 1972).

[41] J. Menéndez, A. Pinczuk, D. J. Werder, J. P. Valladares, T. H. Chiu, and W. T. Tsang, *Solid State Commun.* **61**, 703 (1987).

[42] H. Kroemer, *J. Vac. Sci. Technol. B* **2**, 433 (1984).

[43] J. L. Freeouf and J. M. Woodall, *Appl. Phys. Lett.* **39**, 727 (1981).

[44] W. R. Frensley and H. Kroemer, *J. Vac. Sci. Technol.* **13**, 810 (1976).

[45] W. R. Frensley and H. Kroemer, *Phys. Rev. B* **16**, 2642 (1977).

[46] W. A. Harrison, *J. Vac. Sci. Technol.* **14**, 1016 (1977).

[47] D. J. Chadi and M. L. Cohen, *Phys. Status Solidi (B)* **68**, 405 (1975).

[48] F. Herman and S. Skillman, *Atomic Structure Calculations* (Prentice Hall, Englewood Cliffs, NJ, 1963).

[49] W. A. Harrison, *Phys. Rev. B* **24**, 5835 (1981).

[50] E. A. Kraut, *J. Vac. Sci. Technol. B* **2**, 486 (1984).

[51] J. B. Mann, *Atomic Structure Calculations, I: Hartree-Fock Energy Results for Elements Hydrogen to Lawrencium* (Clearing House for Technical Information, Springfield, VA, 1967).

[52] J. Tersoff, *Phys. Rev. B* **30**, 4874 (1984).

[53] J. Tersoff, *Phys. Rev. Lett.* **56**, 2755 (1986).

[54] W. A. Harrison and J. Tersoff, *J. Vac. Sci. Technol. B* **4**, 1068 (1986).

[55] C. Tejedor and F. Flores, *J. Phys. C* **11**, L19 (1978).

[56] C. Tejedor, F. Flores, and E. Louis, *J. Phys. C* **10**, 2163 (1977).

[57] F. Flores and C. Tejedor, *J. Phys. C* **12**, 731 (1979).

[58] J. Tersoff, *Phys. Rev. Lett.* **52**, 465 (1984).

[59] A. Zunger, *Ann. Rev. Mater. Sci.* **15**, 411 (1985).

[60] A. Zunger, *Solid State Phys.* **39**, 275 (1986).

[61] J. M. Langer and H. Heinrich, *Phys. Rev. Lett.* **55**, 1414 (1985).

[62] J. Tersoff and W. A. Harrison, *Phys. Rev. Lett.* **58**, 2367 (1987).

[63] A. D. Katnani and G. Margaritondo, *J. Appl. Phys.* **54**, 2522 (1983).

[64] A. D. Katnani and G. Margaritondo, *Phys. Rev. B* **28**, 1944 (1983).

[65] G. A. Baraff, J. A. Appelbaum, and D. R. Hamann, *Phys. Rev. Lett.* **38**, 237 (1977).

[66] G. A. Baraff, J. A. Appelbaum, and D. R. Hamann, *J. Vac. Sci. Technol.* **14**, 999 (1977).

[67] C. G. Van de Walle and R. M. Martin, *Phys. Rev. B* **35**, 8154 (1987).

[68] W. E. Pickett, S. G. Louie, and M. L. Cohen, *Phys. Rev. Lett.* **39**, 109 (1977).

[69] C. G. Van de Walle and R. M. Martin, *J. Vac. Sci. Technol. B* **4**, 1055 (1986).

[70] C. G. Van de Walle, *Phys. Rev. B* **39**, 1871 (1989).

[71] M. Cardona and N. E. Christensen, *Phys. Rev. B* **35**, 6182 (1987).

[72] N. E. Christensen, *Phys. Rev. B* **37**, 4528 (1988).

[73] N. E. Christensen, *Phys. Rev. B* **38**, 12687 (1988).

[74] W. R. L. Lambrecht and B. Segall, *Phys. Rev. Lett.* **61**, 1764 (1988).

[75] W. R. L. Lambrecht, B. Segall, and O. K. Andersen, *Phys. Rev. B* **41**, 2813 (1990).

[76] W. R. L. Lambrecht and B. Segall, *Phys. Rev. B* **41**, 2832 (1990).

[77] E. T. Yu, E. T. Croke, T. C. McGill, and R. H. Miles, *Appl. Phys. Lett.* **56**, 569 (1990).

[78] E. T. Yu, E. T. Croke, D. H. Chow, D. A. Collins, M. C. Phillips, T. C. McGill, J. O. McCaldin, and R. H. Miles, *J. Vac. Sci. Technol. B* **8**, 908 (1990).

[79] E. T. Yu, E. T. Croke, T. C. McGill, and R. H. Miles, presented at the SPIE Symposium on Advances in Semiconductors and Superconductors: Physics Toward Device Applications, San Diego, CA (1990).

[80] E. T. Yu, M. C. Phillips, D. H. Chow, D. A. Collins, and T. C. McGill, *Bull. Am. Phys. Soc.* **35**, 416 (1990).

[81] E. T. Yu, M. C. Phillips, D. H. Chow, D. A. Collins, M. W. Wang, J. O. McCaldin, and T. C. McGill, submitted to *Phys. Rev. B* (1991).

[82] R. W. Grant, J. R. Waldrop, and E. A. Kraut, *J. Vac. Sci. Technol.* **15**, 1451 (1978).

[83] J. R. Waldrop, E. A. Kraut, S. P. Kowalczyk, and R. W. Grant, *Surf. Sci.* **132**, 513 (1983).

[84] E. A. Kraut, R. W. Grant, J. R. Waldrop, and S. P. Kowalczyk, *Phys. Rev. B* **28**, 1965 (1983).

[85] S. P. Kowalczyk, W. J. Schaffer, E. A. Kraut, and R. W. Grant, *J. Vac. Sci. Technol.* **20**, 705 (1982).

[86] S. P. Kowalczyk, E. A. Kraut, J. R. Waldrop, and R. W. Grant, *J. Vac. Sci. Technol.* **21**, 482 (1982).

[87] F. Xu, M. Vos, J. P. Sullivan, Lj. Atanasoska, S. G. Anderson, J. H. Weaver, and H. Cheng, *Phys. Rev. B* **38**, 7832 (1988).

[88] G. J. Gualtieri, G. P. Schwartz, R. G. Nuzzo, R. J. Malik, and J. F. Walker, *J. Appl. Phys.* **61**, 5337 (1987).

[89] G. J. Gualtieri, G. P. Schwartz, R. G. Nuzzo, and W. A. Sunder, *Appl. Phys. Lett.* **49**, 1037 (1986).

[90] S. P. Kowalczyk, J. T. Cheung, E. A. Kraut, and R. W. Grant, *Phys. Rev. Lett.* **56**, 1605 (1986).

[91] T. M. Duc, C. Hsu, and J. P. Faurie, *Phys. Rev. Lett.* **58**, 1127 (1987).

[92] P. H. Mahowald, R. S. List, W. E. Spicer, J. Woicik, and P. Pianetta, *J. Vac. Sci. Technol. B* **3**, 1252 (1985).

[93] A. D. Katnani and R. S. Bauer, *Phys. Rev. B* **33**, 1106 (1986).

[94] W.-X. Ni, J. Knall, and G. V. Hansson, *Phys. Rev. B* **36**, 7744 (1987).

[95] W.-X. Ni and G. V. Hansson, *Phys. Rev. B* **42**, 3030 (1990).

[96] B. I. Miller, E. F. Schubert, U. Koren, A. Ourmazd, A. H. Dayem, and R. J. Capik, *Appl. Phys. Lett.* **49**, 1384 (1986).

[97] R. Sauer, T. D. Harris, and W. T. Tsang, *Phys. Rev. B* **34**, 9023 (1986).

[98] D. F. Welch, G. W. Wicks, and L. F. Eastman, *J. Appl. Phys.* **55**, 3176 (1984).

[99] A. Pinczuk, J. Shah, A. C. Gossard, and W. Wiegmann, *Phys. Rev. Lett.* **46**, 1341 (1981).

[100] L. M. Claessen, J. C. Maan, M. Altarelli, P. Wyder, L. L. Chang, and L. Esaki, *Phys. Rev. Lett.* **57**, 2556 (1986).

[101] A. C. Gossard, W. Brown, C. L. Allyn, and W. Wiegmann, *J. Vac. Sci. Technol.* **20**, 694 (1982).

[102] D. H. Chow, J. O. McCaldin, A. R. Bonnefoi, T. C. McGill, I. K. Sou, and J. P. Faurie, *Appl. Phys. Lett.* **51**, 2230 (1987).

[103] S. R. Forrest, P. H. Schmidt, R. B. Wilson, and M. L. Kaplan, *Appl. Phys. Lett.* **45**, 1199 (1984).

[104] R. People, K. W. Wecht, K. Alavi, and A. Y. Cho, *Appl. Phys. Lett.* **43**, 118 (1983).

[105] P. Z. Lee, C. L. Lin, J. C. Ho, L. G. Meiners, and H. H. Wieder, *J. Appl. Phys.* **67**, 4377 (1990).

[106] A. Nakagawa, H. Kroemer, and J. H. English, *Appl. Phys. Lett.* **54**, 1893 (1989).

[107] A. K. Srivastava, J. L. Zyskind, R. M. Lum, B. V. Dutt, and J. K. Klingert, *Appl. Phys. Lett.* **49**, 41 (1986).

[108] J. L. Shay, S. Wagner, and J. C. Phillips, *Appl. Phys. Lett.* **28**, 31 (1976).

[109] W. I. Wang, E. E. Mendez, and F. Stern, *Appl. Phys. Lett.* **45**, 639 (1984).

[110] W. I. Wang, T. S. Kuan, E. E. Mendez, and L. Esaki, *Phys. Rev. B* **31**, 6890 (1985).

[111] G. Abstreiter, U. Prechtel, G. Weimann, and W. Schlapp, *Physica B* **134**, 433 (1985).

[112] M. A. Haase, M. A. Emanuel, S. C. Smith, J. J. Coleman, and G. E. Stillman, *Appl. Phys. Lett.* **50**, 404 (1987).

[113] M. Heiblum, M. I. Nathan, and M. Eizenberg, *Appl. Phys. Lett.* **47**, 503 (1985).

[114] K. W. Goossen, S. A. Lyon, and K. Alavi, *Phys. Rev. B* **36**, 9370 (1987).

[115] H. Kroemer, *Surf. Sci.* **132**, 543 (1983).

[116] H. Kroemer, *Surf. Sci.* **174**, 299 (1986).

[117] F. Flores and C. Tejedor, *J. Phys. C* **20**, 145 (1987).

[118] E. T. Yu, J. O. McCaldin, and T. C. McGill, to appear in *Solid State Phys.* (1991).

[119] P. Dawson, B. A. Wilson, C. W. Tu, and R. C. Miller, *Appl. Phys. Lett.* **48**, 541 (1986).

[120] J. Wagner, W. Stolz, and K. Ploog, *Phys. Rev. B* **32**, 4214 (1985).

[121] Y. Sugiyama, T. Inata, T. Fujii, Y. Nakata, S. Muto, and S. Hiyamizu, *Jpn. J. Appl. Phys.* **25**, L648 (1986).

[122] E. E. Mendez, C.-A. Chang, H. Takaoka, L. L. Chang, and L. Esaki, *J. Vac. Sci. Technol. B* **1**, 152 (1983).

[123] G. Griffiths, K. Mohammed, S. Subbana, H. Kroemer, and J. L. Merz, *Appl. Phys. Lett.* **43**, 1059 (1983).

[124] C. Tejedor, J. M. Calleja, F. Meseguer, E. E. Mendez, C.-A. Chang, and L. Esaki, *Phys. Rev. B* **32**, 5303 (1985).

[125] W. Hansen, T. P. Smith, III, J. Piao, R. Beresford, and W. I. Wang, *Appl. Phys. Lett.* **56**, 81 (1990).

[126] R. Beresford, L. F. Luo, and W. I. Wang, *Appl. Phys. Lett.* **55**, 694 (1989).

[127] H. Sakaki, L. L. Chang, R. Ludeke, C.-A. Chang, G. A. Sai-Halasz, and L. Esaki, *Appl. Phys. Lett.* **31**, 211 (1977).

[128] J. R. Söderström, D. H. Chow, and T. C. McGill, *Appl. Phys. Lett.* **55**, 1094 (1989).

[129] D. A. Collins, D. H. Chow, E. T. Yu, D. Z.-Y. Ting, J. R. Söderström, Y. Rajakarunanayake, and T. C. McGill, presented at the 1990 NATO Workshop on Resonant Tunneling, El Escorial, Spain (1990).

[130] L. F. Luo, R. Beresford, and W. I. Wang, *Appl. Phys. Lett.* **55**, 2023 (1989).

[131] D. V. Lang, M. B. Panish, F. Capasso, J. Allam, R. A. Hamm, A. M. Sergent, and W. T. Tsang, *Appl. Phys. Lett.* **50**, 736 (1987).

[132] M. S. Skolnick, L. L. Taylor, S. J. Bass, A. D. Pitt, D. J. Mowbray, A. G. Cullis, and N. G. Chew, *Appl. Phys. Lett.* **51**, 24 (1987).

[133] M. A. Haase, N. Pan, and G. E. Stillman, *Appl. Phys. Lett.* **54**, 1457 (1989).

[134] J. R. Waldrop, R. W. Grant, and E. A. Kraut, *Appl. Phys. Lett.* **54**, 1878 (1989).

[135] J. R. Waldrop, R. W. Grant, and E. A. Kraut, *J. Vac. Sci. Technol. B* **7**, 815 (1989).

[136] R. S. Bauer and H. W. Sang, Jr., *Surf. Sci.* **132**, 479 (1983).

[137] K. Hirakawa, Y. Hashimoto, and T. Ikoma, *Appl. Phys. Lett.* **57**, 2555 (1990).

[138] D.-W. Tu and A. Kahn, *J. Vac. Sci. Technol. A* **3**, 922 (1985).

[139] K. J. Mackey, P. M. G. Allen, W. G. Herrenden-Harker, R. H. Williams, C. R. Whitehouse, and G. M. Williams, *Appl. Phys. Lett.* **49**, 354 (1986).

[140] W. G. Wilke and K. Horn, *J. Vac. Sci. Technol. B* **6**, 1211 (1988).

[141] W. G. Wilke, R. Seedorf, and K. Horn, *J. Vac. Sci. Technol. B* **7**, 807 (1989).

[142] L. Esaki, *Phys. Rev.* **109**, 603 (1958).

[143] R. Tsu and L. Esaki, *Appl. Phys. Lett.* **22**, 562 (1973).

[144] T. C. L. G. Sollner, W. D. Goodhue, P. E. Tannenwald, C. D. Parker, and D. D. Peck, *Appl. Phys. Lett.* **43**, 588 (1983).

[145] E. R. Brown, C. D. Parker, L. J. Mahoney, J. R. Söderström, and T. C. McGill, presented at the 48th Annual Device Research Conference, Santa Barbara, CA (1990).

[146] A. R. Bonnefoi, D. H. Chow, and T. C. McGill, *Appl. Phys. Lett.* **47**, 888 (1985).

[147] A. R. Bonnefoi, T. C. McGill, and R. D. Burnham, *IEEE Electron Device Lett.* **EDL-6**, 636 (1985).

[148] N. Yokoyama, K. Imamura, S. Muto, S. Hiyamizu, and H. Nishi, *Jpn. J. Appl. Phys.* **24**, L853 (1985).

[149] F. Capasso and R. A. Kiehl, *J. Appl. Phys.* **58**, 1366 (1985).

[150] F. Capasso, S. Sen, A. C. Gossard, A. L. Hutchinson, and J. H. English, *IEEE Electron Device Lett.* **EDL-7**, 573 (1986).

[151] T. K. Woodward, T. C. McGill, and R. D. Burnham, *Appl. Phys. Lett.* **50**, 451 (1987).

[152] K. Imamura, T. Mori, H. Ohnishi, S. Muto, and N. Yokoyama, *Electronics Letters* **25**, 34 (1989).

[153] M. A. Reed, W. R. Frensley, R. J. Matyi, J. N. Randall, and A. C. Seabaugh, *Appl. Phys. Lett.* **54**, 1034 (1989).

[154] C. H. Yang, Y. C. Kao, and H. D. Shih, *Appl. Phys. Lett.* **55**, 2742 (1989).

[155] S. S. Rhee, G. K. Chang, T. K. Carns, and K. L. Wang, *Appl. Phys. Lett.* **56,** 1061 (1990).

[156] D. A. Collins, D. H. Chow, and T. C. McGill, submitted to *Appl. Phys. Lett.* (1990).

[157] E. R. Brown, C. D. Parker, and T. C. L. G. Sollner, *Appl. Phys. Lett.* **54**, 934 (1989).

[158] K. K. Thornber, T. C. McGill, and C. A. Mead, *J. Appl. Phys.* **38**, 2384 (1967).

[159] M. Büttiker and R. Landauer, *Phys. Rev. Lett.* **49**, 1739 (1982).

[160] N. Harada and S. Kuroda, *Jpn. J. Appl. Phys. Pt. 2* **25**, L871 (1986).

[161] S. Collins, D. Lowe, and J. R. Barker, *J. Phys. C* **20**, 6213 (1987).

[162] H. Guo, K. Diff, G. Neofotistos, and J. D. Gunton, *Appl. Phys. Lett.* **53**, 131 (1988).

[163] M. Tsuchiya, T. Matsusue, and H. Sakaki, *Phys. Rev. Lett.* **59**, 2356 (1987).

[164] J. F. Whitaker, G. A. Mourou, T. C. L. G. Sollner, and W. D. Goodhue, *Appl. Phys. Lett.* **53**, 385 (1988).

[165] R. Sauer, K. Thonke, and W. T. Tsang, *Phys. Rev. Lett.* **61**, 609 (1988).

[166] E. T. Yu, M. K. Jackson, and T. C. McGill, *Appl. Phys. Lett.* **55**, 744 (1989).

[167] D. Z.-Y. Ting, E. T. Yu, and T. C. McGill, submitted to *Phys. Rev. B* (1991).

[168] A. Tackeuchi, S. Muto, T. Inata, and T. Fujii, *Jpn. J. Appl. Phys. Pt. 2* **28**, 1098 (1989).

[169] T. Tada, A. Yamaguchi, T. Ninomiya, H. Uchiki, T. Kobayashi, and T. Yao, *J. Appl. Phys.* **63**, 5491 (1988).

[170] T. B. Norris, X. J. Song, W. J. Schaff, L. F. Eastman, G. Wicks, G. A. Mourou, *Appl. Phys. Lett.* **54**, 60 (1989).

[171] B. Ricco and M. Ya. Azbel, *Phys. Rev. B* **29**, 1970 (1984).

[172] W. R. Frensley, *J. Vac. Sci. Technol. B* **3**, 1261 (1985).

[173] S. Luryi, *Appl. Phys. Lett.* **47**, 490 (1985).

[174] J. R. Söderström, E. T. Yu, M. K. Jackson, Y. Rajakarunanayake, and T. C. McGill, *J. Appl. Phys.* **68**, 1372 (1990).

[175] D. Z.-Y. Ting, E. T. Yu, D. A. Collins, D. H. Chow, and T. C. McGill, *J. Vac. Sci. Technol. B* **8**, 810 (1990).

[176] D. Z.-Y. Ting, E. T. Yu, and T. C. McGill, *Appl. Phys. Lett.* **58** 292 (1991).

[177] A. R. Bonnefoi, *Electronic Properties and Device Applications of $GaAs/Al_xGa_{1-x}As$ Quantum Barrier and Quantum Well Heterostructures*, Ph.D. thesis, California Institute of Technology, Pasadena, CA (1987).

[178] E. O. Kane, in *Tunneling Phenomena in Solids*, E. Burstein and S. Lundqvist, eds. (Plenum Press, New York, 1969), p. 1.

[179] E. T. Yu, D. A. Collins, D. Z.-Y. Ting, D. H. Chow, and T. C. McGill, *Appl. Phys. Lett.* **57**, 2675 (1990).

[180] D. Z.-Y. Ting, D. A. Collins, E. T. Yu, D. H. Chow, and T. C. McGill, *Appl. Phys. Lett.* **57**, 1257 (1990).

[181] R. Beresford, L. F. Luo, and W. I. Wang, *Appl. Phys. Lett.* **54**, 1899 (1988).

[182] J. R. Söderström, D. H. Chow, and T. C. McGill, *Appl. Phys. Lett.* **55**, 1348 (1989).

[183] H. Munekata, T. P. Smith, III, and L. L. Chang, *J. Vac. Sci. Technol.* **B7**, 324 (1989).

[184] M. Sweeny and J. Xu, *Appl. Phys. Lett.* **53**, 60 (1989).

[185] J. M. Luttinger and W. Kohn, *Phys. Rev.* **97**, 869 (1955).

[186] Y. C. Chang, *Phys. Rev. B* **37**, 8215 (1988).

[187] G. T. Einevoll and Y. C. Chang, *Phys. Rev. B* **40**, 9683 (1989).

Part I

Measurement of Band Offsets in Semiconductor Heterojunctions

Chapter 2

Measurement of Band Offsets Using X-Ray Photoelectron Spectroscopy

2.1 Introduction

2.1.1 Background and Motivation

The lack of a reliable, predictive theory of band offsets and the paramount importance of band offset values in assessing the viability of heterojunction device concepts have provided strong motivation for the development of accurate yet relatively simple techniques for measuring band offset values experimentally. As discussed in Chapter 1, a number of optical and electrical measurement techniques have been used to determine band offsets for GaAs/$Al_xGa_{1-x}As$ and other material systems of current technological interest. However, most of these band offset measurement techniques require the high–quality growth of complex epitaxial structures such as quantum wells or superlattices[1, 2, 3, 4, 5], and in

addition often demand the ability to process epitaxial wafers into functional electrical devices[6, 7, 8]. For many novel material systems, however, techniques for obtaining high–quality epitaxial growth of complex structures or for processing wafers into electrical devices have not been developed, obviating the use of many band-offset measurement techniques; indeed, one would often desire to measure the band offsets for a novel heterojunction system in order to determine whether or not the development of a sophisticated epitaxial growth and processing technology would be worthwhile.

A technique that requires neither complex epitaxial structures nor the ability to produce electrical devices, and that is widely acknowledged to yield reliable results[9, 10], is the measurement of valence-band offsets using x-ray photoelectron spectroscopy (XPS)[11, 12, 13]. The XPS technique requires only the growth of bulk material and simple heterojunctions, and yields a direct measurement of the valence-band offset; the XPS measurement is therefore ideally suited to the study of band offsets in novel heterojunction systems. The validity of this technique for measuring valence-band offsets for lattice-matched heterojunctions has been well established[11, 12, 13, 14, 15]; we have used the XPS technique to study band offsets and interfacial chemistry in a number of lattice-matched heterojunction systems[13, 16, 17], and have extended its use to the study of band offsets in lattice-mismatched heterojunctions[18].

2.1.2 Outline of Chapter

Section 2.2 discusses the basic physical principles of XPS, with emphasis on capabilities of the technique that have proven to be especially relevant in studies of semiconductor interfaces. The measurement of valence-band offsets by XPS is described in Section 2.3; experimental procedures are presented in Section 2.3.1,

and data analysis techniques that allow the extraction of precise band offset values are explained in Section 2.3.2. The chapter is summarized in Section 2.4.

2.2 Physical Principles of XPS

X-ray photoelectron spectroscopy consists of the excitation of a sample using X rays (photons with energies ranging approximately from 100 eV to $\sim 10,000$ eV), and the detection of the energy spectrum of photoexcited electrons ejected from the sample. XPS is one technique in the category of spectroscopies known as Electron Spectroscopy for Chemical Analysis (ESCA), developed by Kai Siegbahn and coworkers at Uppsala University[19].

The principal feature distinguishing XPS from other ESCA techniques is the energy of the photoexcitation source. In XPS, X rays are typically produced by electron bombardment of a suitable elemental target, most commonly Al or Mg. Mg and Al x-ray sources produce characteristic $K\alpha_{1,2}$ x-ray lines at energies of 1253.6 eV and 1486.6 eV, respectively[20]. Typical natural linewidths for non-monochromatic Mg and Al x-ray sources are 0.7 eV and 0.8 eV full width at half maximum (FWHM), respectively[20]; a monochromator can reduce the Al $K\alpha$ x-ray linewidth to $0.3 - 0.4$ eV FWHM. The $K\alpha_1$ and $K\alpha_2$ characteristic lines are produced by $2p_{3/2} \longrightarrow 1s$ and $2p_{1/2} \longrightarrow 1s$ atomic transitions, and are by far the most intense x-ray lines produced in Mg and Al; the next most important lines are the $K\alpha_3$ and $K\alpha_4$ lines, with intensities of approximately 8% and 4% of the $K\alpha_{1,2}$ intensity.

Photoelectron spectroscopy can also be performed using ultraviolet light sources, which produce photons with energies ranging approximately from 16 eV to 41 eV. This technique, known as ultraviolet photoelectron spectroscopy (UPS), has the advantage that excitation sources with high intensity and narrow linewidths

are readily available, providing higher resolution than available with XPS; however, the photon energies are too low for photoexcitation of electrons from inner shell states to occur in most atoms, reducing the usefulness of the technique for studies of chemical composition and bonding. UPS is typically used in detailed, high-resolution studies of valence-band structure and surface electronic structure in solids. Synchrotron radiation sources, which can provide a continuous spectrum of extremely high-intensity radiation ranging in energy from ~ 10 eV to several keV, have also been used in photoelectron spectroscopy; the availability of monochromators, however, has limited most of these studies to photon energies of approximately 10–300 eV[14], and limited access to synchrotron sources has also restricted their use.

The electron-energy spectrum obtained in x-ray photoelectron spectroscopy is typically presented in terms of the electron binding energy, defined to be the energy required to move the electron from its energy level within the sample to infinity with zero kinetic energy. In XPS measurements, the binding energy is always expressed relative to a reference level, which for solid samples is taken to be the Fermi level of the sample–spectrometer system. This definition of the binding energy, as well as its relation to electron kinetic energy immediately following photoexcitation and as measured by the spectrometer, are shown schematically in Fig. 2.1. For solid, sufficiently conductive specimens, an electrical contact is made and thermodynamic equilibrium is established between the sample and the spectrometer, resulting in a single Fermi level characteristic of both. It can then be seen from Fig. 2.1 that the binding energy E_B is given by

$$h\nu = E_B + T_{sp} + \phi_{sp}, \tag{2.1}$$

or

$$E_B = h\nu - T_{sp} - \phi_{sp}, \tag{2.2}$$

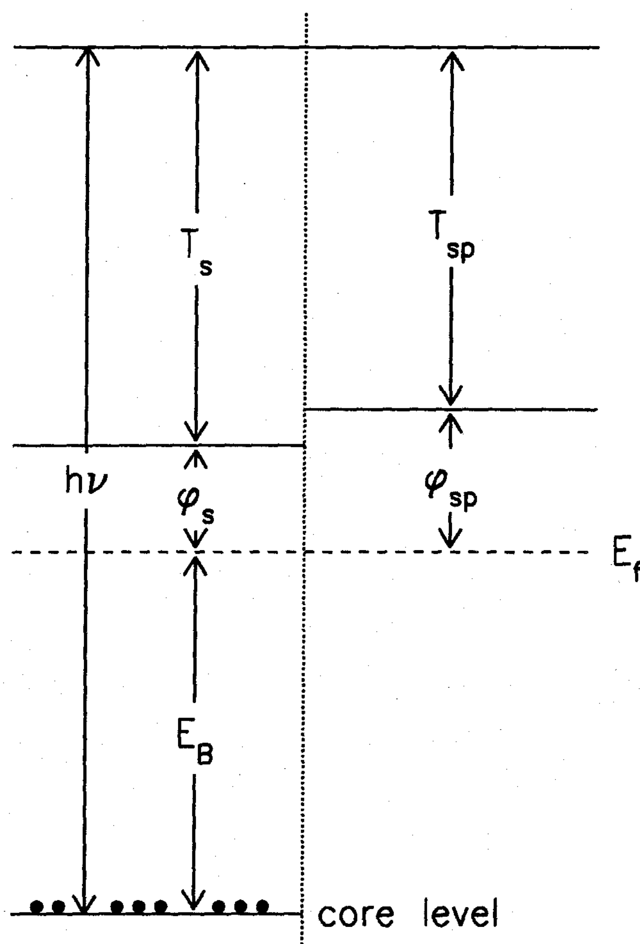

Figure 2.1: Schematic diagram of energy levels relevant for x-ray photoelectron spectroscopy. ϕ_s and ϕ_{sp} are the work functions (separation between the Fermi level and the vacuum level) for the sample and spectrometer, respectively. T_s and T_{sp} are the photoelectron kinetic energies immediately after ejection from the sample, and as measured by the spectrometer, respectively; E_B is the binding energy of the electronic core level with respect to the Fermi level E_f, and $h\nu$ is the energy of the incident photon.

where $h\nu$ is the photon energy, T_{sp} the electron kinetic energy measured by the spectrometer, and ϕ_{sp}, the spectrometer work function. Also labeled in Fig. 2.1 are T_s, the electron kinetic energy immediately following photoexcitation, and ϕ_s, the work function of the sample.

A typical electron binding-energy spectrum for GaAs is shown in Fig. 2.2. As seen in the figure, the spectrum contains peaks corresponding to atomic core levels, and exhibits a continuous density of states near the valence-band edge (at approximately 0 eV binding energy). The ability in XPS to photoexcite electrons from core levels of all naturally occurring elements allows one to obtain a great deal of chemical information about one's sample. A quantitative determination of chemical composition can be extracted by analyzing the relative intensities of different atomic core-level peaks, and information about the chemical bonding states of different atoms can be obtained by measuring energy shifts of atomic core-level peaks. Such shifts occur because atoms in different chemical bonding states transfer an amount of charge correlated approximately with the relative electronegativity of the species to which they are bonded[21, 22]. Thus, atoms in different chemical states have slightly different effective charge, producing shifts in atomic core-level energies to higher or lower binding energies for positively and negatively charged atoms, respectively.

A major distinguishing feature of all electron spectroscopies is that they are extremely sensitive to surface properties, because of the short mean free paths of electrons in solid materials. The main structural features present in the electron binding-energy spectrum are produced by electrons that escape from the sample without losing energy through inelastic scattering; electrons photoexcited from a given energy level in the sample, but which lose energy through inelastic scattering, simply contribute to a broad background signal at greater binding energies (corresponding to lower electron kinetic energy). For photoelectron kinetic en-

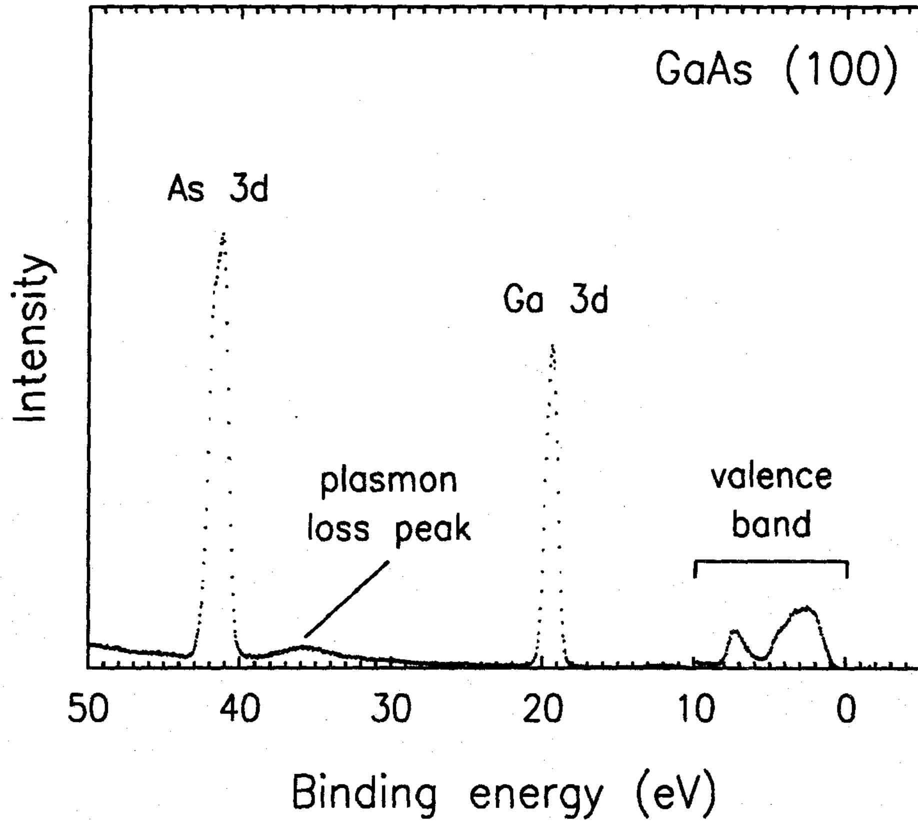

Figure 2.2: A representative XPS electron-energy spectrum obtained from GaAs (100). Peaks are observed for the Ga 3*d* and As 3*d* atomic core levels, and a continuous spectrum is observed for the valence band states. A plasmon loss peak, corresponding to excitation of a single plasmon mode by electrons photoexcited from the Ga 3*d* core level, can also be seen. The discontinuity in the spectrum at 10 eV binding energy is due to the longer sampling times used near the valence band edge.

ergies typical of XPS experiments (approximately 1000–1500 eV), typical elastic escape depths are $10-30$ Å, with the escape depth for semiconductors such as Ge being approximately 25 Å[12, 23]. Elastic electron escape depths decrease considerably with electron kinetic energy; for photoelectron kinetic energies found in UPS experiments ($1-40$ eV), electron escape depths of $5-10$ Å are typical. UPS is therefore extremely sensitive to surface electronic structure, and only moderately sensitive to bulk electronic properties. XPS, while still somewhat sensitive to surface electronic structure, yields an electron-energy spectrum that is essentially characteristic of the bulk material. Fig. 2.3 shows electron mean free paths measured in a number of materials as a function of electron kinetic energy. The mean free path reaches a minimum of only a few Angstroms at electron energies of approximately 50 to 100 eV, and increases steadily to a few tens of Angstroms at kinetic energies of 1000 to 2000 eV. In addition, the mean free path rises quite sharply with decreasing electron energy for energies less than 50 eV, allowing experiments utilizing tunable synchrotron-radiation sources, in which a core-level peak intensity can be monitored as a function of electron escape energy, to achieve considerable sample depth discrimination. The dashed line in Fig. 2.3 was obtained from a calculation of the inelastic mean free path of electrons in a free-electron gas with a density approximating that in the valence band of most solids[24, 25]; as seen in the figure, this model explains the experimental data reasonably well.

The surface sensitivity characteristic of all photoelectron spectroscopies necessitates the creation of an ultrahigh vacuum (UHV) environment in which to conduct these experiments. Typical XPS analytical UHV chambers are maintained at pressures of $\sim 10^{-10}$ Torr. At a background pressure of 10^{-6} Torr, contaminants with unity sticking coefficient will accumulate on the sample surface at a rate of approximately one monolayer per second. Hence, a pressure

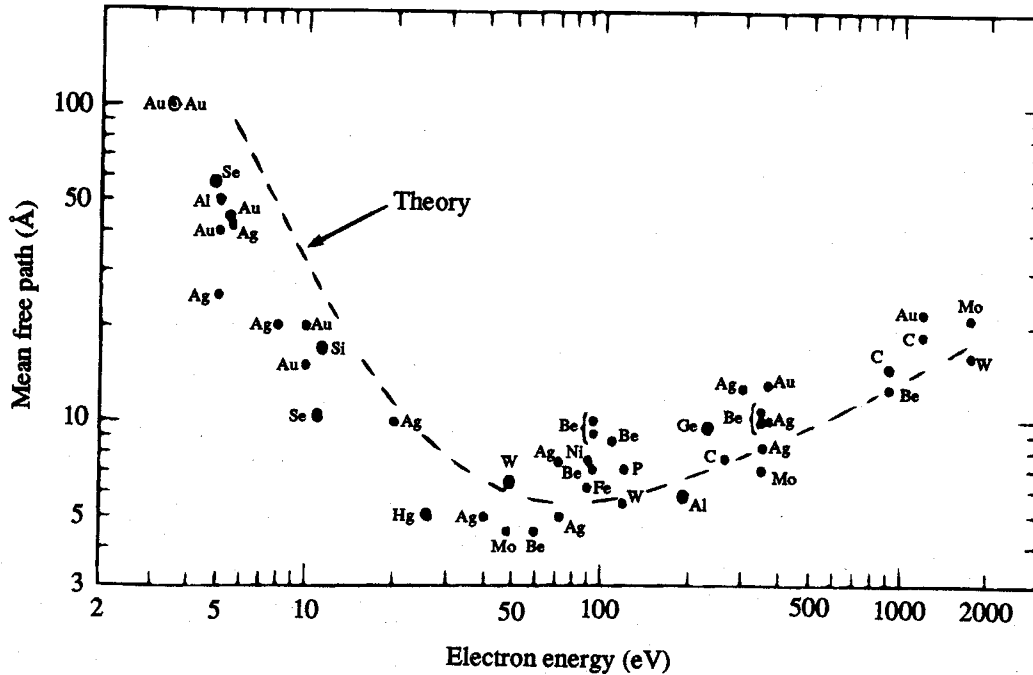

Figure 2.3: Electron mean free path measured in a number of materials as a function of electron kinetic energy. The mean free path reaches a minimum of only a few Angstroms at electron energies of 50 to 100 eV, and rises to a few tens of Angstroms at kinetic energies of 1000 to 2000 eV. The mean free path also increases sharply with decreasing electron energy below 50 eV. The dashed line represents a theoretical calculation of the mean free path in which the solid is modeled as a free electron gas with a density approximating that in the valence band of most solids. This model explains the experimental data reasonably well. (After Ref. [24]).

of 10^{-10} Torr guarantees that a relatively clean surface can be maintained for at least three hours, and in practice clean semiconductor surfaces can often be maintained in a UHV environment over periods of several days or longer.

2.3 Measurement of Band Offsets by XPS

2.3.1 Experimental Considerations

The measurement of valence-band offsets by XPS is based on the ability to measure very precisely characteristic core-level binding energies relative to each other and to the valence-band edge in a semiconductor. Fig. 2.4 shows a schematic energy-band diagram for a typical semiconductor heterojunction illustrating the basic principle of the technique. To determine the value of the valence-band offset, one first measures the binding energy, relative to the valence-band edge, of a characteristic core level in each semiconductor. The core-level binding energy provides a well-defined reference for the position of the valence-band edge in each material. One then measures, in a heterojunction, the separation between the reference core levels of each semiconductor; since the core levels in each material provide a precise reference for the position of the valence-band edge, the core-level energy separation can be translated directly into a value for the valence-band offset,

$$\Delta E_v(1/2) = (E_{cl}^1 - E_v^1) + (E_{cl}^2 - E_{cl}^1) - (E_{cl}^2 - E_v^2), \qquad (2.3)$$

where $\Delta E_v(1/2)$ is the valence-band offset between semiconductor 1 and semiconductor 2, E_{cl}^i is the reference core-level energy of semiconductor i, and E_v^i is the position in energy of the valence-band edge in semiconductor i.

In a typical experiment, reference core-level binding energies are first measured in a thick film (approximately 250–5000 Å) of each semiconductor. Some

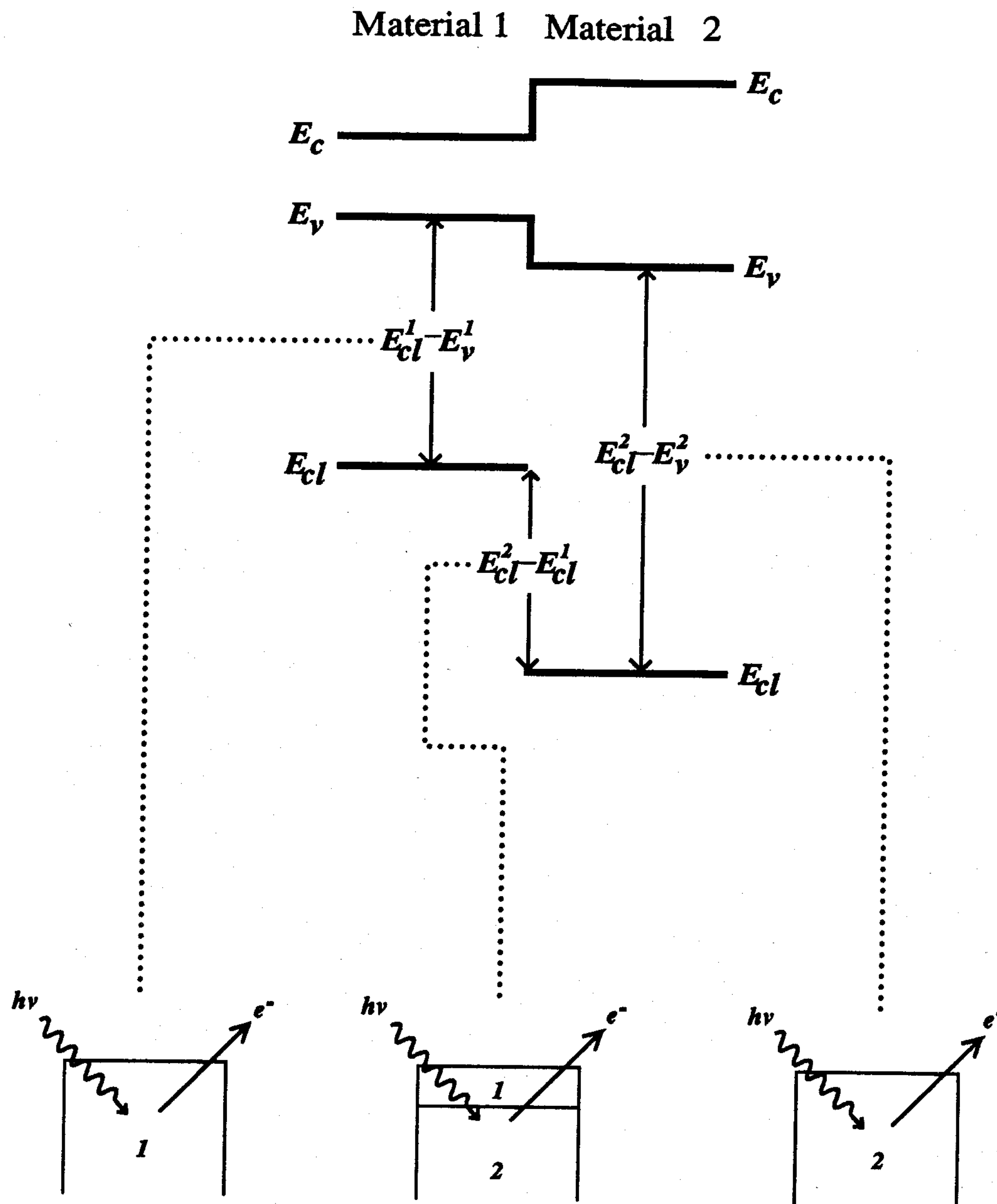

Figure 2.4: A schematic energy-band diagram illustrating the basic principle of the XPS band-offset measurement. Reference core-level binding energies are measured in thick films of each material, and the separation between the two reference core levels is measured in heterojunction samples. These three quantities can then be combined to yield a value for the valence-band offset.

care must be taken in choosing the core level that will be used as a reference. Obviously, the atomic core level to be used must be unique to a single constituent of the heterojunction, e.g., one could not use the As $3d$ core level as a reference to determine the GaAs/AlAs band offset. In addition, the core levels chosen for each heterojunction constituent should have binding energies that differ by at least a few eV, in order to avoid the difficulty of separating peaks in overlapping core-level spectra. Finally, the core levels chosen should not have binding energies that are too large, i.e., much greater than about 100 eV. One typically wishes to determine core-level binding energies to an accuracy of ± 0.02 eV or better, and unnecessarily large absolute binding energies can lead to greater uncertainty in determining the binding energy value.

The core-level energy separation is then measured in heterojunctions typically consisting of approximately 25 Å of one semiconductor grown on a thick layer of the other. A thickness of 25 Å is large enough to ensure that the electronic structure of most of the top layer is characteristic of bulk material[26, 27, 28], yet small enough to allow lossless escape of photoexcited electrons from the underlying layer. In principle, the measured core-level energy separation should be independent of the order in which the interface is grown, e.g., whether GaAs is grown on an AlAs surface, or AlAs on top of GaAs; this property is known as commutativity of the band offset. Some investigators have claimed, however, that growth sequence can affect the detailed atomic structure of the interface, and therefore the value of the band offset[29]. Thus, by checking for band offset commutativity, one might obtain some idea of the structural and electronic quality of the grown interfaces. The existence of a consistent and reproducible growth-sequence dependence in a particular heterojunction system would also have implications for the design of devices utilizing that heterojunction.

Because of the sensitivity of the XPS technique to surface properties and

chemical state, care must be taken to avoid surface and interface contamination in samples used to measure band offsets. Formation of a surface oxide, for example, could lead to a substantial distortion of the valence-band spectrum arising from the alteration of surface states; in addition, surface oxides in many semiconductors are known to yield chemically shifted components in the atomic core-level peaks[30, 31, 32]. Both of these effects could lead to greater uncertainty in the determination of core-level binding energies and core-level energy separations, and therefore in the measured band offset value. Similarly, the contamination or other chemical alteration of an interface could yield chemically shifted components in atomic core-level spectra, and thereby affect the measurement of heterojunction core-level energy separations.

To avoid complications arising from surface and interface contamination, a number of investigators have been forced to employ surface passivation layers to prevent contamination during transfer of samples through atmosphere from the growth chamber to the XPS analytical chamber, both of which are individually maintained under UHV conditions[15, 33, 34, 35, 36]. Passivation layers are generally quite effective in protecting sample surfaces from oxidation by the atmosphere; however, the heating necessary to remove passivation layers, once the sample has been transferred to the analytical chamber, can often affect the surface and interfacial properties of the sample. In particular, it is quite possible that the evaporation of surface passivation layers in samples containing reactive interfaces, such as III–V/II–VI heterojunctions, can enhance the formation of intermediate, chemically reacted layers at the interface[36]. A diagram of the UHV system in which the sample growths and XPS measurements were performed is shown in Fig. 2.5. As seen in the figure, a II-VI MBE system, a Si-Ge MBE system, a III-V MBE system, a metallization chamber, and the XPS analytical chamber are connected via UHV transfer tubes. Samples can be grown using

multiple growth chambers (e.g., III-V/II-VI heterojunctions), and these samples can be transferred directly, under UHV conditions, to the analytical chamber. All three growth chambers were utilized at various times for the work described in this thesis; the metallization chamber was not utilized in these studies.

We have avoided complications associated with surface passivation, exposure of samples to atmosphere, and subsequent evaporation of protective capping layers by transferring samples among the various growth chambers and the XPS analytical chamber entirely under UHV conditions. The various MBE growth chambers and the XPS analytical chamber are interconnected via UHV transfer tubes, allowing samples to be grown and analyzed without being exposed to atmosphere.

Some care must be also be taken to prepare samples with appropriate doping levels. If the doping level is too low, sample charging might occur and produce spurious peak shifts; in practice, we have found that lightly doped ($n \sim 10^{16}$ cm^{-3}) and even nominally undoped specimens are sufficiently conducting to avoid these effects. The doping level must also be low enough to prevent excessive band bending arising from Fermi-level pinning at the sample surface. The surface depletion length is given approximately by[37]

$$L_{depl} = \sqrt{\frac{2\epsilon V}{eN}}, \tag{2.4}$$

where ϵ is the semiconductor dielectric constant, V is the difference in potential between the surface Fermi-level pinning position and the bulk Fermi level, e is the electronic charge, and N is the doping level in the semiconductor. To ensure that XPS spectra from a sample are not distorted by band-bending effects, the doping in the sample must be such that $L_{depl} \gg \lambda_e$, where λ_e is the elastic electron escape depth, typically ~25 Å. In GaAs, for example, the doping level should not greatly exceed $\sim 10^{16}$, which corresponds to a depletion length $L_{depl} \approx 3000$ Å.

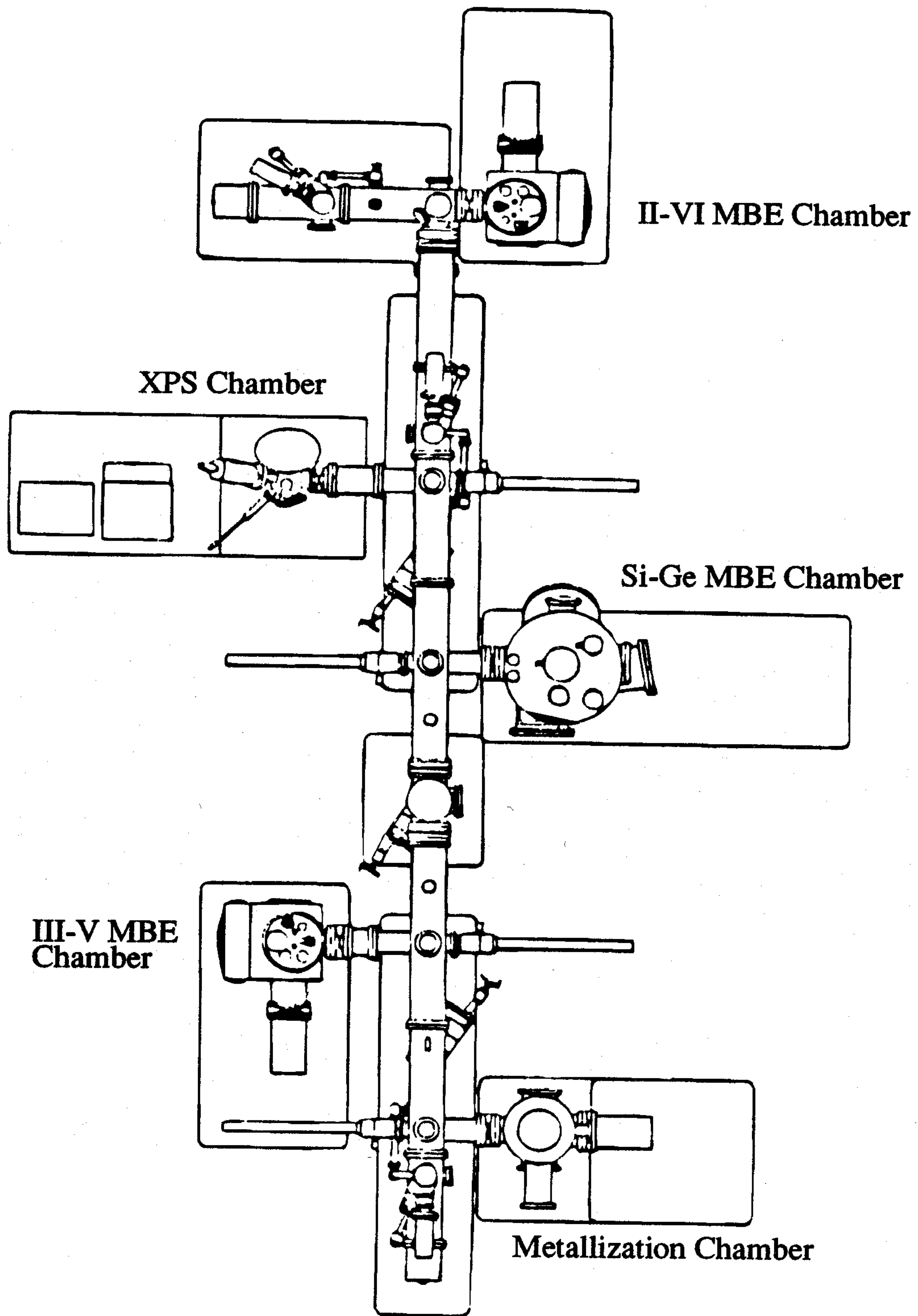
II-VI MBE Chamber
XPS Chamber
Si-Ge MBE Chamber
III-V MBE Chamber
Metallization Chamber

Figure 2.5: Diagram of the UHV system in which the sample growths and XPS measurements were performed. A II-VI MBE system, a Si-Ge MBE system, a III-V MBE system, a metallization chamber, and the XPS analytical chamber are connected via UHV transfer tubes. Samples can be grown using multiple growth chambers (e.g., III-V/II-VI heterojunctions), and these samples can be transferred directly, under UHV conditions, to the analytical chamber. This arrangement allows us to avoid complications associated with surface passivation, exposure of samples to atmosphere, and subsequent evaporation of protective capping layers. All three growth chambers were utilized at various times for the work described in this thesis; the metallization chamber was not utilized in these studies.

The XPS measurements reported in this thesis were all performed using a Perkin-Elmer Model 5100 analysis system with a spherical capacitor electron-energy analyzer and a monochromatic Al $K\alpha$ x-ray source. A monochromatic x-ray source is essential for obtaining an accurate measurement of valence-band offset values; in particular, the lineshape distortion, satellite peaks, and relatively high background level characteristic of a nonmonochromatic x-ray source make a precise determination of the valence-band edge position nearly impossible.

2.3.2 Data Analysis

To determine the valence-band offset to the desired accuracy of better than ± 0.1 eV, it is necessary to measure core-level to valence-band-edge binding energies and core-level energy separations to a very high degree of precision. Using the analysis techniques described in this section, we have routinely been able to measure core-level to valence-band-edge binding energies to an accuracy of ± 0.05 eV or better, and core-level energy separations to ± 0.02 eV.

The positions of atomic core-level peaks are determined using one of two methods. In both cases, a background function (arising from inelastic scattering in the sample) proportional to the integrated photoelectron intensity is first subtracted from each core-level spectrum. For atomic core levels with small spin-orbit splittings ($\lesssim 0.8$ eV), it is sufficient to assign the peak position to be the midpoint of the two energies at which the intensity is half the maximum intensity. For core levels with spin-orbit splittings large enough to produce two distinct peaks in the spectrum, it is necessary to fit a characteristic peak-shape function to the data. The peak-shape function we employed consisted of two identically shaped Voigt functions separated by a fixed spin-orbit splitting, whose relative heights scaled as $(2J+1)$. Voigt functions, consisting of a convolution of Gaussian and

Lorentzian lineshapes, yield peak shapes that are approximately Gaussian near the center and have Lorentzian tails, and have been found to provide accurate descriptions of experimental XPS lineshapes[12, 38].

To locate the position of the valence-band edge in an XPS spectrum, we have employed a precision analysis technique developed by Kraut, Grant, Waldrop, and Kowalczyk[11, 12]. The description of the technique given here has been adapted from the discussion by Kraut et al.[12]. The fundamental problem is that although the electronic density of states in the valence band vanishes abruptly at the valence-band edge, the instrumental broadening introduced by the finite x-ray linewidth and electron spectrometer resolution produces a tail in the valence-band spectrum extending over a few tenths of an eV, obscuring the exact position of the valence-band edge; the precision analysis technique of Kraut et al. is a systematic and accurate method for locating the position of the valence-band edge in the instrumentally broadened XPS spectrum. In this approach, the XPS spectrum near the valence-band edge is modeled as a convolution of a theoretical valence-band density of states with an experimentally determined XPS instrumental resolution function. This model function is then fitted to the experimental data to give the position of the valence-band edge. This analysis technique allows the position of the valence-band edge to be determined to an accuracy of approximately ± 0.04 eV. The usual method[39, 40, 41] of linearly extrapolating the experimental spectrum near the valence-band edge to zero intensity is considerably more arbitrary, and for XPS spectra cannot be expected to yield the position of the valence-band edge to better than ± 0.1 eV.

The instrumental resolution function for our XPS system was determined from experimentally observed Au $4f$ core-level lineshapes[12]. The Au $4f_{7/2}$ and Au $4f_{5/2}$ atomic core levels are known to have an inherent Lorentzian lineshape with a FWHM of 0.317 ± 0.010 eV[42] that is due to lifetime broadening. This inherent

lineshape $L(E)$ is convolved with the XPS instrumental resolution function $g(E)$ to yield the observed experimental lineshape,

$$W_{\mathrm{Au}4f_x}(E) = S_x \int_{-\infty}^{\infty} g(E - E')L(E')dE', \tag{2.5}$$

where S_x is simply a scale factor. To extract the instrumental resolution function $g(E)$, Voigt functions are fitted to the Au $4f$ core-level spectrum, from which a background function proportional to the integrated photoelectron intensity has been subtracted. If $g(E)$ is also assumed to be accurately described by a Voigt function, analytical expressions for the FWHM and relative Lorentzian component of $g(E)$ can be obtained in terms of the inherent Au $4f$ core-level linewidth and the FWHM and relative Lorentzian component of the experimental Au $4f$ lineshapes. A typical Au $4f$ core-level spectrum and a least-squares fit of the sum of two Voigt functions to the experimental data are shown in Fig. 2.6.

The instrumental resolution function $g(E)$ is then used to construct a model function for the XPS spectrum in the vicinity of the valence-band edge. In general, the XPS spectrum $I(E)$ consists of an instrumentally broadened electronic density of states for the sample modulated by a photoelectric cross section,

$$I(E) = \int_{0}^{\infty} \mathcal{D}(E')\sigma(E', h\nu)\mathcal{D}_c(h\nu - E')g(E - E')dE', \tag{2.6}$$

where $h\nu$ is the photon energy, $\mathcal{D}(E')$ the electronic density of states in the sample, $\mathcal{D}_c(h\nu - E')$ the continuum density of states, and $\sigma(E', h\nu)$ the photoelectric cross section. Near the valence-band edge, $\mathcal{D}_c(h\nu - E')$ is approximately constant, since the binding energies of valence-band electrons are much smaller than the photon energy $h\nu$. In addition, experiments have demonstrated that the photoelectric cross section varies slowly with energy near the valence-band edge[43]. Hence, Eq. (2.6) can be simplified near the valence-band edge to

$$I(E) = S \int_{0}^{\infty} \mathcal{D}_v(E')g(E - E')dE' + B, \tag{2.7}$$

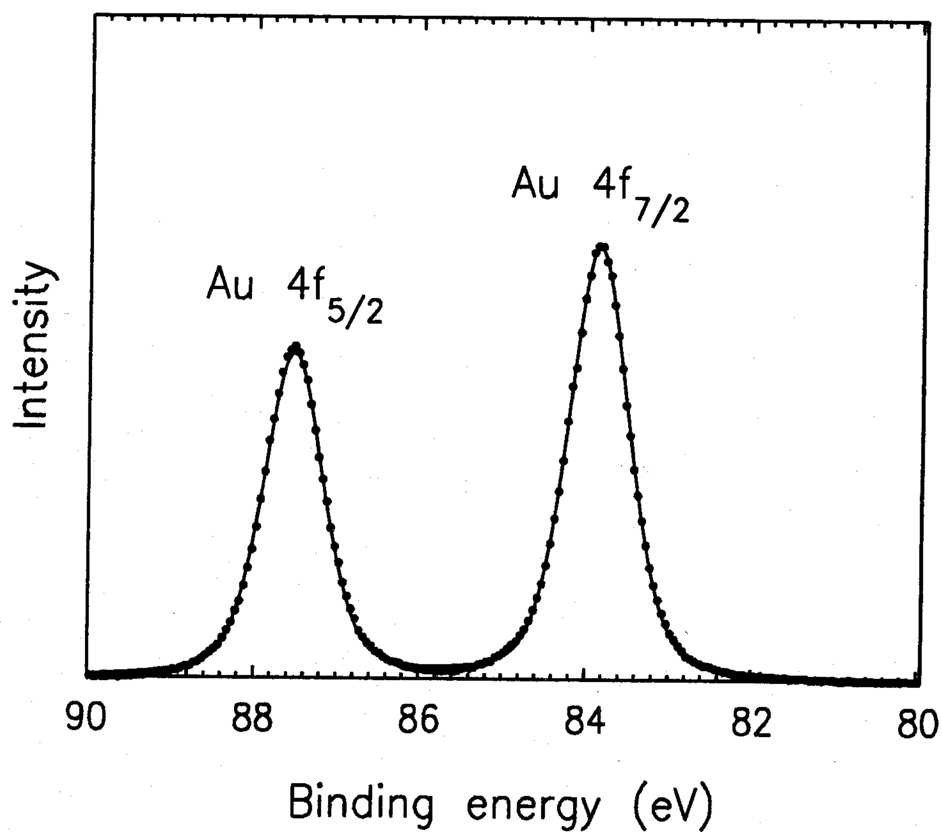

Figure 2.6: Au $4f$ core-level spectrum, following background subtraction, and least-squares fit of the sum of two Voigt functions (solid line) to the experimental data. The Au $4f$ core-level lineshapes are used to determine the XPS instrumental resolution function.

where a constant background B has been added, and the photoelectric cross section and continuum density of states have been pulled out of the integral as constants and incorporated in an overall scale factor S; $\mathcal{D}_v(E')$ is the electronic density of states in the valence band.

In the work of Kraut et al.[12], the valence-band density of states was obtained from published curves calculated by Chelikowsky and Cohen using a nonlocal empirical pseudopotential method[44]. However, the relatively low energy resolution and the apparently approximate nature of the published plots of densities of states introduce considerable ambiguity in the calculated XPS valence-band spectra. In addition, published plots of valence-band densities of states are not available for certain materials, most notably AlAs. For most of the experiments described in this thesis, we have performed calculations of valence-band densities of states using an empirical pseudopotential method[45] in which nonlocal effects have been approximated through the introduction of a nonlocal electron effective mass m^*[46]. Because of the sensitivity of the model function given by Eq. (2.7) to the structure of the valence-band density of states near the valence-band edge, we have included the spin-orbit splitting of the valence bands[47, 48]. We have also extended this method to treat XPS spectra from coherently strained materials by including effects arising from strain explicitly in the calculation of the valence-band densities of states[49], allowing us to study the strain dependence of band offsets in lattice-mismatched heterojunction systems[16, 18]. The calculation of valence-band densities of states by this method is described in detail in Chapter 4.

Figs. 2.7(a) and 2.7(b) show typical XPS valence-band spectra and model functions fitted to the experimental data for Si (100) and Ge (100), respectively. The theoretical valence-band densities of states, calculated by the methods described above, that have been used to construct the model functions are shown

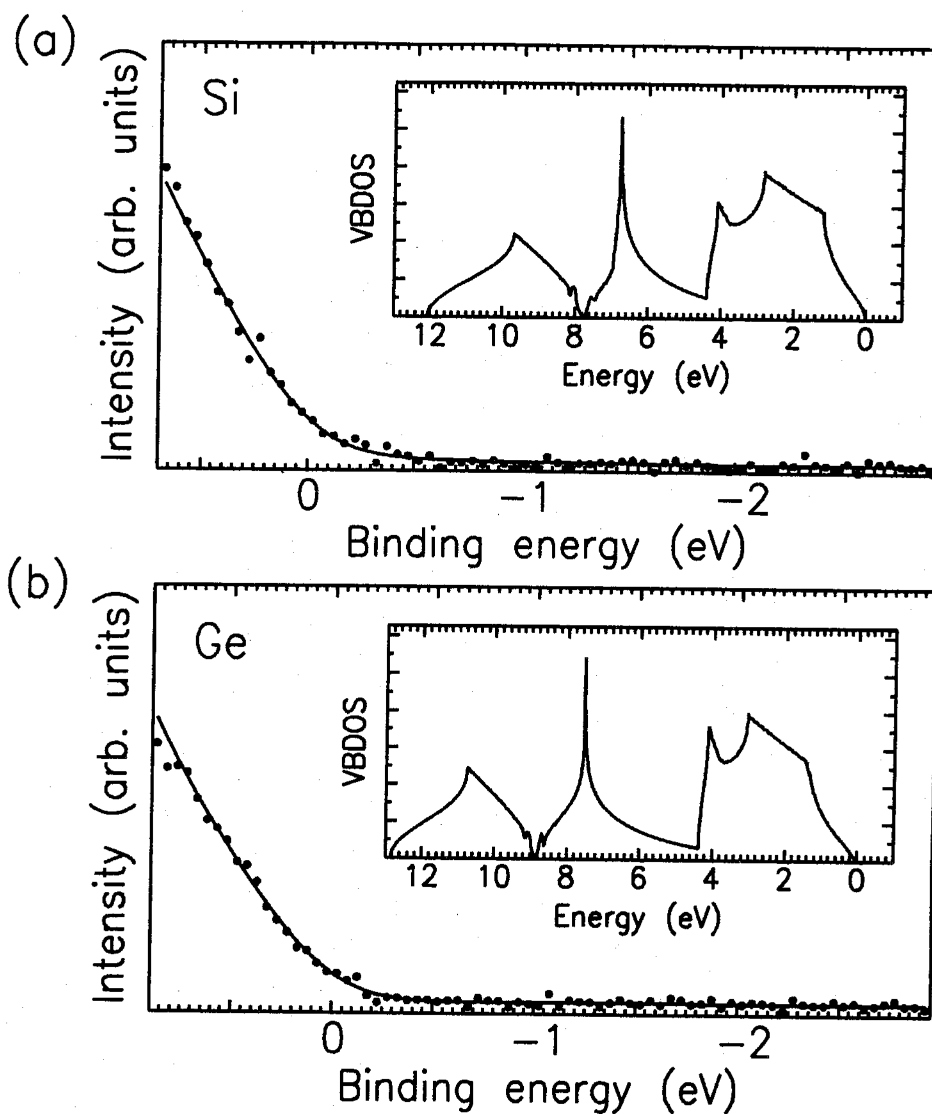

Figure 2.7: Typical XPS valence-band spectra and model functions fitted to the experimental data for (a) Si (100) and (b) Ge (100). The theoretical valence-band densities of states used to construct the model functions are shown in the insets to each figure.

in the insets to each figure. The uncertainty in the position of the valence-band edge as determined by this technique is approximately ± 0.04 eV.

Using the techniques described above, we have been able routinely to measure core-level to valence-band-edge binding energies to accuracies of ± 0.05 eV or better and core-level energy separations to ± 0.02 eV. This level of accuracy allows us to measure valence-band offsets with an uncertainty of approximately ± 0.07 eV. These measurements are therefore sufficiently accurate to allow us to assess the viability of various device concepts in the material systems we have studied, and to obtain quantitative descriptions of the expected behavior of novel heterojunction devices.

2.4 Summary of Chapter

We have presented a discussion of the basic principles of x-ray photoelectron spectroscopy, and described a technique by which XPS may be used to measure valence-band offsets in semiconductor heterojunctions. The advantages of the XPS technique compared to other methods of measuring band offsets are that (a) the epitaxial growths required are quite simple — only bulk material and simple heterojunctions are needed; (b) it is not necessary to fabricate functional electrical devices to perform the measurements needed to determine the band offset; (c) the valence-band offset is determined directly from experimentally measured quantities, rather than indirectly via sophisticated device modeling or band-structure calculations; and (d) the ability in XPS to distinguish among different chemical states allows information about heterojunction chemistry and interfacial reactions to be obtained. These advantages make XPS a powerful method for measuring band offsets in novel heterojunction systems.

The key component in measuring band offsets by XPS is the ability to meas-

ure very precisely core-level to valence-band-edge binding energies in thick semiconductor films and core-level energy separations in heterojunctions. By fitting core-level spectra using characteristic XPS lineshapes, we are able to determine core-level binding energies to an accuracy of ± 0.02 eV; a precision analysis technique developed by Kraut et al.[11, 12] allows us to determine valence-band-edge positions to approximately ± 0.04 eV. Combining the uncertainties in these measurements, we are able to determine valence-band offsets with an uncertainty of ± 0.07–0.08 eV. In addition, we have extended the capabilities of the XPS technique to measure strain-dependent band offsets in lattice-mismatched heterojunctions[16, 18], and have used the sensitivity of XPS to chemical bonding states to obtain information about interfacial reactions in certain heterojunction systems[16, 17]. Details of this work are described in subsequent chapters.

References

[1] R. Dingle, W. Wiegmann, and C. H. Henry, *Phys. Rev. Lett.* **33**, 827 (1974).

[2] R. C. Miller, A. C. Gossard, D. A. Kleinman, and O. Munteanu, *Phys. Rev. B* **29**, 3740 (1984).

[3] D. J. Wolford, T. F. Kuech, J. A. Bradley, M. A. Gell, D. Ninno, and M. Jaros, *J. Vac. Sci. Technol. B* **4**, 1043 (1986).

[4] J. Menéndez, A. Pinczuk, D. J. Werder, A. C. Gossard, and J. H. English, *Phys. Rev. B* **33**, 8863 (1986).

[5] Y. Rajakarunanayake, R. H. Miles, G. Y. Wu, and T. C. McGill, *Phys. Rev. B* **37**, 10212 (1988).

[6] H. Kroemer, W. Y. Chien, J. S. Harris, Jr., and D. D. Edwall, *Appl. Phys. Lett.* **36**, 295 (1980).

[7] J. Batey and S. L. Wright, *J. Appl. Phys.* **59**, 200 (1985).

[8] W. I. Wang and F. Stern, *J. Vac. Sci. Technol. B* **3**, 1280 (1985).

[9] H. Kroemer, *Surf. Sci.* **132**, 543 (1983).

[10] G. Duggan, *J. Vac. Sci. Technol. B* **3**, 1224 (1985).

[11] E. A. Kraut, R. W. Grant, J. R. Waldrop, and S. P. Kowalczyk, *Phys. Rev. Lett.* **44**, 1620 (1980).

[12] E. A. Kraut, R. W. Grant, J. R. Waldrop, and S. P. Kowalczyk, *Phys. Rev. B* **28**, 1965 (1983).

[13] E. T. Yu, D. H. Chow, and T. C. McGill, *Phys. Rev. B* **38**, 12764 (1988).

[14] R. W. Grant, E. A. Kraut, S. P. Kowalczyk, and J. R. Waldrop, *J. Vac. Sci. Technol. B* **1**, 320 (1983).

[15] G. J. Gualtieri, G. P. Schwartz, R. G. Nuzzo, and W. A. Sunder, *Appl. Phys. Lett.* **49**, 1037 (1986).

[16] E. T. Yu, E. T. Croke, D. H. Chow, D. A. Collins, M. C. Phillips, T. C. McGill, and J. O. McCaldin, *J. Vac. Sci. Technol. B* **8**, 908 (1990).

[17] E. T. Yu, M. C. Phillips, D. H. Chow, D. A. Collins, and T. C. McGill, *Bull. Am. Phys. Soc.* **35**, 416 (1990).

[18] E. T. Yu, E. T. Croke, R. H. Miles, and T. C. McGill, *Appl. Phys. Lett.* **56**, 569 (1990).

[19] K. Siegbahn, C. N. Nordling, A. Fahlman, R. Nordberg, K. Hamrin, J. Hedman, G. Johansson, T. Bergmark, S.-E. Karlsson, I. Lindgren, and B. Lindberg, *ESCA: Atomic, Molecular, and Solid–State Structure Studied by Means of Electron Spectroscopy* (Almqvist and Wiksells, Stockholm, 1967).

[20] C. S. Fadley, in *Electron Spectroscopy: Theory, Techniques and Applications*, Vol. 2, C. R. Brundle and A. D. Baker, ed. (Academic Press, New York, 1978), p. 1.

[21] D. A. Shirley, *Adv. Chem. Phys.* **23**, 85 (1973).

[22] C. S. Fadley, S. B. M. Hagstrom, M. P. Klein, and D. A. Shirley, *J. Chem. Phys.* **48**, 3779 (1968).

[23] H. Gant and W. Mönch, *Surf. Sci.* **105**, 217 (1981).

[24] A. Zangwill, *Physics at Surfaces* (Cambridge University Press, Cambridge, 1988), p. 21.

[25] D. R. Penn, *Phys. Rev. B* **13**, 5248 (1976).

[26] G. A. Baraff, J. A. Applebaum, and D. R. Hamann, *Phys. Rev. Lett.* **38**, 237 (1977).

[27] C. G. Van de Walle and R. M. Martin, *Phys. Rev. B* **34**, 5621 (1986).

[28] C. G. Van de Walle and R. M. Martin, *Phys. Rev. B* **35**, 8154 (1987).

[29] J. R. Waldrop, R. W. Grant, and E. A. Kraut, *J. Vac. Sci. Technol. B* **5**, 1209 (1987).

[30] J.–P. Häring, J. G. Werthen, R. H. Bube, L. Gulbrandsen, W. Jansen, and P. Luscher, *J. Vac. Sci. Technol. A* **1**, 1469 (1983).

[31] C. Y. Wong and S. P. Klepner, *Appl. Phys. Lett.* **48**, 1229 (1986).

[32] S. Ingrey, W. M. Lau, and N. S. McIntyre, *J. Vac. Sci. Technol. A* **4**, 984 (1986).

[33] S. P. Kowalczyk, J. T. Cheung, E. A. Kraut, and R. W. Grant, *Phys. Rev. Lett.* **56**, 1605 (1986).

[34] G. J. Gualtieri, G. P. Schwartz, R. G. Nuzzo, R. J. Malik, and J. F. Walker, *J. Appl. Phys.* **61**, 5337 (1987).

[35] G. P. Schwartz, M. S. Hybertsen, J. Bevk, R. G. Nuzzo, J. P. Mannaerts, and G. J. Gualtieri, *Phys. Rev. B* **39**, 1235 (1989).

[36] G. P. Schwartz, G. J. Gualtieri, R. D. Feldman, R. F. Austin, and R. G. Nuzzo, *J. Vac. Sci. Technol. B* **8**, 747 (1990).

[37] S. M. Sze, *Physics of Semiconductor Devices*, Second Edition (John Wiley & Sons, New York, 1981), p. 77.

[38] G. K. Wertheim, M. A. Butler, K. W. West, and D. N. E. Buchanan, *Rev. Sci. Instrum.* **45**, 1369 (1974).

[39] D. E. Eastman, W. D. Grobman, J. L. Freeouf, and M. Erbudak, *Phys. Rev. B* **9**, 3473 (1974).

[40] R. Ludeke, L. Ley, and K. Ploog, *Solid State Commun.* **28**, 57 (1978).

[41] T. M. Duc, C. Hsu, and J. P. Faurie, *Phys. Rev. Lett.* **58**, 1127 (1987).

[42] P. H. Citrin, G. K. Wertheim, and Y. Baer, *Phys. Rev. Lett.* **41**, 1425 (1978).

[43] R. G. Cavell, S. P. Kowalczyk, L. Ley, R. A. Pollak, B. Mills, D. A. Shirley, and W. Perry, *Phys. Rev. B* **7**, 5313 (1973).

[44] J. R. Chelikowsky and M. L. Cohen, *Phys. Rev. B* **14**, 556 (1976).

[45] M. L. Cohen and T. K. Bergstresser, *Phys. Rev.* **141**, 789 (1966).

[46] J. R. Chelikowsky, D. J. Chadi, and M. L. Cohen, *Phys. Rev. B* **8**, 2786 (1973).

[47] S. Bloom and T. K. Bergstresser, *Solid State Commun.* **6**, 465 (1968).

[48] L. R. Saravia and D. Brust, *Phys. Rev.* **176**, 915 (1968).

[49] L. R. Saravia and D. Brust, *Phys. Rev.* **178**, 1240 (1969).

Chapter 3

Commutativity of the GaAs/AlAs (100) Valence-Band Offset

3.1 Introduction

3.1.1 Background and Motivation

Any discussion of heterojunction band offset measurements begins most naturally with the GaAs/AlAs (100) interface. The GaAs/$Al_xGa_{1-x}As$ heterojunction system is the most important technologically, and has therefore been the subject of by far the most extensive experimental investigation. Despite these efforts, there existed until quite recently considerable controversy regarding the actual value of the GaAs/$Al_xGa_{1-x}As$ valence-band offset, and its possible dependence on substrate orientation and growth sequence remains a subject of debate.

For several years the value of the GaAs/$Al_xGa_{1-x}As$ valence-band offset was thought to have been well established. A 1974 experiment in which Din-

gle et al.[1, 2] measured optical-absorption spectra from $Al_xGa_{1-x}As/GaAs/$-$Al_xGa_{1-x}As$ quantum-well heterostructures with $x = 0.2 \pm 0.01$ yielded a conduction-band offset $\Delta E_c = 0.88\Delta E_g$, corresponding to a valence-band offset $\Delta E_v = 0.12\Delta E_g$, where ΔE_g is the difference in band gap between GaAs and $Al_xGa_{1-x}As$. Several other experiments seemed to confirm this measurement. Gossard et al.[3] obtained a conduction-band offset $\Delta E_c \approx 0.85\Delta E_g$ from current–voltage (J–V) measurements performed on $GaAs/Al_xGa_{1-x}As/GaAs$ single-barrier heterostructures with square, triangular, and sawtooth-shaped barriers. People et al.[4] measured a conduction-band offset $\Delta E_c = (0.88 \pm 0.04)\Delta E_g$ by capacitance–voltage (C–V) profiling, and Welch et al.[5] obtained GaAs/-$Al_xGa_{1-x}As$ quantum-well photoluminescence spectra consistent with $\Delta E_c = 0.85\Delta E_g$. Confidence in the so-called "85:15" rule was such that in experiments in which substantially smaller conduction band offsets were observed[6, 7], the authors attributed the discrepancy to compositional grading at the GaAs/-$Al_xGa_{1-x}As$ heterojunction during crystal growth, rather than considering the possibility that their band offset value might be more correct than that given by the 85:15 rule.

More recent experiments, however, have provided strong evidence that the 85:15 rule is indeed incorrect, and that the $GaAs/Al_xGa_{1-x}As$ valence-band offset is substantially larger than had been thought at first. A number of these experiments have also provided detailed data relating the band offset to alloy composition x and energy-gap difference ΔE_g over the entire range of alloy compositions $x \in [0, 1]$. The early experiments supporting the 85:15 rule were conducted for only a limited range of alloy compositions, typically $x \lesssim 0.45$.

The first indication that the 85:15 rule might be incorrect was provided by photoluminescence measurements on parabolic quantum wells reported by Miller, Gossard, Kleinman, and Munteanu[8]. Earlier measurements of band offsets using

quantum-well photoluminescence or optical-absorption techniques utilized data obtained from square quantum wells; in square quantum-well structures, the energies of the bound states depend much more sensitively on parameters such as the quantum-well width and carrier effective mass than on the band offset. For parabolic wells, the bound-state energies depend more strongly on the band offset values; however, controlling the sample growths to ensure that the wells are indeed parabolic is quite difficult. The data obtained by Miller et al. indicated that the conduction-band offset was smaller than had been previously thought, $\Delta E_c \approx 0.50 \Delta E_g$. A subsequent analysis of exciton transitions in both square and parabolic quantum wells by Miller, Kleinman, and Gossard[9] yielded a conduction-band offset $\Delta E_c \approx 0.57 \Delta E_g$.

The results of Miller et al. led to renewed interest in the determination of the GaAs/$Al_xGa_{1-x}As$ band offset, and a large number of subsequent measurements[10, 11, 12, 13, 14, 15, 16, 17, 18, 19, 20, 21] yielded GaAs/-$Al_xGa_{1-x}As$ band offset values consistent with the results of Miller et al. rather than those of Dingle et al. Wang et al.[10, 15, 16], using a charge-transfer technique, reported valence-band offset values of 0.21 ± 0.03 eV, 0.126 ± 0.04 eV, and 0.45 ± 0.05 eV for the GaAs/$Al_{0.5}Ga_{0.5}As$, GaAs/$Al_{0.26}Ga_{0.74}As$, and GaAs/AlAs heterojunctions, respectively, corresponding to $\Delta E_v \approx 0.28$–$0.39 \Delta E_g$. Arnold et al.[11] used current-voltage measurements as a function of temperature to deduce a valence-band offset $\Delta E_v = 0.35 \Delta E_g$ over a range of alloy composition $x \in [0.3, 1.0]$. Okumura et al.[12] obtained a conduction-band offset $\Delta E_c = 0.67 \Delta E_g$ for $x < 0.42$ from capacitance-voltage measurements. Hickmott et al.[13] combined C–V and J–V measurements to obtain a conduction-band offset $\Delta E_c = 0.63 \Delta E_g$ for $x = 0.4$. Watanabe et al.[14] used C–V measurements to determine the conduction- and valence-band offsets independently, and obtained values $\Delta E_c = 0.62 \Delta E_g$ for $x \in [0.15, 0.30]$ and $\Delta E_v = 0.38 \Delta E_g$ for

$x = 0.30$. Batey and Wright[17, 18] used J–V techniques to measure the GaAs/-$Al_xGa_{1-x}As$ valence-band offset as a function of alloy composition x, and obtained $\Delta E_v = 0.55x$ for $x \in [0, 1]$. Wolford et al.[19] studied quantum-well photoluminescence in GaAs/$Al_xGa_{1-x}As$ heterostructures as a function of pressure; from an analysis of the critical pressure for crossing in energy of the Γ–like bound states in GaAs and the X–like states in $Al_xGa_{1-x}As$ as a function of alloy composition, a valence-band offset $\Delta E_v = 0.32 \pm 0.02 \Delta E_g^\Gamma$ was deduced for $x \approx 0.28$ and 0.70. Photoluminescence measurements yielded evidence of a staggered band alignment, corresponding to $\Delta E_v = 342 \pm 4$ meV, in GaAs/$Al_xGa_{1-x}As$ heterostructures with $x = 0.37$[20], and data for other compositions[21] were consistent with $\Delta E_v = 0.55x$. In all cases, measurements indicated that the energy-gap difference was divided more equally between the conduction- and valence-band offsets than had been indicated by the 85:15 rule. Most of these experiments were conducted for GaAs/$Al_xGa_{1-x}As$ heterojunctions in which the band gap of $Al_xGa_{1-x}As$ was still direct, i.e., $x \lesssim 0.4$–0.45, and yielded conduction- and valence-band offsets of $\Delta E_c \approx (0.55$–$0.65)\Delta E_g$ and $\Delta E_v \approx (0.35$–$0.45)\Delta E_g$. For heterojunctions involving $Al_xGa_{1-x}As$ layers with direct band gaps, the conduction- and valence-band offsets could be measured independently; the requirement that $\Delta E_c + \Delta E_v = \Delta E_g$ then provided convincing confirmation that the band offset measurements were indeed valid.

The variation of the GaAs/$Al_xGa_{1-x}As$ valence-band offset with alloy composition x was also a subject of considerable debate. The initial approach was to assume that the conduction-band offset was proportional to the energy-gap difference at the heterojunction, even though the measurements of Dingle et al. were carried out at only a single alloy composition. Arnold et al.[11] measured current-voltage characteristics for p^+-GaAs/$Al_xGa_{1-x}As/p^-$-GaAs capacitor structures, and deduced a valence-band offset $\Delta E_v = 0.35\Delta E_g^\Gamma$ for $x \in [0.3, 1.0]$. Because

the direct band-gap difference ΔE_g^Γ is not linear in x, this result was taken to imply a nonlinear dependence of ΔE_v on x. In contrast, measurements by Batey and Wright[17, 18] of current-voltage characteristics as a function of temperature yielded a GaAs/$Al_xGa_{1-x}As$ valence-band offset linear in alloy composition, $\Delta E_v \approx 0.55x$. Uncertainties and inconsistencies in the actual band offset values obtained by various investigators, however, render the exact form of this dependence a secondary issue.

In conjunction with these experimental determinations of the GaAs/-$Al_xGa_{1-x}As$ valence-band offset, considerable effort has been devoted to theoretical calculations of band offset values for this and other heterojunction systems. The early theories generally predicted very small valence-band offsets, the physical justification being that, near the valence-band edge, the valence-band wave functions were derived primarily from p–like atomic orbitals of the anion. Since the anion in GaAs and AlAs is the same, it was thought that the valence-band edges should be at approximately the same position on an absolute energy scale. In all cases, the AlAs valence-band edge was correctly predicted to be lower in energy than the GaAs valence-band edge. The electron affinity rule[22, 23] yielded a valence-band offset of 0.15 eV, while the theory of Harrison[24], based on linear combination of atomic orbitals (LCAO), predicted a valence-band offset of 0.04 eV. Frensley and Kroemer[25, 26], using a pseudopotential band structure calculation, obtained a valence-band offset of 0 eV without interfacial dipole corrections, and an offset of 0.69 eV with dipole corrections included. With the exception of the dipole-corrected value of Frensley and Kroemer, these predictions were all in general agreement with the value measured by Dingle et al. The common anion rule of McCaldin, McGill, and Mead[27] is often erroneously cited as predicting a very small GaAs/AlAs valence-band offset; because compounds containing Al were not included in the data upon which the rule was based, the

common anion rule should not necessarily apply to GaAs/AlAs heterojunctions.

Following the experimental realization that Dingle's result was substantially in error, a number of new theories predicting generally larger valence-band offsets were developed. Theories based on interface dipoles were developed by Tersoff[28, 29] and by Harrison and Tersoff[30], and predicted valence-band offsets of 0.55 eV and 0.12 eV, respectively. A number of calculations taking into account the electronic structure at specific interfaces were also developed. A self-consistent interface calculation (SCIC) based on *ab initio* pseudopotentials was developed by Van de Walle and Martin[31], and predicted a valence-band offset of 0.37 eV; the "model solid" theory[32] derived from the SCIC calculations yielded a value of 0.60 eV. Linear muffin-tin orbital (LMTO) calculations developed by Christensen[33] and by Lambrecht et al.[34] both predicted valence-band offsets of 0.53 eV. The dielectric midgap energy model of Cardona and Christensen[35] predicts a GaAs/AlAs valence band offset of 0.43 eV.

Additional complications can arise from variations in substrate orientation and interface quality. Using the x-ray photoelectron spectroscopy (XPS) measurement described in Chapter 2, Waldrop et al.[36, 37] observed a dependence of the valence-band offset on both substrate orientation and growth sequence. For samples grown on (100) substrates, valence-band offsets of 0.46 eV and 0.36 eV were measured for AlAs grown on top of GaAs (AlAs-GaAs) and GaAs grown on top of AlAs (GaAs-AlAs), respectively. For samples grown on (110) substrates, valence-band offsets of 0.55 eV and 0.42 eV were reported for the AlAs-GaAs and GaAs-AlAs growth sequences, respectively. These data were contradicted, however, by XPS measurements made by Katnani and Bauer[38] on heterojunctions involving GaAs, AlAs, and Ge. Katnani and Bauer did not observe any dependence of the GaAs/AlAs valence-band offset on growth sequence, obtaining a valence-band offset of 0.39 ± 0.07 eV for both GaAs-AlAs and AlAs-GaAs

heterojunctions.

A dependence of the valence band offset on substrate orientation would appear to be quite plausible, given the variations in atomic structure and chemical bonding for different interface orientations. However, theoretical calculations in which the detailed structure of specific, albeit ideal, interfaces is taken into account generally predict a very small dependence of the band offset value on substrate orientation[39, 40]. In addition, band offset measurements for GaAs/-$Al_{0.26}Ga_{0.74}As$ (100) and (311) heterojunctions failed to show any dependence of band offset values on substrate orientation[16].

For ideal, abrupt interfaces, one would expect that band offset values should not exhibit any dependence on growth sequence; that band offsets should be independent of growth sequence is referred to as the commutativity property. The dependence of the valence-band offset on growth sequence observed by Waldrop et al. was thought to result from detailed, microscopic differences in epitaxial growth on various semiconductor surfaces. It is known, for example, that interrupting MBE growth at an AlAs surface affects photoluminescence spectra from GaAs/-AlAs quantum-well structures very differently than does growth interruption at a GaAs surface[41, 42]. A dependence on growth sequence of band offset values in a given material system large enough to affect device properties, as were the effects observed by Waldrop et al., could have significant implications for the analysis and design of heterojunction devices in that material system. Such a dependence could also provide insight into the properties of an interface that are most relevant in determining band offset values.

3.1.2 Summary of Results

In this chapter we present measurements of the valence-band offset for GaAs-AlAs and AlAs-GaAs heterojunctions[43, 44]. The Ga $3d$ core-level to valence-band-edge binding energy was measured in bulk GaAs (100) samples, the result being $E_{\mathrm{Ga3}d}^{\mathrm{GaAs}} - E_v^{\mathrm{GaAs}} = 18.73 \pm 0.05$ eV. Measurements of the Al $2p$ core-level to valence-band-edge binding energy in bulk AlAs (100) samples yielded $E_{\mathrm{Al2}p}^{\mathrm{AlAs}} - E_v^{\mathrm{AlAs}} = 72.71 \pm 0.04$ eV. The Al $2p$ to Ga $3d$ core-level energy separation was measured in AlAs-GaAs (100) and GaAs-AlAs (100) heterojunction samples. For the GaAs-AlAs interface, we found $E_{\mathrm{Al2}p}^{\mathrm{AlAs}} - E_{\mathrm{Ga3}d}^{\mathrm{GaAs}} = 54.45 \pm 0.02$ eV, corresponding to a valence-band offset of 0.47 ± 0.07 eV; for the AlAs-GaAs (100) interface, we found $E_{\mathrm{Al2}p}^{\mathrm{AlAs}} - E_{\mathrm{Ga3}d}^{\mathrm{GaAs}} = 54.43 \pm 0.02$ eV, corresponding to a valence-band offset of 0.45 ± 0.07 eV. Within experimental error, we obtain a valence-band offset $\Delta E_v = 0.46 \pm 0.07$ eV for the GaAs/AlAs (100) interface, independent of growth sequence. All samples studied were transferred directly from the molecular-beam epitaxy (MBE) growth chamber to the XPS analytical chamber under ultrahigh vacuum (UHV) conditions, eliminating uncertainties associated with deposition and subsequent evaporation of surface passivation layers that are required for samples transported through atmosphere.

Our results establish the commutativity of the GaAs/AlAs (100) valence-band offset, and are consistent with other recent GaAs/$\mathrm{Al}_x\mathrm{Ga}_{1-x}$As band offset measurements refuting the 85:15 rule. We attribute the confirmation of commutativity in our experiments to the high quality of our epitaxial growths. The results of Waldrop et al.[36, 37] suggest that the specific epitaxial growth conditions employed can influence interface quality to an extent sufficient to affect band offset values. Our measurements and those of Katnani and Bauer[38], however, demonstrate that it is possible to grow GaAs/AlAs (100) heterostructures consistently

and reproducibly, which do not suffer from these effects.

3.1.3 Outline of Chapter

The experimental procedure used to measure the GaAs/AlAs (100) valence-band offset is presented in Section 3.2. Sample growth is described in Section 3.2.1, and the XPS measurements and data analysis are discussed in Section 3.2.2. Because of the need to determine bulk core-level to valence-band-edge binding energies and heterojunction core-level energy separations to a high degree of precision, considerable attention is paid to the detailed analysis of the XPS spectra and the determination of core-level and valence-band-edge binding energies. The results of our measurements are presented in Section 3.3; our demonstration of commutativity of the GaAs/AlAs (100) valence-band offset, and the band offset value that we obtain, are discussed in the context of previous results. Our conclusions are summarized in Section 3.4.

3.2 Experiment

3.2.1 Sample Growth

Samples for these experiments were grown by molecular-beam epitaxy in a PHI 430 growth chamber on Si–doped n^+-GaAs (100) substrates. The substrate preparation consisted of a degrease followed by a 90 second etch in 5:1:1 H_2SO_4:H_2O_2:H_2O. The native oxide was desorbed in the growth chamber by heating the substrate to $\sim 610\,^{\circ}C$ in an As flux. All of the samples were grown at $600\,^{\circ}C$ and were lightly doped n-type with Si to avoid both sample charging effects and excessive band bending arising from Fermi-level pinning at the surface of the specimen.

The Ga $3d$ core-level to valence-band-edge binding energy ($E_{\mathrm{Ga3}d}^{\mathrm{GaAs}} - E_v^{\mathrm{GaAs}}$) was measured in three epitaxial GaAs layers >1 μm in thickness. Electron mobilities in these and similarly grown films were comparable to those typically reported for high-quality MBE growth[45], and the samples exhibited good photoluminescence at low temperatures. Two bulk AlAs samples were grown for this study; each consisted of a 2500 Å epitaxial layer of AlAs, with one grown on top of a 1.5 μm GaAs buffer layer and the other on top of a 1500 Å $Al_{0.3}Ga_{0.7}As$ buffer layer. These samples were used to measure the Al $2p$ core-level to valence-band-edge binding energy ($E_{\mathrm{Al2}p}^{\mathrm{AlAs}} - E_v^{\mathrm{AlAs}}$).

Two types of heterojunction samples were grown, allowing the commutativity of the band offset to be checked. One type consisted of 25 Å of GaAs grown on top of AlAs layers ranging in thickness from 100 Å to 500 Å, while the other consisted of 25 Å of AlAs grown on top of 1000 Å of GaAs; growth interruption was not used in fabricating the heterojunction samples. In both cases, the interfaces were believed to be fairly abrupt, given the results from quantum-well photoluminescence measurements and double-barrier resonant tunneling experiments conducted on samples with similarly grown interfaces. Schematic diagrams of the various types of samples grown, and the measurements performed on them, are shown in Fig. 3.1.

3.2.2 X-ray Photoelectron Spectroscopy Measurements

XPS measurements were obtained using a Perkin–Elmer Model 5100 analysis system; samples were excited using a monochromatic Al $K\alpha$ x-ray source ($h\nu =$ 1486.6 eV), and electron energies were measured by a spherical capacitor analyzer. The base pressure in the XPS analysis chamber was typically $\sim 5 \times 10^{-10}$ Torr, and the analysis chamber was connected to the MBE growth chamber via UHV

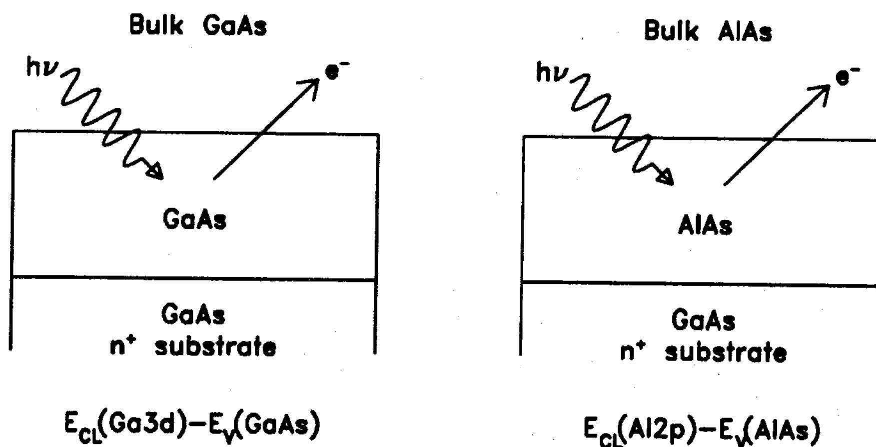

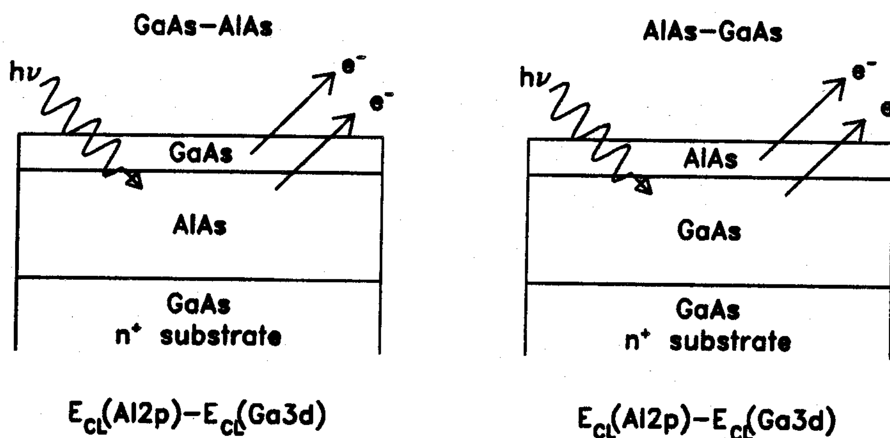

Figure 3.1: Schematic diagrams of samples grown for this study, and the quantities measured in these samples. Bulk GaAs (100) and AlAs (100) samples, shown in (a), are used to obtain the Ga 3*d* and Al 2*p* core-level to valence-band-edge binding energies, respectively. Heterojunction samples, shown in (b), are used to measure the Al 2*p* to Ga 3*d* core-level energy separation.

transfer tubes, allowing samples to be grown and characterized without exposure to atmospheric pressure. This arrangement eliminated experimental uncertainties associated with surface passivation, sputter cleaning, and annealing of samples that had been transferred through atmosphere; a number of other investigators had been forced to employ such techniques to avoid surface contamination during transfer of samples through atmospheric pressure[46, 47, 48, 49, 50].

Measurements were obtained from three pure GaAs (100) samples and two pure AlAs (100) samples, and from three GaAs-AlAs (100) and two AlAs-GaAs (100) heterojunctions. Fig. 3.2 shows a schematic energy-band diagram for the GaAs/AlAs interface. The core levels of interest in the band offset measurement are the Al $2p$ level and the Ga $3d$ level in AlAs and GaAs, respectively. From Fig. 3.2, it can be seen that the valence-band offset is given by

$$\Delta E_v = (E_{\mathrm{Al}2p}^{\mathrm{AlAs}} - E_{\mathrm{Ga}3d}^{\mathrm{GaAs}}) + (E_{\mathrm{Ga}3d}^{\mathrm{GaAs}} - E_v^{\mathrm{GaAs}}) - (E_{\mathrm{Al}2p}^{\mathrm{AlAs}} - E_v^{\mathrm{AlAs}}). \tag{3.1}$$

The core-level to valence-band-edge binding energy differences $(E_{\mathrm{Ga}3d}^{\mathrm{GaAs}} - E_v^{\mathrm{GaAs}})$ and $(E_{\mathrm{Al}2p}^{\mathrm{AlAs}} - E_v^{\mathrm{AlAs}})$ are obtained from measurements on pure GaAs and AlAs samples, respectively, and the Al $2p$ to Ga $3d$ core-level energy separation $(E_{\mathrm{Al}2p}^{\mathrm{AlAs}} - E_{\mathrm{Ga}3d}^{\mathrm{GaAs}})$ is measured in the GaAs-AlAs and AlAs-GaAs heterojunction samples.

For each sample, a binding energy window that included all energy levels of interest was scanned repeatedly for ~15–20 hours. Because of the low count rate for electrons near the valence-band edge, energies in that region were sampled for a longer time than energies in other parts of the spectrum. Spectra from pure GaAs and pure AlAs and from GaAs-AlAs and AlAs-GaAs heterojunctions are shown in Figs. 3.3 and 3.4, respectively. In Fig. 3.3, the discontinuities in the spectra at a binding energy of 10 eV are due to the longer sampling time used near the valence-band edge, which occurs at approximately 0 eV binding energy; the valence-band spectra for GaAs and AlAs are also shown on enlarged scales,

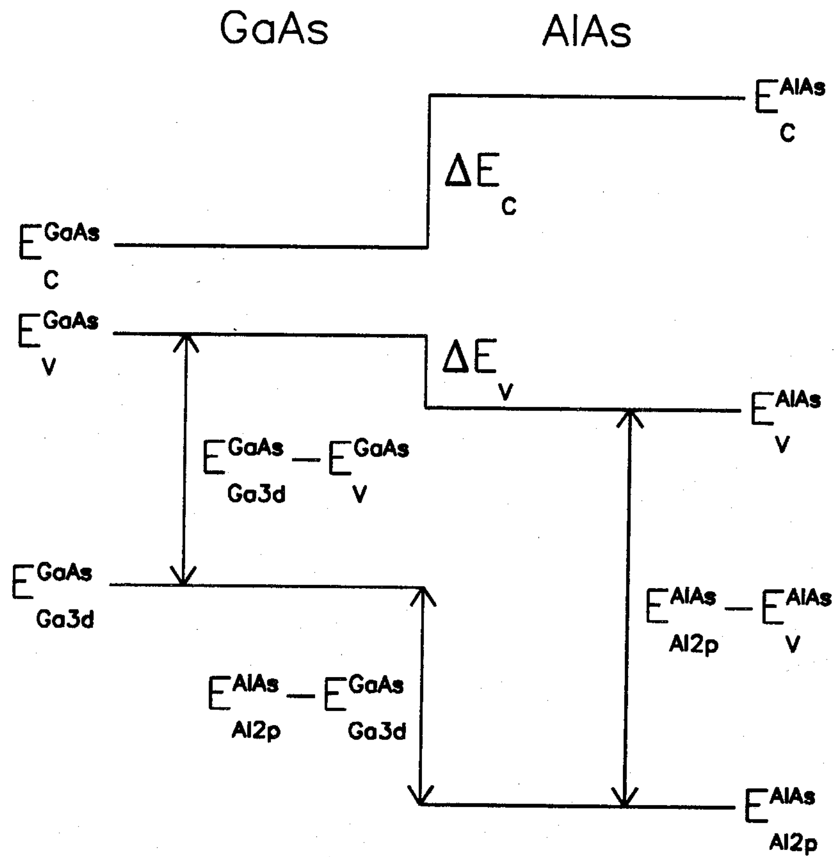

Figure 3.2: Schematic energy-band diagram for the GaAs/AlAs interface. The Al $2p$ and Ga $3d$ core-level to valence-band-edge binding energies are measured in bulk AlAs and GaAs, respectively, and the Al $2p$ to Ga $3d$ core-level energy separation is measured in GaAs/AlAs heterojunction samples.

as indicated in the figure.

To obtain sufficiently accurate core-level energy separations and core-level to valence-band-edge binding energies, it is necesary to determine peak positions and valence-band-edge positions to a high degree of precision. To find core-level peak positions, we subtracted from each core-level peak a background function (arising from inelastic scattering in the sample) proportional to the integrated photoelectron intensity, and defined the peak energy to be the midpoint of the two energies at which the intensity was half the maximum intensity. This procedure was sufficient to determine core-level peak positions with an uncertainty of ± 0.02 eV, and typically core-level energy separations were reproducible to ± 0.01 eV for a given sample.

To locate the position of the valence-band edge in the bulk GaAs and AlAs XPS spectra, we employed the precision analysis technique developed by Kraut et al.[51]. In this approach, described in detail in Section 2.3.2, the XPS spectrum near the valence-band edge is modeled as a convolution of a theoretical valence-band density of states with an experimentally determined XPS instrumental resolution function. This model function is then fitted to the experimental data to give the position of the valence-band edge. Due to the similarity in the valence-band spectra for GaAs and AlAs[37], we were able to use the GaAs valence-band density of states, calculated using a nonlocal empirical pseudopotential method[52], to analyze the valence-band spectra from both materials. For a given sample, core-level to valence-band-edge binding energies were reproducible to better than ± 0.04 eV.

When determining the position of the valence-band edge using this method, complications can arise from the presence of surface states in the energy region near the valence-band edge[51]. These surface states produce contributions to the XPS spectrum that are unaccounted for in the theoretical valence-band density

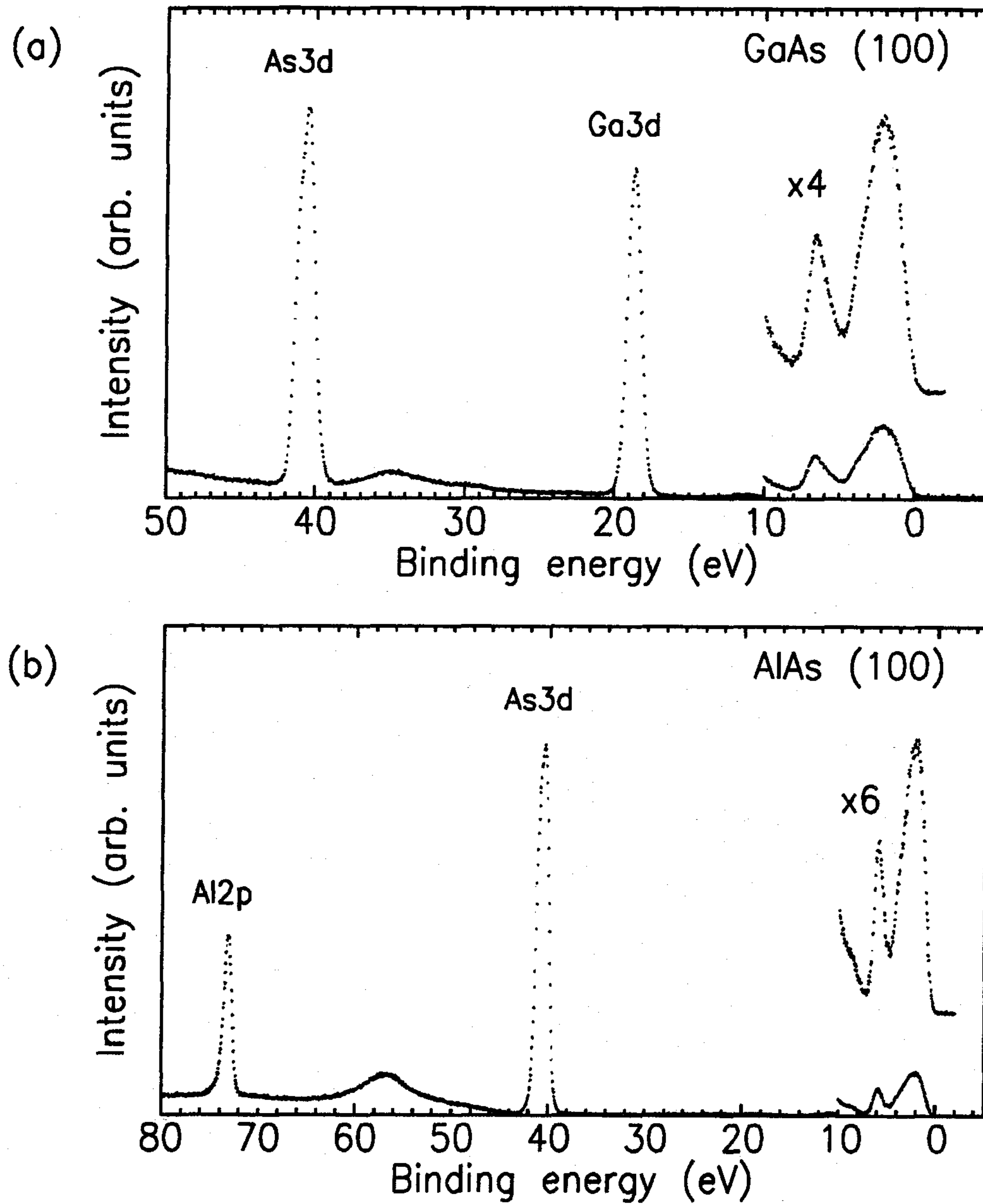

Figure 3.3: Representative binding energy XPS spectra for (a) GaAs (100) and (b) AlAs (100) samples. Ga 3*d* and Al 2*p* core-level to valence-band-edge binding energies are obtained from these spectra. The discontinuities in the spectra at a binding energy of 10 eV are due to the longer sampling times used near the valence-band edge; the valence-band spectra are also shown on enlarged intensity scales, as indicated in the figure.

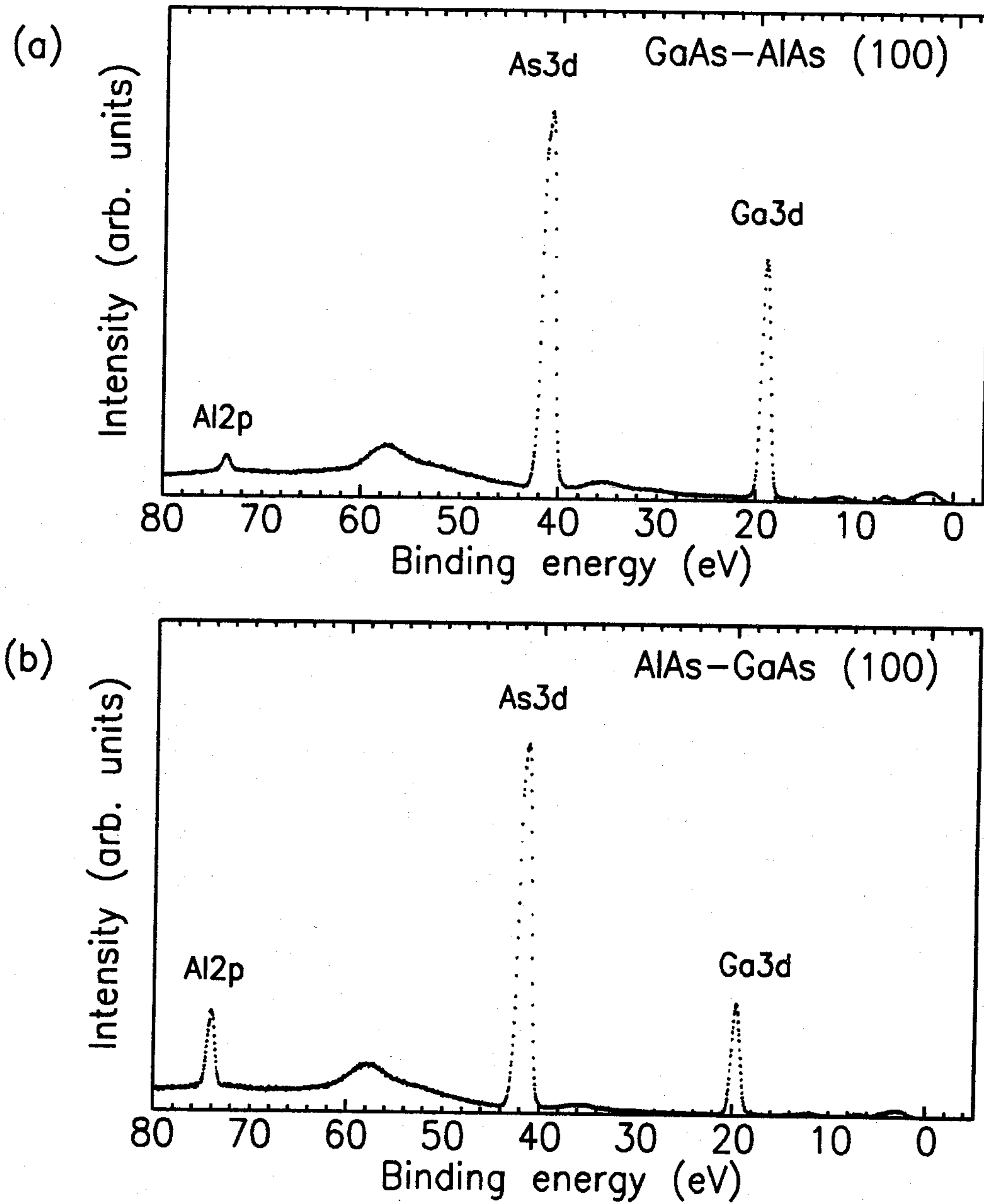

Figure 3.4: Representative binding energy XPS spectra for (a) GaAs-AlAs (100) and (b) AlAs-GaAs (100) heterojunction samples. Al $2p$ to Ga $3d$ core-level energy separations are obtained from these spectra.

of states, and can affect the calculated position of the valence-band edge by $\sim$0.1 eV or more. No such effects were observed in our AlAs (100) samples, but a p_z-like surface state was detected in the GaAs (100) samples, in agreement with previous studies of the (2×4) GaAs (100) surface reconstruction[53]. Thus, the position of the GaAs valence-band edge was determined by analyzing the XPS valence-band spectrum only in an energy region in which no surface states were observed.

3.3 Results and Discussion

The core-level to valence-band-edge binding energies measured for the three GaAs (100) and two AlAs (100) samples are shown in Table 3.1. For GaAs (100), the result is $(E_{\mathrm{Ga3}d}^{\mathrm{GaAs}} - E_v^{\mathrm{GaAs}}) = 18.73 \pm 0.05$ eV, and for AlAs (100) we obtain $(E_{\mathrm{Al2}p}^{\mathrm{AlAs}} - E_v^{\mathrm{AlAs}}) = 72.71 \pm 0.04$ eV. These values are in good agreement with those obtained by Waldrop, Grant, and Kraut[37]. Table 3.2 lists the core-level binding energy separations measured for the AlAs-GaAs (100) and GaAs-AlAs (100) heterojunction samples. For the GaAs-AlAs (100) interface, we find $(E_{\mathrm{Al2}p}^{\mathrm{AlAs}} - E_{\mathrm{Ga3}d}^{\mathrm{GaAs}}) = 54.45 \pm 0.02$ eV. Using Eq. (3.1), we see that this corresponds to a valence-band offset of 0.47 ± 0.07 eV. The core-level binding energy separation for the AlAs-GaAs (100) interface was found to be $(E_{\mathrm{Al2}p}^{\mathrm{AlAs}} - E_{\mathrm{Ga3}d}^{\mathrm{GaAs}}) = 54.43 \pm 0.02$ eV, corresponding to a valence-band offset of 0.45 ± 0.07 eV.

From these measurements it may be seen that the valence-band offsets for the two different growth sequences are within 0.02 eV of each other, demonstrating that the GaAs/AlAs (100) band offset is commutative. The observation of commutativity for the GaAs/AlAs (100) interface is in agreement with the results of Katnani and Bauer[38] and of Wang et al.[16], but disagrees with the observations of Waldrop et al.[37], who reported a dependence of the band offset on

Semiconductor	Sample	$E_{\mathrm{Ga3}d}^{\mathrm{GaAs}} - E_v^{\mathrm{GaAs}}$ (eV)	$E_{\mathrm{Al2}p}^{\mathrm{AlAs}} - E_v^{\mathrm{AlAs}}$ (eV)
GaAs (100)	III024	18.75	
GaAs (100)	III031	18.72	
GaAs (100)	III054	18.73	
AlAs (100)	III027		72.70
AlAs (100)	III058		72.72

Table 3.1: Measured core-level to valence-band-edge binding energies for GaAs (100) and AlAs (100) samples.

Heterojunction	Sample	$E_{\mathrm{Al2}p}^{\mathrm{AlAs}} - E_{\mathrm{Ga3}d}^{\mathrm{GaAs}}$ (eV)
GaAs-AlAs (100)	III036	54.44
GaAs-AlAs (100)	III085	54.46
GaAs-AlAs (100)	III087	54.45
AlAs-GaAs (100)	III045	54.43
AlAs-GaAs (100)	III050	54.42

Table 3.2: Measured Al $2p$ to Ga $3d$ core-level binding energy separations for GaAs-AlAs (100) and AlAs-GaAs (100) heterojunction samples.

both growth sequence and crystal orientation. In particular, Waldrop et al. reported a valence-band offset of 0.46 eV for the AlAs-GaAs (100) heterojunction, in agreement with our result, but obtained a value of 0.36 eV for the GaAs-AlAs (100) band offset. The latter result suggests that, for the GaAs-AlAs (100) heterojunction, differences in growth conditions between our samples and those of Waldrop et al. significantly influenced the quality of the interface, and therefore the value of the band offset.

The fact that XPS band offset measurements are not consistently commutative or noncommutative would seem to indicate that growth conditions and interface quality can have a significant effect on the value of the band offset. If this were the case, one would expect that nearly ideal interfaces would obey the commutativity rule, while nonideal interfaces would exhibit noncommutativity. The confirmation of band offset commutativity in our experiments may therefore be taken as an indication that under sufficiently controlled growth conditions, it is possible to grow consistently high-quality interfaces, with band offsets that are independent of growth sequence, for both normal and inverted GaAs/AlAs (100) heterojunction structures.

The value we have obtained for the GaAs/AlAs (100) valence-band offset, 0.46 ± 0.07 eV, is well within the range of experimental values that have been reported. Fig. 3.5 shows our result among a number of other experimentally measured GaAs/AlAs band offset values. These values range from 0.36 eV to 0.56 eV, with the more commonly accepted values ranging from 0.45 eV to 0.56 eV. Because of the hygroscopic nature of pure AlAs, relatively few *ex situ* (e.g., electrical or photoluminescence) measurements have been made for the GaAs/AlAs heterojunction. Arnold et al.[11] studied current-voltage characteristics as a function of temperature and obtained a valence-band offset $\Delta E_v = 0.35\Delta E_g$, corresponding to $\Delta E_v = 0.56$ eV for the GaAs/AlAs interface. Batey and Wright[17] used J–V

techniques to obtain $\Delta E_v = 0.55x$ for the GaAs/$Al_xGa_{1-x}As$ valence-band offset, corresponding to $\Delta E_v = 0.55$ eV for GaAs/AlAs. XPS measurements by Katnani and Bauer [38] yielded $\Delta E_v = 0.39 \pm 0.07$ eV. Waldrop et al.[37] measured $\Delta E_v = 0.36 \pm 0.05$ eV for the GaAs-AlAs (100) interface, and $\Delta E_v = 0.46 \pm 0.05$ eV for AlAs-GaAs (100).

Fig. 3.6 summarizes several of the experimentally measured conduction- and valence-band offsets that have been reported for GaAs/$Al_xGa_{1-x}As$ heterojunctions. Assuming that the valence-band offset is a linear function of composition x, a least-squares fit to the data yields $\Delta E_v = 0.48x$ eV, as shown in the figure. The corresponding conduction band offsets, for both the the Γ and X valleys in $Al_xGa_{1-x}As$, are also shown in the figure. The Γ-point (direct) and X-point (indirect) band gaps in $Al_xGa_{1-x}As$ as a function of alloy composition x have been taken from the review of Adachi[54].

3.4 Conclusions

We have presented a brief synopsis of the controversy over the GaAs/-$Al_xGa_{1-x}As$ band offset value, beginning with the initial (and erroneous) optical determination by Dingle et al.[1, 2], that the valence-band offset was only a small percentage of the total band-gap difference, $\Delta E_v \approx 0.12$–$0.15\Delta E_g$, and progressing to the currently accepted range of values, $\Delta E_v \approx 0.3$–$0.4\Delta E_g$ and $\Delta E_v \approx 0.45$–$0.55x$, depending on whether one believes that the valence-band offset should depend linearly on the band-gap difference ΔE_g or on the alloy composition x. Numerous attempts have also been made to predict theoretically the value of the GaAs/AlAs valence-band offset; several recently proposed theories [28, 29, 31, 32, 33, 34, 35] have yielded GaAs/AlAs valence-band offsets in reasonable agreement with the experimental values, but only after the

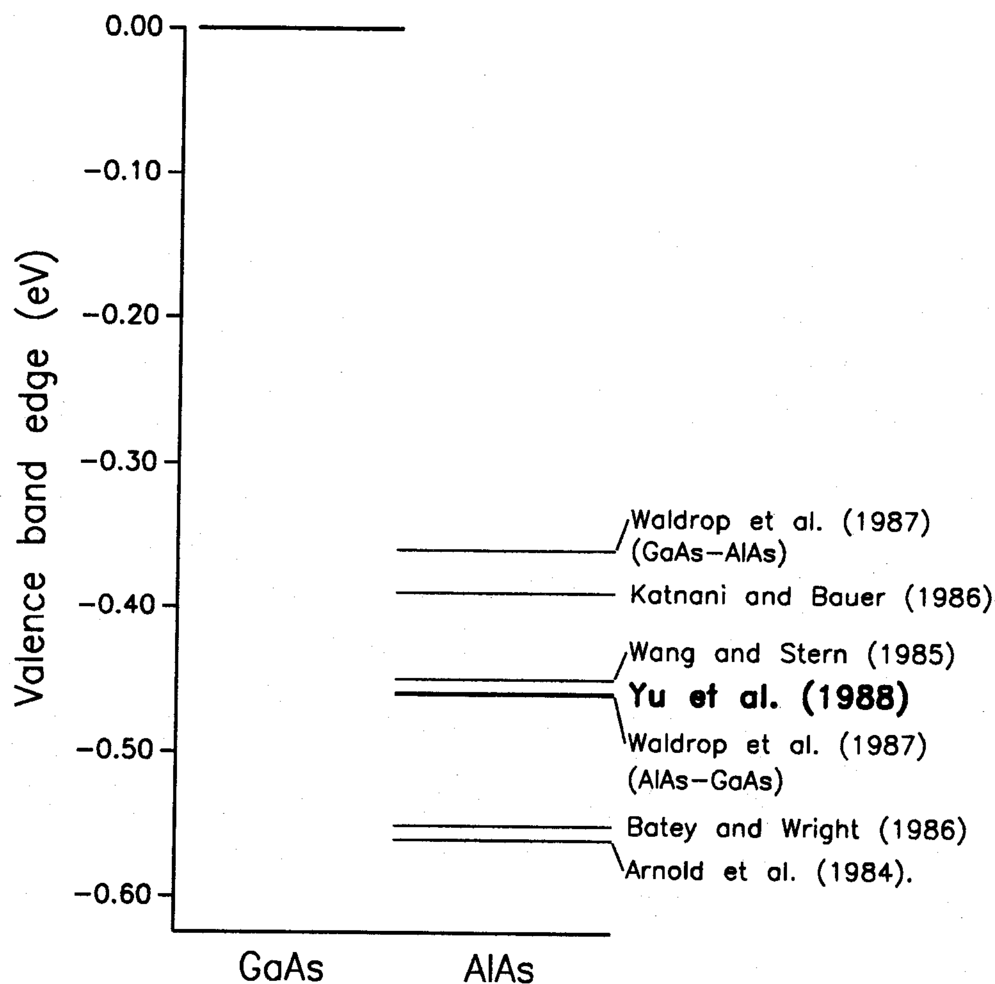

Figure 3.5: GaAs/AlAs valence-band offsets measured by various investigators. The values of Katnani and Bauer (Ref. [38]) and of Waldrop et al. (Ref. [37]) were obtained by XPS. The values of Wang and Stern (Ref. [15]), of Batey and Wright (Ref. [17]), and of Arnold et al. (Ref. [11]) were derived from electrical measurements.

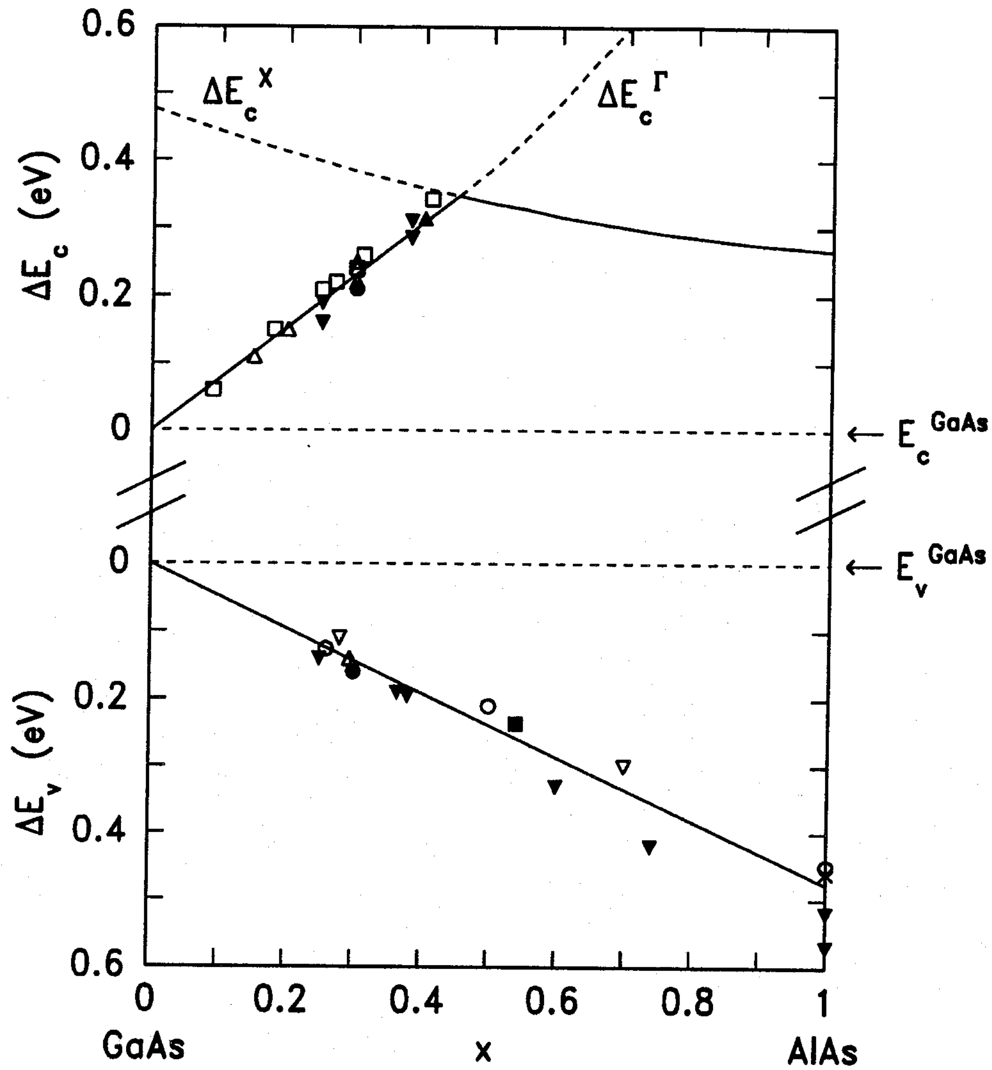

Figure 3.6: Summary of experimental band offset data for the GaAs/$Al_xGa_{1-x}As$ heterojunction. Data are from Miller et al.[9] (•); Wang et al.[10, 15, 16] (○); Arnold et al.[11] (■); Okumura et al.[12] (□); Hickmott et al.[13] (▲); Watanabe et al.[14] (△); Batey and Wright[17, 18] (▼); Wolford et al.[19] (▽); and Yu et al.[43, 44] (×).

experimental values had become known. In general, theories have at best been able to confirm, rather than predict, band offset values in GaAs/AlAs and other heterojunction systems.

Conflicting evidence has been reported regarding the dependence of the GaAs/$Al_xGa_{1-x}As$ valence-band offset on growth sequence and crystal orientation. XPS measurements by Waldrop et al.[37] indicated a dependence of the band offset on both growth sequence and substrate orientation. Other investigators reported that the band offset was independent of both growth sequence[38] and crystal orientation[16].

In this chapter we have described work that attempts to resolve the issue of commutativity in the GaAs/AlAs material system, and that provides an XPS measurement of the valence-band offset obtained using samples known to be of high quality. Our measurements demonstrate that GaAs/AlAs heterostructures can be consistently grown that exhibit commutativity of the band offset, and we obtain a valence-band offset $\Delta E_v = 0.46 \pm 0.07$ eV, independent of growth sequence. This value is in good agreement with the commonly accepted GaAs/-AlAs valence-band offset values determined by XPS, electrical measurements, and optical measurements. Our observation of commutativity is in agreement with some, but not all, published results for the GaAs/AlAs (100) interface. This indicates that we have been able to grow consistently high-quality interfaces for both normal and inverted GaAs/AlAs heterojunctions, since band offset commutativity is to be expected for ideal interfaces, and that commutativity of the GaAs/AlAs (100) band offset may be safely assumed in the design and analysis of quantum-effect device structures.

References

[1] R. Dingle, W. Wiegmann, and C. H. Henry, *Phys. Rev. Lett.* **33**, 827 (1974).

[2] R. Dingle, A. C. Gossard, and W. Wiegmann, *Phys. Rev. Lett.* **34**, 1327 (1975).

[3] A. C. Gossard, W. Brown, C. L. Allyn, and W. Wiegmann, *J. Vac. Sci. Technol.* **20**, 694 (1982).

[4] R. People, K. W. Wecht, K. Alavi, and A. Y. Cho, *Appl. Phys. Lett.* **43**, 118 (1983).

[5] D. F. Welch, G. W. Wicks, and L. F. Eastman, *J. Appl. Phys.* **55**, 3176 (1984).

[6] H. Kroemer, W.–Y. Chien, J. S. Harris, Jr., and D. D. Edwall, *Appl. Phys. Lett.* **36**, 295 (1980).

[7] C. M. Wu and E. S. Yang, *J. Appl. Phys.* **51**, 2261 (1980).

[8] R. C. Miller, A. C. Gossard, D. A. Kleinman, and O. Munteanu, *Phys. Rev. B* **29**, 3740 (1984).

[9] R. C. Miller, D. A. Kleinman, and A. C. Gossard, *Phys. Rev. B* **29**, 7085 (1984).

[10] W. I. Wang, E. E. Mendez, and F. Stern, *Appl. Phys. Lett.* **45**, 639 (1984).

[11] D. Arnold, A. Ketterson, T. Henderson, J. Klem, and H. Morkoç, *Appl. Phys. Lett.* **45**, 1237 (1984).

[12] H. Okumura, S. Misawa, S. Yoshida, and S. Gonda, *Appl. Phys. Lett.* **46**, 377 (1985).

[13] T. W. Hickmott, P. M. Solomon, R. Fischer, and H. Morkoç, *J. Appl. Phys.* **57**, 2844 (1985).

[14] M. O. Watanabe, J. Yoshida, M. Mashita, T. Nakanisi, and A. Hojo, *J. Appl. Phys.* **57**, 5340 (1985).

[15] W. I. Wang and F. Stern, *J. Vac. Sci. Technol. B* **3**, 1280 (1985).

[16] W. I. Wang, T. S. Kuan, E. E. Mendez, and L. Esaki, *Phys. Rev. B* **31**, 6890 (1985).

[17] J. Batey and S. L. Wright, *J. Appl. Phys.* **59**, 200 (1985).

[18] J. Batey and S. L. Wright, *Surf. Sci.* **174**, 320 (1986).

[19] D. J. Wolford, T. F. Kuech, J. A. Bradley, M. A. Gell, D. Ninno, and M. Jaros, *J. Vac. Sci. Technol. B* **4**, 1043 (1986).

[20] P. Dawson, B. A. Wilson, C. W. Tu, and R. C. Miller, *Appl. Phys. Lett.* **48**, 541 (1986).

[21] B. A. Wilson, P. Dawson, C. W. Tu, and R. C. Miller, *J. Vac. Sci. Technol. B* **4**, 1037 (1986).

[22] R. L. Anderson, *Solid–State Electron.* **5**, 341 (1962).

[23] A. G. Milnes and D. L. Feucht, *Heterojunctions and Metal–Semiconductor Junctions* (Academic Press, New York, 1972).

[24] W. A. Harrison, *J. Vac. Sci. Technol.* **14**, 1016 (1977).

[25] W. R. Frensley and H. Kroemer, *J. Vac. Sci. Technol.* **13**, 810 (1976).

[26] W. R. Frensley and H. Kroemer, *Phys. Rev. B* **16**, 2642 (1977).

[27] J. O. McCaldin, T. C. McGill, and C. A. Mead, *Phys. Rev. Lett.* **36**, 56 (1976).

[28] J. Tersoff, *Phys. Rev. B* **30**, 4874 (1984).

[29] J. Tersoff, *Phys. Rev. Lett.* **56**, 2755 (1986).

[30] W. A. Harrison and J. Tersoff, *J. Vac. Sci. Technol. B* **4**, 1068 (1986).

[31] C. G. Van de Walle and R. M. Martin, *J. Vac. Sci. Technol. B* **4**, 1055 (1986).

[32] C. G. Van de Walle, *Phys. Rev. B* **39**, 1871 (1989).

[33] N. E. Christensen, *Phys. Rev. B* **37**, 4528 (1988).

[34] W. R. L. Lambrecht, B. Segall, and O. K. Andersen, *Phys. Rev. B* **41**, 2813 (1990).

[35] M. Cardona and N. E. Christensen, *Phys. Rev. B* **35**, 6182 (1987).

[36] J. R. Waldrop, S. P. Kowalczyk, R. W. Grant, E. A. Kraut, and D. L. Miller, *J. Vac. Sci. Technol.* **19**, 573 (1981).

[37] J. R. Waldrop, R. W. Grant, and E. A. Kraut, *J. Vac. Sci. Technol. B* **5**, 1209 (1987).

[38] A. D. Katnani and R. S. Bauer, *Phys. Rev. B* **33**, 1106 (1986).

[39] C. G. Van de Walle and R. M. Martin, *Phys. Rev. B* **35**, 8154 (1987).

[40] N. E. Christensen, *Phys. Rev. B* **38**, 12687 (1988).

[41] M. K. Jackson, private communication (1990).

[42] R. Köhrbrück, S. Munnix, D. Bimberg, D. E. Mars, and J. N. Miller, *Appl. Phys. Lett.* **57**, 1025 (1990).

[43] E. T. Yu, D. H. Chow, and T. C. McGill, *Phys. Rev. B* **38**, 12764 (1988).

[44] E. T. Yu, D. H. Chow, and T. C. McGill, *J. Vac. Sci. Technol. B* **7**, 391 (1989).

[45] M. Ilegems, in *The Technology and Physics of Molecular beam Epitaxy*, E. H. C. Parker, ed. (Plenum, New York, 1985), pp. 120–121.

[46] G. J. Gualtieri, G. P. Schwartz, R. G. Nuzzo, and W. A. Sunder, *Appl. Phys. Lett.* **49**, 1037 (1986).

[47] S. P. Kowalczyk, J. T. Cheung, E. A. Kraut, and R. W. Grant, *Phys. Rev. Lett.* **56**, 1605 (1986).

[48] G. J. Gualtieri, G. P. Schwartz, R. G. Nuzzo, R. J. Malik, and J. F. Walker, *J. Appl. Phys.* **61**, 5337 (1987).

[49] G. P. Schwartz, M. S. Hybertsen, J. Bevk, R. G. Nuzzo, J. P. Mannaerts, and G. J. Gualtieri, *Phys. Rev. B* **39**, 1235 (1989).

[50] G. P. Schwartz, G. J. Gualtieri, R. D. Feldman, R. F. Austin, and R. G. Nuzzo, *J. Vac. Sci. Technol. B* **8**, 747 (1990).

[51] E. A. Kraut, R. W. Grant, J. R. Waldrop, and S. P. Kowalczyk, *Phys. Rev. B* **28**, 1965 (1983).

[52] J. R. Chelikowsky and M. L. Cohen, *Phys. Rev. B* **14**, 556 (1976).

[53] P. K. Larsen, J. F. Van der Veen, A. Mazur, J. Pollmann, J. H. Neave, and B. A. Joyce, *Phys. Rev. B* **26**, 3222 (1982).

[54] S. Adachi, *J. Appl. Phys.* **58**, R1 (1985).

Chapter 4

Measurement of the Si/Ge (001) Valence-Band Offset: The Role of Strain

4.1 Introduction

4.1.1 Background and Motivation

Advances in epitaxial growth techniques have stimulated great interest in strained–layer heterostructures realized in lattice–mismatched material systems[1, 2, 3, 4, 5, 6, 7, 8]. The study of heterostructures in lattice–mismatched material systems involves a number of issues that do not arise for lattice–matched heterojunctions, chief among these being the conditions under which coherently strained epitaxial structures can be grown, and the effect of strain on electronic structure in a coherently strained semiconductor heterojunction.

We have chosen the Si/Ge (001) heterojunction as a prototypical material system in which to study the effects of strain on band offset values. The Si/Ge (001)

heterojunction system was particularly appropriate for this type of study, because of the large lattice mismatch (4.18%) between Si and Ge, and because conditions under which coherently strained epilayers can be grown are well known[9, 10, 11]. In addition, theoretical calculations of the Si/Ge (001) valence-band offset have been performed that explicitly incorporate the effects of strain[12]; these calculations, as well as a number of experimental results[13, 14, 15, 16], indicate that strain strongly influences the value of the valence-band offset.

The Si/Ge interface is also of significant technological interest, because of the possibility of integrating devices utilizing $Si/Si_{1-x}Ge_x$ heterojunctions directly into existing Si-based structures[17]. A number of $Si/Si_{1-x}Ge_x$ heterostructure devices have been demonstrated or proposed. The demonstration of modulation-doping effects in $Si/Si_{1-x}Ge_x$ heterojunctions for holes[18] and electrons[19, 20] has led to the realization of $Si/Si_{1-x}Ge_x$ modulation-doped field effect transistors (MODFET's) with both p-channel[21] and n-channel[22] conduction. $Si/Si_{1-x}Ge_x$ double-barrier resonant tunneling diodes have been demonstrated for holes[23, 24] and proposed for electrons[25], and $Si/Si_{1-x}Ge_x$ resonant-tunneling hot-electron transistors have been fabricated[26]. $Si/Si_{1-x}Ge_x$ heterostructures have also been proposed for optical and optoelectronic applications. Enhanced optical emission and absorption in $Si/Si_{1-x}Ge_x$ superlattices compared to that in pure Si has been predicted[27, 28, 29, 30, 31, 32, 33, 34, 35], and $Si/Si_{1-x}Ge_x$ superlattices have also been studied as possible long-wavelength infrared detectors based on intersubband absorption[36, 37, 38, 39].

The behavior of $Si/Si_{1-x}Ge_x$ heterostructure devices depends critically on the values of the conduction- and valence-band offsets. Because of the lattice mismatch between Si and Ge, at least one constituent of any dislocation-free $Si/Si_{1-x}Ge_x$ heterojunction will necessarily be strained. In particular, the in-plane lattice constant $a_{||}$ must be the same for each layer, forcing the lattice to

deviate from its natural structure in at least one layer; an interface at which this condition is satisfied is referred to as being coherently strained. Strain reduces the inherent tetragonal symmetry in each layer, leading to changes in the electronic structure of the heterojunction.

Influence of Strain on Bulk Band Structure

The effects of strain on band offset values can be understood most easily by examining first the effect of strain on the electronic structure of a bulk semiconductor using $\vec{k} \cdot \vec{p}$ theory. For simplicity the discussion will be limited to the case of [001] strain. In $\vec{k} \cdot \vec{p}$ theory, the band structure for a crystal with cubic symmetry near a level that is threefold degenerate (neglecting spin degeneracy) at the Γ point ($\vec{k} = 0$) is given by a Hamiltonian of the form[40]

$$H(k_i k_j) = \begin{pmatrix} Lk_x^2 + M(k_y^2 + k_z^2) & Nk_x k_y & Nk_x k_z \\ Nk_x k_y & Lk_y^2 + M(k_x^2 + k_z^2) & Nk_y k_z \\ Nk_x k_z & Nk_y k_z & Lk_z^2 + M(k_x^2 + k_y^2) \end{pmatrix}, \tag{4.1}$$

where the basis elements have been taken to be $\{X, Y, Z\}$, valence band wave functions that transform as p-like atomic orbitals. Bir and Pikus[41] have shown that because strain in a cubic crystal can be described by a strain tensor ϵ_{ij} having the same symmetry as the quadratic tensor $k_i k_j$ in Eq. (4.1), the perturbation Hamiltonian describing strain effects can be written

$$H(\epsilon_{ij}) = \begin{pmatrix} l\epsilon_{xx} + m(\epsilon_{yy} + \epsilon_{zz}) & n\epsilon_{xy} & n\epsilon_{xz} \\ n\epsilon_{xy} & l\epsilon_{yy} + m(\epsilon_{xx} + \epsilon_{zz}) & n\epsilon_{yz} \\ n\epsilon_{xz} & n\epsilon_{yz} & l\epsilon_{zz} + m(\epsilon_{xx} + \epsilon_{yy}) \end{pmatrix}, \tag{4.2}$$

or rewriting Eq. (4.2) in terms of the conventional deformation potentials[41, 42]

a, b, and d,

$$H(\epsilon_{ij}) = \begin{pmatrix} \begin{array}{c} b(3\epsilon_{xx} - \mathrm{Tr}\epsilon_{ij}) \\ + a\mathrm{Tr}\epsilon_{ij} \end{array} & \sqrt{3}c\epsilon_{xy} & \sqrt{3}c\epsilon_{xz} \\ \sqrt{3}c\epsilon_{xy} & \begin{array}{c} b(3\epsilon_{yy} - \mathrm{Tr}\epsilon_{ij}) \\ + a\mathrm{Tr}\epsilon_{ij} \end{array} & \sqrt{3}c\epsilon_{yz} \\ \sqrt{3}c\epsilon_{xz} & \sqrt{3}c\epsilon_{yz} & \begin{array}{c} b(3\epsilon_{zz} - \mathrm{Tr}\epsilon_{ij}) \\ + a\mathrm{Tr}\epsilon_{ij} \end{array} \end{pmatrix}, \tag{4.3}$$

where $\mathrm{Tr}\epsilon_{ij} = (\epsilon_{xx} + \epsilon_{yy} + \epsilon_{zz})$ and

$$a = \frac{l + 2m}{3}, \qquad b = \frac{l - m}{3}, \qquad d = \frac{n}{\sqrt{3}}. \tag{4.4}$$

From Eq. (4.3) it can be seen that purely isotropic strain, also referred to as hydrostatic strain, produces an overall shift in energy; the degeneracy of the bands is not affected, since a pure dilation does not change the symmetry of the crystal. The size of this energy shift is determined by the deformation potential a, also referred to as the hydrostatic deformation potential. For purely uniaxial (volume-preserving) strain in the [001] direction the symmetry of the crystal is reduced, and the bands are split by an energy $3|b(\epsilon_{zz} - \epsilon_{yy})| = 3|b(\epsilon_{zz} - \epsilon_{xx})|$. The size of the splitting for [001] strain is determined by b, which we shall refer to as the uniaxial deformation potential.

To obtain the valence-band splittings with spin-orbit effects included, one must transform from the $\{X, Y, Z\}$ basis in which we have been working to an angular-momentum basis $|j, m\rangle$ given, for example, by[43]

$$|\tfrac{3}{2}, \tfrac{3}{2}\rangle = (1/\sqrt{2})(X + iY)\uparrow, \tag{4.5}$$

$$|\tfrac{3}{2}, \tfrac{1}{2}\rangle = (1/\sqrt{6})[2Z\uparrow - (X + iY)\downarrow], \tag{4.6}$$

$$|\tfrac{3}{2}, -\tfrac{1}{2}\rangle = (1/\sqrt{6})[2Z\downarrow - (X - iY)\uparrow], \tag{4.7}$$

$$|\tfrac{3}{2}, -\tfrac{3}{2}\rangle = (1/\sqrt{2})(X - iY)\downarrow, \tag{4.8}$$

$$
\begin{aligned}
|\tfrac{1}{2},\tfrac{1}{2}\rangle &= (1/\sqrt{3})[Z\uparrow -(X+iY)\downarrow], && (4.9)\\
|\tfrac{1}{2},-\tfrac{1}{2}\rangle &= (1/\sqrt{3})[Z\downarrow +(X-iY)\uparrow]. && (4.10)
\end{aligned}
$$

Spin-orbit effects split the six bands into a fourfold degenerate $p_{3/2}$ multiplet and a twofold degenerate $p_{1/2}$ multiplet; at the Brillouin zone center, $|\frac{3}{2},\pm\frac{3}{2}\rangle$ correspond to the heavy-hole band, $|\frac{3}{2},\pm\frac{1}{2}\rangle$ to the light-hole band, and $|\frac{1}{2},\pm\frac{1}{2}\rangle$ to the split-off band. In the presence of strain, the positions of these three valence bands at the Γ point, relative to the average position of the three bands, are[12, 42]

$$
\begin{aligned}
\Delta E_{hh} &= \tfrac{1}{3}\Delta_0 - \tfrac{1}{2}\delta E_{001}, && (4.11)\\
\Delta E_{lh} &= -\tfrac{1}{6}\Delta_0 + \tfrac{1}{4}\delta E_{001} + \tfrac{1}{2}\sqrt{\Delta_0^2 + \Delta_0\delta E_{001} + \tfrac{9}{4}\delta E_{001}^2}, && (4.12)\\
\Delta E_{so} &= -\tfrac{1}{6}\Delta_0 + \tfrac{1}{4}\delta E_{001} - \tfrac{1}{2}\sqrt{\Delta_0^2 + \Delta_0\delta E_{001} + \tfrac{9}{4}\delta E_{001}^2}, && (4.13)
\end{aligned}
$$

where Δ_0 is the spin-orbit splitting and $\delta E_{001} = 2b(\epsilon_{zz} - \epsilon_{xx})$. For experimentally measured values of the deformation potential b in Si[44] and Ge[45], the linear multiplet splitting δE_{001} can be as large as a few tenths of an electron volt for highly strained Si and Ge crystals.

Influence of Strain on Band Offsets

The effect of strain on band offsets has been studied theoretically by Van de Walle and Martin[12, 46]. For a coherently strained (001) heterojunction with an in-plane lattice constant $a_{\|}$, the strain tensor components and growth-direction lattice constant for material i are

$$
\begin{aligned}
\epsilon_{xx} &= \epsilon_{yy} = \frac{a_{\|} - a_i}{a_i}, && (4.14)\\
\epsilon_{zz} &= -2\frac{c_{12,i}}{c_{11,i}}\epsilon_{xx} \equiv -D_{001}\epsilon_{xx}, && (4.15)\\
\epsilon_{xy} &= \epsilon_{xz} = \epsilon_{yz} = 0, && (4.16)\\
a_{\perp} &= (1+\epsilon_{zz})a_i, && (4.17)
\end{aligned}
$$

where $c_{11,i}$ and $c_{12,i}$ are the elastic constants and a_i is the natural lattice constant of material i. For Si and Ge, these elastic constants yield $D_{001}^{\mathrm{Si}} = 0.76$ and $D_{001}^{\mathrm{Ge}} = 0.72$; the natural lattice constants for Si and Ge are $a_{\mathrm{Si}} = 5.431$ Å and $a_{\mathrm{Ge}} = 5.658$ Å. The uniaxial deformation potential b for strain in the [001] direction has been determined experimentally for both Si and Ge, with the measured value for Si[44] being $b_{\mathrm{Si}} = -2.10 \pm 0.10$ eV, and for Ge[45] being $b_{\mathrm{Ge}} = -2.86 \pm 0.15$ eV. Using these values, one can see that for Ge coherently strained to a Si substrate ($a_{\|} = 5.431$ Å), $\delta E_{001} = -0.395$ eV, and for Si coherently strained to a Ge substrate ($a_{\|} = 5.658$ Å), $\delta E_{001} = 0.309$ eV. Hence, strain in lattice-mismatched heterojunctions can potentially change band offset values by a few tenths of an electron volt or more simply because of splitting of the heavy-hole, light-hole, and split-off valence bands relative to their average position.

The other factor that determines the effect of strain on band offset values is the hydrostatic deformation potential a for the average position of the three valence bands. This quantity is difficult to measure experimentally or even to calculate since it determines energy shifts on an absolute energy scale, whereas most experiments and calculations determine only changes in the relative positions of different bands. The problem of calculating absolute deformation potentials is in fact closely related to the problem of calculating band offsets, since both require that energy-band positions be determined on an absolute energy scale[46]. Van de Walle[46] has calculated the deformation potential a for several materials using his model solid theory, obtaining for Si and Ge $a_{\mathrm{Si}} = 2.46$ eV and $a_{\mathrm{Ge}} = 1.24$ eV. Given a value for a, the absolute shift in energy of the average position of the three valence bands is

$$\delta E_{v,\mathrm{av}} = a\frac{\Delta\Omega}{\Omega} = a\mathrm{Tr}\epsilon_{ij}, \tag{4.18}$$

where $\Delta\Omega/\Omega = \mathrm{Tr}\epsilon_{ij}$ is the fractional volume change induced by the strain.

For Ge coherently strained to Si ($a_{\parallel}$ = 5.431 Å), Eq. (4.18) yields $\delta E_{a,av}$ = −0.064 eV, and for Si coherently strained to Ge ($a_{\parallel}$ = 5.658 Å), a shift $\delta E_{a,av}$ = 0.127 eV is obtained; these values are both quite small compared to the valence band splittings for comparable levels of strain. In addition, a full, self-consistent interface calculation by Van de Walle and Martin[12] indicates that the shifts in valence-band-edge positions arising from hydrostatic deformation potentials should be very small. These calculations suggest that the changes in valence-band offset values induced by strain should be determined primarily by the splittings of the light-hole, heavy-hole, and split-off valence-bands, and that the sizes of these shifts can be as large as a few tenths of an electron volt.

Critical Thickness and Strain Relaxation

An additional issue that arises in studies of lattice-mismatched heterojunctions is the ability to grow actual coherently strained, dislocation-free heterojunctions. Each layer in a coherently strained heterostructure must be kept below the critical thickness for strain relaxation, beyond which strain in the layer will be relieved via the formation of dislocations. A number of theoretical models have been developed to predict the critical thickness for strain relaxation[9, 10, 47, 48, 49, 50, 51, 52], and critical thicknesses for a variety of material systems have been measured experimentally[11, 28, 48, 53, 54, 55].

The early theories of critical thickness, developed primarily by Van der Merwe[9, 10], assumed that the crystal would reach thermodynamic equilibrium and settle into the state of lowest energy. Hence, for film thicknesses below the critical thickness, the film should be coherently strained to match the in-plane lattice parameter of the substrate, and above the critical thickness the mismatch should be accommodated by a network of misfit dislocations. Van der Merwe

calculated the energy associated with a network of misfit dislocations using the Peierls-Nabarro model[9], obtaining

$$E_d \approx \frac{a\mu f}{4\pi(1-\sigma)}\left[1-\ln\left(\frac{2\pi f}{1-\sigma}\right)\right], \tag{4.19}$$

where a is the relaxed lattice constant, f is the fractional lattice mismatch, μ is the shear modulus, and σ is Poisson's ratio. The energy density in a coherently strained layer is obtained from simple elasticity theory,

$$E_s = 2\mu t\left(\frac{1+\sigma}{1-\sigma}\right)f^2, \tag{4.20}$$

where t is the film thickness. By equating the energy densities in a strained layer and in a layer that has relaxed via formation of misfit dislocations, one obtains an expression for the critical thickness for strain relaxation,

$$t_c = \frac{a}{8\pi(1+\sigma)f}\left[1-\ln\left(\frac{2\pi f}{1-\sigma}\right)\right]. \tag{4.21}$$

The validity of Van der Merwe's model depends on the crystal being able to reach a state of thermodynamic equilibrium. It may be possible, however, for crystals grown epitaxially at low temperatures to exist in a metastable state. Consider, for example, an interface for which the critical thickness t_c has some finite value. When the thickness of the overlayer is less than t_c, the film will be coherently strained. As the overlayer thickness increases beyond t_c, the film will remain coherently strained until dislocations nucleate to accommodate the misfit. Formation of these dislocations, however, often requires a nonzero activation energy; if the temperature of the crystal is much lower than this activation energy, the crystal may either remain in the now metastable, coherently strained state, or else form fewer dislocations than needed to minimize the total energy for film thicknesses greater than the critical thickness.

An alternate approach to calculating critical thicknesses was proposed by Matthews and Blakeslee[48]. Rather than minimize the total energy of strain

and dislocations in a crystal, Matthews and Blakeslee considered the forces on dislocation lines in deriving an expression for the critical thickness. The critical thickness in their model depended on the balance between the tension of threading dislocation lines and the lateral force exerted by the misfit strain. Matthews and Blakeslee gave expressions for the misfit force F_e and threading dislocation tension F_l,

$$F_e = 2\mu\left(\frac{1+\sigma}{1-\sigma}\right) btf\cos\lambda, \qquad (4.22)$$

$$F_l = \frac{\mu b^2}{4\pi(1-\sigma)}\left(1-\sigma\cos^2\alpha\right)\left(\ln\left(\frac{t}{b}\right)+1\right), \qquad (4.23)$$

where b is the magnitude of the Burgers vector of the dislocation, and $\cos\lambda$ and $\cos\alpha$ are geometric factors related to the relative orientations of a dislocation line, its Burgers vector, and the interfacial plane. Balancing the forces given in Eqs. (4.22) and (4.23), one obtains an implicit expression for the critical thickness,

$$f = \frac{b}{8\pi t_c}\frac{(1-\sigma\cos^2\alpha)}{(1+\sigma)\cos\lambda}\left(\ln\left(\frac{t_c}{b}\right)+1\right). \qquad (4.24)$$

For small misfit strain forces, the layers will remain coherently strained; for sufficiently large misfit strain forces, however, the threading dislocation line will expand by elongating in the plane of an interface, producing a misfit dislocation line along the interface connecting the threading dislocations in each layer. When this occurs, the mismatch is no longer accommodated completely by coherent strain, but by a combination of misfit dislocations and strain.

More recently, a model for calculating critical thicknesses was proposed by People and Bean[49]. This model is very similar to the original theory of Van der Merwe, in that the critical thickness is determined by minimizing the energy in the entire crystal (thermodynamic equilibrium), rather than by requiring that dislocation lines be in mechanical equilibrium. The main difference between the approaches of Van der Merwe and of People and Bean is in the calculation of

the dislocation energy density. Van der Merwe calculated the energy density of a misfit dislocation by considering the energy density of its strain field, and then adding a "potential energy" term calculated using the Peierls-Nabarro model. People and Bean consider the energy densities of various types of dislocations and assume that all misfit dislocations will be of the type with the lowest energy — the screw dislocation. This assumption is unphysical, however, since a screw dislocation does not accommodate lattice mismatch. In order to accommodate mismatch, a dislocation must somehow incorporate or eliminate extra atoms to produce a change in the lattice constant. Screw dislocations merely shift rows of atoms with respect to adjacent rows and therefore do not accommodate lattice mismatch. The misfit dislocations with lowest energy are therefore edge dislocations. For isolated screw and edge dislocations, respectively, the energy densities are taken to be

$$E_s = \frac{\mu b^2}{8\pi\sqrt{2}a} \ln \frac{t}{b}, \tag{4.25}$$

$$E_e = \left(\frac{1}{1-\sigma}\right)\left(\frac{\mu b^2}{8\pi\sqrt{2}a}\right) \ln \frac{t}{b}. \tag{4.26}$$

Using Eq. (4.20) for the strain energy density, and equating the strain and dislocation energy densities, People and Bean obtain

$$f^2 = \left(\frac{1-\sigma}{1+\sigma}\right) \frac{b^2}{16\pi\sqrt{2}at_c} \ln \frac{t_c}{b}. \tag{4.27}$$

Eq. (4.27) is valid assuming that only screw dislocations are present; for edge dislocations, the right-hand side of Eq. (4.27) should include an extra factor of $1/(1-\sigma)$.

Eqs. (4.25) and (4.26) for the dislocation energy density, however, correspond to an unphysical model for dislocation distribution in the crystal[56]. To obtain these expressions, one must assume a characteristic width over which the dislocation's influence extends; the energy density is then calculated per unit length of

the dislocation line. Since the model assumes that when misfit is accommodated by dislocations, the energy density is independent of position, the correct width to use is roughly the spacing between dislocation lines. Eqs. (4.25) and (4.26), however, assign each dislocation line a width of $2\sqrt{2}a \sim 16$ Å. This means that the dislocation lines are assumed to be ~16 Å apart, independent of the lattice mismatch. To assume both a constant spacing and a constant Burgers vector while letting the lattice mismatch vary is clearly unphysical. The justification proposed by People and Bean for this assumption is that the dislocation line width is a phenomenological parameter that reflects the effective lateral extent of the strain field, and was therefore chosen to yield the best agreement with the experimental data of Bean et al.[28].

The other questionable assumption made in this model is that the characteristic size of the strain field arising from the dislocation is given by the film thickness. In fact, this is true only when the film thickness t is comparable to the dislocation spacing p, or when the film thickness and the dislocation spacing are both much larger than the lattice constant a (because of the logarithmic dependence of the dislocation energy density on strain-field size R, the exact value of R for very large R becomes unimportant[57]). For $a<t\ll p$, the formula used will neglect much of the energy in the film arising from dislocations, and for $t\gg p$, that energy will be overestimated; in the latter case, p would be a more appropriate parameter to use for the strain-field size. In the model of People and Bean this assumption is of less importance than the assumption of constant dislocation spacing, although, as expected, it does produce unusual behavior for small values of the critical thickness. Fig. 4.1 shows predicted critical thicknesses as a function of lattice mismatch for the three models considered. The critical thickness in the Van der Merwe thermodynamic equilibrium model is calculated using Eq. (4.21) with $\sigma = 1/3$ and $a = 5.6$ Å. The critical thickness in the mechanical equilibrium

model of Matthews and Blakeslee is calculated using Eq. (4.24) with $\sigma = 1/3$, $\cos\alpha = \cos\lambda = 1/2$, and $b = 4$ Å. Finally, the critical-thickness curves in the model of People and Bean for edge and screw dislocations are calculated from Eq. (4.27), assuming $\sigma = 1/3$, $b = 4$ Å, and $a = 5.6$ Å.

Attempts have also been made to include the effects of growth temperature and metastability in models of critical thickness. Dodson and Tsao[50, 51] have developed a model for strain relaxation in lattice-mismatched heterojunctions via plastic flow; combining this model with the effects of finite instrumental resolution[58, 59], good agreement with the experimental data of Bean et al.[28] and of Kasper et al.[60] was obtained. Tsao et al.[52] measured the temperature dependence of strain relaxation in Si/Si_xGe_{1-x} heterojunctions, and proposed a model for strain relaxation based on temperature and the difference between stress in the sample due to misfit strain and that due to dislocation line tension.

A number of experiments have been performed in which critical thicknesses were measured experimentally. To test their predictions of critical thickness and strain accommodation by dislocations, Matthews and Blakeslee examined GaAs/-$GaAs_{0.5}P_{0.5}$ superlattice samples with layer thicknesses ranging from 75 Å to 700 Å using transmission and scanning electron microscopy. They found that the critical thicknesses for generation of misfit dislocations were between 160 Å and 350 Å; this result is in agreement with their theory, which predicts a critical thickness of about 250 Å for their structures. For layer thicknesses above 350 Å, however, the amount of lattice mismatch accommodated by dislocations, as determined by measurements of Burger's vector orientations and average distances between dislocation lines, was found to be about one hundred times smaller than predicted. This discrepancy indicates that processes inhibiting the formation of stable dislocations, e.g., interactions between dislocations and barriers for nucleation of dislocations, can be of considerable importance.

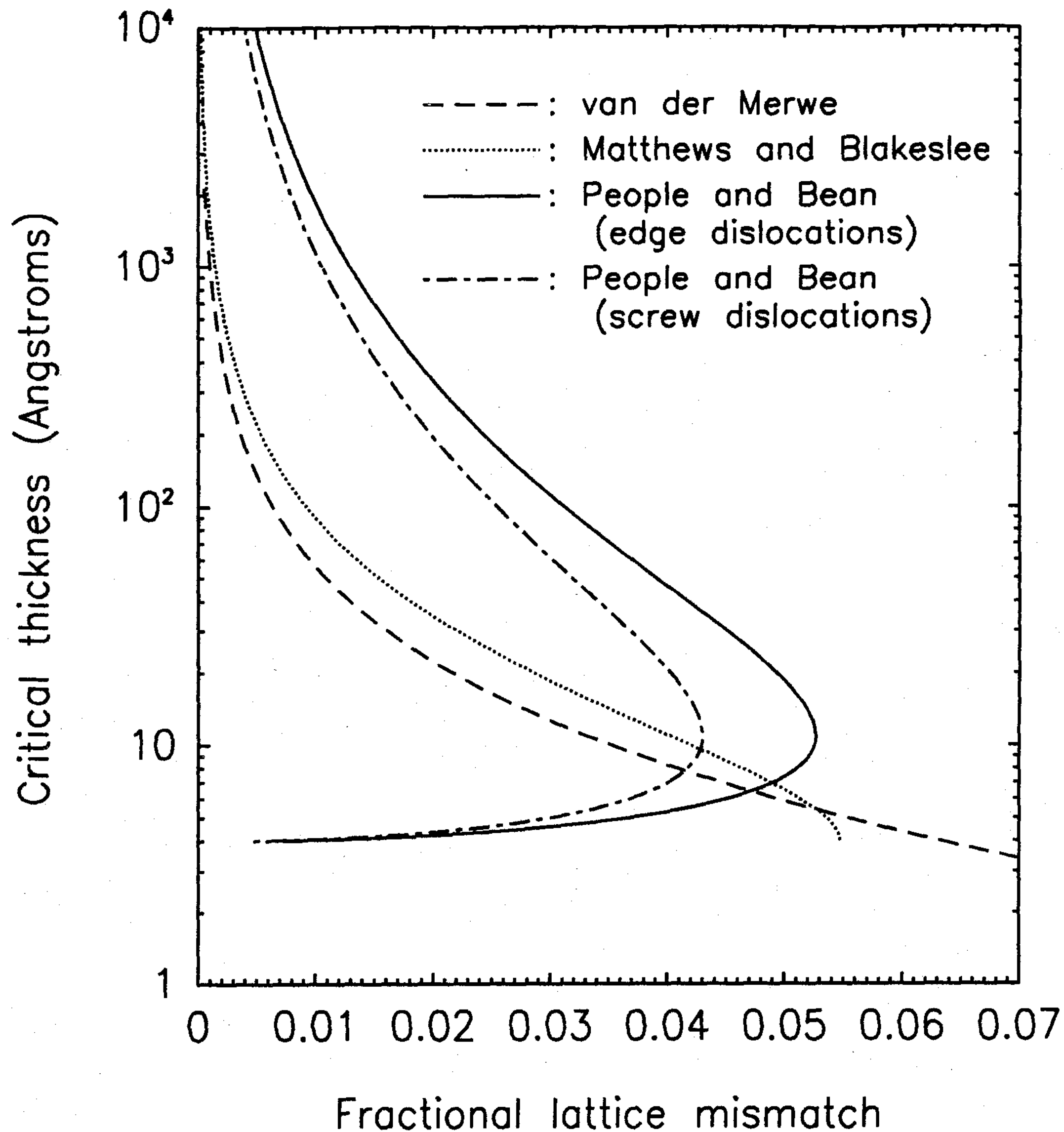

Figure 4.1: Theoretical models of critical thickness for strain relaxation at lattice-mismatched interfaces. The calculated curves apply to lattice-mismatched films grown epitaxially on an infinitely thick substrate. The predictions shown in the figure are from the models of Van der Merwe (Ref. [9, 10]), of Matthews and Blakeslee (Ref. [48]), and of People and Bean (Ref. [49]).

Bean et al.[28] performed transmission electron microscopy, x-ray diffraction, and Rutherford backscattering studies of $Si_{1-x}Ge_x/Si$ superlattices and found that their measured critical thicknesses were actually in good agreement with the theory of People and Bean. However, the presence in their theory of an arbitrary parameter, i.e., the dislocation spacing, and the unphysical assumptions in the model, suggest that a clear understanding of the nature of critical thicknesses has yet to be obtained. The primary significance of the $Si_{1-x}Ge_x/Si$ superlattice data is that the observed critical thicknesses are significantly larger than predicted by the equilibrium model of Van der Merwe. This result, like that of Matthews and Blakeslee, suggests that nonequilibrium effects, such as barriers to dislocation formation, can play a major role in determining critical-thickness values.

There exists considerable other evidence that this is indeed the case. Studies by Fiory et al.[53] have shown that annealing of $Si_{1-x}Ge_x$ films grown on Si (100) substrates at 550 °C increases the number of strain-relieving dislocations in the film. These experiments strongly suggest that the as-grown $Si_{1-x}Ge_x$ film exists in a metastable state, and that annealing at 800 °C to 1000 °C allows the film to relax gradually toward the minimum-energy equilibrium state. Tsao et al.[52] measured the temperature dependence of strain relaxation in Si_xGe_{1-x} layers grown on Ge substrates, and found that the onset of strain relaxation depended quite strongly on temperature. Studies by Miles et al.[11] of $Si/Ge_{0.5}Si_{0.5}$ superlattices have demonstrated a dependence of critical thickness and dislocation density on growth temperature. For superlattices with the same layer thicknesses and same total thickness grown at substrate temperatures ranging between 365 °C and 530 °C, the dislocation density was shown to increase with growth temperature, indicating that the superlattices, as grown, are in metastable states, with fewer dislocations than necesary to minimize the total energy. These studies indicate that a satisfactory theory of critical thicknesses will need to account for

the effects of dislocation interactions, barriers to dislocation formation, and other nonequilibrium processes that, in general, will depend on crystal-growth parameters, and on the growth temperature in particular. For now, however, these studies have provided a great deal of knowledge about the conditions that are necessary to encourage coherently strained growth, especially in the $Si/Si_{1-x}Ge_x$ material system.

4.1.2 Summary of Results

In this chapter we discuss the measurement of the valence-band offset in strained Si/Ge (001) heterojunctions using x-ray photoelectron spectroscopy. These measurements represent the first full extension of the XPS technique to the study of band offsets in heavily lattice-mismatched heterojunctions with well-characterized strain configurations, and include the first experimental determination of strain-dependent semiconductor core-level binding energies. All samples studied in these experiments were transferred directly from the molecular-beam epitaxy (MBE) growth chamber to the XPS analytical chamber under ultrahigh vacuum (UHV) conditions, eliminating uncertainties associated with deposition and subsequent evaporation of surface passivation layers that are often required for samples transported through atmosphere. This capability was especially important in these experiments; the growth of surface passivation layers and subsequent sample heating to evaporate a passivation layer, or the formation of a surface oxide during unprotected exposure to atmosphere, could strongly influence the strain configuration in a sample.

To measure the Si 2*p* and Ge 3*d* core-level to valence-band-edge binding energies as functions of strain, we grew thin (400−1000 Å) films of either pure Si or pure Ge coherently strained to relaxed $Si_{1-x}Ge_x$ alloy layers of varying com-

position. The pure Si and Ge films were kept below the critical thickness for strain relaxation, and were grown at low temperature to encourage the formation of coherently strained structures; by varying the composition, and therefore the in-plane lattice constant, of the underlying $Si_{1-x}Ge_x$ alloy layers, we were able to obtain Si and Ge films with varying degrees of strain. Measurements in Si and Ge films with varying levels of strain allowed the Si $2p$ and Ge $3d$ core-level to valence-band-edge binding energies to be determined as functions of strain; the strain in each of these samples was later determined independently using x-ray diffraction.

The strain dependence of the Si $2p$ to Ge $3d$ heterojunction core-level energy separation was obtained from measurements on several Si/Ge superlattices with varying Si and Ge layer thicknesses. Si/Ge superlattices were grown on $Si_{1-x}Ge_x$ alloy layers with compositions that were the same as the average composition of the superlattice, ensuring that the superlattices would grow in their free-standing strain configurations. By varying the average composition of the superlattices, and therefore the in-plane lattice constant, we obtained heterojunctions with varying degrees of strain, allowing the Si $2p$ to Ge $3d$ core-level energy separation to be measured as a function of strain. The strain configurations in the superlattices were later confirmed using x-ray diffraction measurements combined with known Si and Ge growth rates.

Our measurements yielded the Si/Ge (001) valence band offset as a function of the in-plane lattice constant, or equivalently as a function of strain. For Ge coherently strained to Si ($a_{\parallel} = 5.431$ Å), we obtained $\Delta E_v = 0.83 \pm 0.11$ eV, and for Si coherently strained to Ge ($a_{\parallel} = 5.658$ Å), we obtained $\Delta E_v = 0.22 \pm 0.13$ eV. These results are in good agreement with theoretical studies of Van de Walle and Martin[12] and with experimental studies of Schwartz et al.[13].

We have also used a linear interpolation technique to obtain band offset values

for $Si_{1-x}Ge_x/Si_{1-y}Ge_y$ (001) heterojunctions coherently strained to a $Si_{1-z}Ge_z$ substrate layer. Using this technique to determine band offsets for $Si/Si_{1-x}Ge_x$ (001) heterojunctions, we confirmed that our measured band offsets were in good agreement with measurements of Ni et al.[14, 15, 16], and were consistent with modulation-doping experiments reported by People et al.[18] and by Abstreiter et al.[20].

4.1.3 Outline of Chapter

The experimental procedure used to measure the strain dependence of the Si/Ge (001) valence band offset is explained in Section 4.2. The presence of strain in a heterojunction introduces substantial complications in the determination of core-level to valence-band-edge binding energies and core-level energy separations, and the experimental and analytical techniques developed to account for these complications are discussed. Section 4.3 describes the growth of samples in which strain-dependent core-level to valence-band-edge binding energies and heterojunction core-level energy separations were measured. The XPS measurements and the data analysis techniques developed to account for the presence of strain are presented in Section 4.4. Strain configurations in all samples studied were measured independently using x-ray diffraction; these measurements are discussed in Section 4.5. The strain-dependent band offset values obtained from our measurements are presented in Section 4.6 and compared to other experimental and theoretical results. In Section 4.7 we discuss the application of our measured band offsets to heterojunctions involving $Si_{1-x}Ge_x$ alloys. We present the interpolation scheme developed to estimate band offset values for heterojunctions involving alloys in Section 4.7.1, and in Section 4.7.2 compare the resulting band offsets for alloys with published results from modulation-doping experiments.

Our conclusions are summarized in Section 4.8.

4.2 Experimental Procedure

Figs. 4.2(a) and (b) show schematic energy-band diagrams for Ge coherently strained to Si (001) and Si coherently strained to Ge (001), respectively. As shown in these figures, the valence-band offset, defined to be the discontinuity in energy between the uppermost valence-band edges in each material, is given by

$$\Delta E_v = (E^{\mathrm{Ge}}_{\mathrm{Ge3}d} - E^{\mathrm{Ge}}_v) + (E^{\mathrm{Si}}_{\mathrm{Si2}p} - E^{\mathrm{Ge}}_{\mathrm{Ge3}d}) - (E^{\mathrm{Si}}_{\mathrm{Si2}p} - E^{\mathrm{Si}}_v). \tag{4.28}$$

The biaxial strain in the Ge layer in Fig. 4.2(a) and in the Si layer in Fig. 4.2(b) produces a splitting of the light-hole, heavy-hole, and split-off valence bands, and in addition can result in a strain-dependent shift in the atomic core-level to valence-band-edge binding energies. This dependence of the core-level binding energies on strain must therefore be included, either experimentally or theoretically, in measurements of both the bulk core-level binding energies and the heterojunction core-level energy separations if one hopes to obtain meaningful results for the valence-band offset. The need to account for these effects in any measurement of band offsets using XPS has been discussed by Tersoff and Van de Walle[61] and by Schwartz et al.[13].

To measure the Si $2p$ and Ge $3d$ core-level to valence-band-edge binding energies as a function of strain, we grew thin films of pure Si and Ge coherently strained to $\mathrm{Si}_{1-x}\mathrm{Ge}_x$ alloy layers of varying composition. Schematic diagrams of prototypical heterostructures that were grown to obtain strained Si and Ge films are shown in Fig. 4.3. For the strained Si films, a 5000 Å, fully relaxed layer of Ge was grown on a Si substrate, followed by a relaxed $\mathrm{Si}_{1-x}\mathrm{Ge}_x$ alloy layer with x ranging from 0.00 to 0.30; a coherently strained Si film was then grown

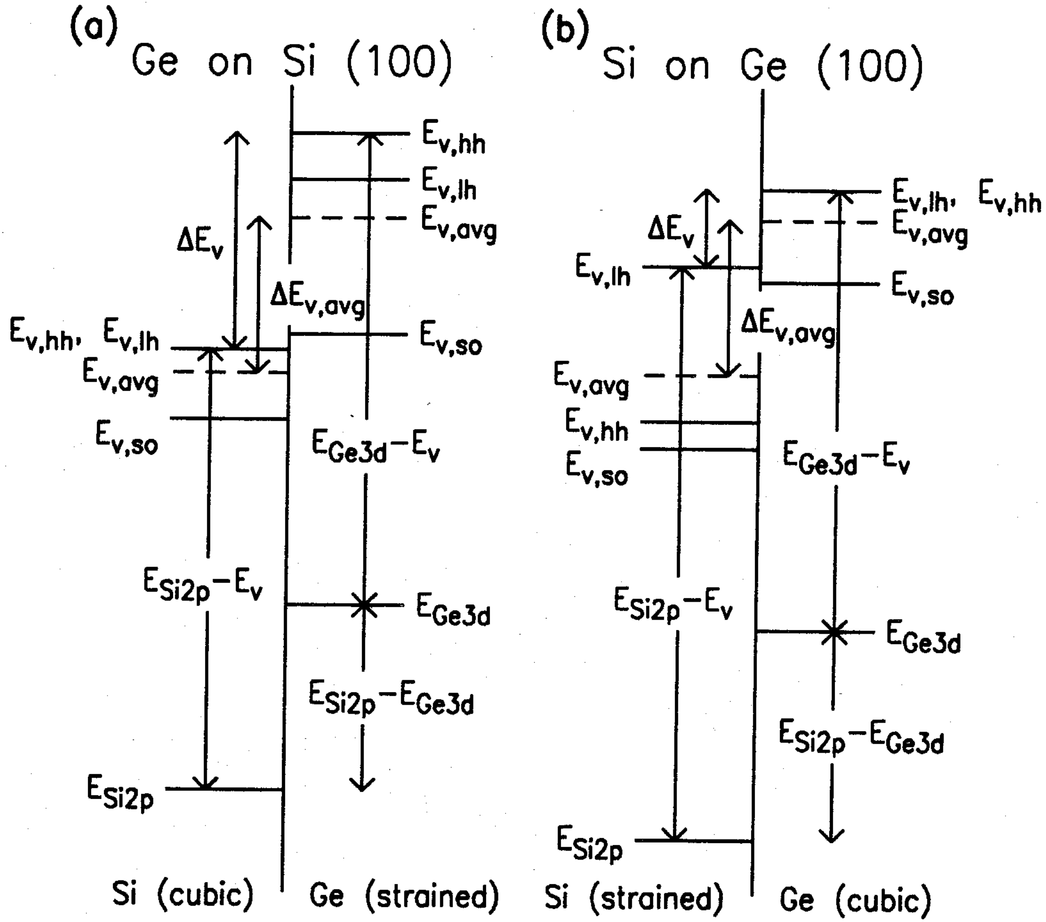

Figure 4.2: Schematic energy-band diagrams for (a) Ge coherently strained to Si ($a_{\|} = 5.431$ Å), and (b) Si coherently strained to Ge ($a_{\|} = 5.658$ Å). Valence-band splittings result from strain and spin-orbit interactions. Weighted averages of the three valence bands in each material are indicated by the dashed lines. As shown in the figure, each of the quantities $(E^{\rm Ge}_{\rm Ge3d} - E^{\rm Ge}_v)$, $(E^{\rm Si}_{\rm Si2p} - E^{\rm Si}_v)$, and $(E^{\rm Si}_{\rm Si2p} - E^{\rm Ge}_{\rm Ge3d})$ is, in principle, a function of strain.

on top of the alloy layer. The initial layer of Ge was grown to ensure that the $Si_{1-x}Ge_x$ alloy layer was fully relaxed. For the strained Ge films, $Si_{1-x}Ge_x$ alloy layers with x ranging from 0.70 to 1.00 were grown directly on a Si substrate; the initial Ge layer was not required because the large lattice mismatch between the alloy layer and the substrate would ensure that the alloy layer was fully relaxed. Thin films of Ge coherently strained to the alloy were then grown. Following the XPS measurements, strain configurations in these films were measured by x-ray diffraction.

The strain dependence of the Si $2p$ to Ge $3d$ heterojunction core-level energy separation was measured by growing a series of Si/Ge superlattices. As shown in Fig. 4.4, each superlattice was grown on a $Si_{1-x}Ge_x$ alloy layer with the same average composition as the superlattice, ensuring that the superlattice would be in its free-standing strain configuration, i.e., the strain configuration that minimized the total strain energy in the superlattice. By varying the individual Si and Ge superlattice layer thicknesses, we were able to obtain superlattices with different in-plane lattice constants, and therefore heterojunctions with different strain configurations. XPS measurements on these samples yielded the Si $2p$ to Ge $3d$ core-level energy separation as a function of strain. Superlattices, rather than single heterojunctions, were grown in order that the strain configurations in these samples could later be confirmed using x-ray-diffraction measurements and the known Si and Ge bulk growth rates.

4.3 Sample Growth

The samples prepared for this study were grown by molecular-beam epitaxy in a Perkin-Elmer 430S Si MBE system. The base pressure in the growth chamber was typically $\sim 8 \times 10^{-11}$ Torr, and growth pressures were typically near

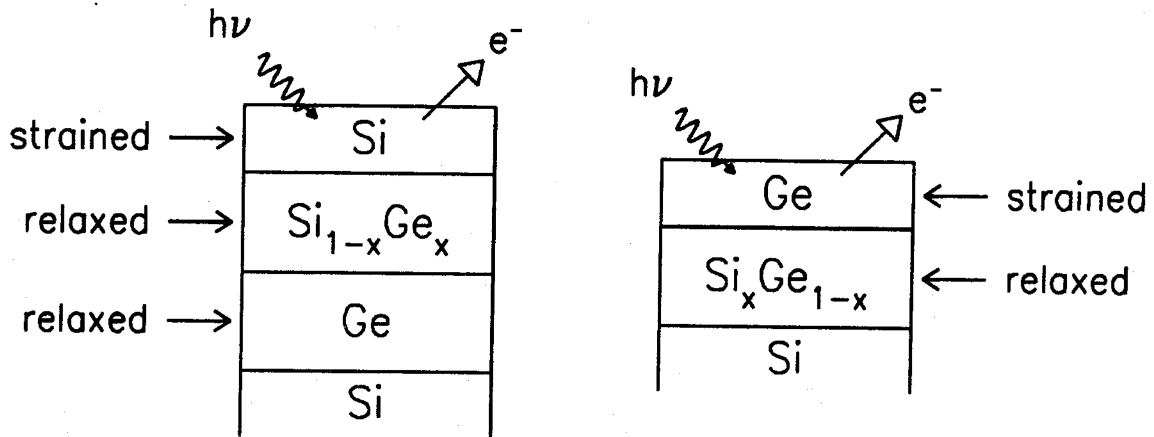

Figure 4.3: Schematic diagrams of heterostructures grown to measure the strain dependence of the Si 2*p* and Ge 3*d* core-level to valence-band-edge binding energies in pure Si and pure Ge, respectively. For the Si films, a fully strain-relaxed layer of Ge was deposited on a Si substrate, followed by a relaxed Si-rich $Si_{1-x}Ge_x$ alloy layer, on top of which a coherently strained layer of Si was grown. For the Ge films, a relaxed Ge-rich $Si_{1-x}Ge_x$ alloy was grown directly on the Si substrate, followed by a coherently strained Ge film. Strain configurations in these samples were confirmed by x-ray-diffraction measurements.

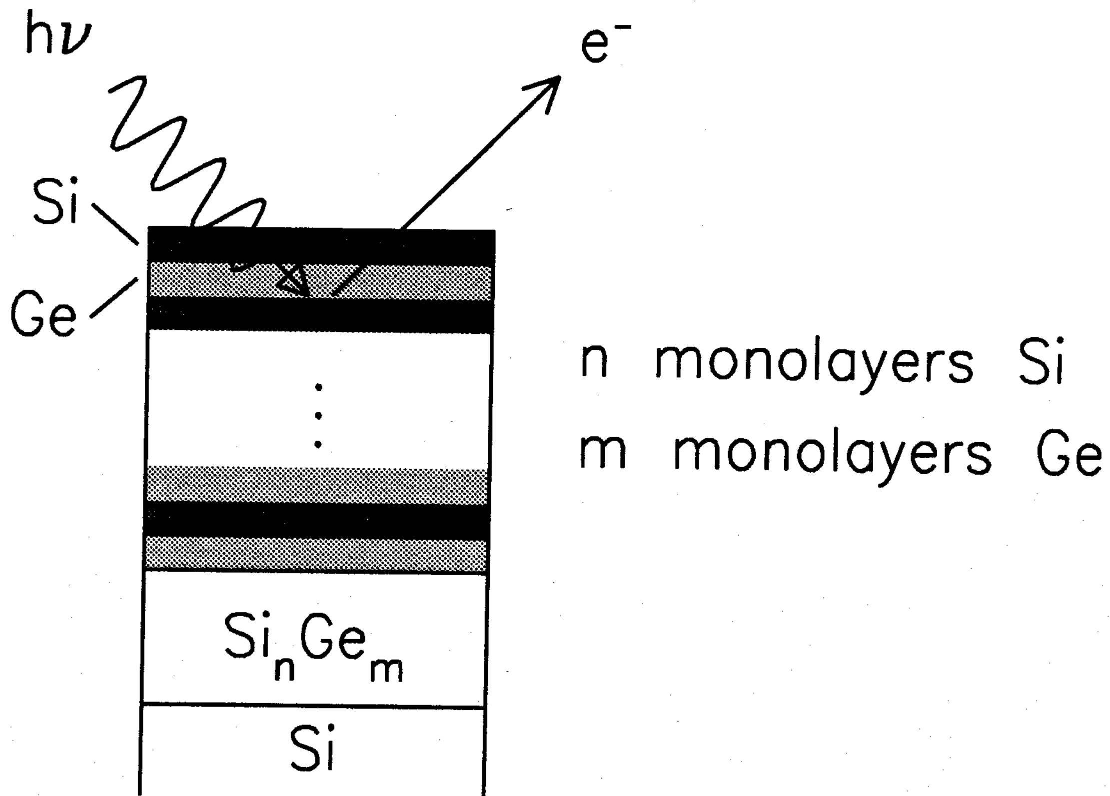

Figure 4.4: Schematic diagram of Si/Ge superlattice samples grown to measure the strain dependence of the Si $2p$ to Ge $3d$ heterojunction core-level energy separation. Si/Ge superlattices were grown on $Si_{1-x}Ge_x$ alloy layers with compositions that were the same as the average composition of the superlattice, ensuring that the superlattices would grow in their free-standing strain configuration. By varying the ratio of the Si and Ge layer thicknesses in the superlattice, we were able to obtain superlattices with different in-plane lattice constants, and therefore heterojunctions with different strain configurations.

2×10^{-9} Torr. Samples were grown on n-type Si (001) substrates (P-doped to 0.02–0.60 Ω·cm). The substrates were degreased at 50–70°C in (1,1,1)-trichloroethane:acetone:methanol and rinsed in deionized water; they were then etched in 1:1 HF:H_2O. The oxide was desorbed by heating the sample to 800°C in a 0.1 Å/s Si flux until a clear (2×1) surface reconstruction pattern was observed using reflection high-energy electron diffraction (RHEED). Following oxide desorption, a 1200 Å Si buffer layer was grown on each substrate as the substrate temperature dropped from 700°C to 530°C to ensure an atomically smooth Si (001) starting surface.

A general strategy involving growth of highly lattice-mismatched interfaces, annealing to help remove dislocations, and low substrate temperatures was developed to obtain samples with the desired strain configurations. To obtain strained Si and Ge films and strained Si/Ge superlattices, it was necessary to grow strain-relaxed $Si_{1-x}Ge_x$ alloy layers with varying composition x to serve as lattice-matched buffer layers upon which coherently strained structures could be grown. To produce relaxed $Si_{1-x}Ge_x$ alloy layers with $x \geq 0.50$, we deposited the alloy layer directly on the Si (001) buffer layer; since the lattice mismatch between the alloy and the Si layer was large (greater than 2.09%), the critical thickness for strain relaxation was small — less than a few hundred Angstroms at most, compared to a typical layer thickness of 5000 Å — and the alloy layer would very quickly relax to its natural lattice constant. The samples were annealed at 700°C for 30 minutes after deposition of the alloy layer in an attempt to reduce the number of dislocations. To produce relaxed alloy layers with $x < 0.50$, we deposited a 5000 Å layer of Ge on the Si (001) buffer layer, which would relax to the natural Ge lattice constant. We would then deposit the $Si_{1-x}Ge_x$ alloy layer on the Ge buffer layer; the lattice mismatch between the alloy and the Ge buffer layer would then be large, ensuring that the alloy layer would relax to its natural

lattice constant rather than grow coherently strained to the Ge layer. For these growths, the samples were annealed at 700 °C for 30 minutes after each layer was grown. Once the relaxed $Si_{1-x}Ge_x$ alloy layers had been grown, we then grew thin films of either Si or Ge coherently strained to the alloy layers, or Si/Ge superlattices with the same average composition, and therefore the same in-plane lattice constant (in the free-standing superlattice configuration), as the alloy.

Three types of samples were grown for this experiment. To measure the Si $2p$ core-level to valence-band-edge binding energy as a function of strain, four samples were grown, each consisting of a 5000 Å layer of Ge grown at 500 °C, followed by a ~5000 Å $Si_{1-x}Ge_x$ alloy layer with x varying from 0.00 to 0.30, also grown at 500 °C; the samples were annealed at 700 °C for 30 minutes after each of these layers was grown, in an attempt to remove misfit dislocations. The alloy layer was followed by a thin (400 to 1000 Å) layer of Si grown at 310 °C. The Ge and $Si_{1-x}Ge_x$ layers were intended to be fully relaxed to their natural lattice constants; the Ge layers were present to allow the $Si_{1-x}Ge_x$ layer to grow on a buffer layer with a large lattice mismatch, and therefore relax fully to its natural lattice constant. The top Si layer was intended to be coherently strained to the in-plane lattice constant of the alloy layer; the Si layer thicknesses were therefore kept well below the critical thickness for strain relaxation[9, 10, 28, 49], and a lower growth temperature was used[11].

To measure the Ge $3d$ core-level to valence-band-edge binding energy as a function of strain, a similar series of five samples was grown. Each sample consisted of a 5000 Å layer of $Si_{1-x}Ge_x$ with x varying from 0.70 to 1.00, grown at 500 °C and annealed at 700 °C for 30 minutes, followed by a thin (400 to 1000 Å) layer of Ge grown at 310 °C. The $Si_{1-x}Ge_x$ layers were intended to be fully relaxed to their natural lattice constants; the intervening Ge layer was not required for these samples, since the alloys were sufficiently Ge-rich to ensure that the critical

thicknesses for strain relaxation were much less than the 5000 Å film thickness. The top Ge layer was intended to be coherently strained to the in-plane lattice constant of the alloy layer. The sample structures used to produce strained Si and Ge films are described in Table 4.1.

The strain dependence of the Si $2p$ and Ge $3d$ heterojunction core-level energy separation was obtained from measurements on pure Si/Ge (001) superlattices of varying composition coherently strained to relaxed $Si_{1-x}Ge_x$ alloy layers with compositions the same as the average composition of the superlattice. This scheme ensured that the superlattices were grown in their free-standing strain configuration. Each sample consisted of a 2000 Å Si/Ge superlattice grown at 310 °C, on top of a 5000 Å $Si_{1-x}Ge_x$ alloy layer, grown at 500 °C. The Si-rich alloys ($x<0.50$) were grown on top of a 5000 Å layer of Ge, grown at 500 °C, to help ensure that the alloy layers were fully relaxed; the Ge-rich alloy layers were grown directly on the Si buffer layer. Superlattice sample characteristics are summarized in Table 4.2.

4.4 XPS Measurements and Data Analysis

XPS measurements were obtained using a Perkin-Elmer Model 5100 analysis system with a monochromatic Al $K\alpha$ x-ray source ($h\nu = 1486.6$ eV). The analysis chamber is connected to the Si MBE growth chamber via an ultrahigh vacuum transfer tube, allowing samples to be grown and characterized without being exposed to atmosphere. This capability was especially important for this study, since unprotected exposure to atmosphere and the resulting oxide formation, or capping with a surface passivation layer followed by heating to evaporate the passivating layer, could have had a substantial influence on the strain configurations in these samples. Representative XPS spectra from bulk Si, bulk Ge, and Si/Ge

Sample	5000 Å Ge buffer layer	$Si_{1-x}Ge_x$ alloy buffer layer	Strained Si layer thickness	Strained Ge layer thickness
88.005	no	5000 Å Si		
88.022	yes	5500 Å $Si_{0.91}Ge_{0.09}$	1000 Å	
88.023	yes	5100 Å $Si_{0.81}Ge_{0.19}$	500 Å	
89.058	yes	5000 Å $Si_{0.72}Ge_{0.28}$	400 Å	
88.003	no	5000 Å Ge		
89.026	no	5000 Å $Si_{0.04}Ge_{0.96}$		1000 Å
89.027	no	5000 Å $Si_{0.16}Ge_{0.84}$		500 Å
89.030	no	5000 Å $Si_{0.26}Ge_{0.74}$		500 Å
89.059	no	5000 Å $Si_{0.30}Ge_{0.70}$		400 Å

Table 4.1: Summary of sample structures grown to obtain strained Si and Ge films to measure the strain dependence of the Si $2p$ and Ge $3d$ core-level to valence-band-edge binding energies. For the strained Si films, the structures consisted of a 5000 Å strain-relaxed layer of Ge grown on a Si (001) substrate, followed by ~5000 Å of $Si_{1-x}Ge_x$ with x ranging from 0.00 to 0.30, on top of which were grown 400–1000 Å of Si coherently strained to the alloy layer. For the strained Ge films, the structures consisted of 5000 Å of a $Si_{1-x}Ge_x$ alloy with x ranging from 0.70 to 1.00, on top of which were grown 400–1000 Å of Ge coherently strained to the alloy layer.

Sample	Layer thicknesses (Si/Ge) (Å)	Periods	$Si_{1-x}Ge_x$ alloy buffer layer	5000 Å Ge buffer layer
89.050	20/30	40	$Si_{0.41}Ge_{0.59}$	no
89.052	30/20	40	$Si_{0.60}Ge_{0.40}$	yes
89.053	60/20	25	$Si_{0.76}Ge_{0.24}$	yes
89.055	20/60	25	$Si_{0.24}Ge_{0.76}$	no

Table 4.2: Si/Ge (001) superlattice sample characteristics. Si/Ge superlattices with different in-plane lattice constants were grown to measure the strain dependence of the Si $2p$ to Ge $3d$ heterojunction core-level energy separation. The total thickness of each superlattice was ~2000 Å, and all superlattices were grown on alloy layers whose composition was the same as the average superlattice composition, ensuring that the superlattices were grown in their free-standing strain configurations. By varying the ratios of the Si and Ge superlattice layer thicknesses, we obtained superlattices with different strain configurations, and therefore heterojunctions with different in-plane lattice constants.

superlattice samples are shown in Figs. 4.5(a), (b), and (c), respectively. The discontinuities in the spectra at 4 eV binding energy in Figs. 4.5(a) and (b) are due to the longer sampling times used near the valence band edge; the valence band spectra for these samples are also shown on enlarged scales, as indicated in the figures.

Core-level peak positions were obtained by subtracting from each core-level peak a background function proportional to the integrated photoelectron intensity, and defining the peak position to be the midpoint of the two energies at which the intensity was half the maximum intensity. The uncertainty in measured core-level energy separations was estimated to be ± 0.02 eV, and measurements of core-level energy separations were typically reproducible to better than ± 0.01 eV. The position of the valence-band edge in each XPS spectrum was determined using the precision analysis technique of Kraut et al.[62], modified to include effects due to strain on the valence band density of states. In this approach, the XPS spectrum near the valence-band edge is modeled as a convolution of a theoretical valence-band density of states with an experimentally determined XPS instrumental resolution function. This model function is then fitted to the experimental data to give the position of the valence-band edge. Typical XPS valence-band spectra, model curves fitted to the data, and calculated valence-band densities of states for unstrained Si and Ge are shown in Figs. 4.6(a) and (b), respectively. The uncertainty in core-level to valence-band-edge binding energies was taken to be ± 0.04 eV; for a given sample, however, measurements were typically reproducible to ± 0.01 eV.

To apply the method of Kraut et al.[62] to coherently strained heterojunction systems, it was necessary to calculate theoretical valence-band densities of states for strained Si and Ge films. The valence-band densities of states for Si and Ge were calculated using the empirical pseudopotential method[63]; spin-

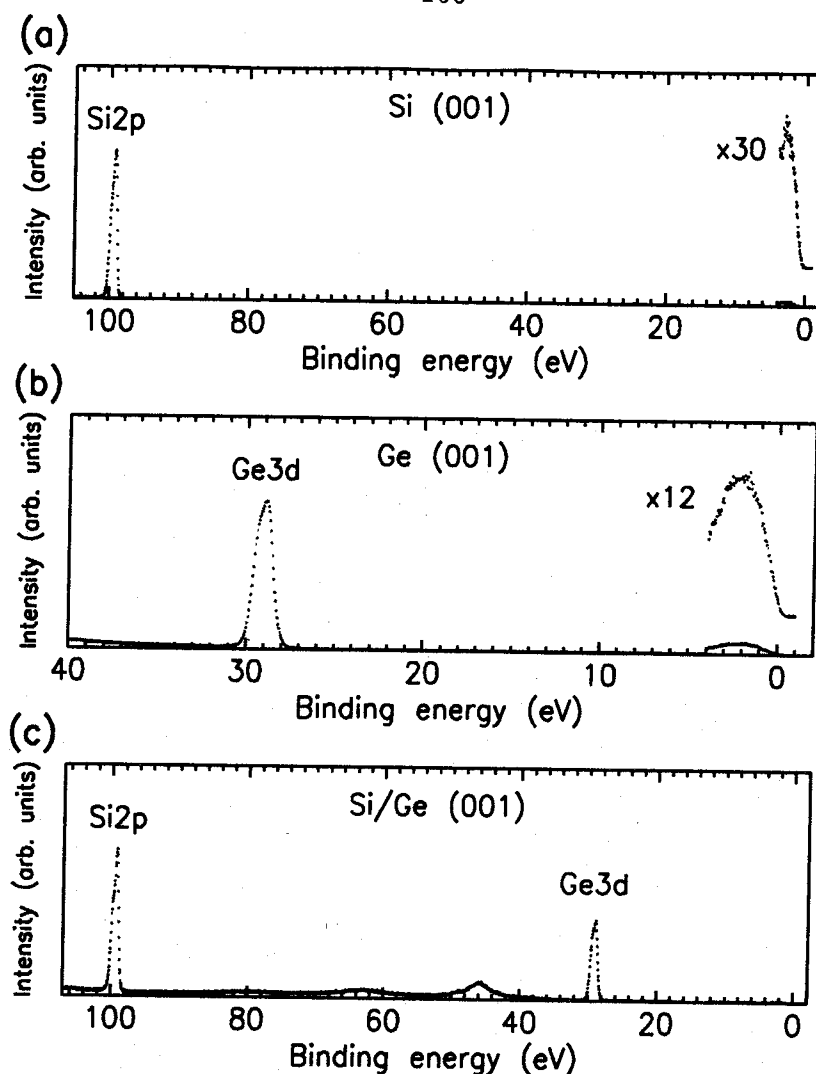

Figure 4.5: Representative binding energy XPS spectra for (a) Si (001) samples, (b) Ge (001) samples, and (c) Si/Ge (001) superlattices. The Si $2p$ core-level to valence-band-edge binding energy is measured in the Si (001) samples, the Ge $3d$ core-level to valence-band-edge binding energy in the Ge (001) samples, and the Si $2p$ to Ge $3d$ heterojunction core-level energy separation in the Si/Ge (001) superlattices. The discontinuities in the spectra in (a) and (b) are due to longer sampling times used in the vicinity of the valence bands. The valence-band spectra for the bulk Si and Ge samples are also shown on enlarged intensity scales, as indicated in the figures.

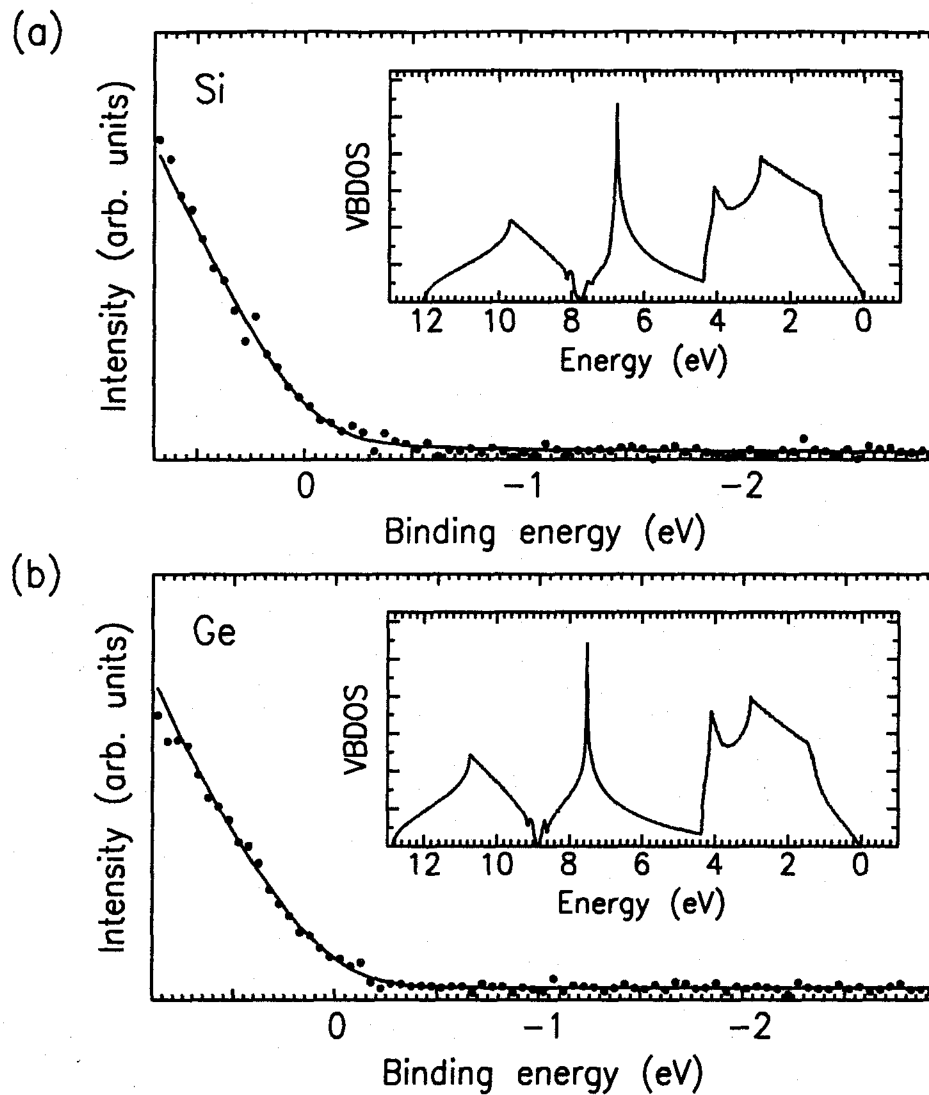

Figure 4.6: Typical XPS valence-band spectra and model functions fitted to the experimental data for (a) unstrained Si (001) and (b) unstrained Ge (001). The theoretical valence-band densities of states used to construct the model functions are shown in the insets to each figure. These model functions are used to determine the position of the valence-band edge in each spectrum.

orbit interactions[64] and a nonlocal effective mass parameter[65] were included in these calculations. Strain effects were included in the densities of states by performing a Pikus-Bir transformation on the Hamiltonian[66], and fitting the resulting splitting of the valence bands to known deformation potentials for Si and Ge[67].

The empirical pseudopotential method is derived from the augmented plane wave (APW)[68] and orthogonalized plane-wave (OPW)[69] methods for calculating electronic structure. A conceptually simple approach for calculating electronic band structure is to write the crystal potential $V(\mathbf{r})$ as a superposition of atomic potentials $v(\mathbf{r})$,

$$V(\mathbf{r}) = \sum_j v(\mathbf{r} - \mathbf{r}_j), \tag{4.29}$$

and to expand the electron wave function in a plane-wave basis $\{|\mathbf{k}\rangle\}$:

$$\psi(\mathbf{r}) = \sum_{\mathbf{k}} c_{\mathbf{k}} |\mathbf{k}\rangle. \tag{4.30}$$

Inserting Eqs. (4.29) and (4.30) into Schrödinger's equation yields a secular equation for the coefficients $c_{\mathbf{k}}$,

$$\frac{\hbar^2}{2m} k^2 c_{\mathbf{k}} + \sum_{\mathbf{k}'} \langle \mathbf{k}|V|\mathbf{k}'\rangle c_{\mathbf{k}'} = E c_{\mathbf{k}}. \tag{4.31}$$

Because of the periodicity of the crystal lattice, one need consider only values of $\mathbf{k}$ and $\mathbf{k}'$ such that $\mathbf{k} - \mathbf{k}' = \mathbf{G}$, where $\mathbf{G}$ is a reciprocal lattice vector of the crystal. Unfortunately, the presence of strong atomic core potentials in $V(\mathbf{r})$ make it necessary to use an extremely large plane wave basis set $\{|\mathbf{k}\rangle\}$, since plane waves with large $\mathbf{k}$ are required to construct the rapidly oscillating wave functions near the atomic cores.

The orthogonalized plane-wave method was developed to circumvent this difficulty. The OPW method is based on the requirement that the band states be

orthogonal to the atomic core states. One can therefore replace the pure plane-wave basis set with an alternate basis $\{|OPW_{\mathbf{k}}\rangle\}$ that is orthogonal to the atomic core-level wavefunctions $|t,j\rangle = \psi_t(\mathbf{r}-\mathbf{r_j})$, i.e.,

$$|OPW_{\mathbf{k}}\rangle = |\mathbf{k}\rangle - \sum_{t,j} |t,j\rangle\langle t,j|\mathbf{k}\rangle. \tag{4.32}$$

The rapid oscillations in the band wave functions will then be contained in the basis elements themselves rather than being constructed explicitly, reducing the number of basis elements needed to obtain an accurate representation of the wave functions.

The pseudopotential method can be considered as an extension of the OPW method. Our discussion of the pseudopotential follows that of Harrison[70]; a number of other extremely detailed references on pseudopotentials are also available[71, 72, 73]. The electron eigenstates ψ in a crystal satisfy the Schrödinger equation,

$$-\frac{\hbar^2}{2m}\nabla^2\psi + V(\mathbf{r})\psi = E\psi. \tag{4.33}$$

The OPW basis elements given by Eq. (4.32) can be rewritten in terms of an atomic core-level projection operator $P = \sum_{t,j} |t,j\rangle\langle t,j|$,

$$|OPW_{\mathbf{k}}\rangle = (1-P)|\mathbf{k}\rangle, \tag{4.34}$$

and the electron wave function ψ can then be expanded in the OPW basis,

$$\psi = \sum_{\mathbf{k}} a_{\mathbf{k}}(1-P)|\mathbf{k}\rangle \tag{4.35}$$

$$= (1-P)\sum_{\mathbf{k}} a_{\mathbf{k}}|\mathbf{k}\rangle \tag{4.36}$$

$$\equiv (1-P)\phi, \tag{4.37}$$

where $\phi \equiv \sum_{\mathbf{k}} a_{\mathbf{k}}|\mathbf{k}\rangle$ is the pseudowave function. Because of the rapid convergence of the OPW expansion, the pseudowave function ϕ can be constructed

from a relatively small number of plane waves and is therefore quite smooth; the rapid oscillations generated by the atomic core potentials are produced by the operator $(1 - P)$ that converts the pseudowave function into the true electron wave function.

Substituting the pseudowave function expansion, Eq. (4.37), into Eq. (4.33) eventually yields

$$-\frac{\hbar^2}{2m}\nabla^2\phi + V_{ps}\phi = E\phi, \tag{4.38}$$

where

$$V_{ps} = V(\mathbf{r}) + \sum_{t,j}(E - E_{t,j})|t,j\rangle\langle t,j|; \tag{4.39}$$

we have used the fact that the atomic core levels $|t,j\rangle$ are eigenstates of the crystal Hamiltonian with eigenvalues $E_{t,j}$ to obtain Eqs. (4.38) and (4.39).

The smoothness of the pseudowave function ϕ would lead one to expect that the pseudopotential V_{ps} should be small. In fact, one can show that this is true. The atomic core potentials $v(\mathbf{r}-\mathbf{r}_j)$ are attractive and therefore negative, meaning that $V(\mathbf{r})$ will also be negative. The energy difference $(E - E_{t,j})$ is positive, as is, in some sense, the projection operator, meaning that the first and second terms in Eq. (4.39) will yield contributions of opposite sign to the pseudopotential V_{ps}. This result is known as the cancellation theorem[71].

An examination of Eq. (4.39) reveals that the true pseudopotential is energy-dependent and nonlocal (because of the projection operator). However, it has been found that many characteristics of the electronic band structure in semiconductors can be explained without accounting for the energy dependence of the pseudopotential[63], and that nonlocal effects can be approximated by introducing a variable electron effective mass, m^*[65]. With these approximations, the pseudopotential Hamiltonian may be written

$$H = -\frac{\hbar^2}{2m^*}\nabla^2 + V(\mathbf{r}). \tag{4.40}$$

The pseudopotential $V(\mathbf{r})$ has the same periodicity as the crystal, and can therefore be expanded in reciprocal lattice vectors $\mathbf{G}$. For a cubic zincblende crystal, this expansion yields a pseudopotential

$$V(\mathbf{r}) = \sum_{\mathbf{G}} \left[V^S(\mathbf{G}) \cos \mathbf{G} \cdot \tau + i V^A(\mathbf{G}) \sin \mathbf{G} \cdot \tau \right] e^{-i\mathbf{G}\cdot\mathbf{r}}, \tag{4.41}$$

where $\tau = \frac{1}{8}a(1,1,1)$, a being the cubic lattice constant of the crystal. The symmetric and antisymmetric pseudopotential form factors V^S and V^A can be expressed in terms of the cation and anion local atomic pseudopotentials $V_c(\mathbf{r})$ and $V_a(\mathbf{r})$,

$$V^S(\mathbf{G}) = \frac{1}{2}(V_c(\mathbf{G}) + V_a(\mathbf{G})), \tag{4.42}$$

$$V^A(\mathbf{G}) = \frac{1}{2}(V_c(\mathbf{G}) - V_a(\mathbf{G})), \tag{4.43}$$

where

$$V_c(\mathbf{G}) = \frac{1}{\Omega} \int V_c(\mathbf{r}) e^{-i\mathbf{G}\cdot\mathbf{r}} d^3r, \tag{4.44}$$

$$V_c(\mathbf{G}) = \frac{1}{\Omega} \int V_c(\mathbf{r}) e^{-i\mathbf{G}\cdot\mathbf{r}} d^3r. \tag{4.45}$$

For the diamond structure, $V_c(\mathbf{r}) = V_a(\mathbf{r})$ and therefore $V^A(\mathbf{G}) = 0$. If we assume that the pseudopotentials $V_c(\mathbf{r})$ and $V_a(\mathbf{r})$ are spherical, the pseudopotential form factors depend only on the magnitude of $\mathbf{G}$, i.e., $V^S(\mathbf{G}) = V^S(G)$ and $V^A(\mathbf{G}) = V^A(G)$.

Spin-orbit interactions may also be incorporated using the method of Saravia and Brust[64]. The large spin-orbit splitting in Ge ($\Delta_0 = 0.29$ eV) made it necessary to include this effect. Very briefly, the Hamiltonian for the spin-orbit interaction is

$$H^{s.o.} = \frac{\hbar}{4m^{*2}c^2}(\nabla V(\mathbf{r}) \times \mathbf{p} \cdot \sigma), \tag{4.46}$$

where $\mathbf{p}$ is the momentum operator and σ is the Pauli spin operator. Various investigators have shown[74, 75, 76] that the spin-orbit Hamiltonian, Eq. (4.46),

can be written in the form

$$H^{s.o.}_{\mathbf{G},\mathbf{G}'}(\mathbf{k}) = ((\mathbf{k}+\mathbf{G})\times(\mathbf{k}+\mathbf{G}'))\cdot\sigma_{s,s'}\times \left\{-i\lambda^S\cos\left[(\mathbf{G}-\mathbf{G}')\cdot\tau\right]+\lambda^A\sin\left[(\mathbf{G}-\mathbf{G}')\cdot\tau\right]\right\}, \quad (4.47)$$

where the symmetric and antisymmetric spin-orbit coefficients λ^S and λ^A each depend on $\mathbf{k}$, $\mathbf{G}$, $\mathbf{G}'$, and an adjustable parameter that is fitted to give the correct spin-orbit splitting at the Γ point. For semiconductors with the diamond structure, such as Si and Ge, $\lambda^A = 0$. The terms from Eqs. (4.40), (4.41), and (4.47) are then combined to yield the pseudopotential Hamiltonian for an unstrained crystal,

$$H_{\mathbf{G},\mathbf{G}'}(\mathbf{k}) = \frac{\hbar^2}{2m^*}(\mathbf{k}+\mathbf{G})^2\delta_{\mathbf{G},\mathbf{G}'} + V(|\mathbf{G}-\mathbf{G}'|) + H^{s.o.}_{\mathbf{G},\mathbf{G}'}(\mathbf{k}). \quad (4.48)$$

The basis states in the pseudopotential method are taken to be plane waves with wave vector $\mathbf{G}+\mathbf{k}$. All reciprocal lattice vectors $\mathbf{G}$ such that $|\mathbf{G}| < G_{\max}$ are included in this basis set. For our calculations, we have taken $G_{\max} = \sqrt{19}(2\pi/a)$; with spin degeneracy included, this yields a basis set with 178 elements.

To determine the actual values of the pseudopotential form factors, we have optimized the agreement between our calculated critical-point energies and those obtained using nonlocal pseudopotential calculations[74], which in turn had been optimized to agree with critical-point energies measured by techniques such as x-ray and ultraviolet photoelectron spectroscopy and optical reflectivity. The pseudopotential form factors were allowed to be nonzero only for $G < \sqrt{11}(2\pi/a)$; it is well known by now that only a few terms in the pseudopotential are necessary to obtain very good results. For Si and Ge, only $V^S(3)$, $V^S(8)$, and $V^S(11)$ needed to be determined; $V^S(0)$ is merely a constant energy added to the pseudopotential and was therefore taken to be zero. In addition to these three form factors, the spin-orbit coupling parameter and electron effective mass were optimized to obtain the best agreement with the results of Chelikowsky and Cohen[74].

Once the band structure was obtained for the unstrained crystals, it was necessary to calculate the effect of strain on the valence-band structure. This was done by performing a Pikus-Bir transformation on the Hamiltonian, Eq. (4.48), following the method of Saravia and Brust[66]. In this method, the coordinate system r'_i of the strained crystal is transformed to an undistorted coordinate system r_i using the strain tensor ϵ_{ij}:

$$
\begin{aligned}
r'_i &= (\delta_{ij} + \epsilon_{ij}) r_j, && (4.49)\\
\partial'_i &= (\delta_{ij} - \epsilon_{ij}) \partial_j, && (4.50)\\
\partial'_i \partial'_i &= \partial_i \partial_i - 2\epsilon_{ij} \partial_i \partial_j, && (4.51)\\
k'_i &= (\delta_{ij} - \epsilon_{ij}) k_j, && (4.52)\\
G'_i &= (\delta_{ij} - \epsilon_{ij}) G_j, && (4.53)\\
V(|\mathbf{G}'|) &= V(|\mathbf{G}' - \epsilon \cdot \mathbf{G}|) && (4.54)\\
&\approx V(G) + (|\mathbf{G}' - \epsilon \cdot \mathbf{G}| - G) \frac{dV(G)}{dG}, && (4.55)
\end{aligned}
$$

where a sum is taken over repeated indices. The Pikus-Bir transformation therefore yields three additional adjustable parameters that are used to fit the known deformation potentials in Si and Ge — $dV^S(3)/dG$, $dV^S(8)/dG$, and $dV^S(11)/dG$. Once these parameters have been determined, one is able to calculate the valence-band structure for Si and Ge under biaxial strain. The valence-band density of states can then be calculated by performing an integration over the entire Brillouin zone, using a standard Gilat-Raubenheimer integration scheme over the irreducible wedge (1/48) of the Brillouin zone[77, 78].

4.5 X-Ray Diffraction Measurements

An essential component of the band offset measurement was an independent determination of the strain configurations in each sample. We therefore per-

formed x-ray rocking-curve measurements on the strained Si and Ge samples to determine the in-plane and growth-direction lattice constants for each sample, and obtained $\theta/2\theta$ x-ray diffraction measurements for the Si/Ge superlattice samples. The measured values of the in-plane and growth-direction lattice constants in each sample were the actual ones used to calculate the valence-band densities of states used in the final analyses of the XPS data, and were also used to determine the Si $2p$ and Ge $3d$ core level to valence-band-edge binding energies and Si $2p$ to Ge $3d$ heterojunction core-level energy separations as functions of strain.

X-ray rocking-curve measurements were performed on the strained Si and Ge samples using a Blake Industries high-resolution x-ray diffractometer equipped with a Philips four-crystal monochromator. Rocking-curve measurements were obtained for the (422) reflection, allowing both the growth-direction and in-plane lattice constants of the relaxed alloy layers and the strained Si and Ge layers to be determined. The x-ray diffraction spectra indicated that the alloy layers were always nearly fully relaxed, and that on average, approximately 81% of the lattice mismatch between the pure Si or Ge layers and the underlying alloy was accommodated by strain. Fig. 4.7 shows (422) rocking-curve x-ray diffraction spectra from sample 89.059, consisting of 400 Å Ge coherently strained to a relaxed, 5000 Å $Si_{0.30}Ge_{0.70}$ alloy layer.

The strain configurations in the superlattice samples were determined from $\theta/2\theta$ x-ray diffraction measurements. The diffraction spectra contained (400)-like superlattice peaks, from which the superlattice period and average composition were deduced. Fig. 4.8 shows a $\theta/2\theta$ x-ray diffraction spectrum from sample 89.055, consisting of a 25 period, 20 Å Si/60 Å Ge superlattice grown on a $Si_{0.24}Ge_{0.76}$ buffer layer. As shown in the figure, the peaks from the Si substrate and $Si_{0.24}Ge_{0.76}$ alloy layer are clearly visible, as are several superlattice peaks.

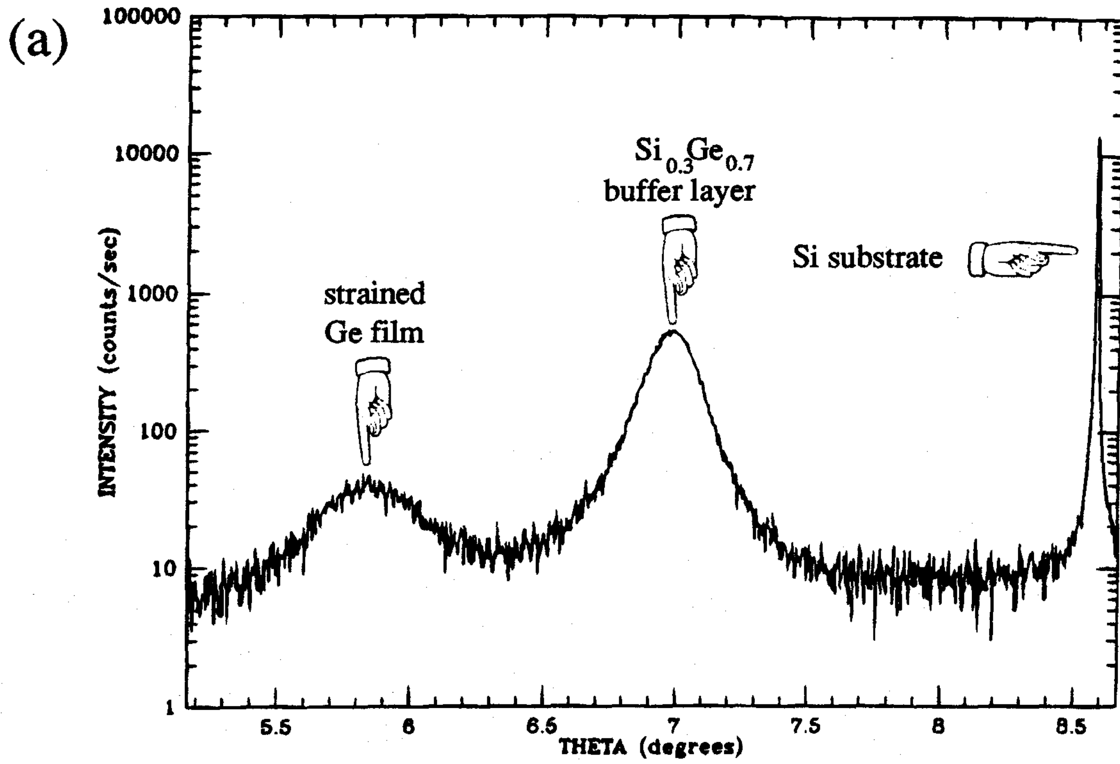
(a)
100000
10000
1000
100
10
1
INTENSITY (counts/sec)
5.5
6
6.5
7
7.5
8
8.5
THETA (degrees)
strained
Ge film
$Si_{0.3}Ge_{0.7}$
buffer layer
Si substrate

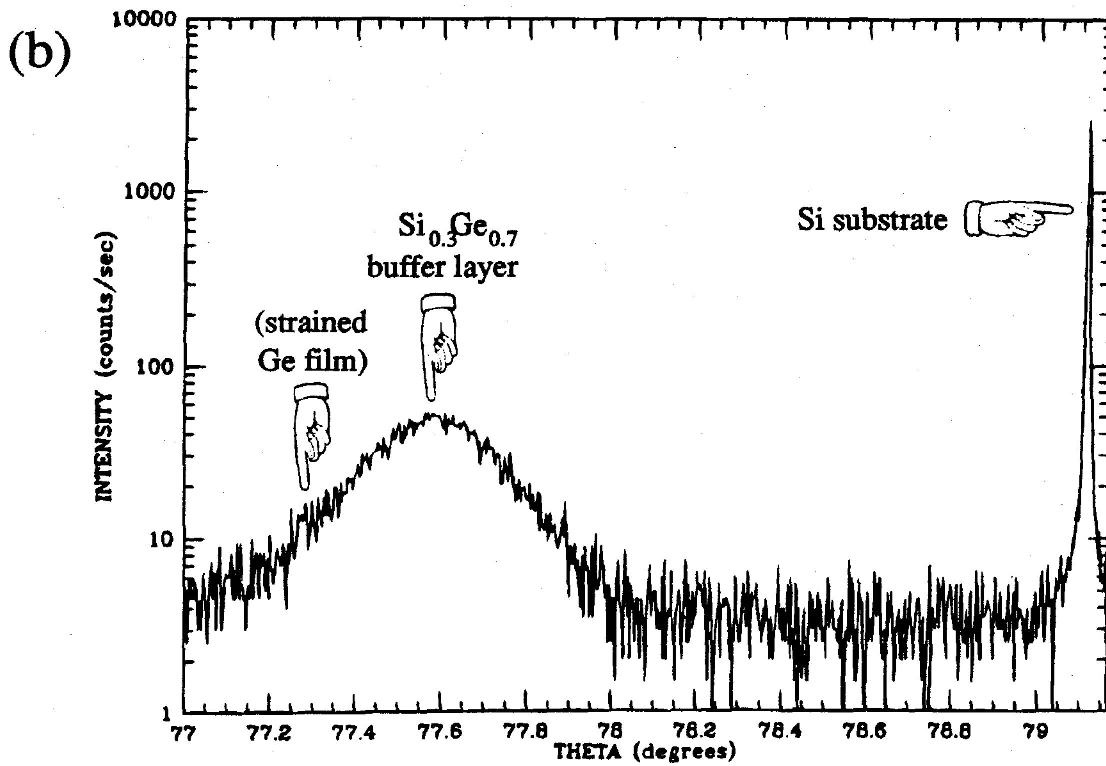
(b)
10000
1000
100
10
1
INTENSITY (counts/sec)
77
77.2
77.4
77.6
77.8
78
78.2
78.4
78.6
78.8
79
THETA (degrees)
(strained
Ge film)
$Si_{0.3}Ge_{0.7}$
buffer layer
Si substrate

Figure 4.7: High-resolution (422) x-ray rocking-curve spectra from sample 89.059, consisting of 400 Å Ge coherently strained to a relaxed, 5000 Å $Si_{0.30}Ge_{0.70}$ alloy layer. For the low-angle spectrum (a), peaks from the Si substrate, $Si_{0.30}Ge_{0.70}$ alloy layer, and strained Ge film are clearly visible. For the high-angle spectrum (b), peaks from the substrate and alloy buffer layer are present. The peak from the strained Ge film is too small to be seen; the label indicates the expected position of the peak. Measurements of this type on samples with strained Si and Ge films allowed us to determine the in-plane and growth-direction lattice constants of the strained layers and of the underlying alloy layers in each sample.

The spacing of the superlattice peaks yields the superlattice period, and, assuming that the superlattice is coherently strained, the average composition can also be deduced. This information, combined with the known growth rates for the individual Si and Ge layers in the superlattice, was consistent with the superlattices being coherently strained to the underlying alloy layers.

4.6 Results and Discussion

The XPS measurements of Si $2p$ and Ge $3d$ core-level to valence-band-edge binding energies and of Si $2p$ to Ge $3d$ heterojunction core-level energy separations and the independent determination of strain configurations in each sample by x-ray diffraction allowed us to determine the core-level to valence-band-edge binding energies and core-level energy separations as functions of the in-plane lattice constant. The Si $2p$ core-level to valence-band-edge binding energies, Ge $3d$ core-level to valence-band-edge binding energies, and Si $2p$ to Ge $3d$ heterojunction core-level energy separations as functions of the in-plane lattice constant $a_{\parallel}$ have been plotted in Figs. 4.9(a), (b), and (c), respectively. The straight lines in each figure were obtained from least-squares fits to the plotted data points. The core-level binding energies and core-level energy separations were found to be

$$E_{\mathrm{Si}2p}^{\mathrm{Si}} - E_{v}^{\mathrm{Si}} = 98.95 + 1.96(a_{\parallel} - 5.431), \quad (4.56)$$

$$E_{\mathrm{Ge}3d}^{\mathrm{Ge}} - E_{v}^{\mathrm{Ge}} = 29.41 - 1.24(a_{\parallel} - 5.658), \quad (4.57)$$

$$E_{\mathrm{Si}2p}^{\mathrm{Si}} - E_{\mathrm{Ge}3d}^{\mathrm{Ge}} = 70.09 + 0.526(a_{\parallel} - 5.431), \quad (4.58)$$

where energies are in eV and $a_{\parallel}$ is in Å. For the strained Si and Ge films, $a_{\parallel}$ was determined directly from x-ray diffraction measurements; the superlattices were assumed to be coherently strained to the alloy layers, in accord with the $\theta/2\theta$ x-ray diffraction measurements previously described.

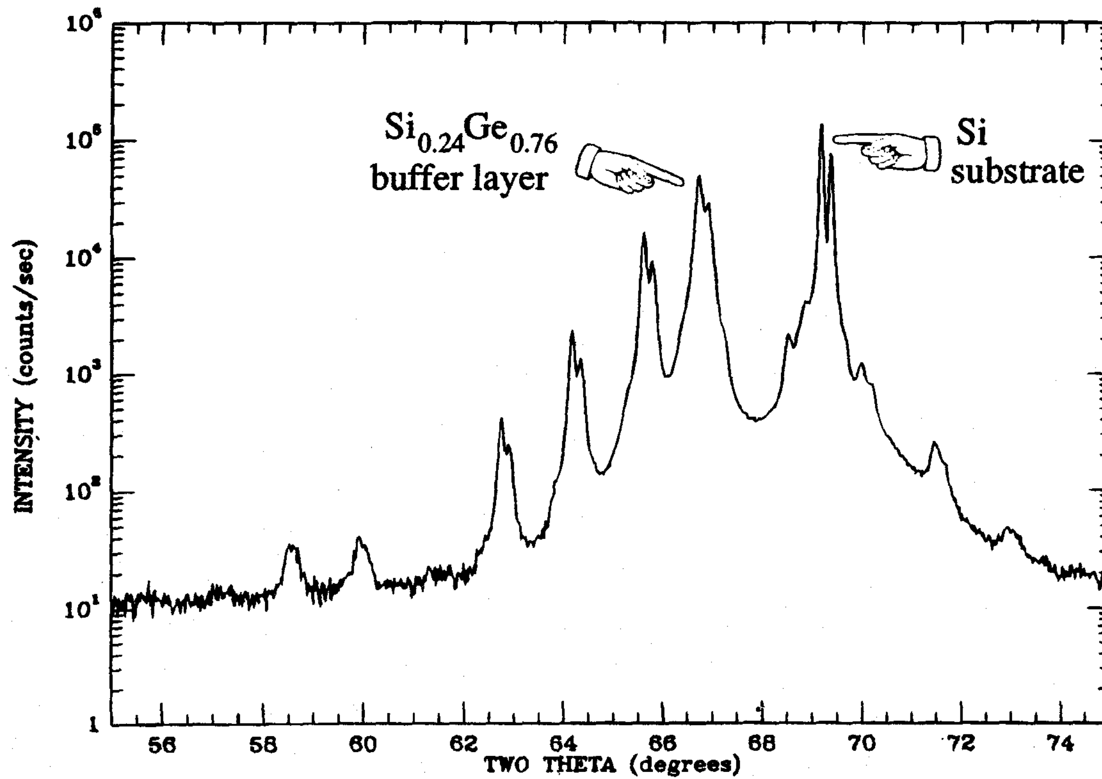

Figure 4.8: A $\theta/2\theta$ x-ray diffraction spectrum from sample 89.055, consisting of a 25 period, 20 Å Si/60 Å Ge superlattice grown on a $Si_{0.24}Ge_{0.76}$ buffer layer. The peaks from the Si substrate and the $Si_{0.24}Ge_{0.76}$ alloy layer are clearly visible, as are several superlattice peaks. The spacing of the superlattice peaks yields the superlattice period, and, assuming that the superlattice is coherently strained, the average composition can also be deduced. This information, combined with the known growth rates for the Si and Ge layers in the superlattice, was for all superlattice samples consistent with the superlattices being coherently strained to the underlying alloy layers.

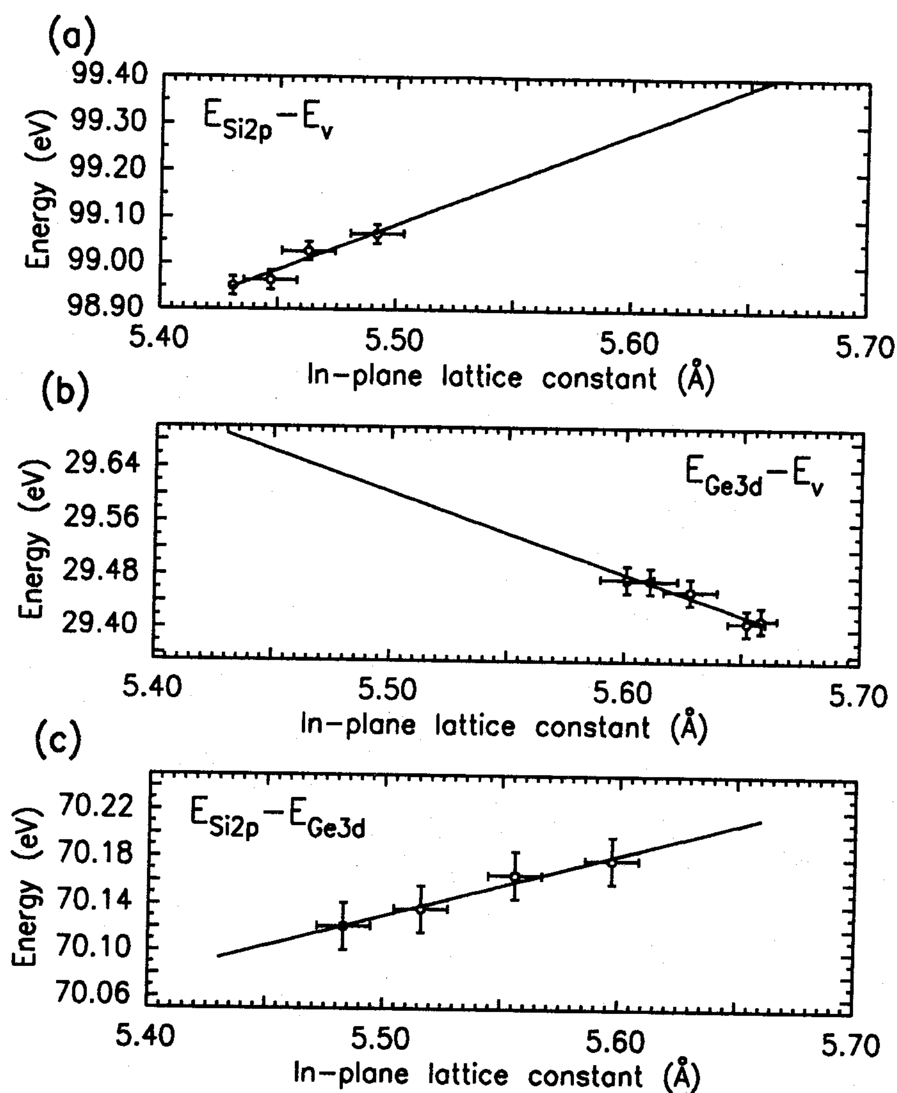

Figure 4.9: Core-level to valence-band-edge binding energies as a function of the in-plane lattice constant for (a) the Si $2p$ core level in strained Si (001), and (b) the Ge $3d$ core level in strained Ge (001). The Si $2p$ to Ge $3d$ heterojunction core-level energy separation as a function of the in-plane lattice constant in Si/Ge (001) superlattices is shown in (c). The valence-band offset in strained Si/Ge (001) heterojunctions can be obtained from these three quantities.

Combining the results from Eqs. (4.56), (4.57), and (4.58), we obtain valence-band offsets of 0.83 ± 0.11 eV and 0.22 ± 0.13 eV for Ge coherently strained to Si (001) ($a_{||} = 5.431$ Å) and Si coherently strained to Ge (001) ($a_{||} = 5.658$ Å), respectively. Uncertainties in the strain-dependent core-level to valence-band-edge binding energies and in the heterojunction core-level energy separations were determined in the least-squares linear fitting procedure, assuming uncertainties of ± 0.02 eV in binding energy measurements between samples, and an uncertainty of approximately ± 0.01 Å in $a_{||}$ for each sample. An additional uncertainty of ± 0.04 eV was estimated for the core-level to valence-band-edge binding energies, independent of strain. These uncertainties were added in quadrature to obtain the total uncertainty in the valence-band offsets.

If we assume that the offset between the weighted averages of the light-hole, heavy-hole, and split-off valence bands is independent of strain[12], we obtain a discontinuity in the average valence-band edge of 0.49 ± 0.13 eV. Within the uncertainties of our measurement, our results are not inconsistent with the hypothesis that the discontinuity in the average position of the three valence bands is approximately independent of strain.

The values obtained for the valence-band offset are in fairly good agreement with the calculations of Van de Walle and Martin[12], who report values of 0.84 eV for Ge on Si (001), and 0.31 eV for Si on Ge (001). In another XPS experiment, Schwartz et al.[13] calculated strain shifts in the core-level binding energies and measured core-level energy separations in strained Ge on Si (001) and Si on Ge (001), obtaining valence-band offsets of 0.74 ± 0.13 eV and 0.17 ± 0.13 eV for the two cases, respectively. The strain dependence of their band offsets agrees well with our observations, although the actual band offset values are shifted by approximately 0.1 eV. Several experiments have also been performed to measure band offsets for heterojunctions in which the strain configuration was unknown,

and in which a substantial number of dislocations may have been present. Kuech et al.[79] obtained $\Delta E_v = 0.39 \pm 0.04$ eV for Ge on Si (001) from reverse-bias capacitance measurements; using photoemission spectroscopy, Margaritondo et al.[80] obtained $\Delta E_v = 0.2$ eV for Ge on Si (111), and Mahowald et al.[81] obtained $\Delta E_v = 0.4 \pm 0.1$ eV for Si on Ge (111).

4.7 Band Offsets for Alloy Heterojunctions

The large lattice mismatch between Si and Ge, resulting in very small critical thicknesses, precludes the use of pure Si/Ge heterostructures for most device applications. However, a large number of devices have been proposed and demonstrated that utilize $Si/Si_{1-x}Ge_x$ heterostructures[17]–[39]. We have used an interpolation scheme to extend our measurements to yield band offset values for $Si_{1-x}Ge_x/Si_{1-y}Ge_y$ heterostructures, and have checked our interpolated band offset values for consistency with published results of modulation-doping experiments[18, 19, 20]. In this section we present the interpolation scheme we have used to calculate band offsets in alloy heterojunctions, and compare the results obtained for various $Si/Si_{1-x}Ge_x$ heterojunctions with measurements on alloy heterojunctions and published observations of modulation doping in Si/-$Si_{1-x}Ge_x$ heterostructures.

4.7.1 Interpolation Method for Alloys

The interpolation scheme we have used to obtain band offsets for alloy heterojunctions is based on a method proposed by Van de Walle and Martin[12]. The method is based on the assumptions that the discontinuity in the average position of the three valence bands is independent, or at most a linear function, of the in-plane lattice constant, and that valence-band offsets should depend lin-

early on alloy composition. The former assumption is equivalent to assuming that a deformation potential can be defined for the absolute position of the average valence-band edge, which should be true since the elements of the strain tensor are all much less than unity. The latter assumption is justified by Van de Walle and Martin on the basis of calculations using their model solid theory[46, 82, 83] that yield reasonably accurate band offset values for several heterojunction systems and that are manifestly linear in alloy composition; in addition, experimental evidence in the GaAs/$Al_xGa_{1-x}As$ material system indicates that, even for material systems in which the band gap is a nonlinear function of alloy composition, the valence-band offset is a linear function of the alloy composition[84, 85].

The calculation of interpolated band offset values requires the use of a number of deformation potentials, elastic constants, and other physical parameters for Si, Ge, and $Si_{1-x}Ge_x$ alloys. For Si and Ge, we have used experimental values for deformation potentials when they have been available; in other cases we have used theoretical values calculated by Van de Walle and Martin. The Si and Ge spin-orbit splittings, lattice constants, and elastic constants have been taken from the Landolt-Börnstein compilations[67]. The physical parameters used in these calculations are summarized in Table 4.3. For $Si_{1-x}Ge_x$ alloys, values of all physical parameters except energy band gap have been obtained by linear interpolation. The band gap for unstrained $Si_{1-x}Ge_x$ alloys has been determined experimentally[86], and is plotted in Fig. 4.10.

The first step in the interpolation procedure is to calculate the discontinuity in the average position of the valence band edges for a Si/Ge heterojunction coherently strained to a $Si_{1-z}Ge_z$ substrate. Using our measured valence-band offset values and deformation potentials from Table 4.3, we obtain values for $\Delta E_{v,avg}(\text{Si/Ge})$ of 0.55 eV and 0.43 eV for heterojunctions coherently strained to Si (001) and Ge (001), respectively. A linear interpolation for a Si/Ge hetero-

Quantity	Si Value	Source	Ge Value	Source
a	5.431 Å	Ref. [67]	5.658 Å	Ref. [67]
c_{11}	16.5	Ref. [67]	12.8	Ref. [67]
c_{12}	6.3	Ref. [67]	4.6	Ref. [67]
Δ_0	0.038 eV	Ref. [67]	0.29 eV	Ref. [67]
b	−2.10 eV	Ref. [44]	−2.86 eV	Ref. [45]
$(\Xi_d + \frac{1}{3}\Xi_u - a)^{\Delta}$	1.50 eV	Ref. [44]	1.31 eV	Ref. [12]
$(\Xi_d + \frac{1}{3}\Xi_u - a)^{L}$	−3.12 eV	Ref. [12]	−2.0 eV	Ref. [88]
Ξ_u^{Δ}	8.6 eV	Ref. [44]	9.42 eV	Ref. [12]
Ξ_u^{L}	16.14 eV	Ref. [12]	16.2 eV	Ref. [88]

Table 4.3: Physical parameters used to calculate interpolated band offsets for $Si_{1-x}Ge_x/Si_{1-y}Ge_y$ alloy heterojunctions coherently strained to $Si_{1-z}Ge_z$ substrates. Experimental deformation potentials for Si and Ge have been given whenever available; otherwise, theoretical values calculated by Van de Walle and Martin[12] have been listed. Parameters for $Si_{1-x}Ge_x$ alloys have been obtained by linear interpolation of values for pure Si and Ge.

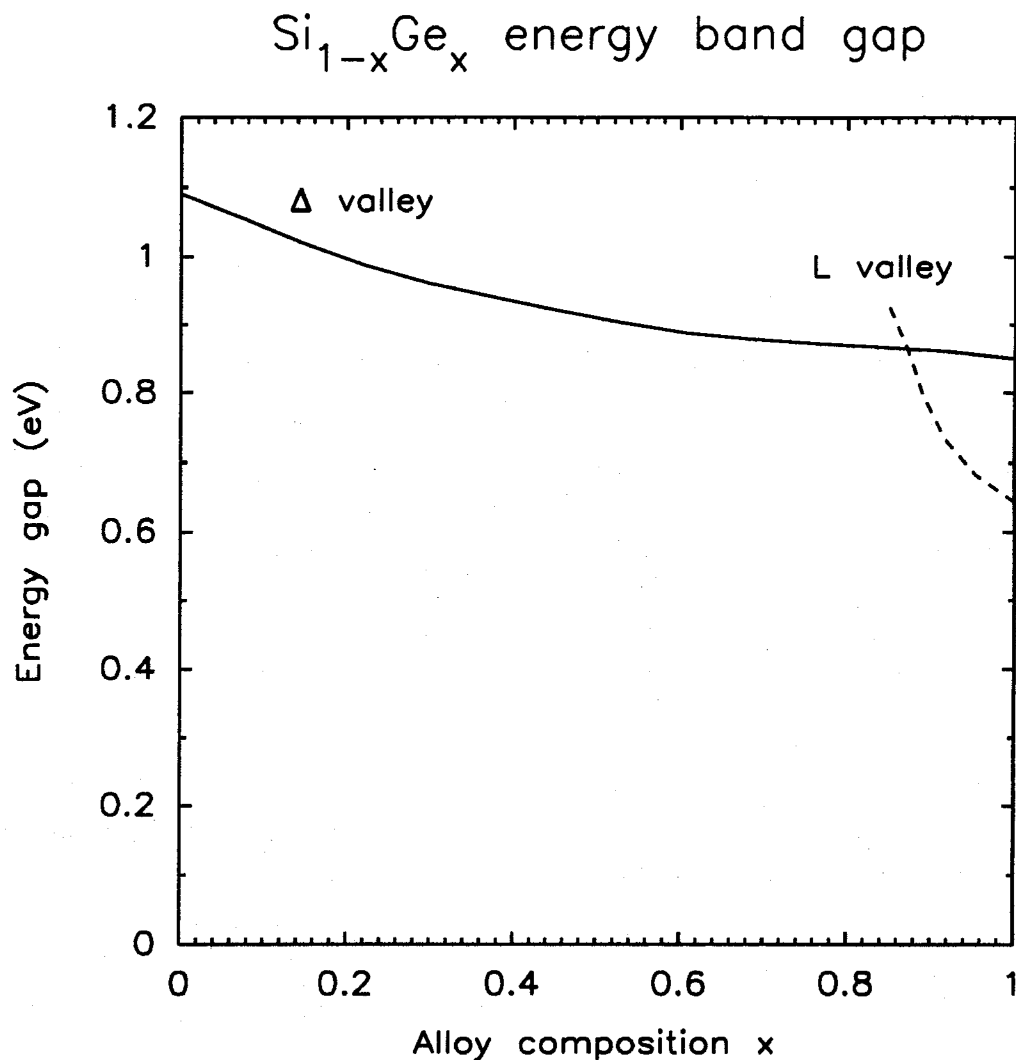

Figure 4.10: Energy band gap for unstrained $Si_{1-x}Ge_x$ alloys, in electron volts. For Si, the lowest conduction band valley is in the Δ direction, near the X point; for Ge, the lowest conduction band valley is at the L point. The solid line in the figure indicates the position of the Δ minimum, and the dashed line the position of the L valley. The band gaps plotted in the figure were obtained from experimental data given in Ref. [86].

potentials Ξ_d^Δ, Ξ_d^L, Ξ_u^Δ, and Ξ_u^L. The shift of a conduction-band valley k is given by[87, 88]

$$\Delta E_c^k = \Xi_d^k \epsilon_{ii} + \Xi_u^k e_i^k e_j^k \epsilon_{ij}, \tag{4.61}$$

where $\mathbf{e}^k$ is the unit vector parallel to the $\mathbf{k}$ vector for valley k, and where a sum is taken over repeated indices. From Eq. (4.61) it can be seen that the average position of the conduction-band edges for valley k is shifted by an energy $(\Xi_d^k + \frac{1}{3}\Xi_u^k)\epsilon_{ii}$. From Eq. (4.18), we see that the shift in energy of the average valence-band-edge position is $a\epsilon_{ii}$, yielding a shift in the energy gap between the average positions of the conduction-band edges associated with the conduction-band valley k and the valence-band edges of

$$\Delta E_{g,\text{avg}} = (\Xi_d^k + \tfrac{1}{3}\Xi_u^k - a)\epsilon_{ii}. \tag{4.62}$$

This strain-induced shift in the energy band gap is then added to the experimentally determined alloy band gap shown in Fig. 4.10 to yield the gap between the average positions of the strain-split conduction- and valence-band edges in each material. As with the valence-band deformation potentials, the conduction-band deformation potentials for alloys are obtained by linear interpolation between the values for pure Si and Ge given in Table 4.3.

In Si and $Si_{1-x}Ge_x$ alloys with $x \lesssim 0.84$, the lowest conduction-band valleys are those in the Δ direction, near the X point. For strain in the (001) direction, the bands in the [100] and [010] directions will be degenerate, and split from the bands in the [001] direction by an energy $\Xi_u^\Delta(\epsilon_{zz} - \epsilon_{xx})$; the positions of the Δ valleys relative to the average position of the conduction-band edge are

$$\Delta E_{[001]} = +\tfrac{2}{3}\Xi_u^\Delta(\epsilon_{zz} - \epsilon_{xx}) \tag{4.63}$$

for the [001] valleys and

$$\Delta E_{[100],[010]} = -\tfrac{1}{3}\Xi_u^\Delta(\epsilon_{zz} - \epsilon_{xx}) \tag{4.64}$$

for the [100] and [010] conduction-band valleys. The L conduction-band valleys, which are the lowest in energy for Ge and $Si_{1-x}Ge_x$ alloys with $x \gtrsim 0.84$, will remain degenerate under strain in the (001) direction. The conduction-band offset is defined to be the separation in energy between the lowest conduction-band edges in each material. The conduction-band offset for a $Si_{1-x}Ge_x/Si_{1-y}Ge_y$ heterojunction coherently strained to a $Si_{1-z}Ge_z$ substrate can be obtained in a straightforward manner from Eqs. (4.60)–(4.64).

Figs. 4.11 and 4.12 show the conduction- and valence-band offsets for $Si_{1-x}Ge_x/Si_{1-y}Ge_y$ heterojunctions coherently strained to Si (001) and Ge (001) substrates, respectively. From the figures one can see that the valence-band offset is nearly linear in alloy composition, with the slight nonlinearity being due to the nonlinearity of the valence-band splittings given in Eqs. (4.11)–(4.13). The conduction-band offsets, however, are highly nonlinear functions of alloy composition, partly because of the nonlinearity of the energy band gap in strained $Si_{1-x}Ge_x$ alloys as a function of the alloy composition x. In addition, the crossover from a conduction-band edge in the Δ direction for $Si_{1-x}Ge_x$ alloys with $x \lesssim 0.84$ to a conduction-band edge at the L point for alloys with $x \gtrsim 0.84$ leads to a slightly nonmonotonic dependence of the conduction band offset on x or y for a $Si_{1-x}Ge_x/Si_{1-y}Ge_y$ (001) heterojunction.

4.7.2 Comparison with Results for Alloy Heterojunctions

The interpolation scheme described in Section 4.7.1 allows us to compare the results of our measurements with published results for $Si/Si_{1-x}Ge_x$ alloy heterojunctions. In an XPS study of $Si/Si_{1-x}Ge_x$ heterojunctions, Ni et al.[14, 15, 16] measured conduction- and valence-band offsets in $Si/Si_{0.74}Ge_{0.26}$ on Si

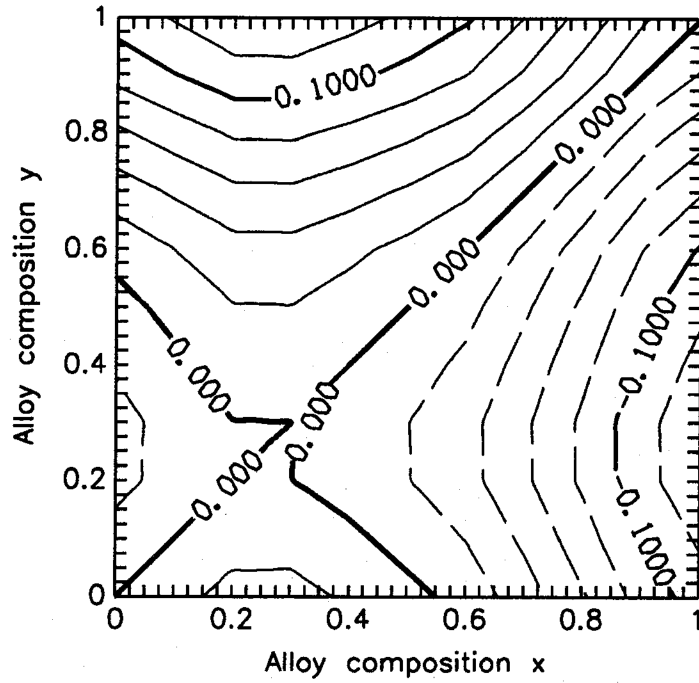

ΔE$_c$(Si$_{1-x}$Ge$_x$/Si$_{1-y}$Ge$_y$) on Si (001)
0.1000
0.000
0.000
0.000
0.000
0.000
0.000
-0.1000
-0.1000
Alloy composition y
Alloy composition x
0
0.2
0.4
0.6
0.8
1

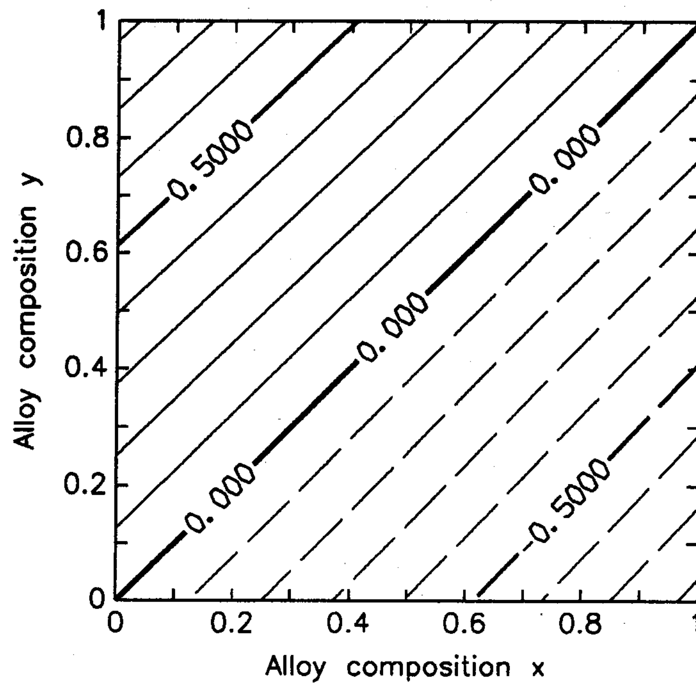

ΔE$_v$(Si$_{1-x}$Ge$_x$/Si$_{1-y}$Ge$_y$) on Si (001)
0.5000
0.000
0.000
0.000
-0.5000
Alloy composition y
Alloy composition x
0
0.2
0.4
0.6
0.8
1

Figure 4.11: Contour plots of conduction-band (upper) and valence-band (lower) offsets for $Si_{1-x}Ge_x/Si_{1-y}Ge_y$ (001) alloy heterojunctions coherently strained to a Si (001) substrate, calculated using our measured Si/Ge (001) valence-band offsets and the interpolation scheme described in Section 4.7.1. The signs of the band offsets are such that the valence- and conduction-band offsets are positive if the band edge in the $Si_{1-y}Ge_y$ layer is higher than in the $Si_{1-x}Ge_x$ layer. In the contour plots, positive band offset values are indicated by the solid contour lines, and negative values by the dashed lines.

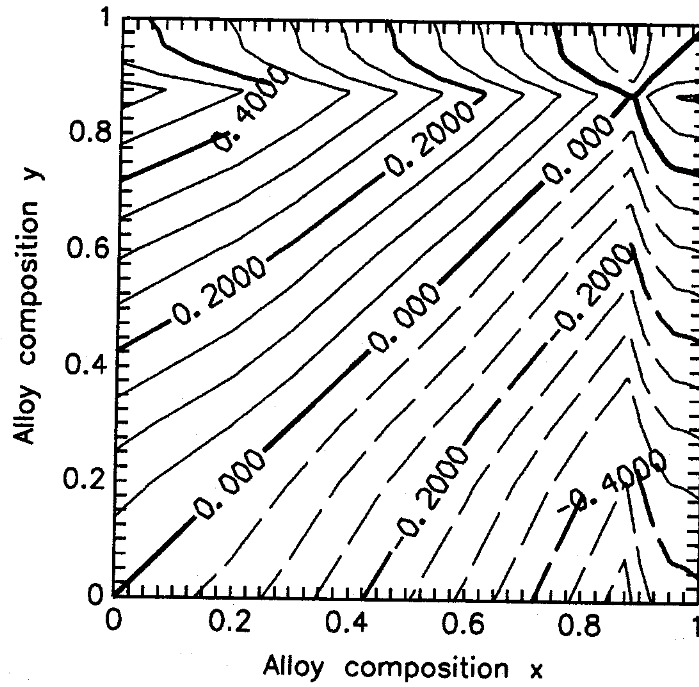
$\Delta E_c(Si_{1-x}Ge_x/Si_{1-y}Ge_y)$ on Ge (001)
Alloy composition y
Alloy composition x
0.4000
0.2000
0.000
0.2000
0.000
-0.2000
0.000
-0.2000
-0.4000
0
0.2
0.4
0.6
0.8
1

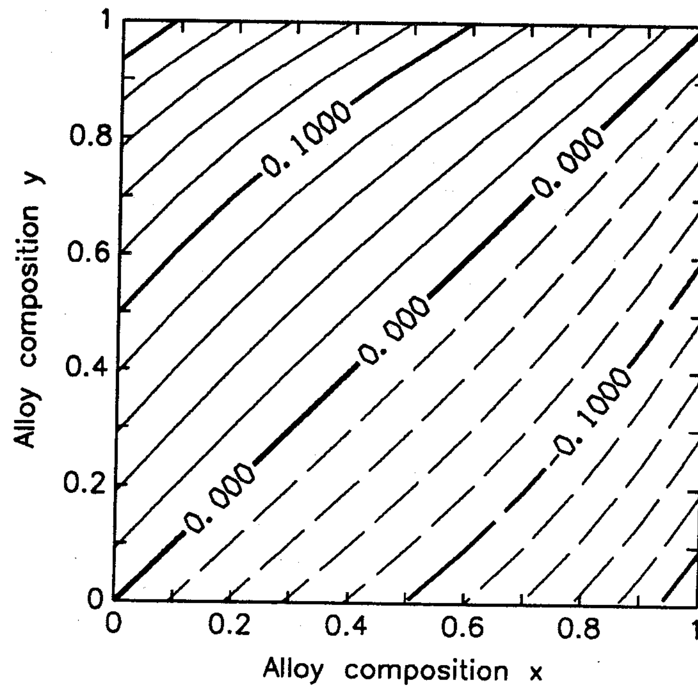
$\Delta E_v(Si_{1-x}Ge_x/Si_{1-y}Ge_y)$ on Ge (001)
Alloy composition y
Alloy composition x
0.1000
0.000
0.000
0.000
-0.1000
0
0.2
0.4
0.6
0.8
1

Figure 4.12: Contour plots of conduction-band (upper) and valence-band (lower) offsets for $Si_{1-x}Ge_x/Si_{1-y}Ge_y$ (001) alloy heterojunctions coherently strained to a Ge (001) substrate, calculated using our measured Si/Ge (001) valence-band offsets and the interpolation scheme described in Section 4.7.1. The signs of the band offsets are such that the valence- and conduction-band offsets are positive if the band edge in the $Si_{1-y}Ge_y$ layer is higher than in the $Si_{1-x}Ge_x$ layer. In the contour plots, positive band offset values are indicated by the solid contour lines, and negative values by the dashed lines.

(001), $Si/Si_{0.52}Ge_{0.48}$ on Si (001), and $Si/Si_{0.52}Ge_{0.48}$ on $Si_{0.75}Ge_{0.25}$ (001). For Si/-$Si_{0.74}Ge_{0.26}$ on Si (001), they obtained $\Delta E_c = 0.00 \pm 0.06$ eV and $\Delta E_v = 0.18 \pm 0.06$ eV, compared to our values $\Delta E_c = -0.03$ eV and $\Delta E_v = 0.21$ eV; for Si/-$Si_{0.52}Ge_{0.48}$ on Si (001), they obtained $\Delta E_c = 0.03 \pm 0.06$ eV and $\Delta E_v = 0.36 \pm 0.06$ eV, compared to our values $\Delta E_c = -0.01$ eV and $\Delta E_v = 0.39$ eV; finally, for $Si/Si_{0.52}Ge_{0.48}$ on $Si_{0.75}Ge_{0.25}$ (001), they obtained $\Delta E_c = 0.13 \pm 0.06$ eV and $\Delta E_v = 0.24 \pm 0.06$ eV, compared to our values $\Delta E_c = 0.14$ eV and $\Delta E_v = 0.26$ eV. The values obtained by Ni et al. are all in very good agreement with the results obtained by interpolation from our measured band offset values.

A number of modulation-doping experiments have also been performed using $Si/Si_{1-x}Ge_x$ heterostructures[18, 19, 20], and the results of these experiments provide qualitative information on band offsets for these heterojunctions. People et al.[18] have observed modulation-doping effects for holes in $Si/Si_{0.8}Ge_{0.2}$ heterojunctions coherently strained to Si (001) substrates; this result, combined with their failure to observe modulation-doping effects for n-type samples, indicates that $\Delta E_v \gg \Delta E_c$ for $Si/Si_{0.8}Ge_{0.2}$ heterojunctions coherently strained to Si (001) substrates. Using the interpolation scheme described above, we find that our measurements correspond to $\Delta E_v = 0.16$ eV and $\Delta E_c = -0.02$ eV; these values are consistent with People's results. The band alignment corresponding to our measured values and the observed modulation-doping behavior are shown schematically in Fig. 4.13(a).

In another experiment, Abstreiter et al.[20] observed enhanced electron mobilities in $Si/Si_{0.5}Ge_{0.5}$ superlattices coherently strained to a $Si_{0.75}Ge_{0.25}$ (001) buffer layer when the $Si_{0.5}Ge_{0.5}$ superlattice layers were doped n-type. For this heterojunction system, our measurements correspond to a valence-band offset of 0.28 eV and a conduction-band offset of 0.14 eV, consistent with Abstreiter's results. The band alignment for this heterojunction corresponding to our measured

values, and the observed modulation-doping behavior, are shown schematically in Fig. 4.13(b). It is interesting to note that, for a $Si/Si_{0.5}Ge_{0.5}$ superlattice grown coherently strained to a pure Si (001) buffer layer, our measurements yield a valence-band offset of 0.41 eV and a conduction-band offset of -0.01 eV, i.e., a Type I band alignment. In this case one would not expect to observe the n-type modulation-doping effect, a clear example of how simply changing the strain configuration in a heterojunction can alter the qualitative behavior of a device structure.

4.8 Conclusions

The effects of strain on band offsets in the Si/Ge (001) material system have been discussed in this chapter. Lattice-mismatched material systems in general have been a subject of considerable interest, and the effect of strain on the electronic structure of a coherently strained heterojunction is a vital aspect of the study of lattice-mismatched materials. We have chosen the Si/Ge (001) material system as a prototype in which to study the effects of strain on band offset values because the conditions under which coherently strained epilayers can be grown are well known, and because theoretical studies had indicated that strain should have a pronounced effect on band offset values. The Si/Ge material system is also of great technological interest[17]-[39], because of the possibility of integrating devices utilizing $Si/Si_{1-x}Ge_x$ heterojunctions directly into existing Si electronic technology. A thorough and accurate knowledge of band offsets in Si/-$Si_{1-x}Ge_x$ heterojunctions is essential in the design of $Si/Si_{1-x}Ge_x$ heterostructure devices.

We have used XPS to measure the valence-band offset in coherently strained Si/Ge (001) heterojunctions as a function of strain. To extend the applicability

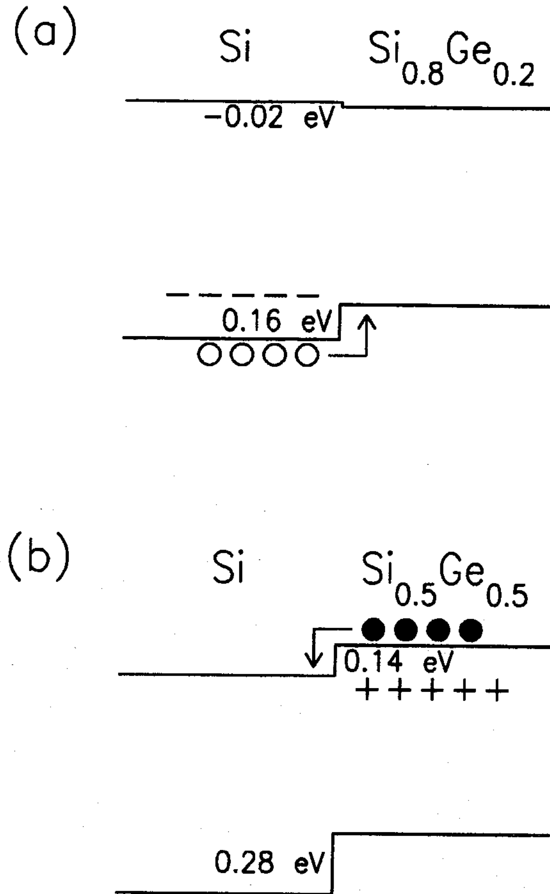

Figure 4.13: Schematic diagrams of modulation-doping effects reported in the literature, and the band alignments obtained by interpolation from our measured band offset values. For the heterojunction shown in (a), People et al.[18] observed modulation-doping effects when the Si layer was doped p-type, but not when the doping was n-type, indicating that $\Delta E_v \gg \Delta E_c$. The band alignment shown in the figure is consistent with People's results. For the heterojunction shown in (b), which is coherently strained to a $Si_{0.75}Ge_{0.25}$ (001) buffer layer, Abstreiter et al.[20] observed enhanced electron mobilities when the $Si_{0.5}Ge_{0.5}$ layer was doped n-type. As seen in the figure, the band alignment obtained by interpolation from our measured values is consistent with this observation.

of the XPS band-offset measurement technique to lattice-mismatched material systems, it was necessary to measure, for the first time, strain-induced shifts in atomic core-level to valence-band-edge binding energies, and to measure the strain dependence of heterojunction core-level energy separations. The strain dependence of these quantities was measured by growing, using low-temperature epitaxial growth techniques, strained films of pure Si and pure Ge, and strained Si/Ge superlattice samples. XPS measurements were performed on these strained structures, and the strain configurations in all samples were confirmed by x-ray diffraction. The strain-dependent core-level to valence-band-edge binding energies in pure Si and Ge, and the strain-dependent heterojunction core-level energy separations, were combined to obtain strain-dependent values for the Si/Ge (001) valence-band offset. For Ge coherently strained to Si (001) we obtained a value $\Delta E_v = 0.83 \pm 0.11$ eV, and for Si coherently strained to Ge (001) our measurements yielded $\Delta E_v = 0.22 \pm 0.13$ eV. These values are in good agreement with the self-consistent density-functional calculations of Van de Walle and Martin[12], and the strain dependence of our results is in good agreement with the measurements of Schwartz et al.[13]. Our results are not inconsistent with the postulate[12] that the discontinuity in the weighted average of the strain-split valence-band-edge positions is independent of strain.

We have also adapted the interpolation scheme of Van de Walle and Martin[12] to extend the applicability of our results to include heterostructures containing $Si_{1-x}Ge_x$ alloys. This interpolation scheme is based on the assumption that the discontinuity in the average position of the valence-band edges in each material should depend linearly on both the alloy composition and the in-plane lattice constant of the heterojunction. Measurements of valence-band offsets in GaAs/-$Al_xGa_{1-x}As$ heterojunctions as a function of x suggest that the valence-band offset should be a linear function of alloy composition, and that the nonlinearity

of the energy band gap should affect only the conduction-band offset[84, 85].

Using this scheme, we have compared band offset values obtained by interpolation from our measurements with experimental results reported for $Si/Si_{1-x}Ge_x$ alloy heterojunctions. Our values are in good agreement with the band offsets obtained by Ni et al.[14, 15, 16] on $Si/Si_{1-x}Ge_x$ heterojunctions coherently strained to Si (100) substrates and $Si_{0.25}Ge_{0.75}$ (001) alloys, and are also consistent with experiments in which modulation-doping effects were observed for both holes[18] and electrons[20] in various $Si/Si_{1-x}Ge_x$ heterostructures.

The results presented here demonstrate that strain effects exert a strong influence on band offset values. Calculations, using known deformation potentials, of the splittings of the valence bands arising from strain indicate that the uniaxial splittings of the valence bands, rather than absolute shifts in the average position of the heavy-hole, light-hole, and split-off valence band edges, are the primary factor in determining the strain dependence of band offset values. Recent calculations of absolute deformation potentials for a large number of materials, including Si and Ge, suggest that this trend could be true for a large number of lattice-mismatched heterojunction systems[46]. As with all conjectures concerning band offsets, however, this rule will be confirmed or refuted only by experiment.

References

[1] G. C. Osbourn, *J. Appl. Phys.* **53**, 1586 (1982).

[2] G. C. Osbourn, R. M. Biefeld, and P. L. Gourley, *Appl. Phys. Lett.* **41**, 172 (1982).

[3] I. J. Fritz, L. R. Dawson, and T. E. Zipperian, *Appl. Phys. Lett.* **43**, 846 (1983).

[4] D. L. Smith, *Solid State Commun.* **57**, 919 (1986).

[5] D. L. Smith and C. Mailhiot, *J. Appl. Phys.* **63**, 2717 (1988).

[6] D. L. Smith and C. Mailhiot, *J. Appl. Phys.* **62**, 2545 (1987).

[7] C. Mailhiot and D. L. Smith, *J. Vac. Sci. Technol. A* **7**, 445 (1989).

[8] D. H. Chow, R. H. Miles, J. R. Söderström, and T. C. McGill, *Appl. Phys. Lett.* **56**, 1418 (1990).

[9] J. H. Van der Merwe, *J. Appl. Phys.* **34**, 117 (1963).

[10] J. H. Van der Merwe, *J. Appl. Phys.* **34**, 123 (1963).

[11] R. H. Miles, T. C. McGill, P. P. Chow, D. C. Johnson, R. J. Hauenstein, C. W. Nieh, and M. D. Strathman, *Appl. Phys. Lett.* **52**, 916 (1988).

[12] C. G. Van de Walle and R. M. Martin, *Phys. Rev. B* **34**, 5621 (1986).

[13] G. P. Schwartz, M. S. Hybertsen, J. Bevk, R. G. Nuzzo, J. P. Mannaerts, and G. J. Gualtieri, *Phys. Rev. B* **39**, 1235 (1989).

[14] W.-X. Ni, J. Knall, and G. V. Hansson, *Phys. Rev. B* **36**, 7744 (1987).

[15] W.-X. Ni, J. Knall, and G. V. Hansson, in *Proceedings of the Second International Symposium on Silicon Molecular Beam Epitaxy*, J. C. Bean and L. J. Schowalter, eds. (The Electrochemical Society, Pennington, NJ, 1988), p. 68.

[16] W.-X. Ni and G. V. Hansson, *Phys. Rev. B* **42**, 3030 (1990).

[17] T. C. McGill, R. H. Miles, R. J. Hauenstein, and O. J. Marsh, in *Proceedings of the Second International Symposium on Silicon Molecular Beam Epitaxy*, J. C. Bean and L. J. Schowalter, eds. (The Electrochemical Society, Pennington, NJ, 1988), p. 1.

[18] R. People, J. C. Bean, D. V. Lang, A. M. Sergent, H. L. Störmer, K. W. Wecht, R. T. Lynch, and K. Baldwin, *Appl. Phys. Lett.* **45**, 1231 (1984).

[19] H. Jorke and H. J. Herzog, *Proceedings of the First International Symposium on Silicon Molecular Beam Epitaxy*, J. C. Bean, ed. (The Electrochemical Society, Pennington, NJ, 1985), p. 352.

[20] G. Abstreiter, H. Brugger, T. Wolf, H. Jorke, and H. J. Herzog, *Phys. Rev. Lett.* **54**, 2441 (1985).

[21] T. P. Pearsall, J. C. Bean, R. People, and A. T. Fiory, *Proceedings of the First International Symposium on Silicon Molecular Beam Epitaxy*, J. C. Bean, ed. (The Electrochemical Society, Pennington, NJ, 1985), p. 400.

[22] H. Daembkes, H. J. Herzog, H. Jorke, H. Kibbel, and E. Kasper, *IEEE Trans. Electron Devices* **ED-33**, 633 (1986).

[23] H. C. Liu, D. Landheer, M. Buchnan, and D. C. Houghton, *Appl. Phys. Lett.* **52**, 1809 (1988).

[24] S. S. Rhee, J. S. Park, R. P. G. Karunasiri, Q. Ye, and K. L. Wang, *Appl. Phys. Lett.* **53**, 204 (1988).

[25] Y. Rajakarunanayake and T. C. McGill, *Appl. Phys. Lett.* **55**, 1537 (1989).

[26] S. S. Rhee, G. K. Chang, T. K. Carns, and K. L. Wang, *Appl. Phys. Lett.* **56**, 1061 (1990).

[27] R. Hull, J. M. Gibson, and J. C. Bean, *Appl. Phys. Lett.* **46**, 179 (1985).

[28] J. C. Bean, L. C. Feldman, A. T. Fiory, S. Nakahara, and I. K. Robinson, *J. Vac. Sci. Technol. A* **2**, 436 (1984).

[29] H. M. Manasevit, I. S. Gergis, and A. B. Jones, *Appl. Phys. Lett.* **41**, 464 (1982).

[30] M. S. Hybertsen and M. Schlüter, *Phys. Rev. B* **36**, 9683 (1987).

[31] S. Satpathy, R. M. Martin, and C. G. Van de Walle, *Phys. Rev. B* **38**, 13237 (1988).

[32] S. Ciraci and T. P. Batra, *Phys. Rev. B* **38**, 1835 (1988).

[33] S. Froyen, D. M. Wood, and A. Zunger, *Phys. Rev. B* **37**, 6893 (1988).

[34] Y. Rajakarunanayake and T. C. McGill, *Phys. Rev. B* **40**, 3054 (1989).

[35] Y. Rajakarunanayake and T. C. McGill, *J. Vac. Sci. Technol. B* **7**, 799 (1989).

[36] C. I. Yang and D. S. Pan, *J. Appl. Phys.* **64**, 1573 (1988).

[37] C. I. Yang, D. S. Pan, and R. Somoano, *J. Appl. Phys.* **65**, 3253 (1989).

[38] E. R. Brown and S. J. Eglash, *Phys. Rev. B* **41**, 7559 (1990).

[39] Y. Rajakarunanayake and T. C. McGill, *J. Vac. Sci. Technol. B* **8**, 929 (1990).

[40] E. O. Kane, *J. Phys. Chem. Solids* **1**, 82 (1956).

[41] G. L Bir and G. E. Pikus, *Symmetry and Strain–Induced Effects in Semiconductors* (John Wiley and Sons, New York, 1974), p. 310ff.

[42] F. H. Pollak and M. Cardona, *Phys. Rev.* **172**, 816 (1968).

[43] C. Kittel, *Quantum Theory of Solids* (John Wiley and Sons, New York, 1963), p. 282.

[44] L. D. Laude, F. H. Pollak, and M. Cardona, *Phys. Rev. B* **3**, 2623 (1971).

[45] M. Chandrasekhar and F. H. Pollak, *Phys. Rev. B* **15**, 2127 (1977).

[46] C. G. Van de Walle, *Phys. Rev. B* **39**, 1871 (1989).

[47] J. H. Van der Merwe and C. A. B. Ball, in *Epitaxial Growth*, J. W. Matthews, ed. (Academic Press, New York, 1975), Part b.

[48] J. W. Matthews and A. E. Blakeslee, *J. Cryst. Growth* **27**, 118 (1974).

[49] R. People and J. C. Bean, *Appl. Phys. Lett.* **47**, 322 (1985).

[50] B. W. Dodson and J. Y. Tsao, *Appl. Phys. Lett.* **51**, 1325 (1987).

[51] B. W. Dodson and J. Y. Tsao, *Appl. Phys. Lett.* **52**, 852 (1988).

[52] J. Y. Tsao, B. W. Dodson, S. T. Picraux, and D. M. Cornelison, *Phys. Rev. Lett.* **59**, 2455 (1987).

[53] A. T. Fiory, J. C. Bean, R. Hull, and S. Nakahara, *Phys. Rev. B* **31**, 4063 (1985).

[54] J.–P. Reithmaier, H. Cerva, and R. Lösch, *Appl. Phys. Lett.* **54**, 48 (1989).

[55] H.–J. Gossmann, G. P. Schwartz, B. A. Davidson, and G. J. Gualtieri, *J. Vac. Sci. Technol. B* **7**, 764 (1989).

[56] R. H. Miles, private communication (1988).

[57] F. R. N. Nabarro, *Theory of Crystal Dislocations* (Oxford University Press, Oxford, England, 1967), p. 75.

[58] I. J. Fritz, P. L. Gourley, and L. R. Dawson, *Appl. Phys. Lett.* **51**, 1004 (1987).

[59] I. J. Fritz, *Appl. Phys. Lett.* **51**, 1080 (1987).

[60] E. Kasper, H. J. Herzog, and H. Kibbel, *Appl. Phys.* **8**, 199 (1975).

[61] J. Tersoff and C. G. Van de Walle, *Phys. Rev. Lett.* **59**, 946 (1987).

[62] E. A. Kraut, R. W. Grant, J. R. Waldrop, and S. P. Kowalczyk, *Phys. Rev. B* **28**, 1965 (1983).

[63] M. L. Cohen and T. K. Bergstresser, *Phys. Rev.* **141**, 789 (1966).

[64] L. R. Saravia and D. Brust, *Phys. Rev.* **176**, 915 (1968).

[65] J. Chelikowsky, D. J. Chadi, and M. L. Cohen, *Phys. Rev. B* **8**, 2786 (1973).

[66] L. R. Saravia and D. Brust, *Phys. Rev.* **178**, 1240 (1969).

[67] O. Madelung, ed., *Landolt-Börnstein: Numerical Data and Functional Relationships in Science and Technology* (Springer, New York, 1982), Group III, Vol. 17a.

[68] J. C. Slater, *Phys. Rev.* **51**, 846 (1937).

[69] C. Herring, *Phys. Rev.* **57**, 1169 (1940).

[70] W. Harrison, *Solid State Theory* (Dover Publications, Inc., New York, 1979), p. 96ff.

[71] V. Heine, *Solid State Physics: Advances in Research and Applications*, Vol. 24, H. Ehrenreich, F. Seitz, and D. Turnbull, eds. (Academic Press, New York, 1970), p. 1.

[72] M. L. Cohen and V. Heine, *Solid State Physics: Advances in Research and Applications*, Vol. 24, H. Ehrenreich, F. Seitz, and D. Turnbull, eds. (Academic Press, New York, 1970), p. 38.

[73] V. Heine and D. Weaire, *Solid State Physics: Advances in Research and Applications*, Vol. 24, H. Ehrenreich, F. Seitz, and D. Turnbull, eds. (Academic Press, New York, 1970), p. 250.

[74] J. R. Chelikowsky and M. L. Cohen, *Phys. Rev. B* **14**, 556 (1976).

[75] G. Weisz, *Phys. Rev.* **149**, 504 (1966).

[76] S. Bloom and T. K. Bergstresser, *Solid State Commun.* **6**, 465 (1968).

[77] G. Gilat and L. J. Raubenheimer, *Phys. Rev.* **144**, 390 (1966).

[78] L. J. Raubenheimer and G. Gilat, *Phys. Rev.* **157**, 586 (1967).

[79] T. F. Kuech, M. Mäenpää, and S. S. Lau, *Appl. Phys. Lett.* **39**, 245 (1981).

[80] G. Margaritondo, A. D. Katnani, N. G. Stoffel, R. R. Daniels, and T.-X. Zhao, *Solid State Commun.* **43**, 163 (1982).

[81] P. H. Mahowald, R. S. List, W. E. Spicer, J. Woicik, and P. Pianetta, *J. Vac. Sci. Technol. B* **3**, 1252 (1985).

[82] C. G. Van de Walle and R. M. Martin, *J. Vac. Sci. Technol. B* **4**, 1055 (1986).

[83] C. G. Van de Walle and R. M. Martin, *Phys. Rev. B* **35**, 8154 (1987).

[84] J. Batey and S. L. Wright, *J. Appl. Phys.* **59**, 200 (1985).

[85] J. Batey and S. L. Wright, *Surf. Sci.* **174**, 320 (1986).

[86] R. Braunstein, A. R. Moore, and F. Herman, *Phys. Rev.* **109**, 695 (1958).

[87] C. Herring and E. Vogt, *Phys. Rev.* **101**, 944 (1956).

[88] I. Balslev, *Phys. Rev.* **143**, 636 (1966).

Chapter 5

III-V/II-VI Heterojunction Systems: The Role of Interfacial Chemistry

5.1 Introduction

5.1.1 Background and Motivation

Recent developments in epitaxial growth techniques for II-VI semiconductors[1, 2, 3] have led to considerable interest in the use of these materials in optoelectronic devices; the wide band gaps available in materials such as ZnSe and ZnTe make them particularly attractive for use in visible light emitters. At present, however, there are no II-VI-based visible light-emitting diodes (LED's) in production; commercially available visible LED's emit light in the red and yellow-green regions of the spectrum, and are based on GaAsP and GaP.

One of the major difficulties encountered in early efforts to fabricate light emitters using wide-gap II-VI semiconductors was the inability to control doping

in those materials; none of the binary II-VI materials with band gaps at visible wavelengths can be doped both p-type and n-type, obviating the possibility of producing visible LED's based on simple p-n homojunctions. In particular, the inability to obtain p-type ZnSe and n-type ZnTe hindered efforts to achieve efficient electroluminescence in these materials. However, the advent of epitaxial growth techniques such as molecular-beam epitaxy (MBE)[1, 2, 3] and metalorganic chemical vapor deposition (MOCVD)[4] has introduced greater flexibility in direct doping of II-VI materials, and has also made possible highly controllable fabrication of heterostructures.

One approach that has been proposed for fabricating visible light emitters based on II-VI semiconductors is the use of heterojunctions to inject carriers into various II-VI materials, e.g., electrons into p-ZnTe or holes into n-ZnSe. Provided that heterojunctions with the appropriate dopabilities, band offset values, and lattice match could be found, this approach would circumvent difficulties in direct doping of many II-VI materials[5]. One such approach that appeared especially promising was a device structure in which an n-AlSb/p-ZnTe heterojunction would provide a mechanism for injection of electrons into ZnTe[6]. The feasibility of this device concept, however, depended critically on the value of the AlSb/ZnTe conduction-band offset.

Fig. 5.1 shows a schematic energy-band diagram for the proposed n-AlSb/-p-ZnTe visible LED structure. As can be seen from the figure, injection of electrons from n-AlSb into p-ZnTe can occur only for sufficiently small values of the conduction-band offset ΔE_c. Specifically, the condition[6]

$$\Delta E_c + \phi_n - \phi_p \lesssim 0, \tag{5.1}$$

where ϕ_n and ϕ_p are the positions of the quasi-Fermi levels relative to the AlSb conduction-band edge and the ZnTe valence-band edge, respectively, must be

satisfied to achieve a reasonable electron injection current i_n from n-AlSb into p-ZnTe, and to suppress the hole injection current i_p from p-ZnTe into n-AlSb; for realistic doping levels in AlSb[7] the conduction-band offset must satisfy $\Delta E_c \lesssim 0.2$ eV for the device concept to be feasible.

Direct predictions for the AlSb/ZnTe conduction-band offset[8, 9, 10, 11, 12, 13, 14, 15] range from 0.24 eV to −0.55 eV, and predictions based on the measured GaSb/AlSb valence-band offset[16] and transitivity yield values as high as ~0.34 eV[17]. Because of these large discrepancies, the available predictions are of little use in assessing the viability of AlSb/ZnTe-based visible electroluminescent devices. Fig. 5.2 shows the range of values proposed for the AlSb/ZnTe valence-band offset, based on the experimentally measured AlSb/-GaSb valence-band offset[16] and predicted band offset values for the GaSb/ZnTe heterojunction[8, 9, 10, 11, 12, 13, 14, 15, 17, 18, 19, 20, 21]. Predictions for the GaSb/ZnTe heterojunction have been combined with the experimental band offset value for AlSb/GaSb because certain theories and empirical rules are known to be either inapplicable[17] or invalid[9, 10, 12] for compounds containing Al. Fig. 5.2 makes apparent the need for a reliable experimental determination of the AlSb/ZnTe band offset value.

The use of III-V/II-VI heterojunctions, while providing added flexibility in the design of semiconductor heterostructure devices, introduces a number of complications not present for pure III-V or pure II-VI heterojunction systems. Substrate temperatures for conventional MBE growth of II-VI materials are typically much lower than for III-V materials; for example, typical substrate temperatures for growth of GaAs are near 600 °C, and typical temperatures for growth of ZnSe or ZnTe are between 240 °C and 420 °C[1]. Because of this disparity in substrate temperatures, growth of III-V materials on II-VI surfaces has been extremely difficult. However, recently developed low-temperature growth techniques such

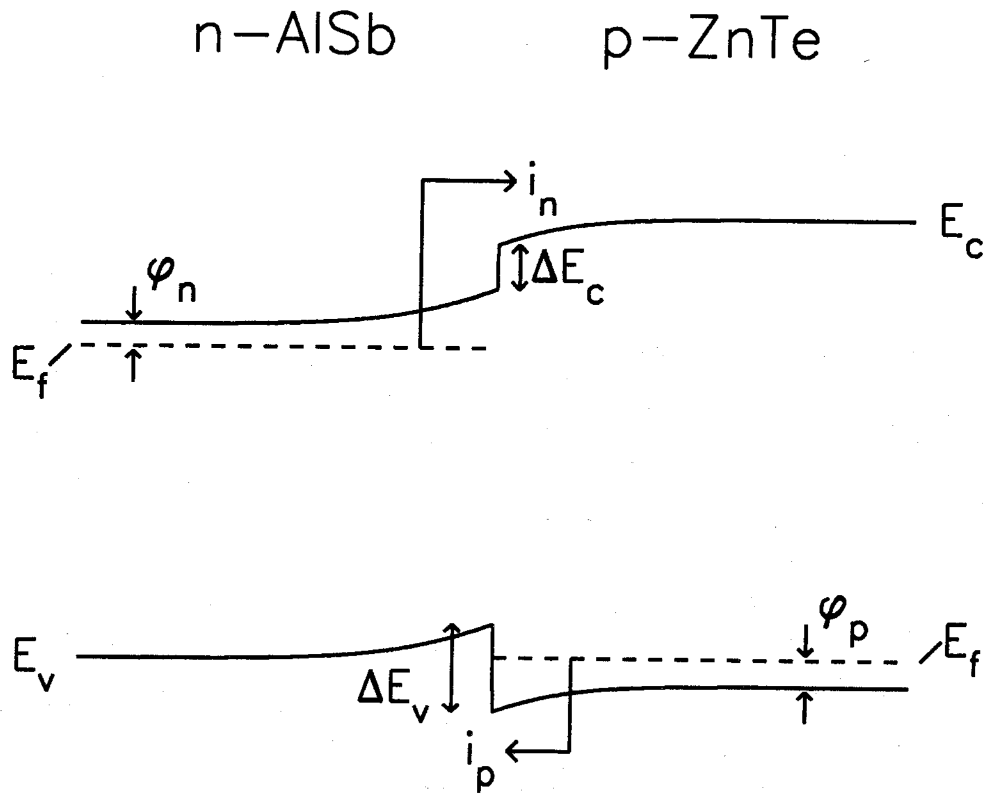

Figure 5.1: Schematic energy-band diagram for the n-AlSb/p-ZnTe visible LED concept proposed by McCaldin and McGill[6]. In such a heterostructure, electrons would be injected from the n-AlSb layer into the p-ZnTe layer. However, the feasibility of this device concept depends critically on the value of the conduction-band offset ΔE_c. The conduction-band offset must be small enough that sufficient electron injection (i_n) occurs, and that the hole injection current i_p from p-ZnTe into n-AlSb is suppressed relative to i_n. For realistic doping levels, the condition on the conduction-band offset for the feasibility of this device concept is that $\Delta E_c \lesssim 0.2$ eV.

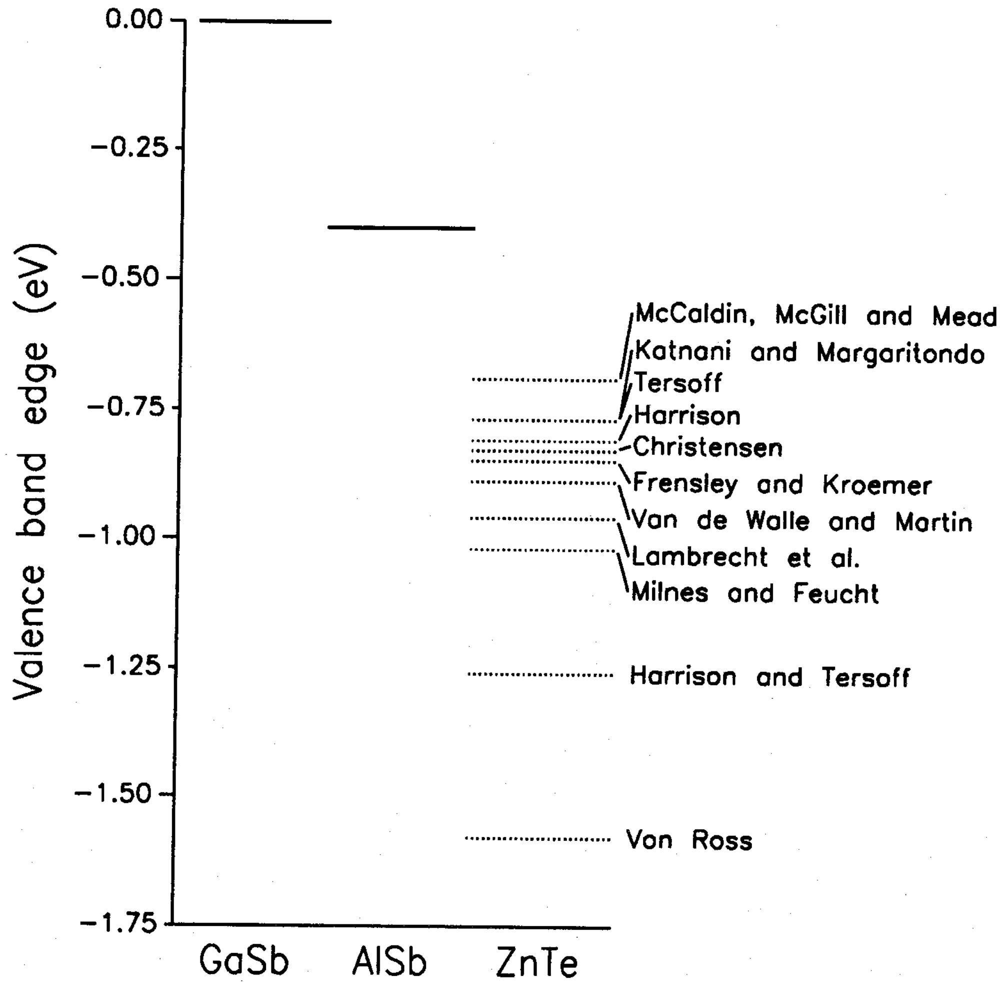

Figure 5.2: Proposed valence-band offset values for the AlSb/ZnTe heterojunction, based on an experimentally measured AlSb/GaSb valence-band offset[16] and predicted values for the GaSb/ZnTe valence-band offset[8, 9, 10, 11, 12, 13, 14, 15, 17, 18, 19, 20, 21]. These values, based on transitivity of band offsets, have been used in lieu of direct predictions of the AlSb/ZnTe valence-band offset because a number of theories are known to be either inapplicable[17] or invalid[9, 10, 12] for compounds containing Al. Conduction-band offset values corresponding to these proposed valence-band offsets range from −0.55 eV to ~0.34 eV.

as migration-enhanced epitaxy[22, 23] allow the growth of GaAs at temperatures of ~250 °C, and these methods may provide a solution to the incompatibility of III-V and II-VI growth temperatures.

Another complication that arises for III-V/II-VI heterojunctions is the chemical reactivity of III-V/II-VI interfaces. Tu and Kahn[24] observed the formation of an intermediate reacted layer containing Ga and Se at ZnSe/GaAs (110) and (100) interfaces, and found that the formation of this reacted layer was enhanced by annealing of the samples. Mackey et al.[25] used x-ray photoelectron spectroscopy to study InSb/CdTe (100) and (110) interfaces, and observed evidence of the formation of an interfacial layer in which the predominant species were In and Te; the interfacial reaction was found to be enhanced for CdTe deposition at elevated (~500 °C) substrate temperatures. Wilke et al. have performed photoemission studies of the ZnTe/GaSb (110)[26] and CdS/InP (110)[27] heterojunctions, and in both cases observed evidence of interfacial reactions and the formation of an intermediate compound between the III-V and II-VI layers, composed primarily of the Group III and Group VI elements.

Given the presence of intermediate compounds in a large number of III-V/-II-VI interfaces, it is of considerable interest to investigate the possible effect of these layers on band offset values in III-V/II-VI heterojunctions. Experiments in various material systems have demonstrated that such effects are possible, and can in fact be quite large. Studies of the ZnSe/GaAs (110) and ZnSe/Ge (110) interfaces by Kowalczyk et al.[28] indicated that details of interface preparation, such as growth sequence, growth temperature, and annealing, changed valence-band offset values by ~0.1–0.2 eV, suggesting that these experimental parameters could affect band offset values via changes induced in interfacial chemistry. For Ge deposited on ZnSe at room temperature, however, Xu et al.[29] did not detect any evidence of an interfacial reaction. Niles et al.[30, 31] observed changes of

up to 0.15 eV in the valence-band offset for CdS/Si and CdS/Ge induced by the deposition of a thin (0.5–2 Å) layer of Al at the interfaces, and for lattice-matched ZnSe/Ge heterojunctions found that the presence of a 2 Å layer of Al at the interface appeared to increase the valence-band offset by 0.2–0.3 eV. Perfetti et al.[32] observed changes in valence-band offset values of −0.5 eV and +0.25 eV induced by the presence of H and Cs interlayers, respectively, at SiO_2/Si interfaces.

The most extensive experiments have been performed on the GaAs/Ge heterojunction system, but contradictory results have been reported. Katnani et al. have performed a number of experiments on the GaAs/Ge heterojunction[33, 34, 35, 36] indicating that the surface reconstruction on which the interface is grown, changes in interface orientation, and the introduction of Al interlayers all had little (±0.05 eV) influence on the GaAs/Ge valence-band offset value. These findings are contradicted, however, by experiments of Waldrop et al.[37]. Waldrop et al. found that depending upon the interface orientation and the surface reconstruction on which the interface was grown, the GaAs/Ge valence-band offset varied from 0.48 to 0.66 eV.

5.1.2 Summary of Results

In this chapter we discuss results obtained in our studies of various III-V/-II-VI heterojunction systems. Sample growth for these experiments involved the use of two separate molecular-beam epitaxial growth chambers connected via ultrahigh vacuum transfer tubes. III-V layers were grown in an MBE chamber dedicated exclusively to the growth of III-V semiconductors; samples were then transferred under vacuum to an MBE chamber dedicated to the growth of II-VI semiconductors, in which the ZnTe layers were grown. Samples were also

transferred from both MBE chambers to the XPS analytical chamber under UHV conditions. The ability to move samples among the two growth chambers and the analytical chamber made possible the growth and characterization of III-V/II-VI heterojunction samples under carefully controlled conditions. In other studies in which samples were exposed to atmosphere during transfer between growth chambers or to the analytical chamber, significant complications arose because of the need to evaporate surface passivation layers protecting the samples during exposure to atmosphere[38].

The initial motivation for these experiments was to measure the AlSb/ZnTe (100) valence band offset and thereby to determine the feasibility of the AlSb/-ZnTe visible light emitting device concept proposed by McCaldin and McGill[6]. Our measurements yielded a valence-band offset $\Delta E_v = 0.42 \pm 0.07$ eV, corresponding to a conduction-band offset $\Delta E_c = 0.21 \pm 0.07$ eV. This value for the conduction-band offset indicated that injection of electrons from n-AlSb into p-ZnTe, the mechanism upon which the AlSb/ZnTe LED concept was based, should be possible if heavily doped AlSb layers were employed.

XPS measurements on AlSb/ZnTe (100) heterojunctions also yielded considerable evidence of chemical reactions occurring at the AlSb/ZnTe interface. Al $2p$, Sb $4d$, and Te $4d$ core level spectra from AlSb/ZnTe heterojunctions contained chemically shifted peak components not present in spectra from bulk AlSb and ZnTe, indicating that intermediate compounds were being formed at the AlSb/-ZnTe interface. An analysis of these core-level spectra suggested that the intermediate compound contained primarily Al and Te, probably in the form Al_2Te_3, and that Sb was present at the ZnTe surface following the deposition of thin layers of ZnTe on AlSb.

To investigate the possible effect of this interfacial reaction on band offset values, we studied band offset transitivity in the AlSb/GaSb/ZnTe material sys-

tem. Considerable theoretical and experimental evidence exists indicating that, for abrupt heterojunctions, band offset transitivity should be satisfied; if band offset values were influenced by the presence of nonideal interfaces, e.g., interfaces at which chemical reactions occurred, transitivity in material systems involving these interfaces should be violated. We have measured the valence-band offset for the AlSb/GaSb and GaSb/ZnTe heterojunctions, obtaining values $\Delta E_v(\text{AlSb/GaSb}) = 0.39 \pm 0.07$ eV and $\Delta E_v(\text{GaSb/ZnTe}) = 0.60 \pm 0.07$ eV. Our measurements demonstrate that band offset transitivity in the AlSb/GaSb/-ZnTe material system is violated by 0.21 ± 0.05 eV, suggesting that III-V/II-VI interfacial reactions do indeed influence band offset values.

We have also attempted to observe the effect of these interfacial reactions on band offset values more directly. Our studies of the AlSb/ZnTe heterojunction had revealed that varying the substrate temperature between 270 °C and 330 °C during deposition of ZnTe on AlSb did not affect the AlSb/ZnTe band offset value. We therefore attempted to suppress the III-V/II-VI interface reaction by exposing the III-V surface to an initial flux of Zn prior to deposition of the ZnTe. This procedure reduced the value of the GaSb/ZnTe valence-band offset by 0.05 eV to 0.55 ± 0.07 eV, and reduced the AlSb/ZnTe valence-band offset by 0.10 eV to 0.32 ± 0.07 eV. In addition, an examination of the Al $2p$ core-level spectra from AlSb/ZnTe heterojunctions grown with and without the initial Zn flux suggested that the initial exposure to Zn produced a slight suppression of the interface reaction.

5.1.3 Outline of Chapter

The measurement of the AlSb/ZnTe (100) valence-band offset is described in Section 5.2. Sample growth is discussed in Section 5.2.1, the XPS measurements

and data analysis are described in Section 5.2.2, and results are presented in Section 5.2.3. Studies of band offset transitivity in the AlSb/GaSb/ZnTe material system are presented in Section 5.3. The measurement of the AlSb/GaSb band offset is presented in Section 5.3.1, and measurement of the GaSb/ZnTe band offset is discussed in Section 5.3.2. The results of these measurements, in particular the demonstration that transitivity is violated, are discussed in Section 5.3.3. Attempts to observe the effects of interface reactions on band offset values more directly are presented in Section 5.4. Our conclusions are summarized in Section 5.5.

5.2 The AlSb/ZnTe (100) Heterojunction

5.2.1 Sample Growth

The samples prepared for this study were grown by molecular-beam epitaxy in two Perkin-Elmer 430P MBE systems. The AlSb layers were grown in a chamber dedicated to the growth of III-V semiconductors, and the ZnTe layers were grown in a chamber devoted to II-VI semiconductor growth; the two growth chambers and the XPS analytical chamber are connected by ultrahigh vacuum transfer tubes, allowing samples to be transported among the two growth chambers and the analytical chamber without exposure to atmospheric pressure. All samples were grown on *p*-type GaSb (100) substrates, with $p \sim 1 \times 10^{17}\text{cm}^{-3}$. Following oxide desorption at 530 °C, a GaSb buffer layer was grown at 100 Å/min., with the substrate at 475 °C. AlSb layers were grown at 62.5 Å/min. with a substrate temperature of 530 °C; for the ZnTe layers, a growth rate of approximately 50 Å/min. and substrate temperatures of 270 °C and 330 °C were used.

Al $2p$ core-level to valence-band-edge binding energies were measured in two

5000 Å AlSb layers grown on the GaSb buffers. To measure the Al $2p$ to Zn $3d$ core-level energy separation, three samples were grown. Each consisted of over 5000 Å of AlSb grown on the GaSb buffer layer, followed by approximately 25 Å of ZnTe grown at either 270 °C or 330 °C. For the ZnTe layers, streaky reflection high-energy electron diffraction (RHEED) patterns were observed within approximately five seconds after the growths were begun, indicating that growth was two-dimensional. For the Zn $3d$ core-level to valence-band-edge binding energy measurement, an additional 250 Å layer of ZnTe was grown at 270 °C on two of the AlSb/ZnTe heterojunction samples after the XPS heterojunction core-level energy separations had been measured in those samples. The heterojunction samples showed relatively little sign of surface deterioration following the XPS measurements, and streaky ZnTe RHEED patterns were observed almost immediately after growth of ZnTe commenced. Growth of the AlSb/ZnTe heterojunction samples required the use of both MBE chambers, with the samples being transported between the two systems under UHV conditions. Immediately following all growths, the samples were transported under UHV conditions to the XPS chamber for analysis. The ability to perform the entire experiment without exposing samples to atmosphere allowed us to eliminate experimental uncertainties associated with surface passivation and subsequent evaporation of protective capping layers. This capability was critical in these experiments, given the propensity to form interfacial reaction layers, particularly at the elevated substrate temperatures required for evaporation of surface passivation layers, that seems to be characteristic of III-V/II-VI heterojunctions.

5.2.2 XPS Measurements and Data Analysis

Fig. 5.3 shows a schematic energy-band diagram for the AlSb/ZnTe heterojunction. Strain-induced effects on the electronic structure of the two materials have been neglected, due to the small lattice mismatch (0.55%) between AlSb and ZnTe. The band gap in AlSb is indirect, with the conduction-band minimum in the Δ direction in the Brillouin zone; the indirect nature of the AlSb band gap is indicated by the dashed line for the AlSb conduction-band edge. As shown in the figure, the valence-band offset is given by

$$\Delta E_v = (E_{\mathrm{Al2}p}^{\mathrm{AlSb}} - E_v^{\mathrm{AlSb}}) - (E_{\mathrm{Zn3}d}^{\mathrm{ZnTe}} - E_v^{\mathrm{ZnTe}}) - (E_{\mathrm{Al2}p}^{\mathrm{AlSb}} - E_{\mathrm{Zn3}d}^{\mathrm{ZnTe}}). \qquad (5.2)$$

XPS measurements were obtained using a Perkin-Elmer Model 5100 analysis system with a monochromatic Al $K\alpha$ x-ray source ($h\nu$ = 1486.6 eV). The measured linewidth for Au $4f$ core-level peaks was ~0.75 eV, and the pressure in the analysis chamber was typically $\sim 5 \times 10^{-10}$ Torr. Sample XPS spectra for bulk AlSb, bulk ZnTe, and AlSb/ZnTe heterojunctions are shown in Figs. 5.4(a), (b), and (c), respectively. The valence band spectra for the bulk AlSb and ZnTe samples are also shown on enlarged scales, as indicated in the figure.

Core-level peak positions were obtained by subtracting from each core-level peak a background function proportional to the integrated photoelectron intensity, and fitting the resulting core-level spectra to characteristic peak-shape functions consisting of two identically shaped Voigt functions separated by a fixed spin-orbit splitting, whose relative heights scaled as $(2J+1)$. The position of a given core level was taken to be an average of the positions of the spin-orbit-split components, weighted by the degeneracy $(2J+1)$. The uncertainty in measured core-level energy separations was estimated to be ± 0.02 eV, and measurements of core-level energy separations were typically reproducible to ± 0.01 eV.

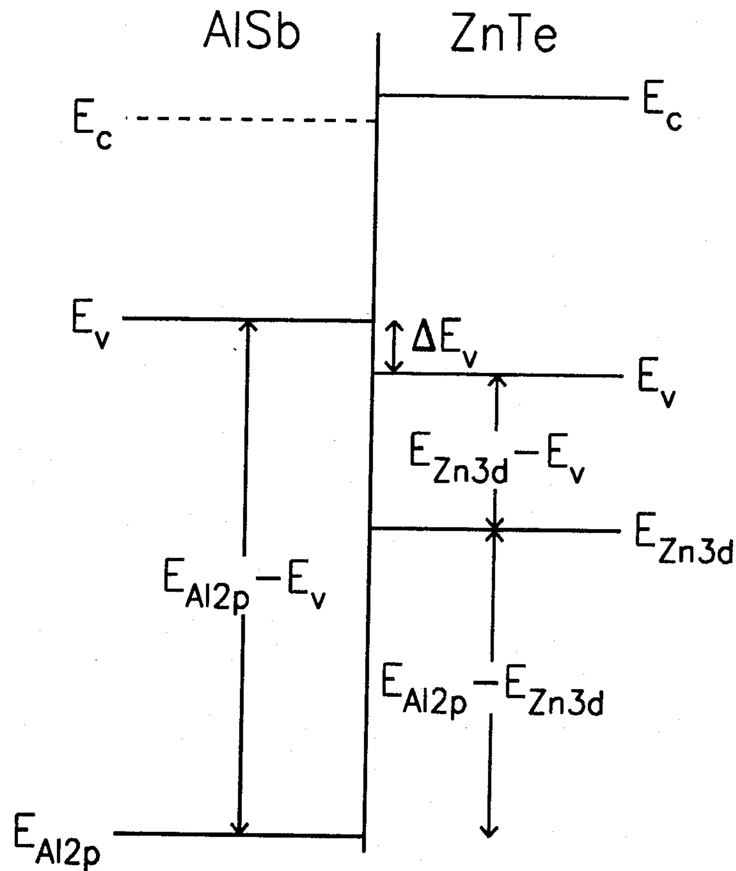

Figure 5.3: Schematic energy-band diagram for the AlSb/ZnTe (100) heterojunction. As indicated by the dashed line for the AlSb conduction-band edge, the band gap in AlSb is indirect, with the conduction-band minimum in the Δ direction in the Brillouin zone.

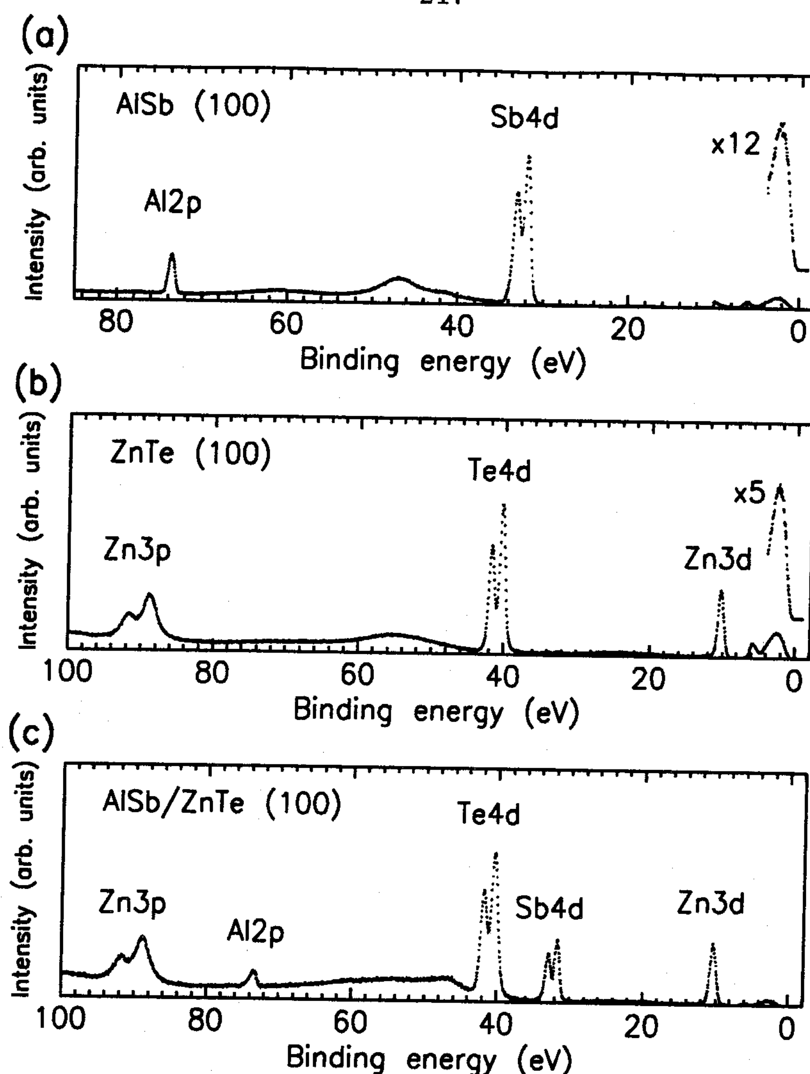

Figure 5.4: Representative binding energy XPS spectra for (a) bulk AlSb (100), (b) bulk ZnTe (100), and (c) an AlSb/ZnTe (100) heterojunction. The Al $2p$ core-level to valence-band-edge binding energy is measured in the bulk AlSb samples, the Zn $3d$ core-level to valence-band-edge binding energy in the bulk ZnTe samples, and the Al $2p$ to Zn $3d$ core-level energy separation in the AlSb/ZnTe heterojunctions. For the bulk AlSb and ZnTe spectra in (a) and (b), respectively, longer sampling times were used in the vicinity of the valence band edges. The valence-band spectra for the bulk AlSb and ZnTe samples are also shown on enlarged intensity scales, as indicated in the figure.

The position of the valence-band edge in each XPS spectrum was determined using the precision analysis technique of Kraut et al.[39]. In this approach, the XPS spectrum near the valence-band edge is modeled as a convolution of a theoretical valence-band density of states with an experimentally determined XPS instrumental resolution function. This model function is then fitted to the experimental data to give the position of the valence-band edge. The XPS instrumental resolution function was determined from measured lineshapes of Au $4f$ core-level peaks, for which the inherent linewidth attributable to lifetime broadening is known[40]. The theoretical valence-band density of states was calculated using the empirical pseudopotential method[41]; spin-orbit interactions[42] and a nonlocal effective mass parameter[43] were included in these calculations. The empirical pseudopotential parameters were obtained by optimizing the calculated band structure to give the best agreement at the Γ, X, and L points in the Brillouin zone with previously calculated band structures and measured critical-point energies for AlSb[41, 44, 45] and ZnTe[41, 46, 47, 48].

Figs. 5.5(a) and (b) show the valence-band spectra, model functions fitted to the XPS data, and calculated valence-band densities of states for AlSb (100) and ZnTe (100), respectively. The valence-band edge in these figures, as determined by the fitting procedure described above, is taken to be at 0 eV.

5.2.3 Results and Discussion

Measurements obtained from the bulk AlSb samples yielded an Al $2p$ core-level to valence-band-edge binding energy of 72.92 ± 0.04 eV. Our measurement is in good agreement with a previously reported value[16] of 72.96 eV. The separation between the Al $2p$ and Sb $4d_{5/2}$ core levels in AlSb was found to be 41.72 ± 0.02 eV; comparison of the Al $2p$ to Sb $4d_{5/2}$ core-level energy separation in bulk and

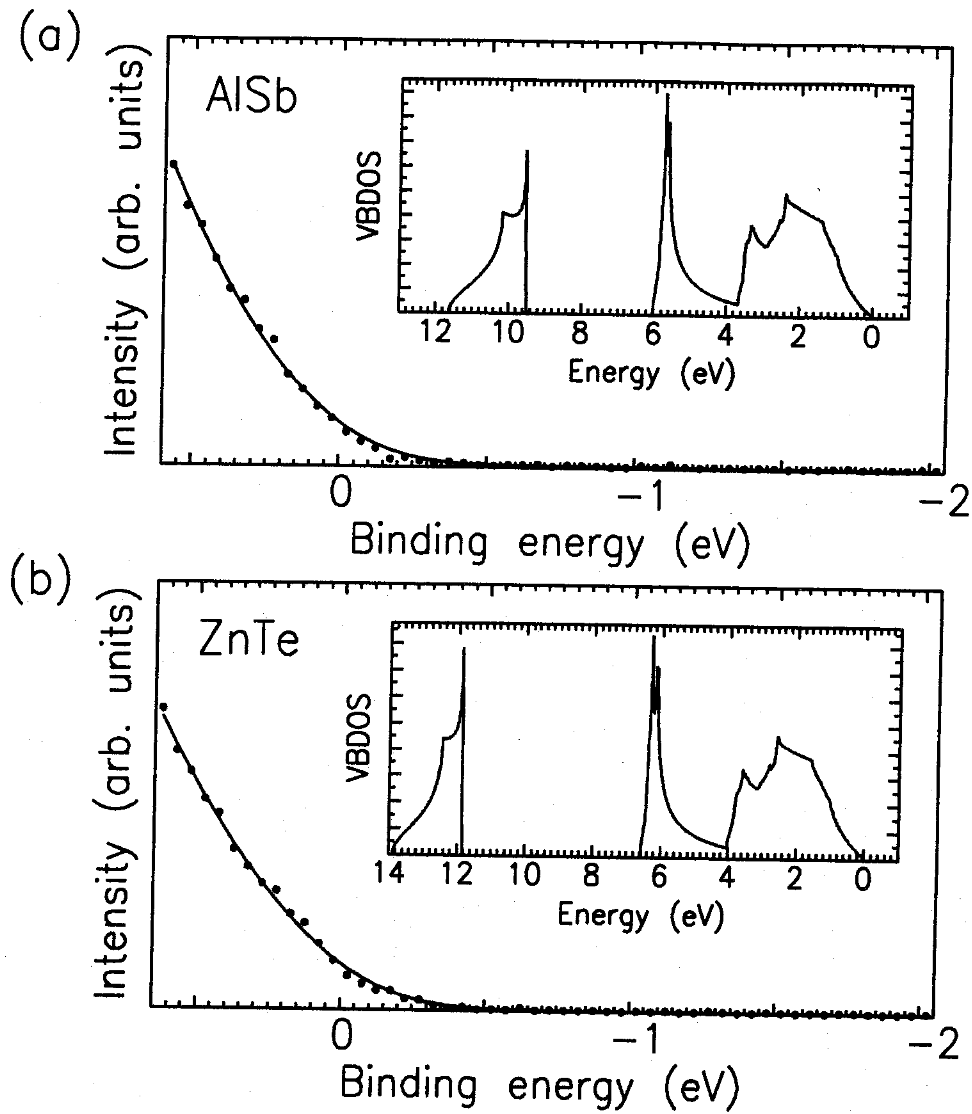

Figure 5.5: Typical XPS valence-band spectra and model functions fitted to the experimental data for (a) AlSb (100) and (b) ZnTe (100). The theoretical valence-band densities of states used to construct the model functions are shown in the insets to each figure. These model functions are used to determine the position of the valence-band edge in each spectrum.

heterojunction samples provides one way to confirm that the core-level binding energies are indeed bulk properties, and are not significantly influenced by the presence of the interface in a heterojunction sample.

For the bulk ZnTe samples, we obtained values of 9.42 ± 0.04 eV and 30.02 ± 0.02 eV for the Zn $3d$ core-level to valence-band-edge binding energy and the Te $4d_{5/2}$ to Zn $3d$ core-level energy separation, respectively. Comparison of these results with previous measurements is difficult, since reported values[38, 49, 50] for the Zn $3d$ core-level to valence-band-edge binding energy range from 9.1 eV to 9.84 eV.

Determination of the Al $2p$ to Zn $3d$ core-level energy separation in the AlSb/-ZnTe heterojunctions was complicated by the apparent formation of a reacted layer at the AlSb/ZnTe interface. Evidence of this reaction can be seen in the spectra for the Al $2p$, Sb $4d$, and Te $4d$ core-level spectra from the heterojunction samples. Figs. 5.6(a) and (b) show Sb $4d$ core-level spectra for bulk AlSb and for an AlSb/ZnTe heterojunction, respectively. The bulk AlSb spectrum contains a small component at higher binding energy compared to the main peak; an analogy with observed surface core-level shifts in the As-rich $c(4 \times 4)$ reconstruction of GaAs[51] suggests that this component may be due to excess Sb on the AlSb surface. The spectrum recorded from a heterojunction sample clearly shows a peak shifted to higher binding energy relative to the main peak structure; this shifted peak was present in all heterojunction samples, independent of the temperature at which the ZnTe layers were grown. By varying the electron take-off angle from the sample, and therefore the effective electron escape depth, we were able to determine that the smaller, shifted peak was due to Sb on the surface of the sample, i.e., on top of the thin ZnTe layer. This conclusion was also supported by the presence of a small but detectable Sb $4d$ core-level peak even for samples with 275 Å of ZnTe deposited on AlSb.

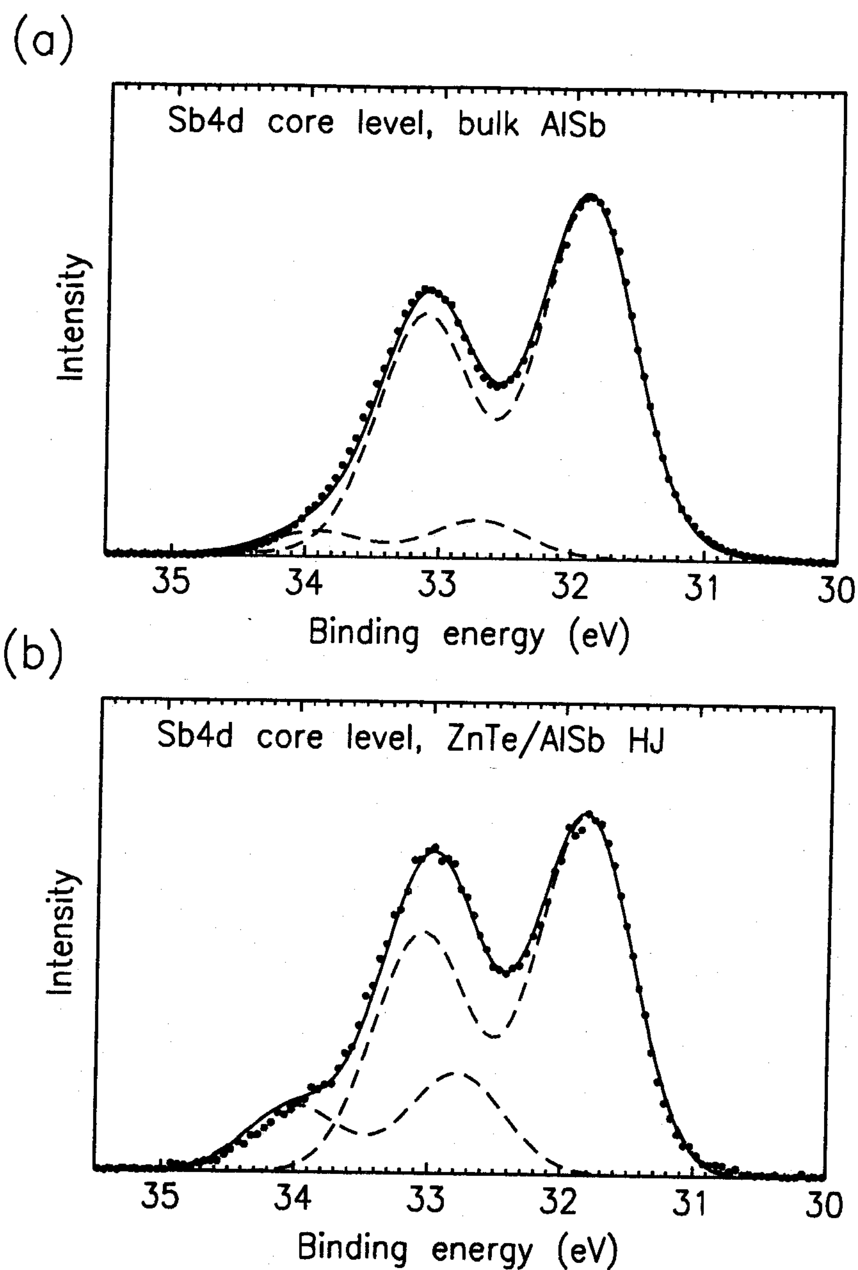

Figure 5.6: Sb 4*d* core-level XPS spectra from (a) bulk AlSb and (b) a ZnTe/-AlSb heterojunction. In the bulk spectrum, the small peak shifted to higher binding energy is thought to be due to excess Sb on the AlSb surface; in the heterojunction spectrum, the peak shifted to higher binding energy was found to originate from Sb at the sample surface, i.e., on top of the ZnTe layer.

The Al 2*p* core-level spectrum from an AlSb/ZnTe heterojunction, shown in Fig. 5.7(b), also exhibits a peak shifted to higher binding energy; the shifted peak is not present in the spectrum shown in Fig. 5.7(a), obtained from bulk AlSb. Electronegativity arguments would suggest that Al in the reacted layer is forming bonds with an element more electronegative than Sb, since a shift of the core level to higher binding energy indicates that more charge is transferred away from the Al atom. The only element present that is more electronegative than Sb is Te (2.1 for Te versus 1.9 for Sb on the Pauling electronegativity scale[52]); if Al and Te are indeed forming bonds in the interfacial layer, a peak shifted to lower binding energy should appear in the Te 4*d* spectrum from an AlSb/ZnTe heterojunction.

Figs. 5.8(a) and (b) show Te 4*d* core-level spectra from bulk ZnTe and an AlSb/ZnTe heterojunction, respectively, and a peak shifted to lower binding energy does indeed appear in the heterojunction spectrum. The Te 4*d* spectra also contain very small peaks shifted to higher binding energy; as with the bulk AlSb spectra, these peaks may be due to excess Te on the ZnTe surface.

The chemical behavior at the AlSb/ZnTe (100) interface thus appears to be quite similar to that observed at a number of other III-V/II-VI heterojunctions. Tu and Kahn[24] observed the formation of an intermediate layer containing Ga and Se at GaAs/ZnSe (110) and (100) interfaces, and detected a layer of Ga_2Se_3 in the wurtzite phase at the GaAs/ZnSe (110) interface. Mackey et al.[25] observed evidence that an interfacial layer containing primarily In and Te was formed at InSb/CdTe (100) and (110) interfaces. Wilke et al. have observed evidence of interfacial reactions and the formation of intermediate compounds composed primarily of the Group III and Group VI elements in GaSb/ZnTe (110)[26] and CdS/InP (110)[27] heterojunctions. Our measurements and analogies with other III-V/II-VI heterojunction systems suggest that a compound containing Al and

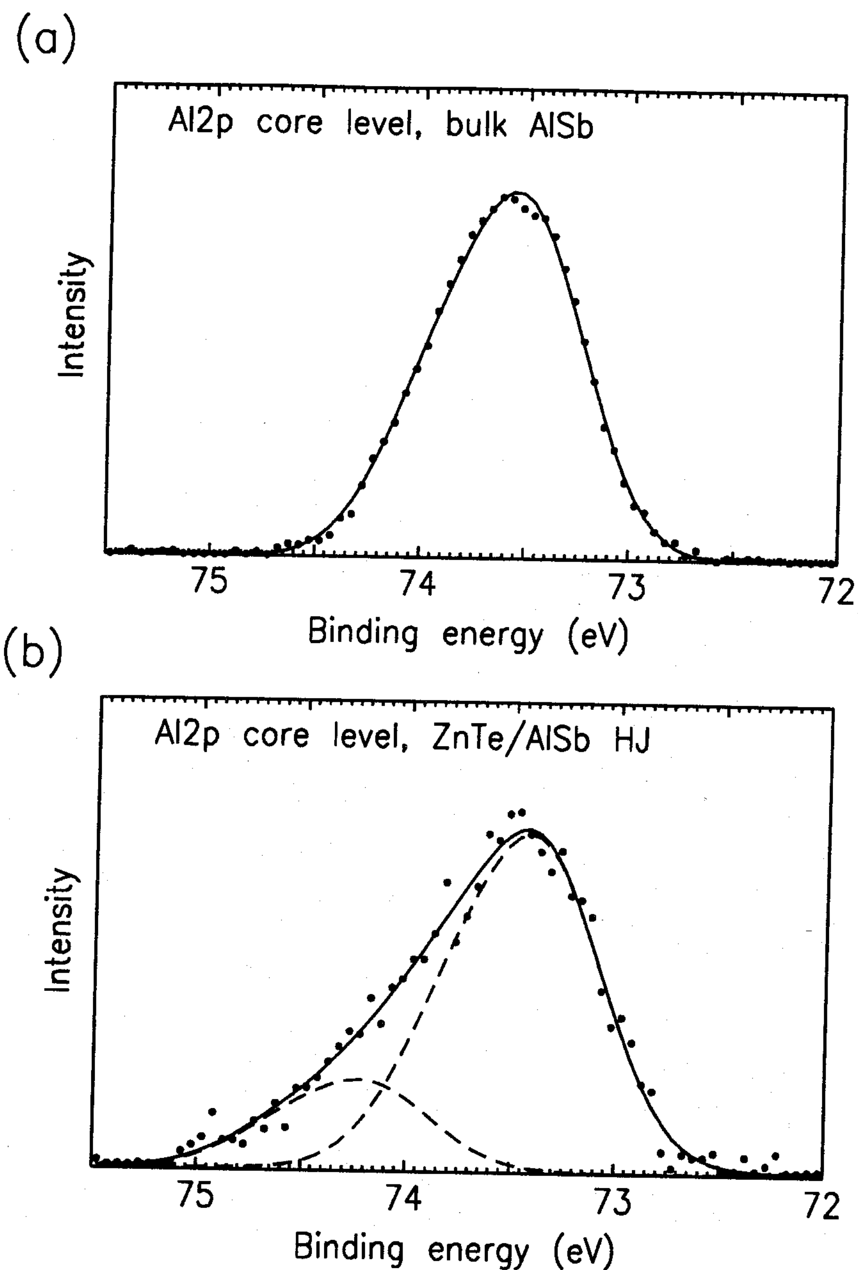

Figure 5.7: Al 2*p* core-level XPS spectra from (a) bulk AlSb and (b) a ZnTe/AlSb heterojunction. The bulk spectrum (a) contains only a single peak component; the heterojunction spectrum in (b) clearly contains a peak shifted to higher binding energy, indicating that Al bonding to Te is present in the reacted layer at the AlSb/ZnTe interface.

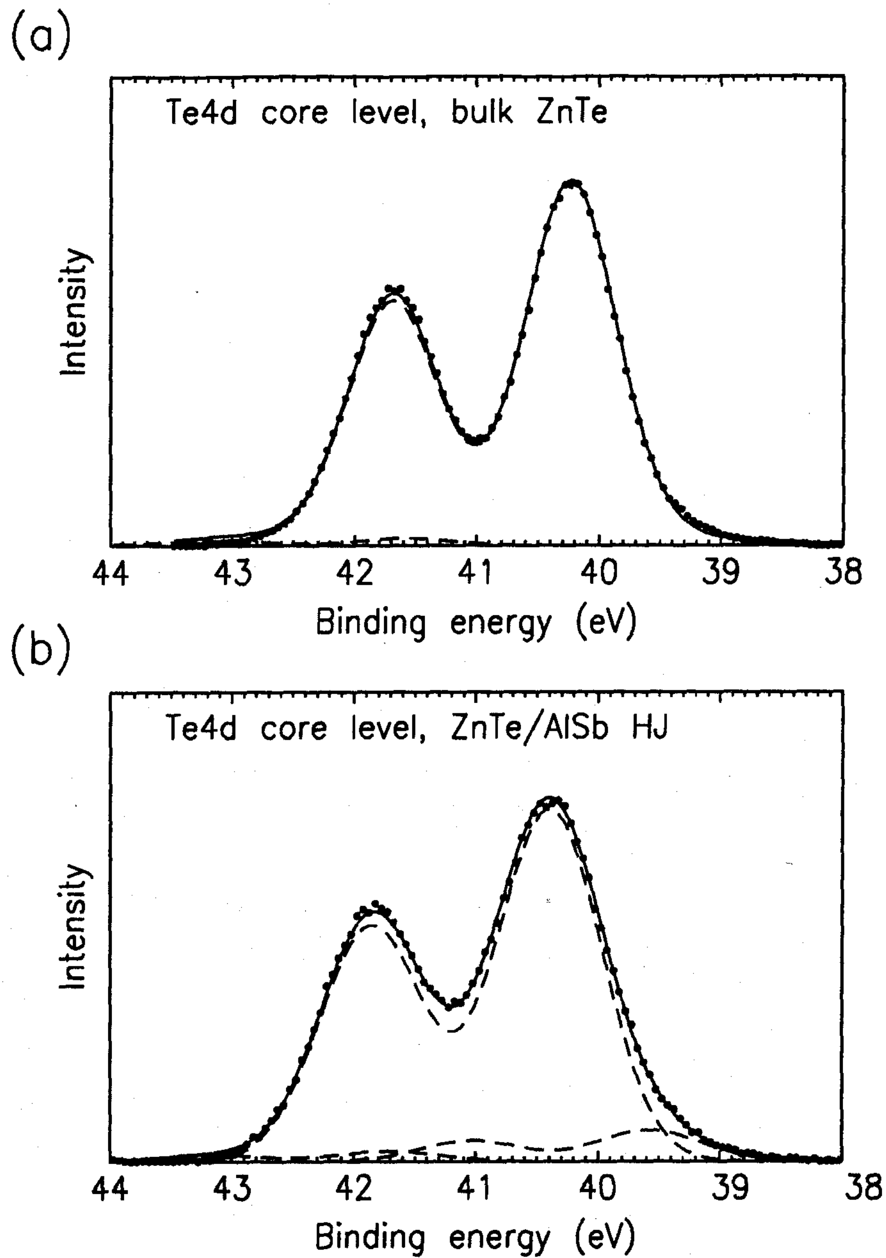

Figure 5.8: Te 4*d* core-level XPS spectra from (a) bulk ZnTe and (b) a ZnTe/-AlSb heterojunction. Both spectra contain a small peak shifted to higher binding energy with respect to the main peak; this peak may originate from excess Te at the ZnTe surface. The heterojunction spectrum also contains a peak shifted to lower binding energy, indicating that Te bonding to Al is present in the reacted layer at the AlSb/ZnTe interface.

Te is formed at the AlSb/ZnTe (100) interface. An examination of the binary alloy phase diagram[53] for Al and Te indicates that the most likely candidate is Al_2Te_3. A schematic diagram of the compounds believed to be present in our AlSb/ZnTe heterojunctions is shown in Fig. 5.9.

The presence of a large shifted peak in the Al $2p$ core-level spectrum from the ZnTe/AlSb heterojunction complicates the determination of the Al $2p$ to Zn $3d$ heterojunction core-level energy separation. To ensure that the position assigned to the Al $2p$ core level corresponded to that in bulk AlSb and was not affected by the presence of the chemically shifted component in the spectrum, we checked the energy separation between the Al $2p$ core-level peak components and the Sb $4d$ peak components. By requiring this energy separation to be equal in the bulk AlSb and AlSb/ZnTe heterojunction samples, we were able to identify unambiguously the peak components corresponding to the pure AlSb layer in the heterojunction. The Zn $3d$ core-level spectrum did not appear to contain a significant chemically shifted component, and the Zn $3d$ to Te $4d_{5/2}$ core-level energy separation in the AlSb/ZnTe heterojunctions was confirmed to be the same as that in bulk ZnTe.

We obtained a value of 63.08 ± 0.04 eV for the Al $2p$ to Zn $3d$ heterojunction core-level energy separation; the relatively large uncertainty in this measurement was due to the presence of the chemically shifted component in the Al $2p$ core-level spectrum. Using Eq. (5.2), we obtain a valence-band offset ΔE_v(AlSb/ZnTe) = 0.42 ± 0.07 eV; the corresponding conduction-band offset is $\Delta E_c = 0.21 \pm 0.07$ eV. The band alignment is therefore Type I, as shown schematically in Fig. 5.3.

Theoretical predictions for the AlSb/ZnTe valence-band offset encompass an extremely wide range of values. At one extreme, the common anion rule[17] predicts $\Delta E_v = 0.69$ eV for the GaSb/ZnTe heterojunction which, when combined with a measured AlSb/GaSb valence-band offset of 0.40 eV[16]

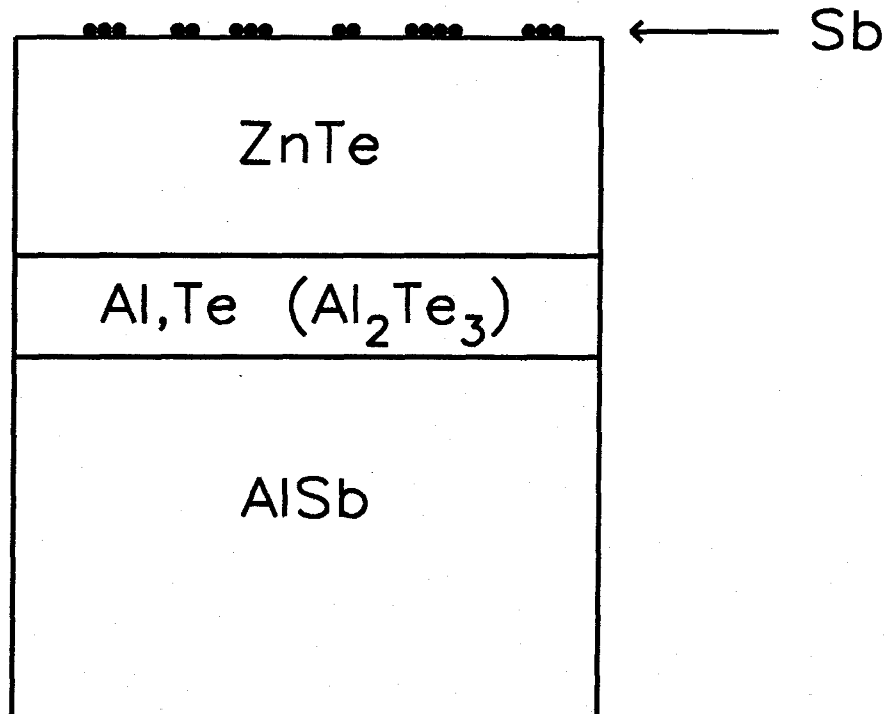

Figure 5.9: Schematic diagram of the compounds believed to be present in our AlSb/ZnTe heterojunctions. For ZnTe deposited on AlSb, an intermediate compound containing Al and Te, most likely in the form Al_2Te_3, is formed at the AlSb/ZnTe interface. In addition, excess Sb accumulates at the ZnTe surface and appears to move along with the ZnTe growth front.

yields ΔE_v(AlSb/ZnTe) = 0.29 eV, with the valence-band edge of ZnTe below that of AlSb — a Type I band lineup; at the other, the model of Von Ross[21] predicts ΔE_v = 1.18 eV, which corresponds to a Type II band lineup, with the valence-band edge of ZnTe below that of AlSb. Fig. 5.10, like Fig. 5.2, shows the range of values proposed for the AlSb/ZnTe valence-band offset, based on the experimental value of 0.40 eV for the AlSb/GaSb valence-band offset[16] and predicted band offset values for the GaSb/ZnTe heterojunction[8, 9, 10, 11, 12, 13, 14, 15, 17, 18, 19, 20, 21], but also includes the valence-band offset value we obtained from our measurements. The serious discrepancies among these theoretical values attest to the need for reliable experimental measurements of band offsets for AlSb/ZnTe and other novel heterojunction systems.

An issue of concern is the effect of the reacted layer on the electronic structure of the interface. Varying the temperature at which the ZnTe in the heterojunction was grown from 270 °C to 330 °C did not have a discernible effect on the value of the band offset, but previously reported measurements of the band offsets in AlSb/GaSb and GaSb/ZnTe heterojunctions suggest that the effect of interface reactions on band offset values may be significant. Recent calculations[13, 15, 20, 54, 55] have suggested that in many material systems band offsets should be transitive, even if one does not assume that band offsets depend only on inherent properties of the constituent bulk materials. Previous experiments on the Ge/GaAs/AlAs material system[56] have shown that, for high-quality interfaces, band offsets obey the transitivity rule. The reported valence-band offset for AlSb/GaSb heterojunctions is ~0.40 eV, and for the GaSb/ZnTe (110) heterojunction a value of 0.34 eV has been obtained[26]; assuming that transitivity is valid, these results yield a valence band offset of −0.06 eV for AlSb/ZnTe, which differs from our result by 0.48 eV. This discrepancy suggests

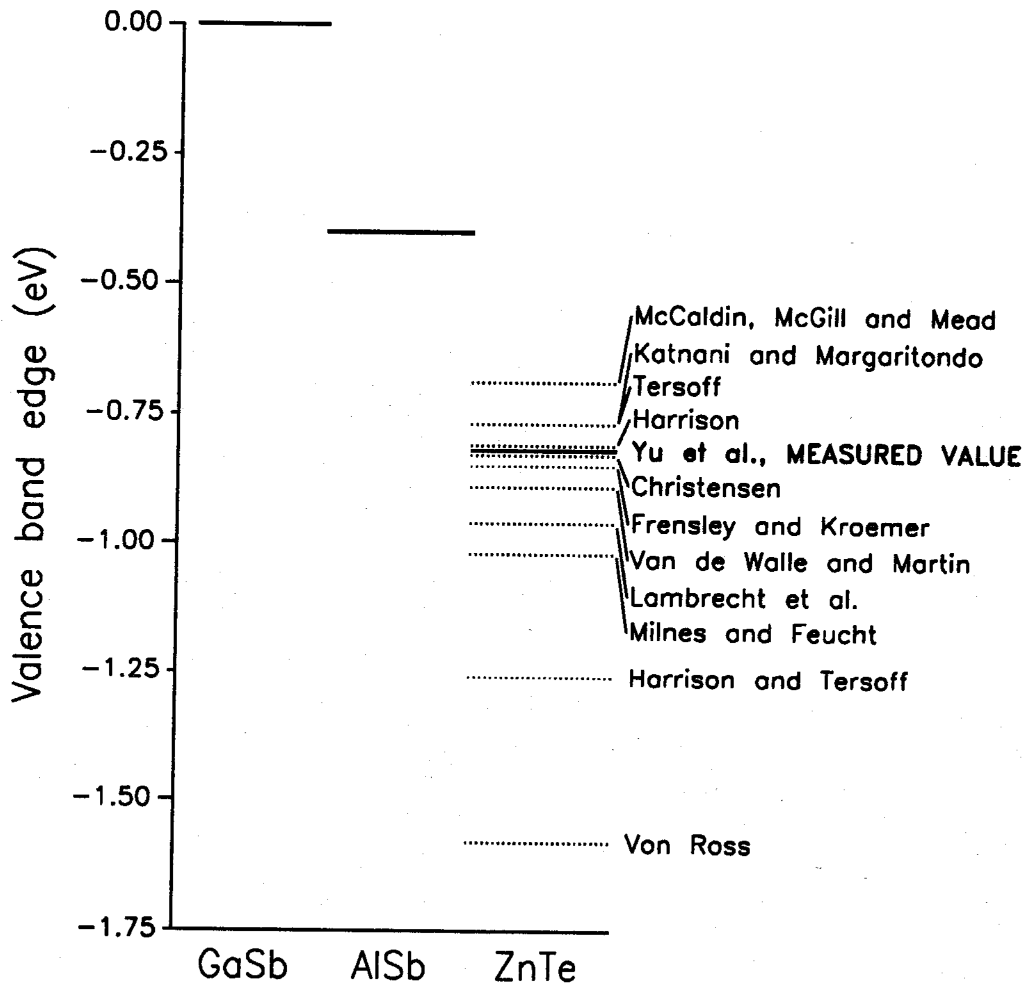

Figure 5.10: Our measured AlSb/ZnTe valence-band offset, $\Delta E_v = 0.42 \pm 0.07$ eV, shown amidst a range of proposed valence-band offset values for the AlSb/ZnTe heterojunction, based on the experimental value of 0.40 eV for the AlSb/GaSb valence-band offset and predicted values for the GaSb/ZnTe valence-band offset[8, 9, 10, 11, 12, 13, 14, 15, 17, 18, 19, 20, 21].

that effects due to the detailed structure of the interfaces, and possibly related to the nonideal interfaces formed in III-V/II-VI heterojunctions, could have a significant influence on band offset values.

Our results also have implications for the viability of n-AlSb/p-ZnTe light-emitting diode structures. In their original proposal, McCaldin and McGill[6] argued that efficient electron injection from AlSb into ZnTe would be difficult to achieve if the conduction-band offset were too large; high doping levels in the AlSb layers would also be required, unless the conduction-band offset were small, i.e., $\Delta E_c \lesssim 0.2$ eV. Recent efforts[7] to dope AlSb using PbTe have resulted in n-type AlSb with carrier concentrations as high as $\sim 9 \times 10^{17}\text{cm}^{-3}$. A conduction-band offset of 0.21 eV therefore indicates that reasonably efficient electron injection from AlSb into ZnTe may be possible, provided that the AlSb layers are heavily doped.

5.3 Transitivity in the AlSb/GaSb/ZnTe Material System

Section 5.2.3 alluded to possible effects of interfacial reactions on band offset values, and ways in which such effects might manifest themselves as violations of band offset transitivity. The transitivity rule for band offsets is simply the statement that, for three semiconductors A, B, and C, the following relationship for band offsets should be valid:

$$\Delta E_v(A/B) + \Delta E_v(B/C) + \Delta E_v(C/A) = 0. \tag{5.3}$$

There exists considerable theoretical and experimental evidence that for abrupt interfaces, the transitivity rule should apply. Eq. (5.3) is obviously valid for theories that treat band offsets simply as properties of the bulk constituent ma-

terials forming a heterojunction. However, a number of theories that include effects arising from the detailed structure of specific interfaces also yield results that, within the accuracy of the calculations, are consistent with the transitivity rule[13, 15, 20, 54, 55].

The self-consistent density-functional calculations of Van de Walle and Martin[13] using *ab initio* nonlocal pseudopotentials yield valence-band offsets for the Si/GaP/AlP (110) and GaAs/AlAs/Ge/ZnSe (110) material systems that satisfy the transitivity rule to within ± 0.05–0.10 eV, which is well within the accuracy of their calculations. Calculations by Christensen[20, 54] using a self-consistent, relativistic linear muffin-tin orbital (LMTO) scheme yielded valence-band offsets for the Si/GaP/AlP (110), GaAs/AlAs/Ge/ZnSe (110), and InAs/-GaSb/ZnTe (110) material systems that obey transitivity to within ± 0.10 eV; however, Christensen also noted that for a few compounds such as CuBr interface states tended to form at heterojunctions, causing band offset values to deviate from transitivity. Lambrecht et al.[15, 55] performed calculations of band offset values, also using LMTO methods, and obtained valence-band offset values for the Si/GaP/AlP (110), GaAs/AlAs/Ge/ZnSe (110), and InAs/GaSb/AlSb/ZnTe (110) material systems that are transitive to within ± 0.10 eV.

Experimentally, there is substantial evidence that for interfaces of sufficiently high quality, band offsets should obey the transitivity rule. Katnani and Bauer[56] have demonstrated the validity of the transitivity rule for valence-band offsets in the Ge/GaAs/AlAs material system, obtaining band offsets using XPS that satisfy Eq. (5.3) to within ± 0.05 eV. Our measurements demonstrating the commutativity of the GaAs/AlAs (100) valence-band offset, discussed in Chapter 3 and Ref. [57], and similar results of Hirakawa et al.[58], provide further evidence that band offsets for high-quality, lattice-matched interfaces should be both commutative and transitive. There is also evidence, however, that even in the relatively

well-understood Ge/GaAs/AlAs material system, under certain conditions interface chemistry can affect band offset values. Waldrop et al.[37] observed that depending on the interface orientation and surface reconstruction upon which a heterojunction was grown, the GaAs/Ge valence-band offset varied from 0.48 to 0.66 eV. In addition, measurements by Waldrop et al.[59, 60] yielded a dependence of the GaAs/AlAs valence-band offset on both interface orientation and growth sequence.

These results indicate that although the detailed atomic structure of the interface can have a sizable effect on band offset values, interfaces of sufficiently high quality should exhibit the behavior expected theoretically, e.g., commutativity and transitivity, from abrupt, ideal interfaces. We have therefore attempted to elucidate the influence of interfacial reactions on band offset values by testing the validity of the transitivity rule for the lattice-matched AlSb/GaSb/ZnTe material system. If the presence of nonideal interfaces, such as the III-V/II-VI interfaces at which interfacial reactions were observed, were affecting band offset values, a deviation from transitivity should be observed; if the interfacial reactions were not affecting band offset values, the transitivity rule should be valid. To test the transitivity rule for the AlSb/GaSb/ZnTe material system, we measured the valence-band offsets for the AlSb/GaSb (100) and GaSb/ZnTe (100) heterojunctions. These measurements were then combined with the value we obtained for the AlSb/ZnTe (100) valence-band offset, 0.42 ± 0.07 eV, to determine the deviation from the transitivity condition, Eq. (5.3).

5.3.1 The AlSb/GaSb (100) Heterojunction

Fig. 5.11 shows a schematic energy-band diagram for the AlSb/GaSb heterojunction. The indirect nature of the AlSb band gap is indicated by the dashed

line for the AlSb conduction-band edge. As shown in the figure, the valence-band offset is given by

$$\Delta E_v = (E_{\mathrm{Ga3}d}^{\mathrm{GaSb}} - E_v^{\mathrm{GaSb}}) + (E_{\mathrm{Al2}p}^{\mathrm{AlSb}} - E_{\mathrm{Ga3}d}^{\mathrm{GaSb}}) - (E_{\mathrm{Al2}p}^{\mathrm{AlSb}} - E_v^{\mathrm{AlSb}}). \tag{5.4}$$

Samples for this study were grown in a Perkin-Elmer 430P MBE system on GaSb (100) substrates, either *p*-type ($p \sim 1 \times 10^{17}\mathrm{cm}^{-3}$) or degenerately doped *n*-type. Following oxide desorption at 530 °C, a GaSb buffer layer was grown at 100 Å/min., with the substrate at 475 °C. The AlSb layers were grown at 62.5 Å/min. with a substrate temperature of 530 °C. All samples were transferred directly from the MBE growth chamber to the XPS analytical chamber under UHV conditions.

The Ga 3*d* and Al 2*p* core-level to valence-band-edge binding energies were measured in bulk GaSb (100) and AlSb (100) films, respectively. The Al 2*p* core-level to valence-band-edge binding energy was measured in two samples, as described in Section 5.2. We obtained an Al 2*p* core-level to valence-band-edge binding energy of 72.92±0.04 eV. The Ga 3*d* core-level to GaSb valence-band-edge binding energy was measured in one sample, consisting of 5000 Å of nominally undoped GaSb grown on a *p*-type ($p \sim 1 \times 10^{17}\mathrm{cm}^{-3}$) GaSb (100) substrate. Our measurements yielded a Ga 3*d* core-level to valence-band-edge binding energy of 18.86 ± 0.04 eV, in reasonable agreement with a previously reported value of ~ 18.90 eV[16]. Figs. 5.12(a) and (b) show representative XPS spectra for bulk AlSb (100) and bulk GaSb (100), respectively; the valence-band spectra are also shown on enlarged scales, as indicated in the figure.

The position of the GaSb valence-band edge was determined using the precision analysis technique of Kraut et al.[39], as described in Section 5.2.2. For GaSb, the empirical pseudopotential parameters were obtained by optimizing our

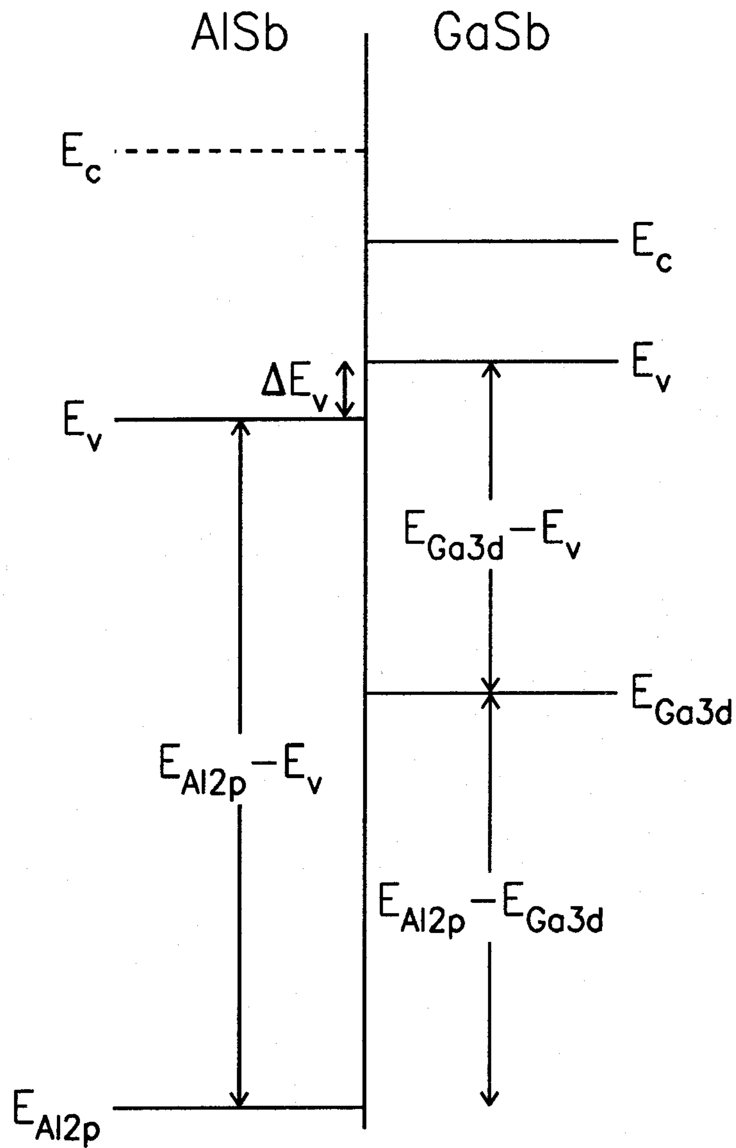

Figure 5.11: Schematic energy-band diagram for the AlSb/GaSb (100) heterojunction. As indicated by the dashed line for the AlSb conduction-band edge, the band gap in AlSb is indirect, with the conduction-band minimum in the Δ direction in the Brillouin zone.

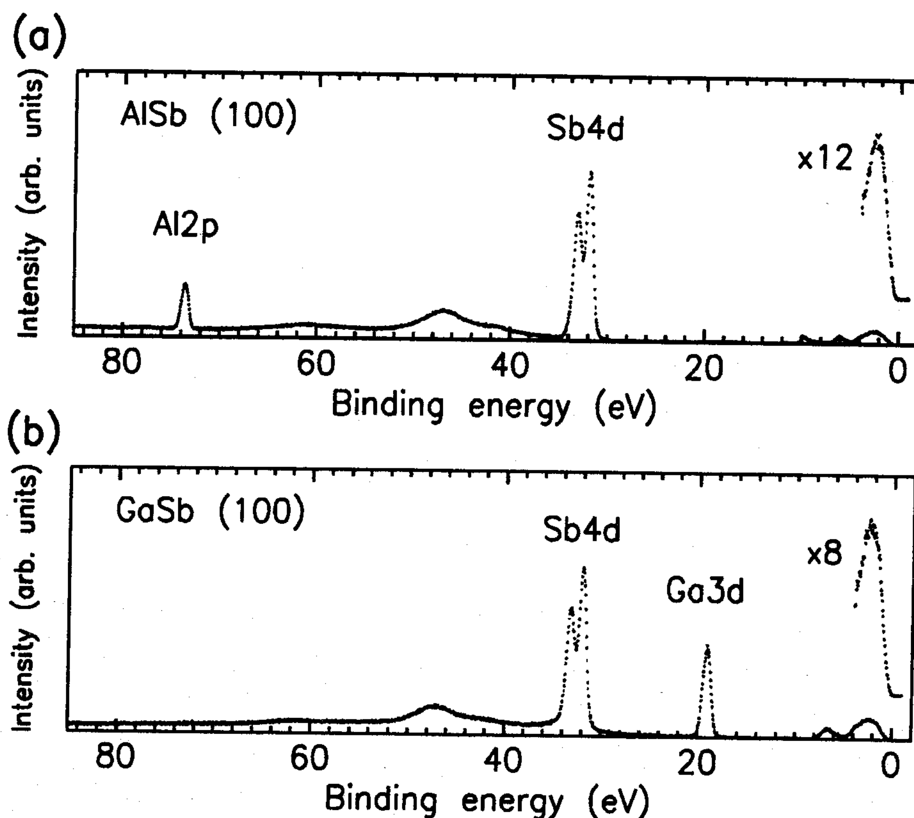

Figure 5.12: Representative binding energy XPS spectra for (a) bulk AlSb (100), and (b) bulk GaSb (100). The Al $2p$ core-level to valence-band-edge binding energy is measured in the bulk AlSb samples, and the Ga $3d$ core-level to valence-band-edge binding energy is measured in the bulk GaSb samples. Longer sampling times were used in the vicinity of the valence-band edges to obtain adequate intensities in the valence-band spectra. The valence-band spectra for each material are also shown on enlarged intensity scales, as indicated in the figure.

calculated band structure to give the best agreement at the Γ, X, and L points in the Brillouin zone with the band structure calculated by Chelikowsky and Cohen[61] using a nonlocal empirical pseudopotential method. Fig. 5.13 shows the valence-band spectrum, model function fitted to the XPS data, and calculated valence-band density of states used to construct the model function, for GaSb (100).

The Al $2p$ to Ga $3d$ core-level energy separation was measured in two heterojunctions, one consisting of 25 Å of AlSb grown on top of $\sim$5000 Å of GaSb, and the other consisting of 20 Å of GaSb grown on top of $\sim$5000 Å of AlSb. For the sample consisting of AlSb grown on top of GaSb, the separation between the Al $2p$ and Ga $3d$ core levels was measured to be 54.43 ± 0.02 eV; for GaSb grown on top of AlSb, our measurements yielded an Al $2p$ to Ga $3d$ core-level energy separation of 54.46 ± 0.02 eV. Combining the measurements obtained from these two heterojunctions, we obtain an Al $2p$ to Ga $3d$ core-level energy separation of 54.45 ± 0.03 eV. Within the range of experimental error, our measurements confirm the commutativity of the valence-band offset for the AlSb/GaSb (100) heterojunction, suggesting that we have been able to grow abrupt AlSb/GaSb interfaces in which the influence of chemical reactivity is minimal. The slight difference in core-level energy separations for the two different growth sequences could arise from a variety of sources, one notable possibility being the slight lattice mismatch between AlSb and GaSb ($\sim 0.7\%$), which would induce strain in the top layer of the heterojunction, resulting in a slight asymmetry for the two growth sequences. Typical XPS spectra for AlSb grown on GaSb and for GaSb grown on AlSb are shown in Figs. 5.14(a) and (b), respectively.

Combining the measurements of the Al $2p$ and Ga $3d$ core-level to valence-band-edge binding energies and the Al $2p$ to Ga $3d$ heterojunction core-level energy separation using Eq. (5.4), we obtain an AlSb/GaSb valence-band off-

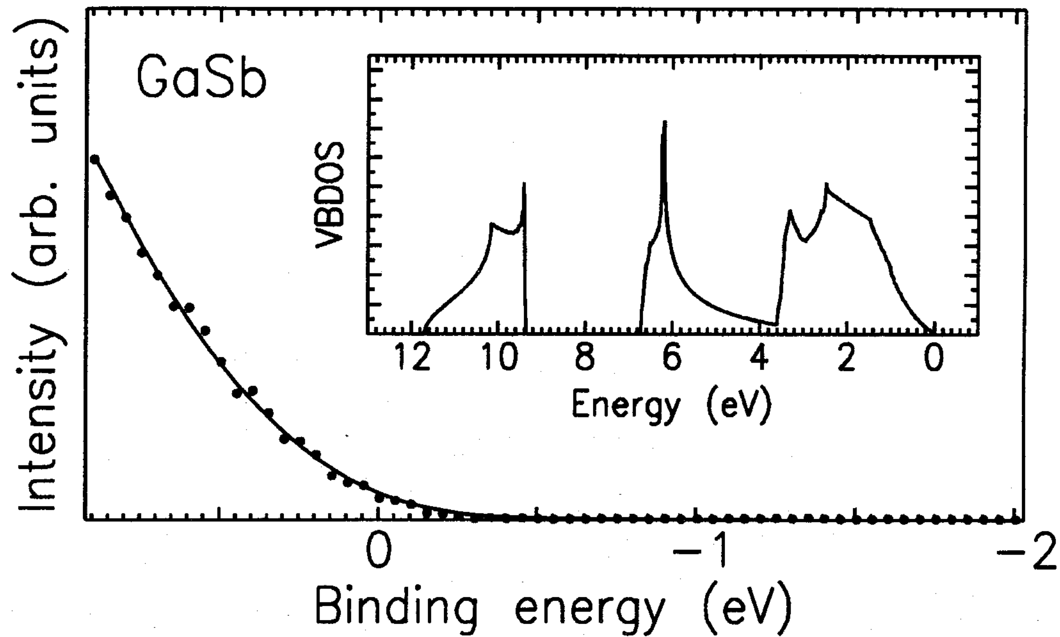

Figure 5.13: Typical XPS valence-band spectrum and model function fitted to the experimental data for GaSb (100). The theoretical valence-band density of states used to construct the model function is shown in the inset to the figure. The model function is used to determine the position of the valence-band edge in the spectrum.

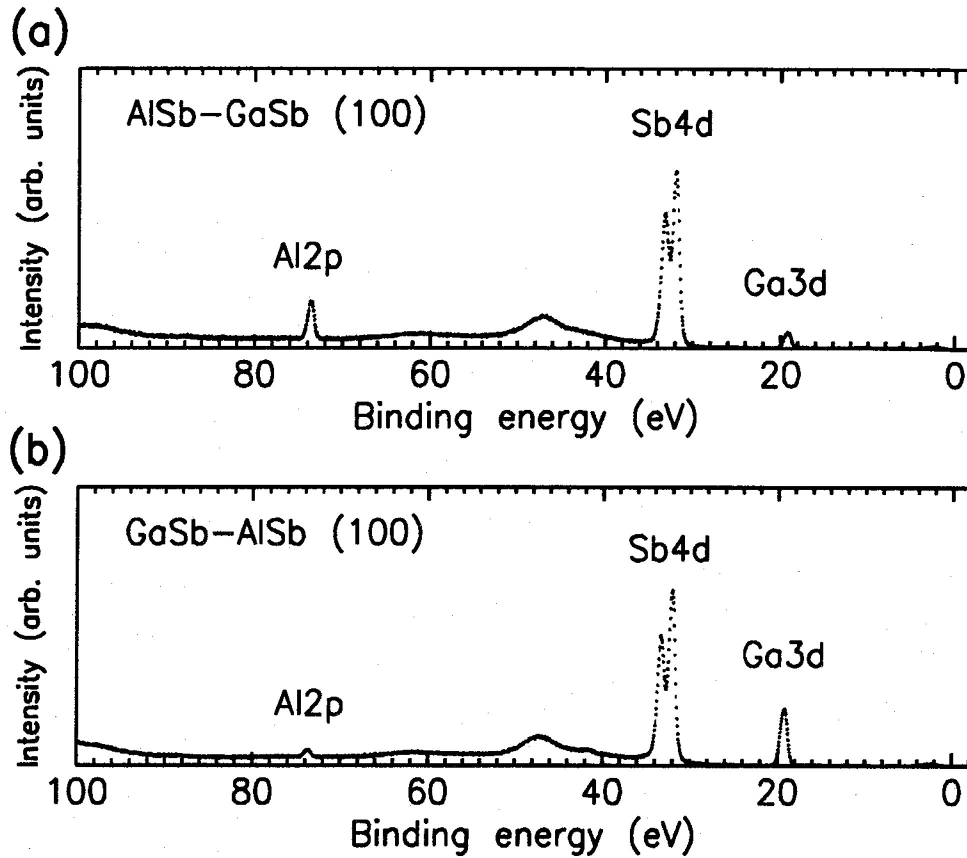

Figure 5.14: Representative binding energy XPS spectra for (a) 25 Å AlSb grown on GaSb, and (b) 20 Å GaSb grown on AlSb. The Al $2p$ to Ga $3d$ core-level energy separation is measured in these samples. Comparing the results from the two different growth sequences allowed the commutativity of the AlSb/GaSb band offset to be checked.

set $\Delta E_v = 0.39 \pm 0.07$ eV. This measurement is in good agreement with previously reported values. Tejedor et al.[63] used resonant Raman scattering to study the electronic structure of GaSb/AlSb superlattices, and concluded that ΔE_v(AlSb/GaSb) > 0.267 eV. Gualtieri et al.[16] obtained a AlSb/GaSb valence-band offset of 0.40 ± 0.15 eV using XPS measurements. Menéndez et al.[62] obtained $\Delta E_v(\text{AlSb/GaSb}) = 0.45 \pm 0.08$ eV using a light-scattering method. Measurements of optical absorption and excitation in GaSb/AlSb multiple quantum wells by Cebulla et al.[65] yielded a valence-band offset $\Delta E_v(\text{AlSb/GaSb}) =$ 0.35 eV. Finally, Beresford et al.[66] have observed resonant tunneling of holes in GaSb/AlSb/GaSb/AlSb/GaSb heterostructures, consistent with a substantial valence-band offset, $\Delta E_v(\text{AlSb/GaSb}) \sim 0.4$ eV.

5.3.2 The GaSb/ZnTe (100) Heterojunction

Fig. 5.15 shows a schematic energy-band diagram for the GaSb/ZnTe heterojunction. The effects of strain on the electronic structure of the heterojunction have been neglected because of the extremely small lattice mismatch ($\sim 0.15\%$) between GaSb and ZnTe. As shown in the figure, the valence-band offset is given by

$$\Delta E_v = (E_{\text{Ga3}d}^{\text{GaSb}} - E_v^{\text{GaSb}}) - (E_{\text{Zn3}d}^{\text{ZnTe}} - E_v^{\text{ZnTe}}) - (E_{\text{Ga3}d}^{\text{GaSb}} - E_{\text{Zn3}d}^{\text{ZnTe}}). \tag{5.5}$$

The samples for this study were grown in two Perkin-Elmer 430P MBE systems, as described in Sections 5.2 and 5.3.1. Samples were grown on p-type GaSb (100) substrates ($p \sim 1 \times 10^{17}\text{cm}^{-3}$). Following oxide desorption at $\sim 530\,^\circ$C, a GaSb layer was grown at 100 Å/min., with the substrate at 475 °C. The ZnTe layers were grown at 50 Å/min. and using a substrate temperature of 270 °C. The GaSb layers were grown in an MBE chamber dedicated to the growth of III-

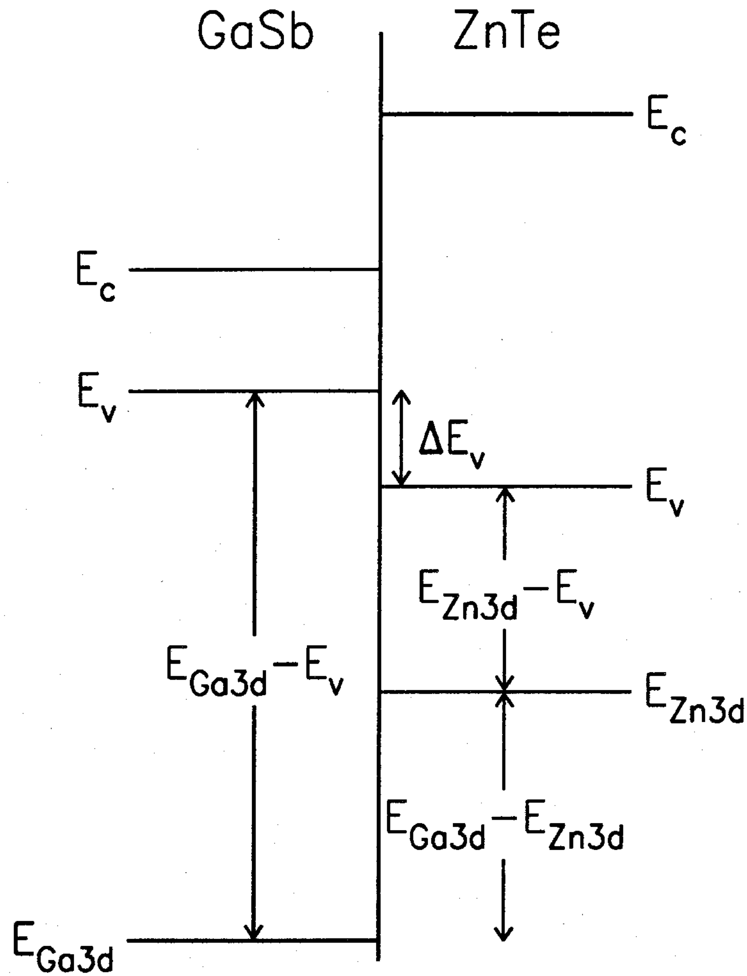

Figure 5.15: Schematic energy-band diagram for the GaSb/ZnTe (100) heterojunction. The valence-band offset ΔE_v is obtained by measuring the Ga $3d$ and Zn $3d$ core-level to valence-band-edge binding energies in bulk GaSb (100) and ZnTe (100), respectively, and by measuring the Ga $3d$ to Zn $3d$ core level energy separation in a GaSb/ZnTe (100) heterojunction.

V semiconductors, and the ZnTe layers in a growth chamber dedicated to II-VI materials. All samples were transferred among the two MBE chambers and the XPS analytical chamber under UHV conditions.

The measurement of the Zn *3d* core-level to valence-band-edge binding energy in bulk ZnTe has been described in Section 5.2; the determination of the Ga *3d* core-level to valence-band-edge binding energy in bulk GaSb was presented in Section 5.3.1. Our measurements yielded a Zn *3d* core-level to valence-band-edge binding energy of 9.42 ± 0.04 eV, and a Ga *3d* core-level to valence-band-edge binding energy of 18.86 ± 0.04 eV. Core-level energy separations were also measured in each material. For ZnTe, we obtained a Te $4d_{5/2}$ to Zn *3d* core-level energy separation of 30.02 ± 0.02 eV; for GaSb, we measured a Sb $4d_{5/2}$ to Ga *3d* core-level energy separation of 12.80 ± 0.02 eV.

To measure the Ga *3d* to Zn *3d* heterojunction core-level energy separation, a heterojunction sample was grown consisting of ~ 25 Å ZnTe grown on GaSb. The GaSb surface exhibited an initial (1×3) RHEED pattern; a streaky (2×1) ZnTe RHEED pattern appeared within approximately five seconds after the ZnTe growths were begun, indicating that growth was two-dimensional. Growth of the GaSb/ZnTe heterojunction sample required the use of both MBE growth chambers, with the samples being transported between the two systems under UHV conditions. Immediately following all growths, samples were transported under UHV conditions to the XPS analytical chamber for analysis.

Representative XPS spectra for bulk GaSb, bulk ZnTe, and GaSb/ZnTe heterojunctions are shown in Figs. 5.16(a), (b), and (c), respectively. The valence-band spectra for the bulk GaSb and bulk ZnTe samples are shown on enlarged scales, as indicated in the figure. The Ga *3d* core-level to valence-band-edge binding energy and the Sb $4d_{5/2}$ to Ga *3d* core-level energy separation were measured in bulk GaSb; the Zn *3d* core-level to valence-band-edge binding energy and the

Te $4d_{5/2}$ to Zn $3d$ core-level energy separation were measured in bulk ZnTe. In the GaSb/ZnTe heterojunction sample we measured the Ga $3d$ to Zn $3d$ heterojunction core-level energy separation and the Sb $4d_{5/2}$ to Ga $3d$ and Te $4d_{5/2}$ to Zn $3d$ core-level energy separations. The Sb $4d_{5/2}$ to Ga $3d$ and Te $4d_{5/2}$ to Zn $3d$ core-level energy separations were measured in both the bulk and the heterojunction samples to ensure that the core-level binding energies we measured in the GaSb/ZnTe heterojunction were truly characteristic of the bulk material.

Our measurements on the GaSb/ZnTe (100) heterojunction sample yielded a Ga $3d$ to Zn $3d$ core-level energy separation of 8.84 ± 0.03 eV. An analysis of Sb $4d$, Ga $3d$, and Te $4d$ core-level spectra from bulk GaSb or ZnTe and from the GaSb/-ZnTe heterojunction revealed some evidence of an interfacial reaction similar to that occurring for the AlSb/ZnTe interface; however, the chemically shifted peaks in core-level spectra from the GaSb/ZnTe heterojunction were considerably less pronounced than those observed in the AlSb/ZnTe heterojunction. Figs. 5.17(a), (b), and (c) show the Sb $4d$, Ga $3d$, and Te $4d$ core-level spectra, respectively, from bulk GaSb or ZnTe and from the GaSb/ZnTe heterojunction. The Sb $4d$ core-level spectrum from the heterojunction contains a sizable component shifted to higher binding energy, arising from Sb atoms on the ZnTe surface; the Ga $3d$ heterojunction spectrum appears to contain a small peak component shifted to higher binding energy that is not present in the bulk spectrum, which would arise from Ga atoms in a reacted layer formed at the GaSb/ZnTe interface; the Te $4d$ heterojunction spectrum contains a peak component shifted to lower binding energy that is not present in the bulk spectrum, which would arise from Te atoms in an intermediate layer at the GaSb/ZnTe interface. Shifts of the Ga $3d$ peak component to higher binding energy and of the Te $4d$ peak component to lower binding energy are consistent with what one would expect, on the basis of electronegativity arguments similar to those presented in Section 5.2.3, for a

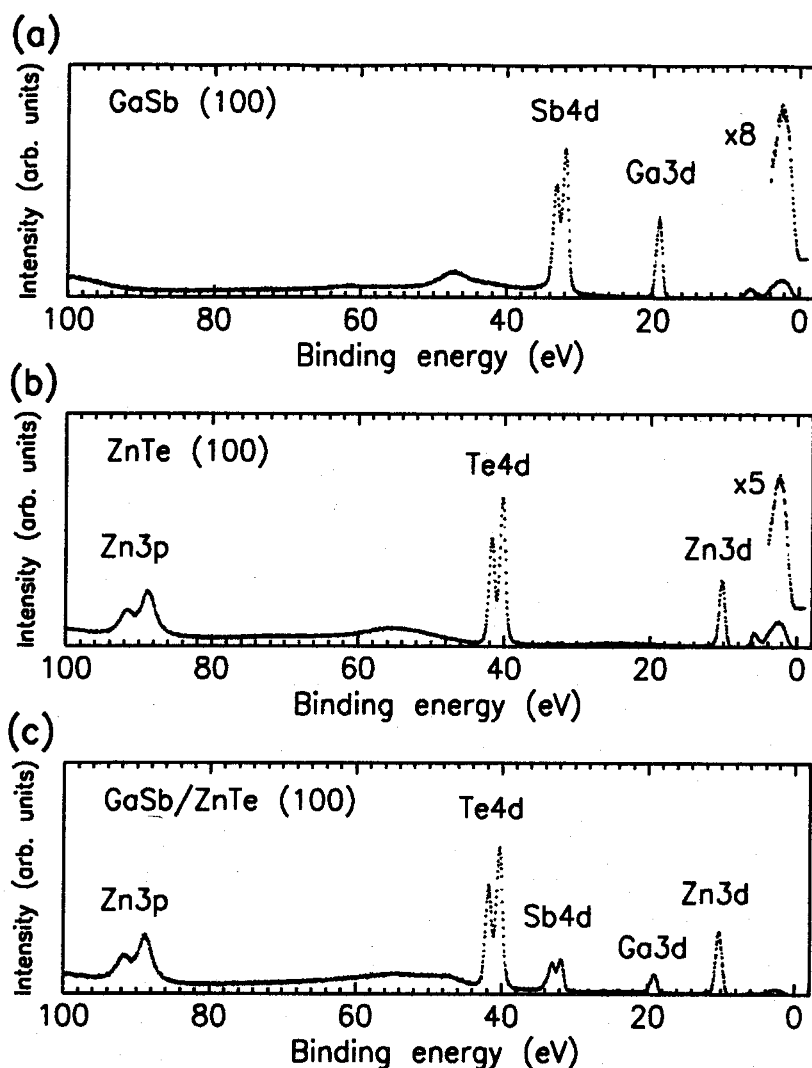

Figure 5.16: Representative binding energy XPS spectra for (a) bulk GaSb (100), (b) bulk ZnTe (100), and (c) a GaSb/ZnTe (100) heterojunction. The Ga 3*d* core-level to valence-band-edge binding energy was measured in the bulk GaSb samples, the Zn 3*d* core-level to valence-band-edge binding energy in the bulk ZnTe samples, and the Ga 3*d* to Zn 3*d* core-level energy separation in the GaSb/-ZnTe heterojunction. Longer sampling times were used in the vicinity of the valence-band edges to obtain adequate intensity in the valence-band spectra. The valence-band spectra for the bulk GaSb and ZnTe samples are also shown on enlarged intensity scales, as indicated in the figure.

reacted layer containing Ga and Te.

Using Eq. (5.5), we obtain a GaSb/ZnTe (100) valence-band offset $\Delta E_v(\text{GaSb/ZnTe}) = 0.60 \pm 0.07$ eV. This result is in fairly poor agreement with the value of 0.34 ± 0.05 eV obtained by Wilke and Horn[26] for the GaSb/ZnTe (110) heterojunction. The origin of this discrepancy is unknown, but a number of possibilities exist. Wilke and Horn observed considerable evidence of a GaSb/ZnTe interfacial reaction, which could affect the value of the band offset differently for their measurement than for ours. In addition, the difference in crystal orientation ((100) for our measurements compared to (110) for Wilke and Horn) will affect the detailed structure of the interface and could therefore influence the band offset value. Theoretical values for the GaSb/ZnTe valence-band offset are shown in Figs. 5.2 and 5.10, and range from 0.69 eV[17] to 1.58 eV[21].

5.3.3 Demonstration of Nontransitivity

Combining our measured valence band offsets for the AlSb/ZnTe, AlSb/-GaSb, and GaSb/ZnTe heterojunctions of 0.42 eV, 0.39 eV, and 0.60 eV, respectively, we see from Eq. (5.3) that transitivity for the AlSb/GaSb/ZnTe (100) material system is violated by 0.21 ± 0.05 eV. This discrepancy is far larger than the experimental uncertainty of our measurements. From Eqs. (5.2), (5.4), and (5.5), we can see that the transitivity rule can be verified simply from the measured core-level energy separations in the three heterojunctions:

$$\Delta E_v(\text{AlSb/ZnTe}) + \Delta E_v(\text{AlSb/GaSb}) + \Delta E_v(\text{GaSb/ZnTe}) = \quad (5.6)$$
$$(E^{\text{GaSb}}_{\text{Ga3}d} - E^{\text{ZnTe}}_{\text{Zn3}d}) + (E^{\text{AlSb}}_{\text{Al2}p} - E^{\text{GaSb}}_{\text{Ga3}d}) - (E^{\text{AlSb}}_{\text{Al2}p} - E^{\text{ZnTe}}_{\text{Zn3}d}).$$

If transitivity were valid for the AlSb/GaSb/ZnTe material system, one would expect Eq. (5.3) to be true to within ± 0.05 eV or better; our measurements

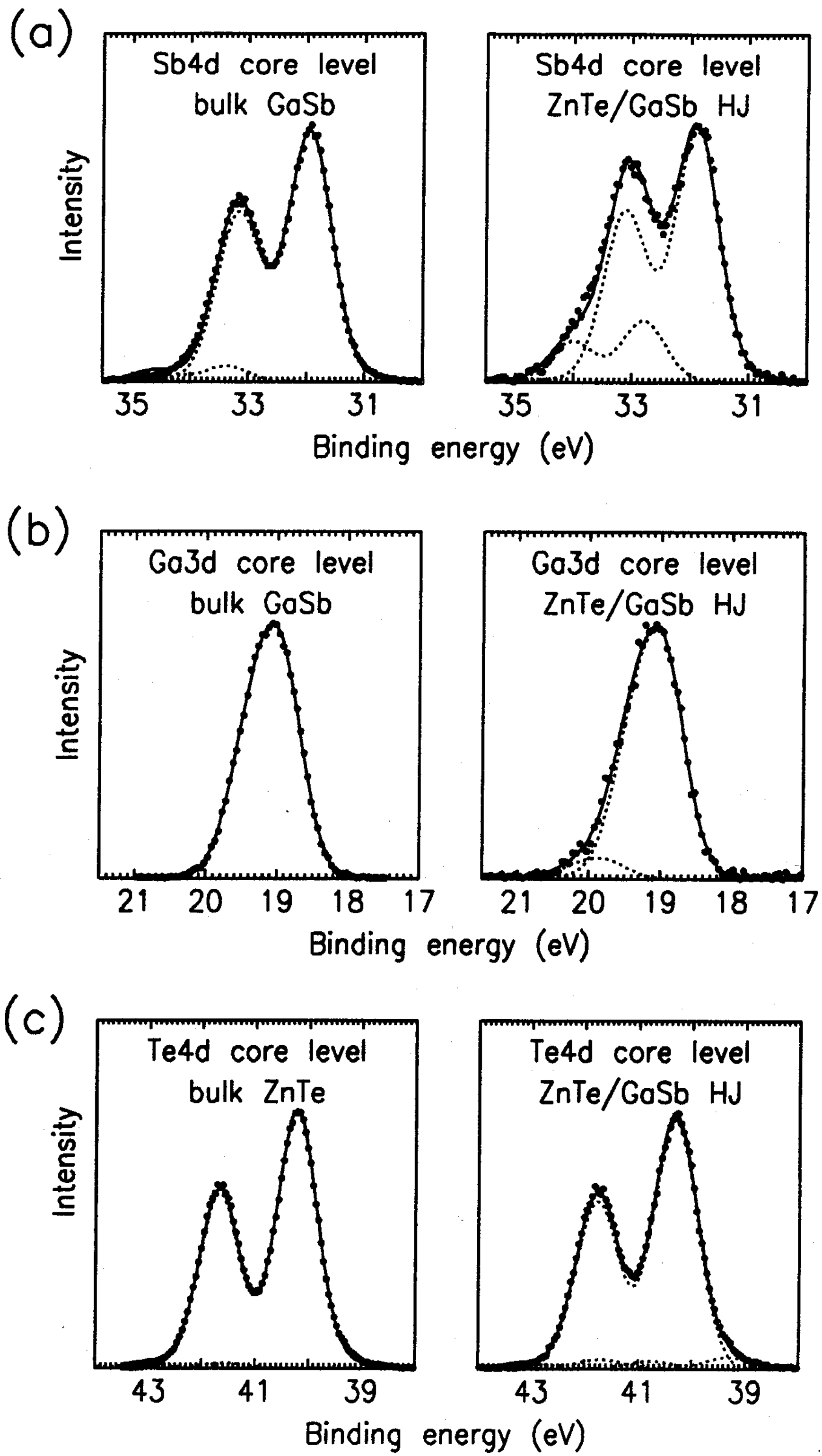
(a)
Sb4d core level
bulk GaSb
Sb4d core level
ZnTe/GaSb HJ
Intensity
35
33
31
35
33
31
Binding energy (eV)
(b)
Ga3d core level
bulk GaSb
Ga3d core level
ZnTe/GaSb HJ
Intensity
21
20
19
18
17
21
20
19
18
17
Binding energy (eV)
(c)
Te4d core level
bulk ZnTe
Te4d core level
ZnTe/GaSb HJ
Intensity
43
41
39
43
41
39
Binding energy (eV)

Figure 5.17: XPS spectra for (a) the Sb 4*d* core level, (b) the Ga 3*d* core level, and (c) the Te 4*d* core level from bulk GaSb or ZnTe and from a GaSb/ZnTe heterojunction. For the Sb 4*d* core level, the bulk spectrum exhibits a small component shifted to higher binding energy that is thought to be due to excess Sb on the GaSb surface; in the heterojunction spectrum, the peak shifted to higher binding energy originates from Sb on top of the ZnTe layer. For the Ga 3*d* core level, the bulk spectrum contains only a single component; the heterojunction spectrum contains a small peak component shifted to higher binding energy, indicating that Ga bonding to Te is present in a reacted layer at the GaSb/-ZnTe interface. For the Te 4*d* core level, the heterojunction spectrum contains a component shifted to lower binding energy that is not present in the bulk spectrum; the presence of this peak indicates that Te bonding to Ga is present in the reacted layer at the GaSb/ZnTe interface.

therefore demonstrate a clear violation of the transitivity rule.

Fig. 5.18 illustrates the deviation from transitivity by placing the conduction- and valence-band edges of AlSb, GaSb, and ZnTe on a common energy scale, with the relative positions of adjacent materials determined by our measured valence-band offsets. As shown in the figure, it is not possible to place all three materials on this common energy scale in a manner consistent with our measurements. This result indicates that for the AlSb/GaSb/ZnTe material system, band offsets are not determined solely by the properties of the bulk constituent materials, but are strongly influenced by properties of specific interfaces. The experimental verification of transitivity in the Ge/GaAs/AlAs material system[56], and theoretical calculations indicating that even when the detailed structure of abrupt interfaces is taken into account, band offsets are still expected to obey transitivity[13, 15, 20, 54, 55], then suggest that in the AlSb/GaSb/ZnTe (100) material system, chemical reactivity at the III-V/II-VI interfaces has a significant influence on band offset values. Our confirmation of commutativity for the AlSb/GaSb (100) valence band offset suggests that the AlSb/GaSb interfaces are abrupt and that chemical reactivity is relatively unimportant in AlSb/GaSb heterojunctions. This is what one would expect, given the presence of the common anion (Sb) in each constituent in the AlSb/GaSb heterojunction. Chemical reactions at the AlSb/ZnTe and GaSb/ZnTe interfaces, for which considerable evidence was observed in XPS core-level spectra from AlSb/ZnTe and GaSb/-ZnTe heterojunctions, would therefore appear to exert a substantial influence on valence-band offsets in the AlSb/GaSb/ZnTe material system.

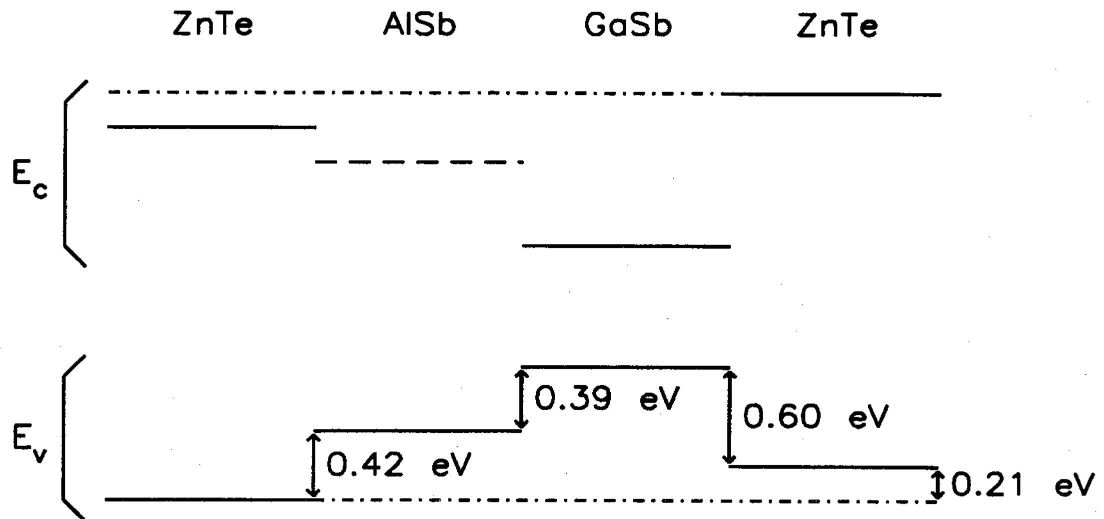

Figure 5.18: An illustration of nontransitivity in the AlSb/GaSb/ZnTe material system. The conduction- and valence-band edges of AlSb, GaSb, and ZnTe have been placed on a common energy scale determined by our measured band offset values; we have measured band offsets between adjacent materials in the figure. It is not possible to place all three materials on a common energy scale consistent with our measurements, indicating that properties of specific interfaces, rather than simply bulk properties, are a major factor in determining band offset values. Reported theoretical and experimental results indicate that for abrupt interfaces, band offset values should be transitive; these results therefore suggest that chemical reactions at the AlSb/ZnTe and GaSb/ZnTe interfaces exert a substantial influence on band offset values.

5.4 Direct Observation of Band Offset Variation Arising from Interface Chemistry

The observation of nontransitivity of band offsets in the AlSb/GaSb/ZnTe (100) material system, although suggestive, still provides only indirect evidence of the influence of III-V/II-VI interface reactions on band offset values. We have therefore conducted a series of experiments that demonstrate more directly the effect of chemical reactivity on band offset values for the AlSb/ZnTe (100) and GaSb/ZnTe (100) heterojunction systems.

As discussed in Section 5.2, varying the temperature at which the AlSb/-ZnTe heterojunction was grown between 270 °C and 330 °C did not have any effect on the value of the AlSb/ZnTe band offset. Petruzzello et al.[64], however, have reported that the structural quality of ZnSe grown on GaAs is strongly influenced by exposure of the GaAs surface to an initial flux of Zn or Se prior to growth of the ZnSe layer. Initial exposure of the substrate to a Zn flux leads to extremely high structural quality at the interface and throughout the ZnSe film, whereas initial exposure to a Se flux results in significant deterioration of sample quality. We have therefore studied the effect on band offset values in III-V/II-VI heterojunctions of exposing the III-V substrate surface to an initial Zn flux just prior to growth of ZnTe.

Two samples were grown for this study, one consisting of $\sim$25 Å ZnTe grown on GaSb with the GaSb surface exposed to a Zn flux for $\sim$1 min. immediately preceding growth of the ZnTe layer, and one consisting of $\sim$25 Å ZnTe grown on AlSb with the AlSb surface exposed to a Zn flux for 60 seconds prior to growth of the ZnTe. Both the GaSb and the AlSb surfaces exhibited sharp (1×3) RHEED patterns before and during exposure to the Zn flux, and a streaky (2×1) ZnTe

RHEED pattern was observed within approximately five seconds (~ 4 Å) after growth of ZnTe commenced.

Figs. 5.19(a) and (b) show representative XPS binding-energy spectra for the GaSb/ZnTe and AlSb/ZnTe heterojunction samples, respectively. For the GaSb/ZnTe heterojunction, we measured the Ga $3d$ to Zn $3d$, Sb $4d_{5/2}$ to Ga $3d$, and Te $4d_{5/2}$ to Zn $3d$ core-level energy separations, and for the AlSb/ZnTe sample we measured the Al $2p$ to Zn $3d$, Al $2p$ to Sb $4d_{5/2}$, and Te $4d_{5/2}$ to Zn $3d$ core-level energy separations. GaSb/ZnTe and AlSb/ZnTe valence-band offset values were determined from the measured Ga $3d$ to Zn $3d$ and Al $2p$ to Zn $3d$ core-level energy separations, respectively, and the Sb $4d_{5/2}$ to Ga $3d$, Al $2p$ to Sb $4d_{5/2}$, and Te $4d_{5/2}$ to Zn $3d$ core-level energy separations were compared to values obtained in bulk GaSb, AlSb, and ZnTe to confirm that the core-level energies were indeed those characteristic of bulk material.

For the GaSb/ZnTe heterojunction grown with an initial exposure of the GaSb surface to Zn preceding growth of the ZnTe layer, our measurements yielded a Ga $3d$ to Zn $3d$ core-level energy separation of 8.89 ± 0.03 eV, compared to 8.84 ± 0.03 eV for the GaSb/ZnTe heterojunction grown without the initial exposure to Zn. This value corresponds to a valence-band offset of 0.55 ± 0.07 eV, compared to our previous value of 0.60 ± 0.07 eV. The initial exposure to Zn at the interface therefore induces a slightly greater deviation from transitivity. However, the evidence for enhancement or suppression of the interfacial reaction is inconclusive. From Fig. 5.17, one sees that the chemically shifted peak component for the Ga $3d$ core-level spectrum from the original GaSb/ZnTe heterojunction sample is quite small. An analysis of the Ga $3d$ core-level spectrum from the GaSb/ZnTe heterojunction grown with the initial Zn exposure yields a chemically shifted peak component of similar size, the difference between the two being smaller than the uncertainties inherent in the fitting procedure.

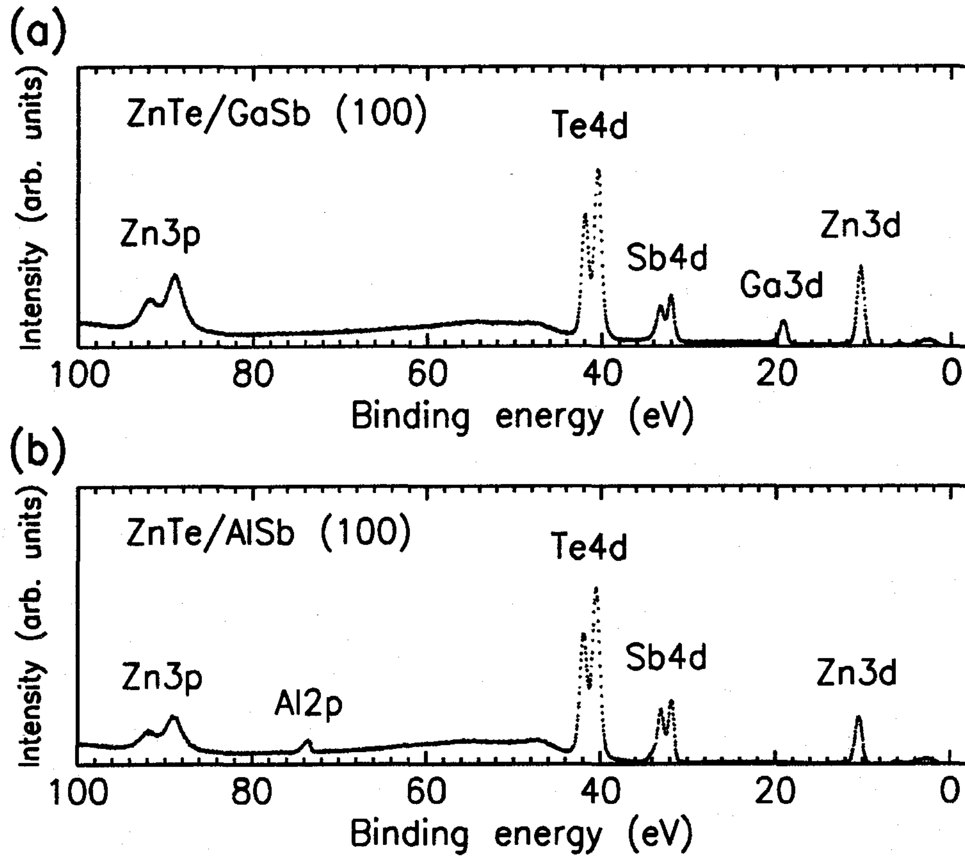

Figure 5.19: Representative binding-energy XPS spectra for (a) GaSb/ZnTe (100) and (b) AlSb/ZnTe (100) heterojunctions. For these samples, the III-V surface was exposed to an initial flux of Zn immediately preceding growth of the ZnTe layer. Band offsets for the GaSb/ZnTe and AlSb/ZnTe heterojunctions were determined by measuring the Ga $3d$ to Zn $3d$ and Al $2p$ to Zn $3d$ core-level energy separations, respectively, in the XPS spectra.

For the AlSb/ZnTe heterojunction grown with an initial Zn exposure at the AlSb/ZnTe interface, we obtained an Al $2p$ to Zn $3d$ core-level energy separation of 63.18 ± 0.03 eV, corresponding to a valence-band offset of 0.32 ± 0.07 eV. Our measurements on AlSb/ZnTe heterojunctions grown without an initial Zn exposure yielded an Al $2p$ to Zn $3d$ core-level energy separation of 63.08 ± 0.03 eV, corresponding to a valence-band offset of 0.42 ± 0.07 eV. In this case, the initial Zn exposure leads to a smaller deviation from transitivity. In addition, an analysis of the Al $2p$ core-level spectra from samples grown with and without an initial exposure to Zn suggests that the Zn treatment does indeed suppress partially the interfacial reaction. Figs. 5.20(a) and (b) show, respectively, Al $2p$ core-level spectra for samples grown with and without the initial exposure to Zn. As seen in the figures, the relative height of the chemically shifted component compared to the peak from the bulk AlSb layer is somewhat smaller for the sample grown with the initial Zn exposure, suggesting that the Zn treatment has partially suppressed the formation of the interfacial layer.

A comparison of the heterojunction spectra for the Sb $4d$ and Te $4d$ core levels would not yield information about the relative degrees of interfacial reactivity in samples grown with and without an initial Zn exposure, since the signal from a given layer decreases exponentially with depth in the sample. For the Ga $3d$ and Al $2p$ core levels, the signals from the bulk GaSb or AlSb and from the interface layer are both attenuated by the presence of the ZnTe layer; the relative height of the two components is therefore independent of the ZnTe layer thickness. For the Sb $4d$ and Te $4d$ core levels, the relative height of the chemically shifted component compared to the main peak is quite sensitive to the precise ZnTe layer thickness, rendering comparisons of spectra between samples somewhat questionable.

These results demonstrate that it is possible, under certain growth conditions,

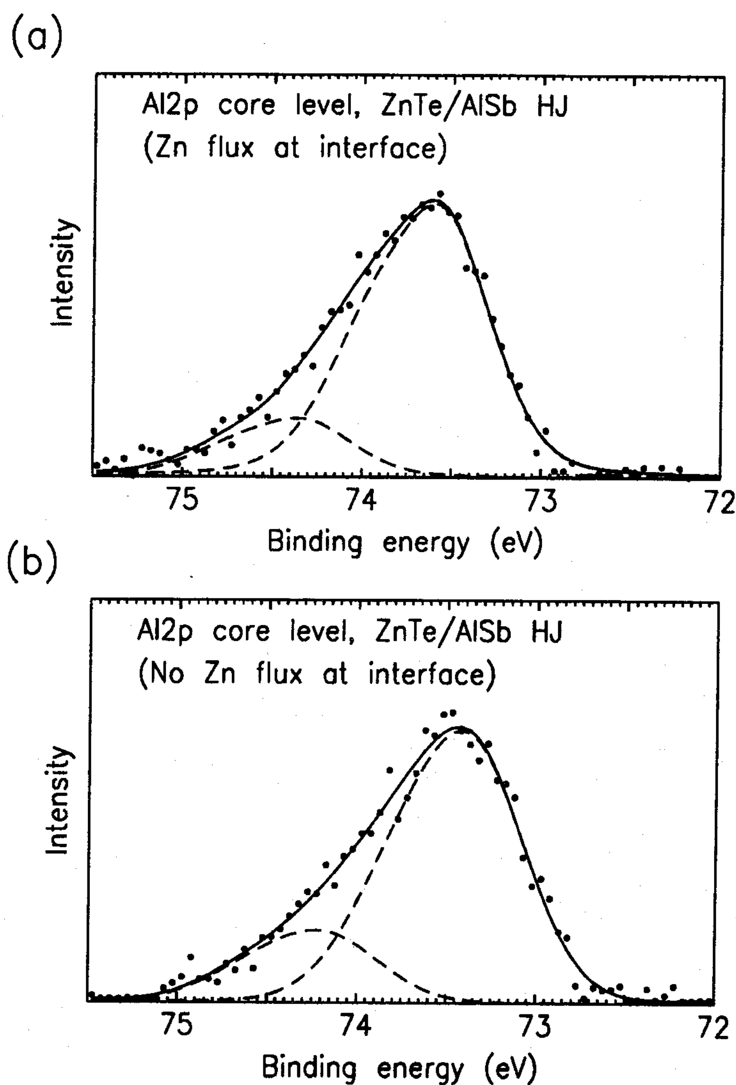

Figure 5.20: Al $2p$ core-level XPS spectra from AlSb/ZnTe heterojunction samples grown (a) with and (b) without an initial exposure of the AlSb surface to Zn immediately preceding growth of the ZnTe layer. The chemically shifted component appearing at higher binding energy, arising from Al atoms present in the reacted interface layer, is smaller compared to the component from bulk AlSb for the sample with the initial exposure to Zn at the interface. This result suggests that the initial Zn flux might partially suppress the reaction at the interface.

to alter the nature or the degree of the chemical reaction at III-V/II-VI interfaces, and that such alterations can exert a substantial influence on band offset values in these heterojunctions. For the GaSb/ZnTe heterojunction, the initial Zn flux induced a slightly greater deviation from transitivity, but the effect of the Zn treatment on the interfacial reaction could not be determined. For the AlSb/-ZnTe heterojunction, the initial Zn flux reduced the deviation from transitivity and appeared to suppress partially the interfacial reaction between AlSb and ZnTe. In the case of AlSb/ZnTe, therefore, the Zn treatment appeared to produce an interface that in some sense was more abrupt, and brought the band offset values for the AlSb/GaSb/ZnTe material system into closer agreement with the transitivity rule that is expected to hold for ideal, abrupt interfaces.

5.5 Conclusions

In this chapter we have presented a series of studies of band offsets in III-V/II-VI heterojunction systems. The growth and characterization of the III-V/-II-VI samples used in these experiments required the use of two MBE growth chambers and the XPS analytical chamber, all of which were connected via UHV transfer tubes. The ability to transfer samples among the two growth chambers and the analytical chamber under UHV conditions allowed samples to be grown and characterized under carefully controlled conditions, and was critical for these experiments. The elevated substrate temperatures required to evaporate surface passivation layers used to protect samples transferred through atmosphere would have introduced substantial complications because of the highly reactive nature of III-V/II-VI interfaces, and could have severely hindered efforts to observe variations in interfacial reactivity with growth conditions.

The original motivation for these experiments was to determine the feasibility

of an AlSb/ZnTe heterojunction-based LED concept proposed by McCaldin and McGill[6]; the viability of this device concept depended critically on the band offset value for the AlSb/ZnTe heterojunction. Our measurements yielded a valence-band offset of 0.42 ± 0.07 eV, corresponding to a conduction-band offset of 0.21 ± 0.07 eV. The value we obtained for the AlSb/ZnTe conduction-band offset is compatible with efficient operation of the proposed AlSb/ZnTe heterojunction LED, provided that the AlSb layer in the device is heavily doped n-type.

Our experiments in the AlSb/ZnTe material system yielded considerable evidence of a chemical reaction that occurred at the AlSb/ZnTe interface. An analysis of the Al $2p$, Sb $4d$, and Te $4d$ core-level spectra from AlSb/ZnTe heterojunction samples indicated that an intermediate layer containing primarily Al and Te, probably in the form Al_2Te_3, was formed at the AlSb/ZnTe interface. In addition, our measurements on the heterojunction samples and on thicker (275 Å) layers of ZnTe grown on AlSb indicated that a layer of Sb was present on the ZnTe surface, and moved along the growth front as ZnTe was deposited.

An issue of particular interest was the possible effect of the interface layer on the value of the band offset in this material system. To address this issue, we studied band offset transitivity in the lattice-matched AlSb/GaSb/ZnTe material system. For lattice-matched material systems, there is considerable theoretical and experimental evidence that band offsets should obey the transitivity rule, provided that the actual experimental interfaces have an atomic structure sufficiently close to that of a perfect crystalline interface. Agreement of the band offsets we measured for the AlSb/GaSb/ZnTe material system with the transitivity rule would therefore have suggested that the electronic structure of the III-V/II-VI interfaces was close to that of abrupt interfaces, and that the interfacial reactions were not strongly influencing band offset values. A significant deviation from transitivity, however, would have suggested that the nonideal structure of

the III-V/II-VI interfaces was affecting the band offset values.

To test the transitivity rule, we measured valence-band offsets for the AlSb/-GaSb and GaSb/ZnTe heterojunction systems, obtaining values of 0.39 ± 0.07 eV and 0.60 ± 0.07 eV, respectively. Combining these values with our measured AlSb/ZnTe valence-band offset, we determined that the transitivity rule was violated by 0.21 ± 0.05 eV, suggesting that chemical reactions at the III-V/II-VI interfaces were affecting band offset values. We also verified the commutativity of the AlSb/GaSb valence-band offset, which indicated that the AlSb/GaSb interfaces in our samples were abrupt and relatively unaffected by chemical reactions.

We also made attempts to observe more directly the effect of III-V/II-VI interface reactions on band offset values. Because the substrate temperatures at which the III-V/II-VI interfaces were grown were quite low, we felt that a reduction in substrate temperature would not help to suppress the formation of an interfacial layer. We therefore attempted to suppress the interface reaction between the Group III (Ga or Al) and Group VI (Te) atoms by exposing the III-V surfaces to a pure Zn flux immediately preceding growth of the ZnTe layer in the heterojunction. This procedure reduced the valence-band offset in the GaSb/-ZnTe heterojunction by 0.05 eV to 0.55 ± 0.07 eV, and reduced the valence-band offset in the AlSb/ZnTe heterojunction by 0.10 eV to 0.32 ± 0.07 eV. The shift in the GaSb/ZnTe valence-band offset increased slightly the deviation from transitivity, but the shift in the AlSb/ZnTe valence-band offset decreased the violation of transitivity. In addition, an examination of the Al $2p$ core-level spectra from AlSb/ZnTe heterojunctions grown with and without the initial exposure to Zn at the interface suggested that the initial Zn flux produced a partial suppression of the interface reaction between AlSb and ZnTe. These results therefore seemed to indicate that, in the case of AlSb/ZnTe, a partial suppression of the interfacial reaction yielded a band offset value in closer agreement with the transitivity rule

that is expected to be valid for ideal interfaces.

References

[1] T. Yao, in *The Technology and Physics of Molecular Beam Epitaxy*, E. H. C. Parker, ed. (Plenum Press, New York, 1985), pp. 313-343.

[2] Y. Rajakarunanayake, B. H. Cole, J. O. McCaldin, D. H. Chow, J. R. Söderström, T. C. McGill, and C. M. Jones, *Appl. Phys. Lett.* **55**, 1217 (1989).

[3] M. C. Phillips, Y. Rajakarunanayake, J. O. McCaldin, D. H. Chow, J. R. Söderström, D. A. Collins, and T. C. McGill, presented at the SPIE Symposium on Advances in Semiconductors and Superconductors: Physics Toward Device Applications, San Diego, CA (1990).

[4] H. Mitsuhashi, I. Mitsuishi, and H. Kukimoto, *J. Cryst. Growth* **77**, 219 (1986).

[5] E. T. Yu, Y. Rajakarunanayake, M. C. Phillips, J. O. McCaldin, and T. C. McGill, presented at the 1990 International Conference on Solid State Devices and Materials, Sendai, Japan (1990).

[6] J. O. McCaldin and T. C. McGill, *J. Vac. Sci. Technol. B* **6**, 1360 (1988).

[7] S. Subbanna, G. Tuttle, and H. Kroemer, *J. Elec. Mater.* **17**, 297 (1988).

[8] A. G. Milnes and D. L. Feucht, *Heterojunctions and Metal-Semiconductor Junctions* (Academic Press, New York, 1972).

[9] W. A. Harrison, *J. Vac. Sci. Technol.* **14**, 1016 (1977).

[10] W. R. Frensley and H. Kroemer, *J. Vac. Sci. Technol.* **13**, 810 (1976).

[11] J. Tersoff, *Phys. Rev. Lett.* **56**, 2755 (1986).

[12] W. A. Harrison and J. Tersoff, *J. Vac. Sci. Technol. B* **4**, 1068 (1986).

[13] C. G. Van de Walle and R. M. Martin, *Phys. Rev. B* **35**, 8154 (1987).

[14] C. G. Van de Walle, *Phys. Rev. B* **39**, 1871 (1989).

[15] W. R. L. Lambrecht, B. Segall, and O. K. Andersen, *Phys. Rev. B* **41**, 2813 (1990).

[16] G. J. Gualtieri, G. P. Schwartz, R. G. Nuzzo, and W. A. Sunder, *Appl. Phys. Lett.* **49**, 1037 (1986).

[17] J. O. McCaldin, T. C. McGill, and C. A. Mead, *Phys. Rev. Lett.* **36**, 56 (1976).

[18] A. D. Katnani and G. Margaritondo, *J. Appl. Phys.* **5**, 2522 (1983).

[19] A. D. Katnani and G. Margaritondo, *Phys. Rev. B* **28**, 1944 (1983).

[20] N. E. Christensen, *Phys. Rev. B* **37**, 4528 (1988).

[21] O. Von Ross, *Solid–State Electron.* **23**, 1069 (1980).

[22] Y. Horikoshi, M. Kawashima, and H. Yamaguchi, *Jpn. J. Appl. Phys.* **25**, L868 (1986).

[23] S. Ramesh, N. Kobayashi, and Y. Horikoshi, *Appl. Phys. Lett.* **57**, 1102 (1990).

[24] D.-W. Tu and A. Kahn, *J. Vac. Sci. Technol. A* **3**, 922 (1985).

[25] K. J. Mackey, P. M. G. Allen, W. G. Herrenden-Harker, R. H. Williams, C. R. Whitehouse, and G. M. Williams, *Appl. Phys. Lett.* **49**, 354 (1986).

[26] W. G. Wilke and K. Horn, *J. Vac. Sci. Technol. B* **6**, 1211 (1988).

[27] W. G. Wilke, R. Seedorf, and K. Horn, *J. Vac. Sci. Technol. B* **7**, 807 (1989).

[28] S. P. Kowalczyk, E. A. Kraut, J. R. Waldrop, and R. W. Grant, *J. Vac. Sci. Technol.* **21**, 482 (1982).

[29] F. Xu, M. Vos, J. P. Sullivan, Lj. Atanasoska, S. G. Anderson, J. H. Weaver, and H. Cheng, *Phys. Rev. B* **38**, 7832 (1988).

[30] D. W. Niles, G. Margaritondo, P. Perfetti, C. Quaresima, and M. Capozi, *Appl. Phys. Lett.* **47**, 1092 (1985).

[31] D. W. Niles, E. Colavita, G. Margaritondo, P. Perfetti, C. Quaresima, and M. Capozi, *J. Vac. Sci. Technol. A* **4**, 962 (1986).

[32] P. Perfetti, C. Quaresima, C. Coluzza, C. Fortunato, and G. Margaritondo, *Phys. Rev. Lett.* **57**, 2065 (1986).

[33] A. D. Katnani, P. Chiaradia, H. W. Sang, Jr., P. Zurcher, and R. S. Bauer, *Phys. Rev. B* **31**, 2146 (1985).

[34] A. D. Katnani, P. Chiaradia, H. W. Sang, Jr., and R. S. Bauer, *J. Vac. Sci. Technol. B* **2**, 471 (1984).

[35] A. D. Katnani and R. S. Bauer, *J. Vac. Sci. Technol. B* **3**, 1239 (1985).

[36] A. D. Katnani, P. Chiaradia, H. W. Sang, Jr., and R. S. Bauer, *J. Elec. Mater.* **14**, 25 (1985).

[37] J. R. Waldrop, E. A. Kraut, S. P. Kowalczyk, and R. W. Grant, *Surf. Sci.* **132**, 513 (1983).

[38] G. P. Schwartz, G. J. Gualtieri, R. D. Feldman, R. F. Austin, and R. G. Nuzzo, *J. Vac. Sci. Technol. B* **8**, 747 (1990).

[39] E. A. Kraut, R. W. Grant, J. R. Waldrop, and S. P. Kowalczyk, *Phys. Rev. B* **28**, 1965 (1983).

[40] P. H. Citrin, G. K. Wertheim, and Y. Baer, *Phys. Rev. Lett.* **41**, 1425 (1978).

[41] M. L. Cohen and T. K. Bergstresser, *Phys. Rev.* **141**, 789 (1966).

[42] L. R. Saravia and D. Brust, *Phys. Rev.* **176**, 915 (1968).

[43] J. R. Chelikowsky, D. J. Chadi, and M. L. Cohen, *Phys. Rev. B* **8**, 2786 (1973).

[44] I. Topol, H. Neumann, and E. Hess, *Czech. J. Phys. B* **24**, 107 (1974).

[45] C. W. Higginbotham, *Band Structure and Optical Properties of Semiconductors: The $\vec{k} \cdot \vec{p}$ Method*, Ph.D. thesis, Brown University, Providence, RI (1970).

[46] M. Cardona and D. L. Greenaway, *Phys. Rev.* **131**, 98 (1963).

[47] J. P. Walter, M. L. Cohen, Y. Petroff, and M. Balkanski, *Phys. Rev. B* **1**, 2661 (1970).

[48] P. Eckelt, *Phys. Status Solidi* **23**, 307 (1967).

[49] R. W. Grant, E. A. Kraut, S. P. Kowalczyk, and J. R. Waldrop, *J. Vac. Sci. Technol. B* **1**, 320 (1983).

[50] T. M. Duc, C. Hsu, and J.-P. Faurie, *Phys. Rev. Lett.* **58**, 1127 (1987).

[51] P. K. Larsen, J. H. Neave, J. F. Van der Veen, P. J. Dobson, and B. A. Joyce, *Phys. Rev. B* **27**, 4966 (1983).

[52] S. M. Sze, *Physics of Semiconductor Devices*, Second Edition (John Wiley and Sons, New York, 1981), p. 277.

[53] T. B. Massalski, ed., *Binary Alloy Phase Diagrams*, (American Society for Metals, Metals Park, OH, 1986), Vol. 1, p. 172.

[54] N. E. Christensen, *Phys. Rev. B* **38**, 12687 (1988).

[55] W. R. L. Lambrecht and B. Segall, *Phys. Rev. Lett.* **61**, 1764 (1988).

[56] A. D. Katnani and R. S. Bauer, *Phys. Rev. B* **33**, 1106 (1986).

[57] E. T. Yu, D. H. Chow, and T. C. McGill, *Phys. Rev. B* **38**, 12764 (1988).

[58] K. Hirakawa, Y. Hashimoto, and T. Ikoma, *Appl. Phys. Lett.* **57**, 2555 (1990).

[59] J. R. Waldrop, S. P. Kowalczyk, R. W. Grant, E. A. Kraut, and D. L. Miller, *J. Vac. Sci. Technol.* **19**, 573 (1981).

[60] J. R. Waldrop, R. W. Grant, and E. A. Kraut, *J. Vac. Sci. Technol. B* **5**, 1209 (1987).

[61] J. R. Chelikowsky and M. L. Cohen, *Phys. Rev. B* **14**, 556 (1976).

[62] J. Menéndez, A. Pinczuk, D. J. Werder, J. P. Valladares, T. H. Chiu, and W. T. Tsang, *Solid State Commun.* **61**, 703 (1987).

[63] C. Tejedor, J. M. Calleja, F. Meseguer, E. E. Mendez, C.-A. Chang, and L. Esaki, *Phys. Rev. B* **32**, 5303 (1985).

[64] J. Petruzzello, B. Greenberg, and J. Gaines, *Bull. Am. Phys. Soc.* **35**, 237 (1990).

[65] U. Cebulla, G. Tränkle, U. Ziem, A. Forchel, G. Griffiths, H. Kroemer, and S. Subbanna, *Phys. Rev. B* **37**, 6278 (1988).

[66] R. Beresford, L. F. Luo, and W. I. Wang, *Appl. Phys. Lett.* **55**, 694 (1989).

Chapter 6

Measurement of Band Offsets in II-VI Heterojunction Systems: CdSe/ZnTe

6.1 Introduction

6.1.1 Background and Motivation

The CdSe/ZnTe material system has been considered as a possible candidate for the fabrication of green light emitters based on heterojunction injection of electrons into p-type ZnTe, using either n-CdSe/p-ZnTe or n-$(CdSe)_{1-x}(ZnTe)_x$/-p-ZnTe heterojunctions. As discussed in Chapter 5, the inability to dope ZnTe n-type obviates the possibility of fabricating ZnTe-based green light emitters using simple ZnTe p-n homojunctions; the use of heterojunctions has been proposed as a particularly promising alternative for injecting electrons into p-type ZnTe and achieving visible electroluminescence[1, 2, 3]. CdSe is a potentially attractive candidate for this application because it can be doped n-type, and although its

equilibrium crystal structure is wurtzite, it can be grown in the cubic zincblende structure on ZnTe with a lattice mismatch of only $\sim 0.44\%$. However, the feasibility of this approach depends critically on the conduction-band offset in the CdSe/ZnTe heterojunction system.

In addition, the band offset in the CdSe/ZnTe heterojunction is of interest for the information its value might provide about band offsets for other heterojunction systems involving Se and Te compounds, such as ZnSe/ZnTe. The "common anion rule" of McCaldin, McGill, and Mead[4] states that, for a wide range of semiconductor compounds (materials containing Al being the most notable exception), the valence-band offset between two materials will depend only on the anion contained in each compound; the physical basis for this rule was discussed in some detail in Chapter 1. The value of the CdSe/ZnTe valence-band offset might provide insight into the general validity of the common anion rule and possibly a basis for determining band offset values in other heterojunction systems such as ZnSe/ZnTe.

Theoretical predictions for the CdSe/ZnTe valence-band offset extend, as usual, over a wide range of values. Fig. 6.1 shows the range of values predicted for the CdSe/ZnTe valence-band offset. The electron affinity rule[5] predicts $\Delta E_v = 0.93$ eV using the electron affinity data of Milnes and Feucht[6], and $\Delta E_v = 0.86$ eV if the compilation of Freeouf and Woodall is used[7]. Harrison's LCAO theory[8] yields a value of 0.85 eV for the CdSe/ZnTe valence-band offset, and Kraut's adaptation of Harrison's theory[9] using Hartree-Fock neutral atom energies predicts $\Delta E_v = 1.11$ eV. Frensley and Kroemer's pseudopotential theory yields a valence-band offset of 0.55 eV without interfacial dipole corrections[10], and 0.64 eV with dipole corrections included[11]. The theory of Harrison and Tersoff[12] predicts $\Delta E_v = 0.31$ eV. Among the more empirical models, the common anion rule[4] predicts $\Delta E_v = 0.55$ eV, and Katnani and Margaritondo[13, 14]

obtain $\Delta E_v = 0.35$ eV. Not shown in Fig. 6.1 is the prediction of Von Ross[15], $\Delta E_v = -0.36$ eV, which disagrees with all of the other predictions by 0.86 eV or more. Because of these large discrepancies, theoretical predictions are of little use in determining the actual value of the CdSe/ZnTe valence-band offset.

A number of studies of the CdSe/ZnTe heterojunction system have been performed, but the samples used for these investigations were typically of low quality compared to those that can be grown currently by techniques such as molecular-beam epitaxy (MBE). Gashin and Simashkevich[16, 17] fabricated CdSe/ZnTe heterojunctions by evaporating CdSe onto (110) ZnTe, obtaining cubic CdSe with the same crystallographic orientation as the substrate for substrate temperatures ranging from 450 to 700°C. On the basis of electrical measurements and the electron affinity rule for conduction-band offsets[5], Gashin and Simashkevich proposed a valence-band offset of ~0.13 eV and a conduction-band offset of ~0.4 eV, corresponding to a Type I band lineup. However, their estimate of the band offset assumed an electron affinity for CdSe of 3.93 eV, whereas Milnes and Feucht[6] give an electron affinity of 4.95 eV for CdSe. Gashin and Simashkevich also observed, depending on the method of sample preparation, either red (a main peak at 1.87 eV and a secondary peak at 2.05 eV at 80 K) or green (a single peak at 2.24 eV) electroluminescence from CdSe/ZnTe heterojunctions, all of which corresponded to recombination in the ZnTe layer. Yellow electroluminescence (a peak at 2.05 eV at 80 K) was also observed from Cu-doped CdSe/ZnTe heterojunctions[18]. Fedotov et al.[19] have also observed both red and green electroluminescence in CdSe/ZnTe heterojunctions. Buch et al.[20, 21] studied photovoltaic properties of n-CdSe/p-ZnTe heterojunctions and proposed a CdSe/-ZnTe band diagram with a valence-band offset of 0.23 eV and a conduction-band offset of 0.75 eV, corresponding to a Type II band alignment.

Various investigators have also observed evidence for interdiffusion of atoms,

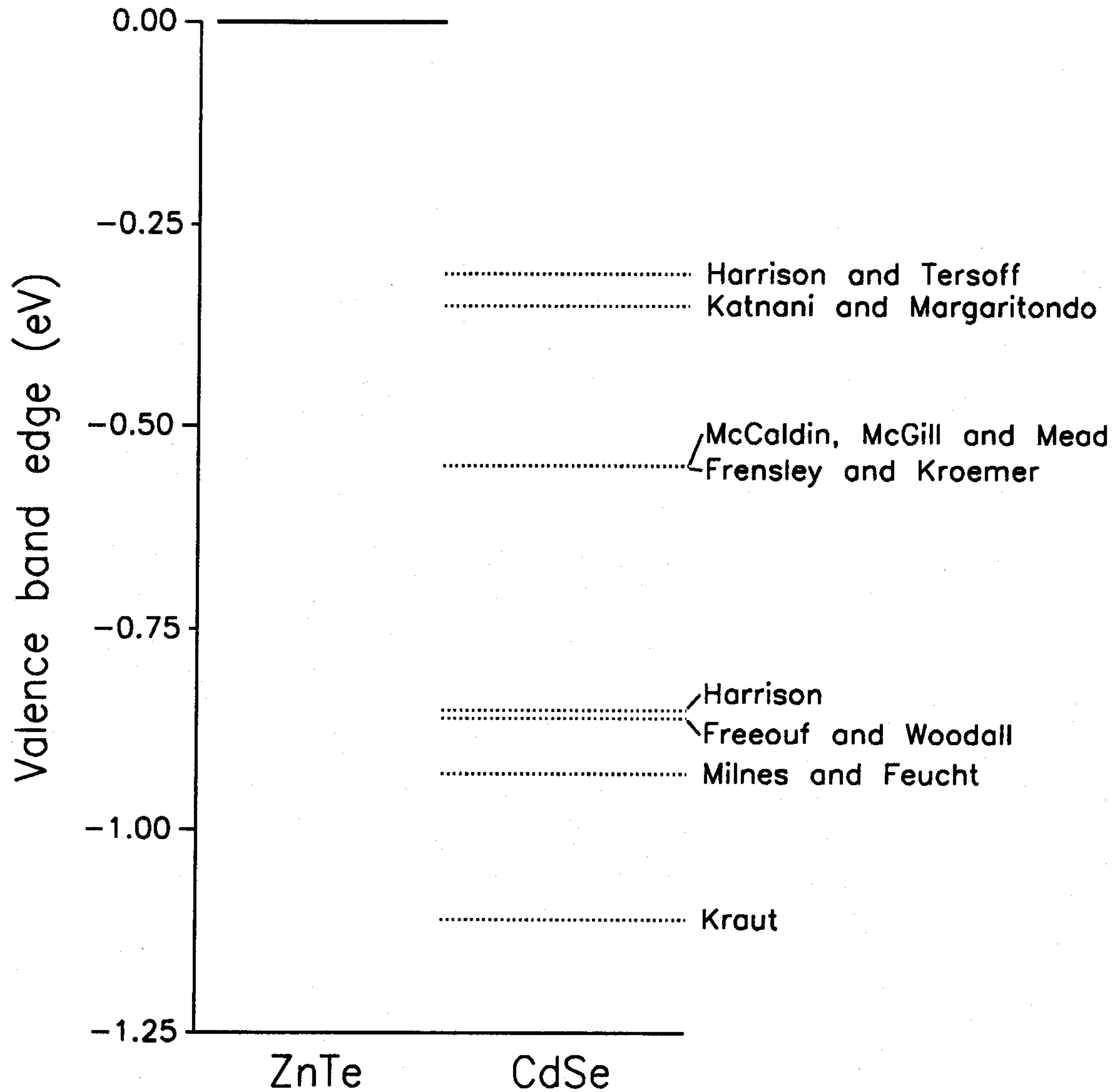

Figure 6.1: Valence-band offset values for the CdSe/ZnTe heterojunction predicted by several theories[5, 4, 6, 8, 9, 10, 11, 12, 13, 14]. Theoretical predictions for the CdSe/ZnTe valence-band offset extend over an extremely wide range of values, making them of little use in determining the actual band offset value.

and the resulting formation of an intermediate compound or solid solution, at the CdSe/ZnTe interface. Fedotov et al.[19] observed diffusion of Cd, Zn, and Te atoms in CdSe/ZnTe and CdS/ZnTe heterojunctions, and a resulting region of solid solution, with apparent diffusion lengths of up to several μm. Buch et al.[20, 21] postulated the formation of a $CdSe_{1-x}Te_x$ layer at the CdSe/ZnTe interface on the basis of evidence of absorption near the heterojunction interface at energies as low as 1.45 eV. Photocurrent and cathodoluminescence studies by Simashkevich and Tsiulyanu[22] have suggested that a CdSe/ZnTe solid solution is formed at the CdSe/ZnTe heterojunction interface. Finally, Senokosov and Usatyĭ[23] postulated, on the basis of electrical and photoresponse measurements, that a high-resistivity layer of CdTe was formed by interdiffusion at an n-CdSe/-p-ZnTe heterojunction.

6.1.2 Summary of Results

In this chapter we discuss our measurement of the CdSe/ZnTe (100) valence band offset by x-ray photoelectron spectroscopy (XPS). Sample growth for these experiments involved the use of two separate molecular-beam epitaxy growth chambers connected via ultrahigh vacuum (UHV) transfer tubes. An MBE chamber dedicated to growth of III-V semiconductors was used to deposit GaSb buffer layers on GaSb substrates. These samples were then transferred under UHV conditions to a growth chamber devoted to growth of II-VI materials, in which CdSe and ZnTe films were grown. The samples were then transferred under UHV to the XPS analytical chamber for characterization.

CdSe films were grown to thicknesses up to ~400 Å on ZnTe surfaces. Observations of reflection high-energy electron diffraction (RHEED) patterns during growth of the CdSe films indicated that the CdSe was growing in cubic zincblende

form, rather than its natural wurtzite structure. XPS measurements were performed for thick films of CdSe (100) and ZnTe (100), and for heterojunctions consisting of either ~ 25 Å of CdSe grown on ZnTe or ~ 25 Å of ZnTe grown on CdSe. Measurements of the Se $3d_{5/2}$ and Te $4d_{5/2}$ core-level to valence-band-edge binding energies in bulk CdSe and bulk ZnTe, respectively, and measurements of the Te $4d_{5/2}$ to Se $3d_{5/2}$ core-level energy separation in CdSe/ZnTe heterojunctions yielded a valence-band offset $\Delta E_v = 0.64 \pm 0.07$ eV. The corresponding conduction-band offset for CdSe/ZnTe is $\Delta E_c = 1.22 \pm 0.07$ eV for room-temperature band gaps for ZnTe and for cubic CdSe of 2.25 eV and 1.67 eV, respectively. These results indicate that injection of electrons directly from n-CdSe into p-ZnTe is not feasible. However, electron injection from n-$(\text{CdSe})_{1-x}(\text{ZnTe})_x$ into p-ZnTe remains a possibility, depending on the dopability of n-$(\text{CdSe})_{1-x}(\text{ZnTe})_x$ alloys.

6.1.3 Outline of Chapter

We describe the growth of the bulk CdSe and ZnTe films and of the CdSe/-ZnTe heterojunction samples in Section 6.2.1. The XPS measurements and data analysis are described in Section 6.2.2. Values are obtained for the Te $4d_{5/2}$ core-level to valence-band-edge binding energy in ZnTe, the Se $3d_{5/2}$ core-level to valence-band-edge binding energy in CdSe, and the Te $4d_{5/2}$ to Se $3d_{5/2}$ core-level energy separation in CdSe/ZnTe heterojunctions. Results are discussed in Section 6.3, and conclusions are presented in Section 6.4.

6.2 Experiment

6.2.1 Sample Growth

The samples prepared for this study were grown by molecular-beam epitaxy in two Perkin-Elmer 430P MBE systems. An MBE chamber dedicated to the growth of III-V semiconductors was used to grow GaSb buffer layers on GaSb (100) substrates to provide a smooth starting surface for growth of the ZnTe and CdSe layers. All samples were grown on p-type GaSb (100) substrates, with $p \sim 1 \times 10^{17}$ cm^{-3}. Following oxide desorption at 530 °C, a GaSb buffer layer was grown at 100 Å/min. with the substrate at 475 °C. Once the GaSb buffer layers were grown, the samples were transferred under UHV conditions to an MBE chamber devoted to the growth of II-VI materials. ZnTe layers were grown at rates of 50 – 75 Å/min. and with the substrate at 270 °C; a growth rate of ~60 Å/min. and a substrate temperature of 270 °C were used for growth of the CdSe layers.

The Te $4d_{5/2}$ core-level to valence-band-edge binding energy was measured in two 275 Å films of ZnTe, as discussed in Section 5.2. To measure the Se $3d_{5/2}$ core-level to valence-band-edge binding energy in CdSe, two samples were grown, each consisting of ~400 Å CdSe grown on ZnTe. Reflection high-energy electron diffraction patterns monitored during growth of the CdSe layers showed very little deviation from the initial (2×1) ZnTe surface pattern, indicating that the CdSe film was growing in cubic zincblende form rather than its natural wurtzite structure. X-ray diffraction measurements for cubic CdSe epilayers grown on GaAs (100) substrates have yielded[24] a cubic lattice constant $a_{\mathrm{CdSe}} = 6.077$ Å; the lattice mismatch between cubic CdSe and ZnTe ($a_{\mathrm{ZnTe}} = 6.104$ Å) should therefore be only ~0.44 %.

The Se $3d_{5/2}$ to Te $4d_{5/2}$ core level energy separation was measured in two heterojunctions consisting of $\sim$25 Å of CdSe grown on ZnTe, and in two heterojunctions consisting of $\sim$ 25 Å of ZnTe grown on CdSe. Immediately following all growths, the samples were transported under UHV conditions to the XPS chamber for analysis. The ability to perform both sample growth and XPS characterization without exposing samples to atmosphere allowed us to eliminate experimental uncertainties associated with surface passivation and subsequent evaporation of protective capping layers. This aspect of the experiment was of considerable importance, in light of the evidence discussed in Section 6.1.1 that interdiffusion of atoms and the resulting formation of intermediate compounds or a solid solution can occur at the CdSe/ZnTe interface.

6.2.2 XPS Measurements and Data Analysis

Fig. 6.2 shows a schematic energy-band diagram for the CdSe/ZnTe heterojunction. Strain-induced effects on the electronic band structure of the two materials have been neglected, because of the small lattice mismatch (0.44%) between cubic CdSe and ZnTe. As shown in the figure, the valence-band offset is given by

$$\Delta E_v = (E^{\mathrm{ZnTe}}_{\mathrm{Te4}d_{5/2}} - E^{\mathrm{ZnTe}}_v) + (E^{\mathrm{CdSe}}_{\mathrm{Se3}d_{5/2}} - E^{\mathrm{ZnTe}}_{\mathrm{Te4}d_{5/2}}) - (E^{\mathrm{CdSe}}_{\mathrm{Se3}d_{5/2}} - E^{\mathrm{CdSe}}_v). \quad (6.1)$$

XPS measurements were obtained using a Perkin-Elmer Model 5100 analysis system with a monochromatic Al $K\alpha$ x-ray source ($h\nu = 1486.6$ eV). The measured linewidth for Au $4f$ core-level peaks was $\sim$0.75 eV, and the pressure in the analysis chamber was typically $\sim 5 \times 10^{-10}$ Torr. The analysis chamber is connected to the MBE growth chambers via UHV transfer tubes, allowing samples to be grown and characterized without being exposed to atmosphere. This capability may have helped to reduce interdiffusion of atoms and inhibit the formation

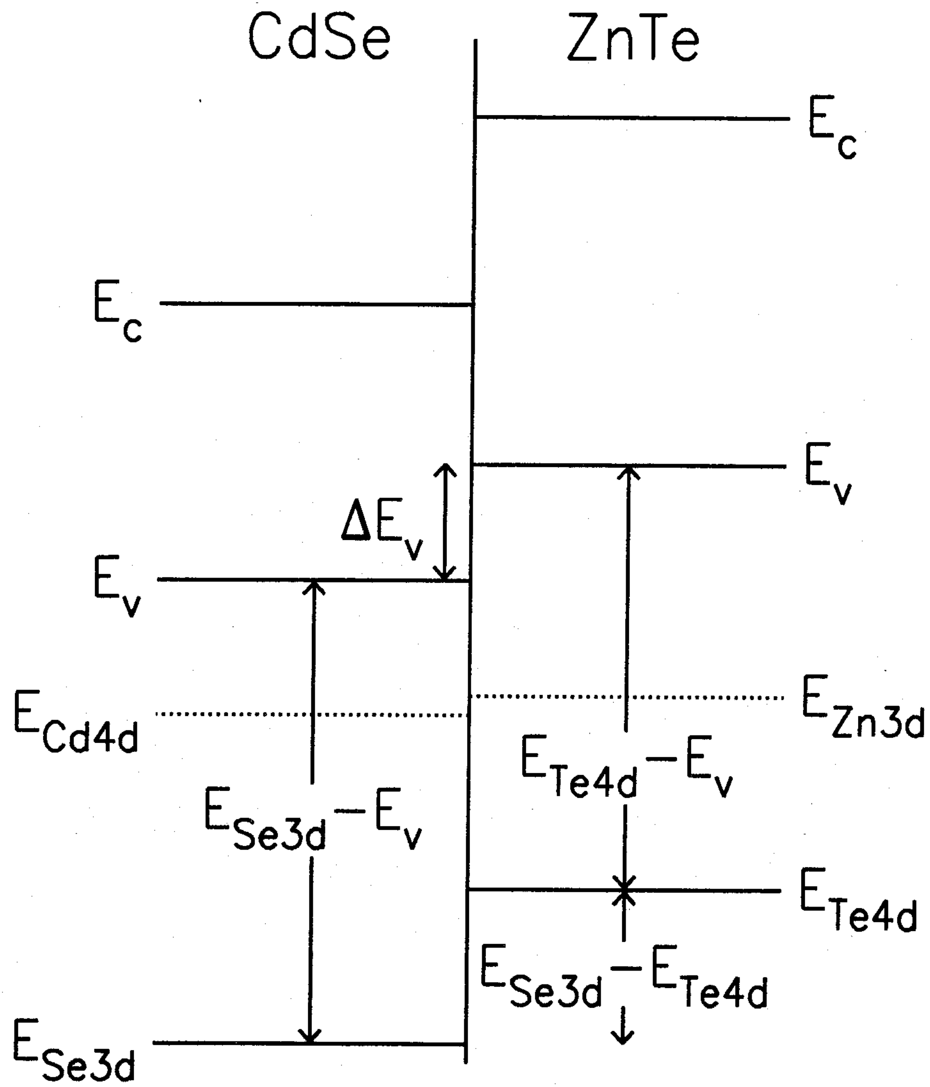

Figure 6.2: Schematic energy-band diagram for the CdSe/ZnTe heterojunction. Because the Cd 4*d* and Zn 3*d* core-level peaks overlap in energy, the Se 3*d* and Te 4*d* core levels in CdSe and ZnTe, respectively, have been used to measure the valence-band offset.

of an intermediate compound or solid solution at the CdSe/ZnTe interface. Such reactions had been observed in some previous studies of CdSe/ZnTe heterojunctions, as discussed in Section 6.1.1. Representative XPS spectra for bulk CdSe, bulk ZnTe, and a CdSe/ZnTe heterojunction are shown in Figs. 6.3(a), (b), and (c), respectively. The valence-band spectrum for the bulk ZnTe sample is also shown on an enlarged intensity scale, as indicated in the figure.

As seen in Fig. 6.3, the Cd $4d$ and Zn $3d$ atomic core levels overlap in energy, making the determination of the Cd $4d$ to Zn $3d$ core-level energy separation in the CdSe/ZnTe heterojunction relatively difficult. We have therefore chosen, as indicated in Eq. (6.1), to use the Se $3d_{5/2}$ and Te $4d_{5/2}$ atomic core levels as reference levels in CdSe and ZnTe, respectively.

Core-level peak positions were obtained by subtracting from each core-level peak a background function proportional to the integrated photoelectron intensity, and fitting the resulting core-level spectra to characteristic peak-shape functions consisting of two identically shaped Voigt functions separated by a fixed spin-orbit splitting, whose relative heights scaled as $(2J + 1)$. For the Cd $4d$ and Zn $3d$ core levels, the peak position was taken to be the average of the positions of the spin-orbit-split components, weighted by the degeneracy $(2J + 1)$. The relatively large spin-orbit splittings of the Se $3d$ and Te $4d$ atomic core levels ($\Delta_0^{\mathrm{Se}3d} = 0.86$ eV and $\Delta_0^{\mathrm{Te}4d} = 1.46$ eV) allowed us to resolve clearly the spin-orbit-split components of each core-level peak; the Se $3d_{5/2}$ and Te $4d_{5/2}$ core-level peak components were therefore used as reference levels for the band offset measurement. The uncertainty in measured core-level energy separations was estimated to be ± 0.02 eV, and measurements of core-level energy separations were typically reproducible to approximately ± 0.01 eV.

The position of the valence-band edge in each bulk XPS spectrum was determined using the precision analysis technique of Kraut et al.[25]. In this approach,

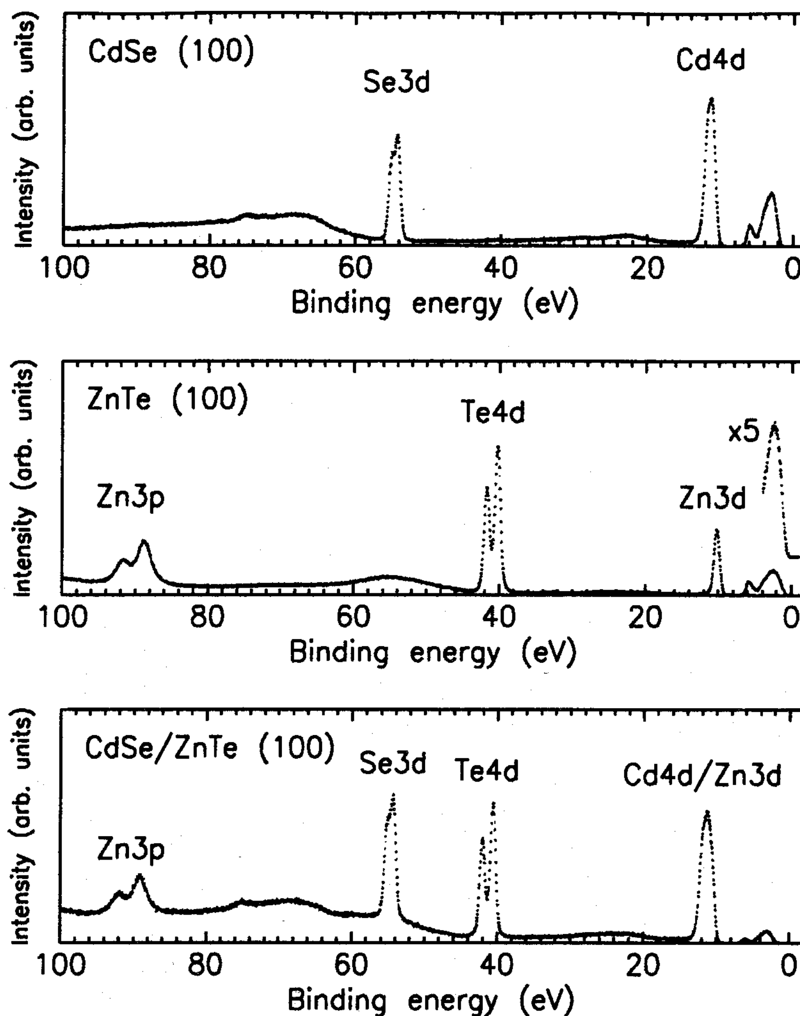

Figure 6.3: Representative binding-energy XPS spectra for (a) bulk cubic CdSe (100), (b) bulk ZnTe (100), and (c) a CdSe/ZnTe (100) heterojunction. The Se $3d_{5/2}$ core-level to valence-band-edge binding energy is measured in the bulk cubic CdSe samples, the Te $4d_{5/2}$ core-level to valence-band-edge binding energy in the bulk ZnTe samples, and the Se $3d_{5/2}$ to Te $4d_{5/2}$ core-level energy separation in the CdSe/ZnTe heterojunctions. Longer sampling times have been used in the vicinity of the valence-band edge for the spectra in (a) and (b). The valence-band spectrum for the bulk ZnTe sample is also shown on an enlarged intensity scale, as indicated in the figure.

the XPS spectrum near the valence-band edge is modeled as a convolution of a theoretical valence-band density of states with an experimentally determined XPS instrumental resolution function. This model function is then fitted to the experimental data to give the position of the valence-band edge. The XPS instrumental resolution function was determined from measured XPS spectra for Au $4f$ core-level peaks, for which the inherent linewidth attributable to lifetime broadening is known[26]. The theoretical valence-band density of states was calculated using the empirical pseudopotential method[27]; spin-orbit interactions[28] and a nonlocal effective mass parameter[29] were included in these calculations. The empirical pseudopotential parameters were obtained by optimizing the calculated band structure to give the best agreement at the Γ, X, and L points in the Brillouin zone with previously calculated band structures and measured critical-point energies for CdSe[30] and ZnTe[27, 31, 32, 33].

Figs. 6.4(a) and (b) show the valence-band spectra, model functions fitted to the XPS data, and calculated valence-band densities of states for cubic CdSe (100) and ZnTe (100), respectively. The valence-band edge in these figures, as determined by the fitting procedure described above, is taken to be at 0 eV.

6.3 Results and Discussion

Measurements obtained from the two bulk cubic CdSe samples yielded a Se $3d_{5/2}$ core-level to valence-band-edge binding energy of 52.51 ± 0.05 eV. The separation between the Se $3d_{5/2}$ and Cd $4d$ was determined to be 42.78 ± 0.03 eV, yielding a Cd $4d$ to core-level to valence-band-edge binding energy of 9.73 ± 0.05 eV. To our knowledge, these are the first measurements of atomic core-level binding energies in cubic CdSe.

As discussed in Section 5.2.3, measurements on bulk ZnTe samples yielded

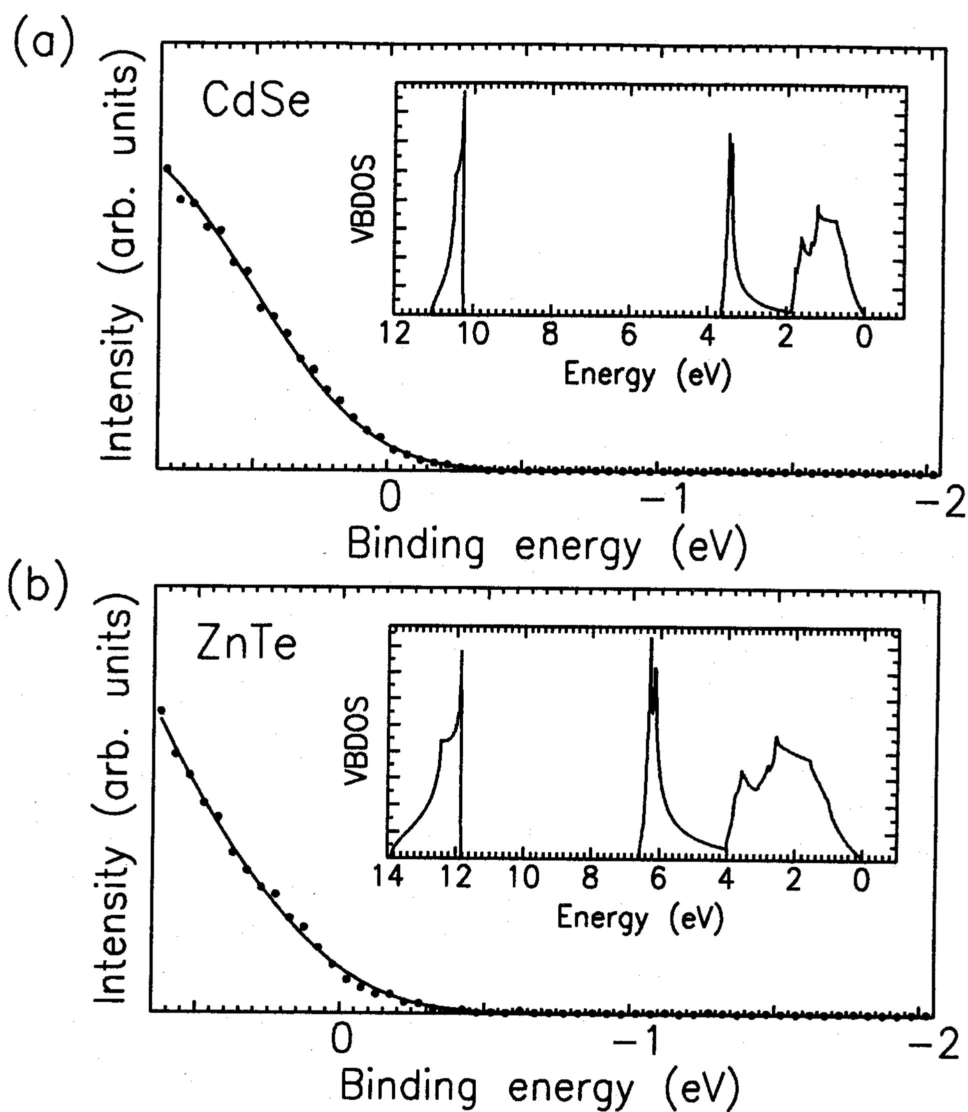

Figure 6.4: Typical XPS valence-band spectra and model functions fitted to the experimental data for (a) cubic CdSe (100) and (b) ZnTe (100). The theoretical valence-band densities of states used to construct the model functions are shown in the insets to each figure. These model functions are used to determine the position of the valence-band edge in each spectrum.

values of 9.42 ± 0.04 eV and 30.02 ± 0.02 eV for the Zn $3d$ core-level to valence-band-edge binding energy and the Te $4d_{5/2}$ to Zn $3d$ core-level energy separation, respectively. These values correspond to a Te $4d_{5/2}$ core-level to valence-band-edge binding energy in ZnTe of 39.44 ± 0.04 eV. Comparison of these results with previous measurements is difficult; reported values[34, 35, 36] for the Zn $3d$ core-level to valence-band-edge binding energy range from 9.1 eV to 9.84 eV.

The Se $3d_{5/2}$ to Te $4d_{5/2}$ core-level energy separation was measured in two heterojunctions consisting of $\sim$25 Å of CdSe grown on ZnTe, and in one heterojunction consisting of $\sim$25 Å of ZnTe grown on CdSe. For these three heterojunctions, the core-level energy separation was measured to be $(E^{\mathrm{CdSe}}_{\mathrm{Se3}d_{5/2}} - E^{\mathrm{ZnTe}}_{\mathrm{Te4}d_{5/2}}) = 13.71 \pm 0.02$ eV, yielding a valence-band offset $\Delta E_v = 0.64 \pm 0.07$ eV. A measurement of the Se $3d_{5/2}$ to Te $4d_{5/2}$ core-level energy separation was also made in one additional heterojunction consisting of $\sim$25 Å of ZnTe grown on $\sim$120 Å of CdSe that was deposited on a thicker CdSe film that had been used for bulk CdSe XPS measurements. This heterojunction yielded a core-level energy separation $(E^{\mathrm{CdSe}}_{\mathrm{Se3}d_{5/2}} - E^{\mathrm{ZnTe}}_{\mathrm{Te4}d_{5/2}}) = 13.85 \pm 0.02$ eV, suggesting that adverse growth conditions might influence band offset values in the CdSe/ZnTe material system. Earlier observations of interdiffusion and the formation of solid solutions at the CdSe/-ZnTe interface, as discussed in Section 6.1.1, lend support to the possibility that specific growth conditions might influence the detailed structure of the interface, and thereby induce shifts in band offset values.

Theoretical predictions for the CdSe/ZnTe valence-band offset extend over a wide range of values, ranging from the value of Harrison and Tersoff[12], $\Delta E_v = 0.31$ eV, to Kraut's calculation[9] of 1.11 eV for the CdSe/ZnTe valence band offset. Fig. 6.5, like Fig. 6.1, shows the range of values proposed for the CdSe/ZnTe valence-band offset, and also includes the valence-band offset value we obtained from our measurements. The large discrepancies among

the theoretical values in Fig. 6.5 clearly indicate the need for reliable experimental measurements of band offsets for CdSe/ZnTe and other novel heterojunction systems.

Using room-temperature band gaps for ZnTe and for cubic CdSe[24] of 2.25 eV and 1.67 eV, respectively, we obtain a conduction-band offset ΔE_c(CdSe/ZnTe) = 1.22 ± 0.07 eV, corresponding to a Type II, staggered band alignment. The size of the conduction-band offset indicates that injection of electrons directly from n-CdSe into p-ZnTe is probably not practical. However, electron injection from n-$(CdSe)_{1-x}(ZnTe)_x$ into p-ZnTe remains a possibility, depending on the dopability of n-$(CdSe)_{1-x}(ZnTe)_x$ alloys. Fig. 6.6 shows the valence- and conduction-band alignments for the CdSe/ZnTe heterojunction obtained from our measurements.

We also note that the value we obtain for the CdSe/ZnTe valence-band offset differs significantly from the valence-band offset value obtained for the ZnSe/-ZnTe heterojunction by Rajakarunanayake et al.[37] by analyzing the optical experiments of Kobayashi et al.[38] and interpreting their data using theoretical calculations of superlattice band structure. The analysis of Rajakarunanayake et al. yielded a ZnSe/ZnTe valence-band offset of 0.98 ± 0.10 eV, compared to our value of 0.64 ± 0.07 eV for the CdSe/ZnTe valence-band offset. On the basis of the common anion rule[4], one would expect the valence-band offsets for the ZnSe/-ZnTe and the CdSe/ZnTe heterojunctions to be quite close. One possible source of this discrepancy is that the ZnSe/ZnTe heterojunction is heavily strained, with a lattice mismatch of over 7%. The band offset value obtained in Ref. [37] is the discontinuity in the average position of the light-hole, heavy-hole, and split-off valence bands in each material, a quantity that is expected to depend only weakly on strain[39, 40]. It is possible, however, that a dependence of the average valence-band offset on strain might significantly augment an actual deviation from the

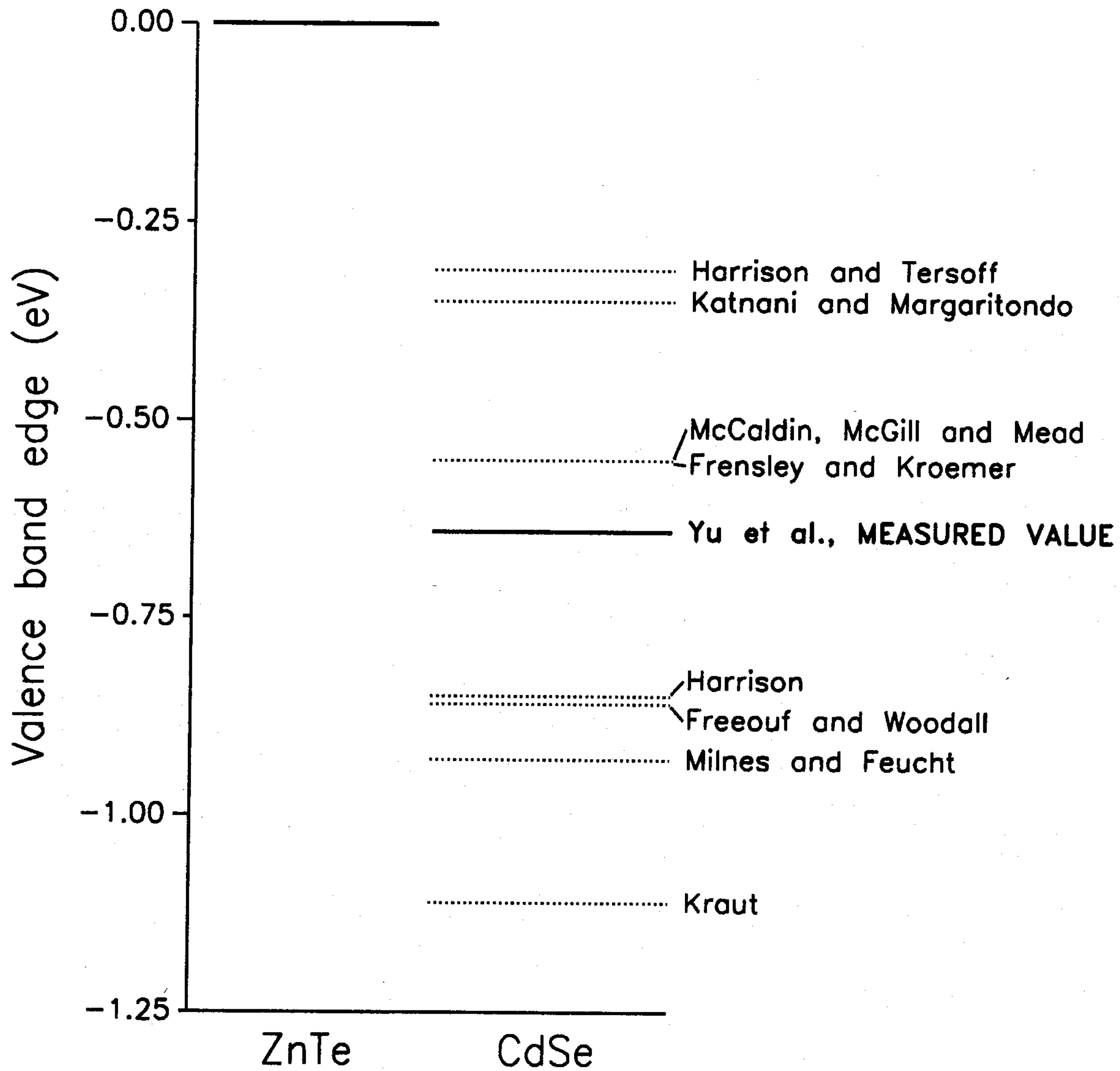

Figure 6.5: Valence-band offset values for the CdSe/ZnTe heterojunction predicted by several theories[5, 4, 6, 7, 8, 9, 10, 11, 12, 13, 14], and the valence-band offset value obtained from our measurements, $\Delta E_v = 0.64 \pm 0.07$ eV.

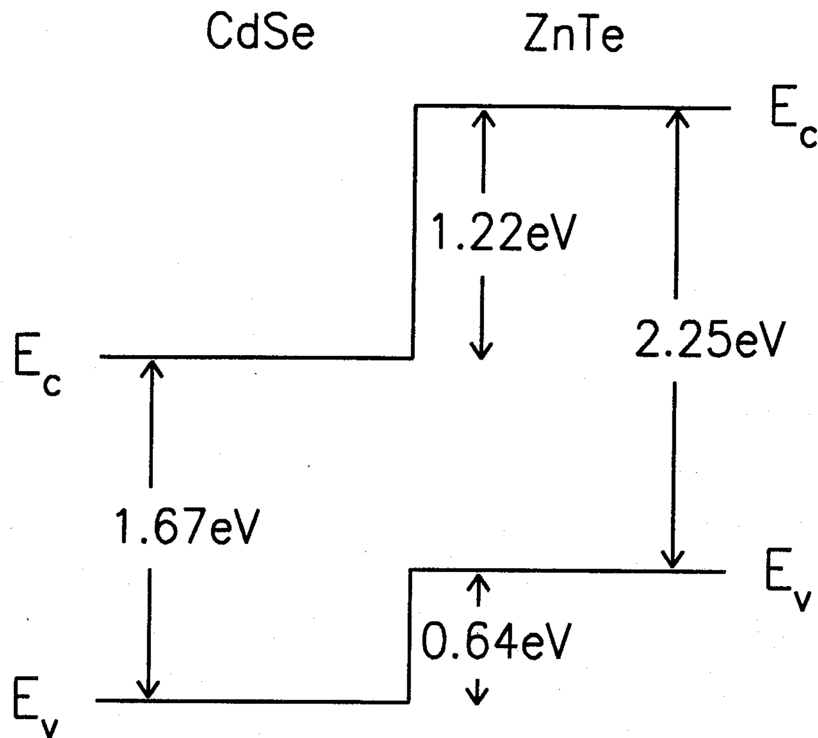

Figure 6.6: Conduction- and valence-band alignments determined by our measurements for the CdSe/ZnTe heterojunction. We obtained $\Delta E_v = 0.64 \pm 0.07$ eV, corresponding to $\Delta E_c = 1.22 \pm 0.07$ eV, yielding a Type II, staggered band alignment. As seen in the figure, the conduction-band offset is too high to allow efficient injection of electrons from n-CdSe into p-ZnTe.

common anion rule to produce the discrepancy we have observed between the CdSe/ZnTe and ZnSe/ZnTe valence-band offsets.

6.4 Conclusions

In this chapter we have presented the measurement of the CdSe/ZnTe (100) heterojunction valence-band offset by x-ray photoelectron spectroscopy. The CdSe/ZnTe material system is of potential interest for heterojunction injection of electrons from n-CdSe or n-$(CdSe)_{1-x}(ZnTe)_x$ into p-ZnTe to achieve visible electroluminescence in ZnTe. In addition, the CdSe/ZnTe valence-band offset could provide insight into the validity of the common anion rule for valence-band offsets, and possibly information about band offsets in other material systems containing Se and Te, such as ZnSe/ZnTe.

We have been able to grow cubic CdSe on ZnTe with a lattice mismatch of only $\sim$0.44%, and have performed, to our knowledge, the first measurements of atomic core-level binding energies in cubic CdSe. Our measurements of the Se $3d_{5/2}$ and Te $4d_{5/2}$ core-level to valence-band-edge binding energies in CdSe and ZnTe, respectively, and of the Se $3d_{5/2}$ to Te $4d_{5/2}$ core-level energy separation in CdSe/-ZnTe heterojunctions, have yielded a valence-band offset ΔE_v(CdSe/ZnTe) = 0.64 ± 0.07 eV, corresponding to a conduction-band offset ΔE_c(CdSe/ZnTe) = 1.22 ± 0.07 eV. The size of the CdSe/ZnTe conduction-band offset obviates the possibility of achieving practical electron injection directly from n-CdSe into p-ZnTe; however, electron injection from n-$(CdSe)_{1-x}(ZnTe)_x$ into p-ZnTe remains a possibility, depending on the dopability of n-$(CdSe)_{1-x}(ZnTe)_x$ alloys. We have also observed evidence that details of growth conditions might also affect band offset values for the CdSe/ZnTe interface; this possibility is supported by earlier observations of atomic interdiffusion and formation of solid solutions and

intermediate compounds in CdSe/ZnTe heterojunctions. Finally, a comparison of our result for the CdSe/ZnTe valence-band offset with a determination of the ZnSe/ZnTe average valence-band offset appears to yield a substantial deviation from the common anion rule. However, complications arising from strain in the ZnSe/ZnTe heterojunction system may be at least partially responsible for this discrepancy.

References

[1] J. O. McCaldin and T. C. McGill, *J. Vac. Sci. Technol. B* **6**, 1360 (1988).

[2] J. O. McCaldin, in *Growth and Optical Properties of Wide-Gap II-VI Low-Dimensional Semiconductors*, T. C. McGill, C. M. Sotomayor-Torres, and W. Gebhardt, eds. (Plenum Press, New York, 1988), p. 39.

[3] E. T. Yu, Y. Rajakarunanayake, M. C. Phillips, J. O. McCaldin, and T. C. McGill, presented at the 1990 International Conference on Solid State Devices and Materials, Sendai, Japan (1990).

[4] J. O. McCaldin, T. C. McGill, and C. A. Mead, *Phys. Rev. Lett.* **36**, 56 (1976).

[5] R. L. Anderson, *Solid–State Electron.* **5**, 341 (1962).

[6] A. G. Milnes and D. L. Feucht, *Heterojunctions and Metal–Semiconductor Junctions* (Academic Press, New York, 1972).

[7] J. L. Freeouf and J. M. Woodall, *Appl. Phys. Lett.* **39**, 727 (1981).

[8] W. A. Harrison, *J. Vac. Sci. Technol.* **14**, 1016 (1977).

[9] E. A. Kraut, *J. Vac. Sci. Technol. B* **2**, 486 (1984).

[10] W. R. Frensley and H. Kroemer, *J. Vac. Sci. Technol.* **13**, 810 (1976).

[11] W. R. Frensley and H. Kroemer, *Phys. Rev. B* **16**, 2642 (1977).

[12] W. A. Harrison and J. Tersoff, *J. Vac. Sci. Technol. B* **4**, 1068 (1986).

[13] A. D. Katnani and G. Margaritondo, *J. Appl. Phys.* **5**, 2522 (1983).

[14] A. D. Katnani and G. Margaritondo, *Phys. Rev. B* **28**, 1944 (1983).

[15] O. Von Ross, *Solid-State Electron.* **23**, 1069 (1980).

[16] P. A. Gashin and A. V. Simashkevich, *Phys. Status Solidi (A)* **19**, 379 (1973).

[17] P. A. Gashin and A. V. Simashkevich, *Phys. Status Solidi (A)* **19**, 615 (1973).

[18] P. A. Gashin, D. A. Sherban, and A. V. Simashkevich, *J. Lumin.* **15**, 109 (1977).

[19] Ya. A. Fedotov, S. G. Konnikov, V. A. Supalov, N. M. Kondaurov, A. N. Kovalev, and A. V. Vanyukov, translated from *Izvestiya Akademii Nauk SSSR, Neorganicheskie Materialy* **11**, 2148 (1975).

[20] F. Buch, A. L. Fahrenbruch, and R. H. Bube, *Appl. Phys. Lett.* **28**, 593 (1976).

[21] F. Buch, A. L. Fahrenbruch, and R. H. Bube, *J. Appl. Phys.* **48**, 1596 (1977).

[22] A. V. Simashkevich and R. L. Tsiulyanu, *J. Cryst. Growth* **35**, 269 (1976).

[23] É. A. Senokosov and A. N. Usatyĭ, *Sov. Phys. Semicond.* **12**, 575 (1978).

[24] N. Samarth, H. Luo, J. K. Furdyna, S. B. Qadri, Y. R. Lee, A. K. Ramdas, and N. Otsuka, *Appl. Phys. Lett.* **54**, 2680 (1990).

[25] E. A. Kraut, R. W. Grant, J. R. Waldrop, and S. P. Kowalczyk, *Phys. Rev. B* **28**, 1965 (1983).

[26] P. H. Citrin, G. K. Wertheim, and Y. Baer, *Phys. Rev. Lett.* **41**, 1425 (1978).

[27] M. L. Cohen and T. K. Bergstresser, *Phys. Rev.* **141**, 789 (1966).

[28] L. R. Saravia and D. Brust, *Phys. Rev.* **176**, 915 (1968).

[29] J. R. Chelikowsky, D. J. Chadi, and M. L. Cohen, *Phys. Rev. B* **8**, 2786 (1973).

[30] D. J. Stukel, R. N. Euwema, T. C. Collins, F. Herman, and R. L. Kortum, *Phys. Rev.* **179**, 740 (1969).

[31] M. Cardona and D. L. Greenaway, *Phys. Rev.* **131**, 98 (1963).

[32] J. P. Walter, M. L. Cohen, Y. Petroff, and M. Balkanski, *Phys. Rev. B* **1**, 2661 (1970).

[33] P. Eckelt, *Phys. Status Solidi* **23**, 307 (1967).

[34] R. W. Grant, E. A. Kraut, S. P. Kowalczyk, and J. R. Waldrop, *J. Vac. Sci. Technol. B* **1**, 320 (1983).

[35] T. M. Duc, C. Hsu, and J.-P. Faurie, *Phys. Rev. Lett.* **58**, 1127 (1987).

[36] G. P. Schwartz, G. J. Gualtieri, R. D. Feldman, R. F. Austin, and R. G. Nuzzo, *J. Vac. Sci. Technol. B* **8**, 747 (1990).

[37] Y. Rajakarunanayake, R. H. Miles, G. Y. Wu, and T. C. McGill, *Phys. Rev. B* **37**, 10212 (1988).

[38] M. Kobayashi, N. Mino, H, Katagiri, R. Kimura, M. Konagai, and K. Takahashi, *Appl. Phys. Lett.* **48**, 296 (1986).

[39] C. G. Van de Walle and R. M. Martin, *Phys. Rev. B* **34**, 5621 (1986).

[40] C. G. Van de Walle, *Phys. Rev. B* **39**, 1871 (1989).

Part II

Theoretical and Experimental Studies of Tunneling in Semiconductor Heterostructures

Chapter 7

Theoretical Simulation of Novel Semiconductor Tunnel Structures

7.1 Introduction

7.1.1 Background and Motivation

Interest in quantum-mechanical tunneling in semiconductors, and in particular in tunnel devices exhibiting negative differential resistance, can be traced to the invention of the tunnel diode by Leo Esaki in the 1950's[1]. The proposal of semiconductor device structures such as superlattices and multiple-barrier heterostructures whose operation is based on tunneling phenomena[2], and the subsequent demonstration of resonant tunneling in a double-barrier heterostructure[3], initiated the development of an entire field of research directed towards the elucidation and utilization of tunneling phenomena in various types of semiconductor heterostructures. The development of sophisticated epitaxial growth techniques

such as molecular-beam epitaxy (MBE) and metalorganic chemical vapor deposition (MOCVD) has made possible the fabrication of heterostructures with dimensions controllable at the atomic level, and the observation of high-speed oscillations in $GaAs/Al_xGa_{1-x}As$ double-barrier heterostructures[4] has led to intense interest in the application of double-barrier resonant tunneling diodes in particular for developing high-speed semiconductor devices.

In conjunction with experimental advances in the performance, variety, and applicability of resonant-tunneling heterostructures, a general theoretical framework has gradually been developed[2, 5, 6, 7, 8, 9, 10] for understanding and theoretically simulating the behavior of resonant tunneling devices. Such an understanding is critical in attaining the highest possible performance from these devices, since the ultimate limits for speed and other device characteristics may be determined eventually by factors such as quantum-mechanical tunneling times, electron coherence lengths, and other basic physical considerations. In addition, the fundamentally quantum-mechanical nature of resonant tunneling allows one to use structures such as double barriers, quantum wells, superlattices, and eventually quantum wires and dots, to investigate some very basic issues in quantum mechanics.

A theoretical understanding of tunneling in heterostructures also allows one to simulate, at least semiquantitatively, the electrical behavior of these devices. This capability enables one to explore a large region of device parameter space and to investigate new device concepts much more efficiently than could be done experimentally, and also provides insight into many aspects of the observed electrical behavior of tunneling devices. Theoretical modeling and simulation have proven to be particularly useful in the study of interband tunnel structures in the InAs/GaSb/AlSb material system, in which transport can occur between conduction-band states in InAs and valence-band states in GaSb[11, 12, 13, 14].

For device structures realized in this material system, band-structure effects are of essential importance and lead in some cases to device behavior which, while somewhat nonintuitive, can be explained very clearly by appropriate theoretical modeling[15].

7.1.2 Outline of Chapter

In this chapter are explained the basic theoretical models we have used to simulate a wide variety of tunnel structures. The simulations begin with a calculation of electrostatic band bending in device structures by solving Poisson's equation in one dimension with an overall charge-neutrality condition imposed across the entire device. These band-bending calculations are described in Section 7.2. The computed device profiles are then used to calculate transmission coefficients for our device structures, using transfer-matrix methods based on the original technique of Kane[16]. The transfer-matrix method, and its implementation for a variety of band structure models, are presented in Section 7.3. Section 7.3.1 describes the basic transfer-matrix method as implemented for a simple one-band (electron) band-structure model; Sections 7.3.2 and 7.3.3 discuss the calculation of transmission coefficients for more realistic band-structure models. Transmission coefficients computed as a function of a carrier's incident energy are then used to calculate actual current-voltage characteristics in devices. Our calculated currents do not include transport mechanisms that rely upon scattering processes, and are therefore somewhat idealized. Nevertheless, the agreement between currents calculated using the methods described in this chapter and currents measured in actual devices is relatively good. Our method for calculating current-voltage characteristics is described in Section 7.4. In Section 7.5, we illustrate the use of these methods by calculating current-voltage characteristics

for double-barrier tunnel structures realized in the III-V/II-VI material systems GaAs/ZnSe and InAs/ZnTe. The main results are summarized in Section 7.6.

7.2 Calculation of Electrostatic Band Bending

The first step in simulating the electrical behavior of a quantum heterostructure device is to calculate the energy-band profile of the structure. In our models, we compute the energy-band profile by solving Poisson's equation across the device, imposing a condition of charge neutrality over the entire structure. Because we are concerned primarily with transport in the direction perpendicular to the direction of growth in a heterostructure, we calculate band profiles only in the growth direction, and assume that the potential does not vary in the other directions. Our model employs the Thomas-Fermi approximation, assuming that the positions of the band edges at a given point in space are determined solely by the carrier concentrations at that point. We also assume that a quasi-Fermi level can be defined at every point in the device, and that the positions of the band edges relative to the quasi-Fermi level are determined by carrier concentrations calculated using simple parabolic band structures.

For a one-dimensional semiconductor heterostructure, Poisson's equation can be written, in MKS units,

$$\frac{d^2\phi(z)}{dz^2} = -\frac{\rho(z)}{\epsilon}, \tag{7.1}$$

or, relating the electrostatic potential $\phi(z)$ to the conduction-band-edge profile $E_c(z)$ by the expression $E_c(z) = -e\phi(z)$,

$$\frac{d^2E_c(z)}{dz^2} = \frac{e\rho(z)}{\epsilon}, \tag{7.2}$$

where e is the electron charge, ϵ is the dielectric constant, and $\rho(z)$ is the charge

density. The charge density $\rho(z)$ is given by the expression

$$\rho(z) = -e(n(z) - p(z) + N_A(z) - N_D(z)), \tag{7.3}$$

where $n(z)$ and $p(z)$ are the electron and hole densities, respectively, $N_A(z)$ is the density of ionized acceptors, and $N_D(z)$ is the density of ionized donors. The concentrations of donors and acceptors are determined by doping profiles incorporated during growth, and it is typically assumed that the dopants are fully ionized. The electron and hole densities $n(z)$ and $p(z)$ are calculated as functions of the conduction- and valence-band-edge positions $E_c(z)$ and $E_v(z)$ using an approximation to the full Fermi integral for each carrier type and assuming a parabolic structure for both bands. For simplicity, we will describe the calculation of the electron concentration $n(z)$ as a function of the conduction-band-edge position $E_c(z)$; the calculation relating $p(z)$ to $E_v(z)$ is completely analogous.

In general, the carrier concentration as a function of the chemical potential μ (equal at zero temperature to the Fermi energy E_f) is given by

$$\begin{aligned} n &= \int_0^\infty \mathcal{D}(E) f(E) dE && (7.4) \\ &= \frac{1}{2\pi^2}\left(\frac{2m^*}{\hbar^2}\right)^{3/2} \int_{E_c}^\infty (E - E_c)^{1/2} \frac{1}{e^{(E-\mu)/k_B T} + 1} dE, && (7.5) \end{aligned}$$

where we have used the expressions for the Fermi function $f(E)$ and the electronic density of states $\mathcal{D}(E)$

$$\begin{aligned} f(E) &= \frac{1}{e^{(E-\mu)/k_B T} + 1}, && (7.6) \\ \mathcal{D}(E) &= \frac{1}{2\pi^2}\left(\frac{2m^*}{\hbar^2}\right)^{3/2} (E - E_c)^{1/2}. && (7.7) \end{aligned}$$

In Eqs. (7.5) – (7.7), m^* is the conduction band effective mass, k_B is the Boltzmann constant, and T is the carrier temperature.

To obtain tractable expressions for $n(z)$ as a function of E_c, we consider separately the cases of a nondegenerate ($\mu < E_c$) and a degenerate ($\mu > E_c$) electron

gas, and then interpolate between the two cases. For $\mu < E_c$, we approximate the Fermi function $f(z)$ by a simple exponential, obtaining

$$
\begin{aligned}
n &\approx \frac{1}{2\pi^2}\left(\frac{2m^*}{\hbar^2}\right)^{3/2}\int_{E_c}^{\infty}(E-E_c)^{1/2}e^{-(E-\mu)/k_BT}dE && (7.8)\\
&= \frac{1}{2\pi^2}\left(\frac{2m^*}{\hbar^2}\right)^{3/2}e^{(E_c-\mu)/k_BT}\int_0^{\infty}E'^{1/2}e^{-E'/k_BT}dE' && (7.9)\\
&= \frac{1}{4}\left(\frac{2m^*}{\hbar^2}\right)^{3/2}(k_BT)^{3/2}e^{-(E_c-\mu)/k_BT} && (7.10)\\
&\equiv F_1(\mu-E_c), \qquad (\mu < E_c). && (7.11)
\end{aligned}
$$

For $\mu > E_c$, we again start from Eq. (7.5), but use the Sommerfeld expansion for Fermi integrals[17]:

$$
\begin{aligned}
n &= \frac{1}{2\pi^2}\left(\frac{2m^*}{\hbar^2}\right)^{3/2}\int_{E_c}^{\infty}\frac{(E-E_c)^{1/2}dE}{e^{(E_c-\mu)/k_BT}+1} && (7.12)\\
&\approx \frac{1}{2\pi^2}\left(\frac{2m^*}{\hbar^2}\right)^{3/2}\left[\int_{E_c}^{E_f}(E-E_c)^{1/2}dE+(\mu-E_f)(E_f-E_c)^{1/2}\right.\\
&\qquad \left.+\frac{\pi^2}{6}(k_BT)^2\frac{1}{2}(E_f-E_c)^{-1/2}\right]. && (7.13)
\end{aligned}
$$

Using the fact that n is independent of T, we see from Eq. (7.13) evaluated at $T = 0$ that

$$
n = \frac{1}{3\pi^2}\left(\frac{2m^*}{\hbar^2}\right)^{3/2}(E_f-E_c)^{3/2}. \qquad (7.14)
$$

We can then obtain from Eq. (7.13) a relation between the Fermi energy E_f and the chemical potential μ,

$$
\mu = E_f - \frac{\pi^2}{12}\frac{(k_BT)^2}{(E_f-E_c)}, \qquad (7.15)
$$

or

$$
E_f - E_c = \frac{1}{2}\left[(\mu-E_c)+\sqrt{(\mu-E_c)^2+\frac{\pi^2}{3}(k_BT)^2}\right]. \qquad (7.16)
$$

Substituting Eq. (7.16) into Eq. (7.14), we finally obtain

$$
\begin{aligned}
n &\approx \frac{1}{3\pi^2}\left(\frac{m^*}{\hbar^2}\right)^{3/2}\left[(\mu-E_c)+\sqrt{(\mu-E_c)^2+\frac{\pi^2}{3}(k_BT)^2}\right]^{3/2} && (7.17)\\
&\equiv F_2(\mu-E_c), \qquad (\mu > E_c). && (7.18)
\end{aligned}
$$

We then perform an interpolation between the two cases $\mu < E_c$ and $\mu > E_c$ using the expressions for n given in Eqs. (7.10)–(7.11) and (7.17)–(7.18):

$$\begin{aligned} n(\mu - E_c) &\approx \frac{F_1(\mu - E_c)}{1 + e^{2(\mu - E_c)/k_B T}} + \frac{F_2(\mu - E_c)}{1 + e^{-2(\mu - E_c)/k_B T}} \qquad (7.19) \\ &= \frac{1}{1 + e^{-2(\mu - E_c)/k_B T}} \left[\frac{1}{4} \left(\frac{2m^*}{\pi \hbar^2} \right)^{3/2} (k_B T)^{3/2} e^{-(\mu - E_c)/k_B T} + \right. \\ &\left. \frac{1}{3\pi^2} \left(\frac{m^*}{\hbar^2} \right)^{3/2} \left\{ (\mu - E_c) + \sqrt{(\mu - E_c)^2 + \frac{\pi^2}{3} (k_B T)^2} \right\}^{3/2} \right]. \qquad (7.20) \end{aligned}$$

Fig. 7.1 shows the electron density as a function of chemical potential μ for GaAs ($m^* = 0.067 m_e$), calculated using Eq. (7.20) for temperatures of 10 K, 77 K, and 300 K.

Defining a new potential variable $\Phi(z) \equiv \mu - E_c(z)$, we can then write Poisson's equation (7.2) as

$$\frac{d^2 \Phi(z)}{dz^2} = \frac{e^2}{\epsilon} (n(\Phi(z)) - p(\Phi(z)) + N_A(z) - N_D(z)). \qquad (7.21)$$

To obtain a numerical solution to Eq. (7.21), it is convenient to convert the single second-order differential equation to a system of first-order differential equations. Defining $\Psi(z) \equiv d\Phi(z)/dz$, we can write Eq. (7.21) in the form

$$\frac{d}{dz} \begin{pmatrix} \Phi(z) \\ \Psi(z) \end{pmatrix} = \begin{pmatrix} \Psi(z) \\ (e^2/\epsilon)(n(\Phi(z)) - p(\Phi(z)) + N_A(z) - N_D(z)) \end{pmatrix}. \qquad (7.22)$$

To complete the specification of the problem, we impose on the solution a boundary condition that the total charge integrated across the entire device structure, taken to be the interval $z \in [0, L]$, be zero, i.e.,

$$\int_0^L \rho(z) dz = -e \int_0^L n(z) - p(z) + N_A(z) - N_D(z) dz = 0. \qquad (7.23)$$

Given the type of problem specified by Eqs. (7.22) and (7.23), there are two approaches that are commonly used for obtaining a numerical solution for $\Phi(z)$.

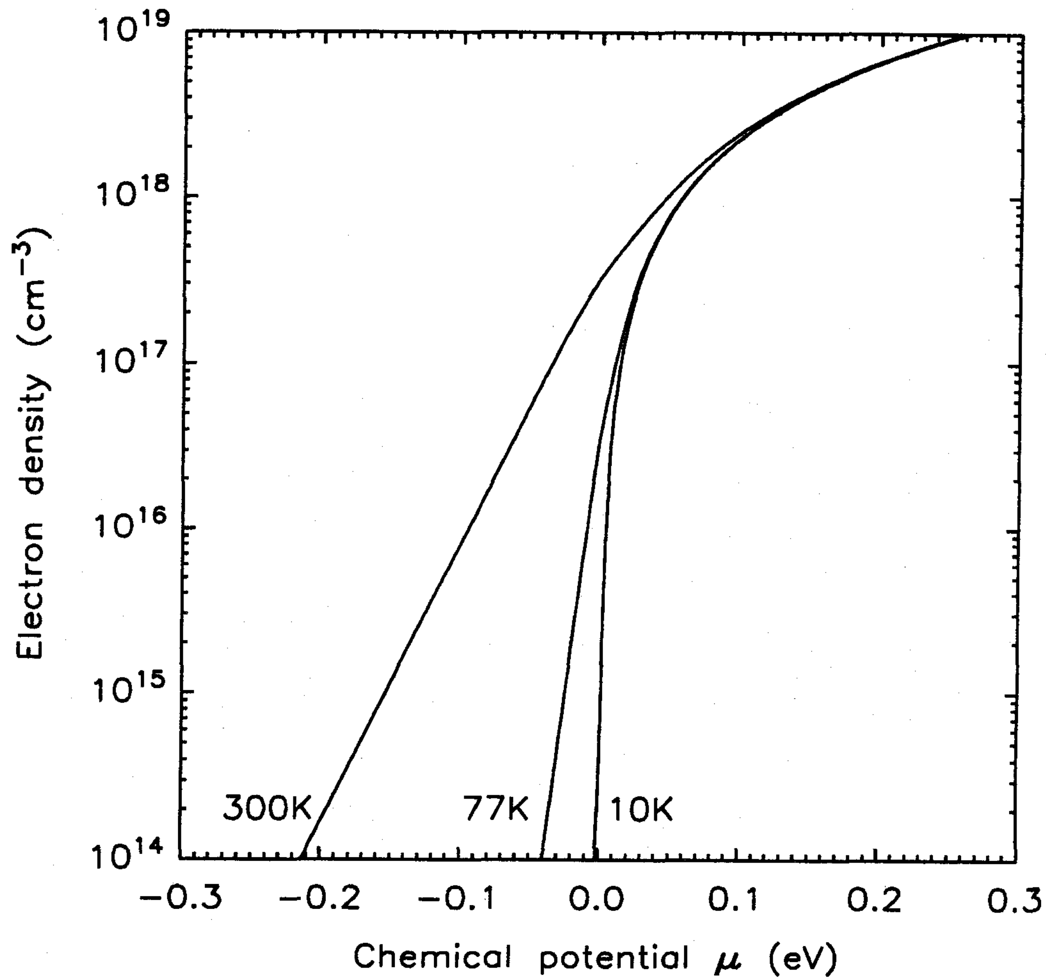

Figure 7.1: Electron density as a function of chemical potential for GaAs ($m^* = 0.067m_e$) calculated using Eq. (7.20) for temperatures of 10 K, 77 K, and 300 K. The energy of the conduction band edge has been taken to be 0 eV.

In one approach, an initial guess is made for $\Phi(z)$ and $\Psi(z)$ at some suitable initial position $z = z_0$. A solution for all z is then obtained by a combination of numerical and analytical integration of the differential equation (7.22) from the initial point $z = z_0$. Once this solution has been obtained, the total charge density in the structure is computed using Eq. (7.23); the result is then used to generate a new guess for $\Phi(z_0)$ and $\Psi(z_0)$, and the procedure is repeated until the boundary condition (7.23) is satisfied to within the desired tolerance. The implementation of a method of this type for simplified conditions (e.g., zero temperature) and device structures is described in detail in the Ph.D. thesis of A. R. Bonnefoi[18]. Although this method is adequate for the structures and conditions considered by Bonnefoi, it is not easily generalized to more complicated device structures or functional forms for $n(\Phi(z))$. In addition, the technique is not terribly robust — an incorrect initial guess for $\Phi(z_0)$ and $\Psi(z_0)$ can often lead to divergences in the integration across the device structure. A somewhat related problem is that the band-edge profile obtained by integration across the device structure is often extremely sensitive to small changes in the initial guess, making convergence to the correct solution difficult to achieve. This method is therefore not particularly attractive for treating band bending in complicated device structures and in the presence of conditions such as nonzero carrier temperature, degenerate and non-degenerate carrier populations, and the presence of substantial densities of both electrons and holes.

The other approach is based upon so-called "relaxation" techniques, and is described in detail by Press et al.[19]. In this approach, the differential equation (7.22) is approximated by a finite-difference equation on a mesh of points across the device structure. An initial guess is made for the solution in the entire device structure. One then calculates, to linear order, the corrections to the guess that would be needed for the solution to satisfy the finite-difference equation and the

boundary conditions. These corrections are then applied to the solution, and the procedure is iterated until the solution satisfies the finite difference equation and the boundary conditions to the desired tolerance.

To apply this relaxation technique to the calculation of electrostatic band banding, one slight modification was required in the specification of the problem by Eqs. (7.22) and (7.23). The implementation of the relaxation technique requires that the boundary conditions be local. However, the charge neutrality condition (7.23) is nonlocal, since an integral over the entire device is required. Fortunately, one can use Poisson's equation (7.22) to write the charge-neutrality condition as a local boundary condition:

$$\begin{aligned} 0 &= \int_0^L \rho(z)dz && (7.24)\\ &= -e\int_0^L n(z) - p(z) + N_A(z) - N_D(z)dz && (7.25)\\ &= -\frac{1}{e}\int_0^L \epsilon\frac{d\Psi(z)}{dz}dz && (7.26)\\ &= \left[\epsilon\Psi(z)\right]_0^L = \epsilon\Psi(z)\Big|_L - \epsilon\Psi(z)\Big|_0. && (7.27) \end{aligned}$$

For the complete specification of the problem two boundary equations are required, since there are two first-order differential equations in (7.22). We therefore chose to require that $\Psi(z) = 0$ at both endpoints of the device structure. Physically, this corresponds to the condition that the electric field vanish at both endpoints of the device.

An outstanding advantage of the relaxation method is that it has proven, in our experience, to be extremely robust. Provided that the device structure specification includes the entire region over which appreciable band bending occurs, the technique converges to the correct solution even for very rough initial guesses, and the solutions do not diverge to infinity within the device structure during the iteration procedure. The technique also does not depend on analytic

approximations based on specific functional forms for quantities such as carrier concentrations, and therefore can be generalized quite easily to include secondary effects such as, for example, nonparabolic band structure. The stability of the iteration procedure would also seem to make a relaxation technique a natural choice for more fully self-consistent band-bending calculations that include, for example, coupled computations of electron and hole wave functions using the Schrödinger equation and of band bending using the Poisson equation.

Figs. 7.2(a), (b), and (c) show band-edge and Fermi-level profiles, electric field, and charge density, respectively, for an InAs/AlSb/InAs/AlSb/InAs double-barrier tunnel structure under an applied bias of 400 mV at a temperature of 300 K. The conduction- and valence-band-edge profiles were calculated using the relaxation technique described above, and the electric field $E = (dE_c(z)/dz)/e$ and charge density $\rho(z)$ were derived from these calculated band-edge profiles.

7.3 Calculation of Transmission Coefficients

Once the energy band profiles for a device structure have been obtained, transmission coefficients are calculated using the transfer-matrix method developed by Kane[16], adapted to account for various band-structure models and the resulting boundary conditions on wave functions at interfaces between different materials. As described in the following sections, the transfer-matrix method allows transmission coefficients to be calculated for arbitrary energy-band-edge profiles, and is, in principle, easily adapted to include band-structure models more realistic than the simple one-band model that has typically been used. The transmission coefficient alone yields a great deal of information about transport across semiconductor heterostructures, and as described in Section 7.4, provides the basis for calculating current-voltage characteristics for heterostructure devices.

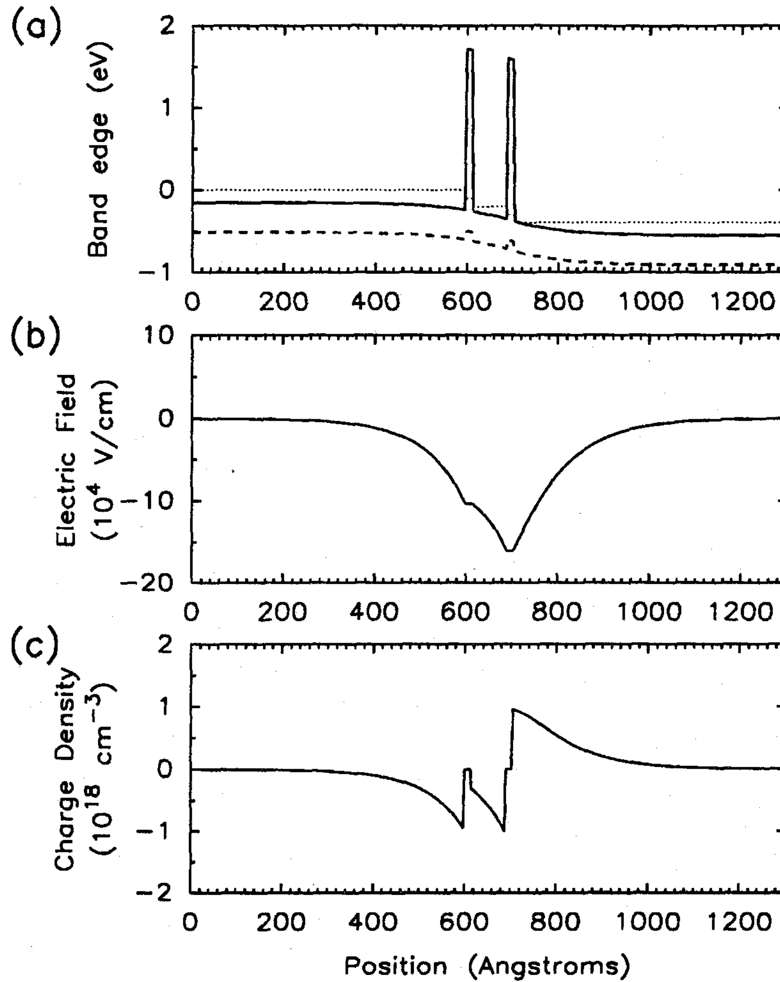

Figure 7.2: (a) Conduction-band-edge (solid line) and valence-band-edge (dashed line) profiles and the quasi-Fermi levels (dotted line), (b) electric field, and (c) charge density calculated for an InAs/AlSb/InAs/AlSb/InAs double-barrier tunnel structure using the relaxation method described in the text. The calculations were performed for a donor concentration of 1×10^{18} cm^{-3} in the InAs electrodes and at a carrier temperature of 300 K. The barrier and quantum-well layers were assumed to be undoped. A bias of 0.4 V was applied to the device.

7.3.1 The One-Band Model

The transfer-matrix method is based on the ability to describe, for a carrier in a crystal with constant external potential, the carrier wave function and its derivative at a point z' as a linear function of the wave function and its derivative at a point z. For a band-structure model that includes only a single parabolic conduction band with an effective mass m^*, the implementation of the transfer-matrix method is especially simple. Schrödinger's equation for such a model is

$$H\psi(z) = -\frac{\hbar^2}{2}\frac{d}{dz}\left(\frac{1}{m^*}\frac{d\psi(z)}{dz}\right) + V(z)\psi(z) = E\psi(z). \tag{7.28}$$

The probability current for the Hamiltonian in Eq. (7.28) is given by

$$J = \frac{i\hbar}{2}\left[\psi^*\left(\frac{1}{m^*}\frac{d\psi}{dz}\right) - \left(\frac{1}{m^*}\frac{d\psi^*}{dz}\right)\psi\right]. \tag{7.29}$$

From Eqs. (7.28) and (7.29), and the physical requirement that probability current be conserved, we obtain the requirements that $\psi(z)$ and $(1/m^*)(d\psi(z)/dz)$ be continuous across the device structure. In a constant external potential $V(z) = V_0$, the wave functions are simply plane waves; a general wave function and its derivative divided by the effective mass can therefore be written

$$\begin{pmatrix} \psi(z) \\ \dfrac{1}{m^*}\dfrac{d\psi(z)}{dz} \end{pmatrix} = \begin{pmatrix} Ae^{ikz} + Be^{-ikz} \\ \dfrac{ik}{m^*}(Ae^{ikz} - Be^{-ikz}) \end{pmatrix}, \tag{7.30}$$

where $k = \sqrt{2m^*(E - V_0)/\hbar^2}$. From Eq. (7.30), one can derive the form of the transfer matrix $\mathbf{T}(z_1, z_0)$:

$$\begin{aligned} \begin{pmatrix} \psi(z) \\ \dfrac{1}{m^*}\dfrac{d\psi(z)}{dz} \end{pmatrix}_{z=z_1} &= \begin{pmatrix} \cos k(z_1 - z_0) & \dfrac{m^*}{k}\sin k(z_1 - z_0) \\ -\dfrac{k}{m^*}\sin k(z_1 - z_0) & \cos k(z_1 - z_0) \end{pmatrix} \begin{pmatrix} \psi(z) \\ \dfrac{1}{m^*}\dfrac{d\psi(z)}{dz} \end{pmatrix}_{z=z_0} \\ &\equiv \mathbf{T}(z_1, z_0) \begin{pmatrix} \psi(z) \\ \dfrac{1}{m^*}\dfrac{d\psi(z)}{dz} \end{pmatrix}_{z=z_0}. \end{aligned} \tag{7.31}$$

For $E < V_0$, k is imaginary and it is convenient to write the transfer matrix as a function of $\kappa = \sqrt{2m^*(V_0 - E)/\hbar^2}$:

$$\begin{pmatrix} \psi(z) \\ \frac{1}{m^*}\frac{d\psi(z)}{dz} \end{pmatrix}_{z=z_1} = \begin{pmatrix} \cosh\kappa(z_1 - z_0) & \frac{m^*}{\kappa}\sinh\kappa(z_1 - z_0) \\ \frac{\kappa}{m^*}\sinh\kappa(z_1 - z_0) & \cosh\kappa(z_1 - z_0) \end{pmatrix} \begin{pmatrix} \psi(z) \\ \frac{1}{m^*}\frac{d\psi(z)}{dz} \end{pmatrix}_{z=z_0}$$

$$\equiv \mathbf{T}(z_1, z_0) \begin{pmatrix} \psi(z) \\ \frac{1}{m^*}\frac{d\psi(z)}{dz} \end{pmatrix}_{z=z_0} . \tag{7.32}$$

To calculate the transmission coefficient across a device structure with an arbitrary energy band profile, we specify a mesh of points $\{z_i\}$, typically equally spaced, over the device and approximate the true energy-band profile by a piecewise-constant profile with constant band edges in the intervals between mesh points. The transmission coefficient is obtained by calculating the amplitude of the transmitted and reflected plane waves scattered by the device structure for an incident plane wave of unit amplitude. The incident and scattered plane waves are described by a wave function of the form

$$\psi(z) = \begin{cases} e^{ikz} + re^{-ikz} & z \leq 0 \\ te^{ikz} & z \geq L \end{cases} . \tag{7.33}$$

The wave functions for $z \leq 0$ and $z \geq L$ can then be related by the transfer matrix calculated for the device structure:

$$\begin{pmatrix} 1 + r \\ \frac{ik_{z=0}}{m^*_{z=0}}(1 - r) \end{pmatrix} = \mathbf{T}(0, z_1) \cdot \ldots \cdot \mathbf{T}(z_{n-1}, L) \begin{pmatrix} te^{ik_{z=L}L} \\ \frac{ik_{z=L}}{m^*_{z=L}} te^{ik_{z=L}L} \end{pmatrix}$$

$$= \mathbf{T}(0, L) \begin{pmatrix} te^{ik_{z=L}L} \\ \frac{ik_{z=L}}{m^*_{z=L}} te^{ik_{z=L}L} \end{pmatrix} . \tag{7.34}$$

The amplitude of the transmitted wave t is then given by

$$t = \frac{2}{\mathbf{T}_{11} + \frac{m_{z=0}k_{z=L}}{m_{z=L}k_{z=0}}\mathbf{T}_{22} + i\left(\frac{k_{z=L}}{m_{z=L}}\mathbf{T}_{12} - \frac{m_{z=0}}{k_{z=0}}\mathbf{T}_{21}\right)} . \tag{7.35}$$

The transmission coefficient T is simply the ratio of the transmitted to the incident current. From Eq. (7.29) we therefore obtain

$$T = \frac{m_{z=0}k_{z=L}}{m_{z=L}k_{z=0}}|t|^2 \tag{7.36}$$

$$= \frac{m_{z=0}k_{z=L}}{m_{z=L}k_{z=0}} \times \frac{4}{\left(\mathbf{T}_{11} + \frac{m_{z=0}k_{z=L}}{m_{z=L}k_{z=0}}\mathbf{T}_{22}\right)^2 + \left(\frac{k_{z=L}}{m_{z=L}}\mathbf{T}_{12} - \frac{m_{z=0}}{k_{z=0}}\mathbf{T}_{21}\right)^2}. \tag{7.37}$$

7.3.2 Two-Band Models

For certain device structures a simple one-band model is insufficient for describing even the relatively basic principles upon which the operation of the device is based. This is the case, for example, for interband tunnel structures in the InAs/GaSb/AlSb material system. In these structures, transport occurs between conduction-band states in InAs and valence-band states in GaSb; it is therefore necessary to include both a conduction band and a valence band in one's model if one hopes to obtain even a rudimentary description of these devices. Various two-band models have been employed[8, 9] to simulate transport in interband tunnel structures. These models include the lowest conduction band and the light-hole valence band, with the heavy-hole valence band being neglected on the basis of the small coupling between the conduction and heavy-hole bands near the Brillouin zone center. For computational purposes the tight-binding model employed by Ting et al.[9] has proven to be more efficient, since the transfer matrices contain only rational functions rather than the trigonometric functions present in the transfer matrices for the two-band $\vec{k} \cdot \vec{p}$ model employed by Söderström et al.[8]. For pedagogical purposes, however, the $\vec{k} \cdot \vec{p}$ model is conceptually simpler, and therefore it will be presented here.

A two-band $\vec{k} \cdot \vec{p}$ model based on the theory of Bastard[20, 21] has been

used to develop a transfer-matrix approach for simulating the electrical behavior of interband devices. In general, the Schrödinger equation for an electron in a periodic potential may be written

$$H\psi_n(\vec{k},\vec{r}) = \left[\frac{P^2}{2m_e} + V(\vec{r})\right]\psi_n(\vec{k},\vec{r}) = E_n\psi_n(\vec{k},\vec{r}), \tag{7.38}$$

where $\vec{P}$ is the momentum operator, $V(\vec{r})$ is the periodic potential, $\psi_n(\vec{k},\vec{r})$ is the electron wave function for the band n, E_n is the energy eigenvalue for the band n, and m_e is the free electron mass. The electron wave function $\psi_n(\vec{k},\vec{r})$ may be written in terms of the Bloch function u_n as $\psi_n(\vec{k},\vec{r}) = e^{i\vec{k}\cdot\vec{r}}u_n(\vec{k},\vec{r})$, which, when substituted into Eq. (7.38), yields

$$\left[\frac{P^2}{2m_e} + \frac{\hbar\vec{k}\cdot\vec{P}}{m_e} + \frac{\hbar^2k^2}{2m_e} + V\right]u_n(\vec{k},\vec{r}) = E_nu_n(\vec{k},\vec{r}). \tag{7.39}$$

For a semiconductor in which we consider n bands, the n Bloch functions at $\vec{k} = 0$ can be chosen to form a complete, orthonormal set; thus, every Bloch function $u_i(\vec{k},\vec{r})$ may be written as a linear combination of the n Bloch functions at $\vec{k} = 0$,

$$u_{i'}(\vec{k},\vec{r}) = \sum_i c_{i'i}u_i(\vec{k} = 0,\vec{r}), \tag{7.40}$$

and the Bloch functions at $\vec{k} = 0$ may be chosen to satisfy the orthonormality condition

$$\int u_i^*(\vec{k} = 0,\vec{r})u_{i'}(\vec{k} = 0,\vec{r})d^3r = \delta_{ii'}, \tag{7.41}$$

where the integral is taken over a unit cell in the crystal. Substituting the expansion (7.40) into Eq. (7.39), multiplying by $u_j^*(\vec{k} = 0,\vec{r})$, and integrating over the unit cell, we obtain

$$\left(E_i(\vec{k} = 0) + \frac{\hbar^2k^2}{2m_e} - E_{i'}\right)\delta_{ij}c_{i'i} + \frac{\hbar}{m_e}\vec{k}\cdot\vec{P}_{ji}c_{i'i} = 0. \tag{7.42}$$

Noting that the index i' in Eq. (7.42) is unnecessary and letting $c_{i'} \to \psi$, and exchanging indices $i \leftrightarrow j$, we obtain

$$\left(E_i(\vec{k}=0) + \frac{\hbar^2 k^2}{2m_e} - E\right)\delta_{ij}\psi_j + \frac{\hbar}{m_e}\vec{k}\cdot\vec{P}_{ij}\psi_j = 0. \tag{7.43}$$

Solving Eq. (7.43) for the eigenvalues E and corresponding eigenvector components ψ_j yields the energy band structure in the semiconductor.

In the two-band model of Bastard[20, 21], only the lowest conduction band and the light-hole valence band, labeled c and v, respectively, are included. In addition, the electron kinetic energy term $\hbar^2 k^2/2m_e$ is neglected, which is valid near $k = 0$ and is consistent with the neglect of other bands in the semiconductor[21]. We may choose coordinate axes such that $\vec{k}\cdot\vec{P} = kP$, and because the momentum operator $\vec{P}$ has odd parity, the matrix elements P_{ij} satisfy

$$P_{ij} = \int u_i^*(k=0,z)Pu_j(k=0,z)dz = (1-\delta_{ij})p. \tag{7.44}$$

Using Eq. (7.44), we obtain the following form for the eigenvalue equation for the Bastard model, Eq. (7.43):

$$\begin{pmatrix} E_c - E & \frac{\hbar p}{m_e}k \\ \frac{\hbar p}{m_e}k & E_v - E \end{pmatrix} \begin{pmatrix} \psi_c \\ \psi_v \end{pmatrix} = 0, \tag{7.45}$$

where E_c and E_v are the energies of the conduction and valence bands, respectively, at $k = 0$. The eigenvalues E of Eq. (7.45) are then given by the solutions to

$$(E_c - E)(E_v - E) - \left(\frac{\hbar p}{m_e}\right)^2 k^2 = 0, \tag{7.46}$$

or

$$E = \frac{1}{2}\left[(E_c + E_v) \pm (E_c - E_v)\sqrt{1 + 4\left(\frac{\hbar p}{m_e(E_c - E_v)}\right)^2 k^2}\right] \tag{7.47}$$

$$\approx \begin{cases} E_c + \frac{\hbar^2}{2m_e}(2\frac{p^2}{m_e(E_c - E_v)})k^2, \\ E_v - \frac{\hbar^2}{2m_e}(2\frac{p^2}{m_e(E_c - E_v)})k^2. \end{cases} \tag{7.48}$$

From Eq. (7.48) it is apparent that the conduction and valence band effective masses m_c^* and m_v^* are equal; this is approximately true in most direct-gap semiconductors, and we therefore determine p^2 from the known values for m_c^* and m_v^* using the relation

$$p^2 = \frac{m_e(E_c - E_v)}{4}\left(\frac{m_e}{m_c^*} + \left|\frac{m_e}{m_v^*}\right|\right). \tag{7.49}$$

The eigenvectors corresponding to the eigenvalues $E(k)$ then satisfy

$$\psi_v = \frac{m_e(E - E_c)}{\hbar pk}\psi_c \tag{7.50}$$

$$= -\frac{\hbar pk}{m_e(E_v - E)}\psi_c. \tag{7.51}$$

In the Bastard model, it is also assumed that the matrix element p is equal in all materials. In the work presented here, p is not taken to be constant, but instead varies slightly from material to material. We have, however, assumed the Bloch functions $u_i(k = 0, z)$ to be the same in all materials.

The probability current J in the Bastard model is obtained in the standard way from the continuity equation

$$\frac{d}{dt}\int_{-\infty}^{\infty} |\psi|^2 dz - \int_{-\infty}^{\infty} \frac{dJ}{dz} dz = 0, \tag{7.52}$$

and is given by

$$J = \frac{p}{m_e}\left[\psi_c\psi_v^* + \psi_v\psi_c^*\right]. \tag{7.53}$$

From Eq. (7.53) it can be seen that requiring continuity of the probability current is not sufficient to yield boundary conditions at an interface for both the wave function and its derivative. To obtain the appropriate boundary conditions, consider the the first row of Eq. (7.45), and substitute Eq. (7.51) for ψ_v to obtain

$$(E_c - E)\psi_c - \left(\frac{\hbar}{m_e}\right)^2 pk\left(\frac{p}{E_v - E}\right)k\psi_c = 0. \tag{7.54}$$

Expressing k as an operator, $k = -i(d/dz)$, yields

$$(E_c - E)\psi_c + \left(\frac{\hbar}{m_e}\right)^2 p \frac{d}{dz}\left(\frac{p}{E_v - E}\frac{d\psi_c}{dz}\right) = 0, \tag{7.55}$$

from which we see that the appropriate boundary conditions to apply at an interface are that ψ_c and $(p/(E_v - E))(d\psi_c/dz)$ should be continuous. A similar procedure yields the boundary conditions for the valence band components — ψ_v and $(p/(E_c - E))(d\psi_v/dz)$ should be continuous across an interface.

The relationships (7.50) and (7.51) between the conduction- and valence-band components contributing to the wave function at a given energy allow one to consider only one of the components in computing transfer matrices and transmission coefficients. The results for the other component will follow from Eq. (7.50) or (7.51). We therefore consider only the conduction-band component ψ_c in deriving expressions for the transfer matrices and transmission coefficients in this model. This simplification allows one to apply the formulae derived for the one-band model directly to the determination of transfer matrices for the two-band $\vec{k}\cdot\vec{p}$ model, with only small modifications required to account for the different boundary conditions in the two-band model. The resulting expressions for transfer matrices are, for $E > E_c$ or $E < E_v$,

$$\begin{pmatrix} \psi_c \\ \dfrac{p}{E_v - E}\dfrac{d\psi_c}{dz} \end{pmatrix}_{z=z_1} \tag{7.56}$$

$$= \begin{pmatrix} \cos k(z_1 - z_0) & \dfrac{1}{k}\left(\dfrac{E_v - E}{p}\right)\sin k(z_1 - z_0) \\ -k\left(\dfrac{p}{E_v - E}\right)\sin k(z_1 - z_0) & \cos k(z_1 - z_0) \end{pmatrix}\begin{pmatrix} \psi_c \\ \dfrac{p}{E_v - E}\dfrac{d\psi_c}{dz} \end{pmatrix}_{z=z_0}$$

$$\equiv \mathbf{T}(z_1, z_0)\begin{pmatrix} \psi_c \\ \dfrac{p}{E_v - E}\dfrac{d\psi_c}{dz} \end{pmatrix}_{z=z_0}, \tag{7.57}$$

and, for $E_v < E < E_c$,

$$\begin{pmatrix} \psi_c \\ \dfrac{p}{E_v - E}\dfrac{d\psi_c}{dz} \end{pmatrix}_{z=z_1} \tag{7.58}$$

$$= \begin{pmatrix} \cosh \kappa(z_1 - z_0) & \dfrac{1}{\kappa}\left(\dfrac{E_v - E}{p}\right) \sinh \kappa(z_1 - z_0) \\ \kappa\left(\dfrac{p}{E_v - E}\right) \sinh \kappa(z_1 - z_0) & \cosh \kappa(z_1 - z_0) \end{pmatrix} \begin{pmatrix} \psi_c \\ \dfrac{p}{E_v - E}\dfrac{d\psi_c}{dz} \end{pmatrix}_{z=z_0}$$

$$\equiv \mathbf{T}(z_1, z_0) \begin{pmatrix} \psi_c \\ \dfrac{p}{E_v - E}\dfrac{d\psi_c}{dz} \end{pmatrix}_{z=z_0} , \tag{7.59}$$

where $k = (m/\hbar p)\sqrt{(E - E_c)(E - E_v)}$ and $\kappa = (m/\hbar p)\sqrt{-(E - E_c)(E - E_v)}$.

To obtain an expression for the transmission coefficient in the two-band model, one again considers transmitted and reflected wave functions scattered by the device structure from an incident plane wave of unit amplitude. ψ_c can then be written

$$\psi_c(z) = \begin{cases} e^{ikz} + re^{-ikz} & z \leq 0 \\ te^{ikz} & z \geq L \end{cases} . \tag{7.60}$$

The transfer matrix across the device structure is then used to relate the wave functions for $z \leq 0$ and $z \geq L$:

$$\begin{pmatrix} 1 + r \\ ik_{z=0}\left(\dfrac{p_{z=0}}{E_{v,z=0} - E}\right)(1 - r) \end{pmatrix} = \mathbf{T}(0, L) \begin{pmatrix} te^{ik_{z=L}L} \\ ik_{z=L}\left(\dfrac{p_{z=L}}{E_{v,z=L} - E}\right) te^{ik_{z=L}L} \end{pmatrix} . \tag{7.61}$$

The amplitude of the transmitted wave is then given by

$$t = \frac{2}{\mathbf{T}_{11} + \dfrac{p_{z=L}k_{z=L}(E_{v,z=0} - E)}{p_{z=0}k_{z=0}(E_{z=L} - E)}\mathbf{T}_{22} + i\left(\dfrac{p_{z=L}k_{z=L}}{E_{v,z=L} - E}\mathbf{T}_{12} - \dfrac{E_{v,z=0} - E}{p_{z=0}k_{z=0}}\mathbf{T}_{21}\right)} . \tag{7.62}$$

From Eqs. (7.53) and (7.50) we then obtain for the transmission coefficient

$$T = \left(\frac{k_{z=0}}{k_{z=L}}\right)\left(\frac{E - E_{c,z=L}}{E - E_{c,z=0}}\right)|t|^2 \tag{7.63}$$

$$= \left(\frac{k_{z=0}}{k_{z=L}}\right)\left(\frac{E-E_{c,z=L}}{E-E_{c,z=0}}\right) \times$$
$$\frac{4}{\left(\mathbf{T}_{11}+\frac{p_{z=L}k_{z=L}(E_{v,z=0}-E)}{p_{z=0}k_{z=0}(E_{v,z=L}-E)}\mathbf{T}_{22}\right)^2+\left(\frac{p_{z=L}k_{z=L}}{E_{v,z=L}-E}\mathbf{T}_{12}-\frac{E_{v,z=0}-E}{p_{z=0}k_{z=0}}\mathbf{T}_{21}\right)^2}. \tag{7.64}$$

7.3.3 Beyond Two-Band Models

It is also possible to perform more elaborate calculations of transport in semiconductor heterostructures that include the effects of interactions with the heavy-hole and split-off bands. For transport in the z direction, only the conduction band and light-hole band states are coupled for $\vec{k}_{\|} \equiv (k_x, k_y) = 0$; for $\vec{k}_{\|} \neq 0$, however, there are band-mixing effects that can affect the detailed structure of transmission coefficients in interband tunnel structures.

Ting, Yu, and McGill[22] have performed calculations of transport in interband tunnel structures using the eight-band effective-bond-orbital model of Chang[23, 24], which includes the light-hole, heavy-hole, and split-off valence bands and the lowest conduction band. The effective-bond-orbital model is essentially an adaptation of Kane's eight-band $\vec{k}\cdot\vec{p}$ model[25] using a tight-binding formalism, and provides a realistic description of the band structure relevant for transport in interband tunnel devices. The method of Ting et al. also circumvents numerical difficulties that arise in transfer-matrix calculations for multiband models of semiconductor electronic structure. Because of the many complex bands that are present in multiband models, exponentially growing states tend to produce instabilities in transfer-matrix calculations for devices larger than a few tens of Angstroms[26]. Ting et al. have adapted a method used by Lent and Kirkner[27] to solve the two-dimensional Schrödinger equation for quantum wave guides and formulated the problem of calculating transmission coefficients as a

banded linear system of equations that can be solved without encountering the numerical problems present in the transfer-matrix method.

Fig. 7.3 shows (a) a schematic energy-band diagram for a prototypical interband transport structure, InAs/GaSb/InAs, and (b) transmission coefficients calculated for this structure at various values of $\vec{k}_{\parallel}$. As can be seen from Fig. 7.3(a), transport in the InAs/GaSb/InAs device involves both conduction-band states in the InAs electrodes and valence-band states in the GaSb quantum-well layer. The transmission coefficients calculated using both the eight-band model and a simpler two-band model, shown in Fig. 7.3(b), show that although the presence of the heavy-hole states in the full eight-band model introduces considerable structure in the transmission coefficients for $\vec{k}_{\parallel} \neq 0$, the largest resonances, which will dominate the resonant current in the device, are well described by the simple two-band model. For the InAs/GaSb/InAs structure, it therefore suffices to include only the conduction and light-hole bands in modeling current transport. In other devices, however, it has been found[22] that the presence of the heavy-hole states induces more significant changes in calculated transmission coefficients, and that the full eight-band model is needed to describe transport properties accurately.

7.4 Calculation of Current-Voltage Characteristics

Once the transmission coefficient has been calculated as a function of incident energy for a device structure, an integral can be computed over the incident electron distribution to yield the current density in the device. The general prescription for calculating the current density from the transmission coefficient

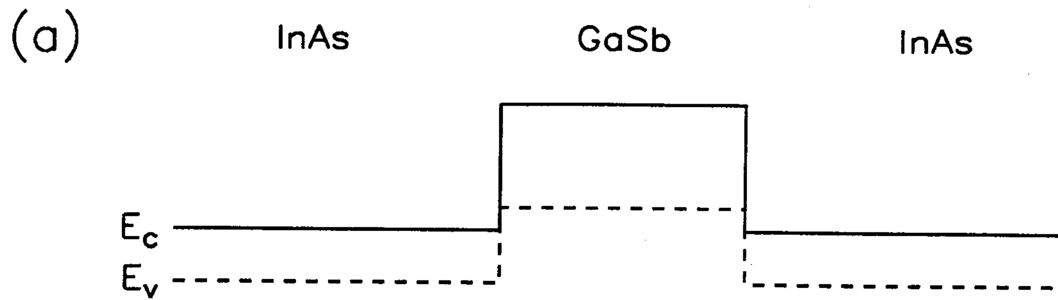

(b)

$k_x=0$

8-Band

2-Band

$k_x=0.01$

$k_x=0.02$

Transmission Coefficient $[k_{\|}=(k_x,0,0)]$

1
0.8
0.6
0.4
0.2
0

0 0.02 0.04 0.06 0.08 0.1 0.12 0.14

Energy (eV)

Figure 7.3: (a) A schematic energy-band diagram for the InAs/GaSb/InAs interband transport structure, and (b) transmission coefficients calculated for this structure using both the eight-band effective-bond-orbital model (solid line) and a simple two-band model (dotted line), for various values of $\vec{k}_{||}$ (in units of $2\pi/a$, where a is the cubic lattice constant of InAs and GaSb). As seen in (a), transport in this device involves conduction-band states in InAs and valence-band states in GaSb. The eight-band model describes the full interactions among the conduction, light-hole, heavy-hole, and split-off bands, while the two-band model includes only the conduction and light-hole bands. Figure (b) shows that, while the presence of the heavy-hole band produces extra structure in the transmission coefficient for $\vec{k}_{||} \neq 0$, the largest resonances, which will dominate the resonant current through the device, are described quite accurately by the two-band model. The two-band model therefore provides a relatively accurate description of transport in the InAs/GaSb/InAs device. In other structures, however, it has been found that the full eight-band model is necessary to describe interband transport processes.

has been adapted from the approach of Tsu and Esaki[2]. Briefly stated, the method consists of integrating over the Fermi distribution of the incident electron population, including appropriate Fermi factors for occupied states in the emitter and empty states in the collector, and including appropriate velocity factors for the incident electrons. The total energy E and the wave vector component parallel to the device profile $\vec{k}_{\|}$ are taken to be conserved.

For a device structure to which a voltage V has been applied, the current density can be written

$$J = \frac{e}{4\pi^3}\left(\int T(E_{\perp,z=0},\vec{k}_{\|})f(E)[1-f(E+eV)]\frac{1}{\hbar}\left(\frac{\partial E}{\partial k_\perp}\right)_{z=0} dk_{\perp,z=0}d^2k_{\|} - \int T(E_{\perp,z=L},\vec{k}_{\|})f(E+eV)[1-f(E)]\frac{1}{\hbar}\left(\frac{\partial E}{\partial k_\perp}\right)_{z=L} dk_{\perp,z=L}d^2k_{\|}\right), \quad (7.65)$$

where $k_\perp$ is the component of the wave vector normal to the device profile, $E_\perp$ is the energy corresponding to $k_\perp$, $f(E)$ and $f(E+eV)$ are the Fermi distributions for the emitter and collector electrodes, respectively, and $(1/\hbar)(\partial E/\partial k_\perp)$ is the group velocity in the direction normal to the device profile. $T(E_{\perp,z=0},\vec{k}_{\|})$ is the transmission coefficient for a carrier incident at $z=0$ to be transmitted to $z=L$, and $T(E_{\perp,z=L},\vec{k}_{\|})$ is the transmission coefficient for a carrier incident at $z=L$ to be transmitted to $z=0$. By an argument based essentially upon time-reversal symmetry[28], it can be demonstrated that, for given values of E and $\vec{k}_{\|}$, $T(E_{\perp,z=0},\vec{k}_{\|}) = T(E_{\perp,z=L},\vec{k}_{\|}) \equiv T(E_\perp,\vec{k}_{\|})$. For the remainder of this chapter, therefore, $E_\perp$ will refer to $E_{\perp,z=0}$. Eq. (7.65) can then be simplified to

$$\begin{aligned} J &= \frac{e}{4\pi^3\hbar}\left(\int T(E_\perp,\vec{k}_{\|})f(E)[1-f(E+eV)]dE_\perp d^2k_{\|} - \int T(E_\perp,\vec{k}_{\|})f(E+eV)[1-f(E)]dE_\perp d^2k_{\|}\right) \quad (7.66) \\ &= \frac{e}{4\pi^3\hbar}\int T(E_\perp,\vec{k}_{\|})[f(E)-f(E+eV)]dE_\perp d^2k_{\|}. \quad (7.67) \end{aligned}$$

In principle, the transmission coefficient $T(E_\perp, \vec{k}_\|)$ always has some dependence on $\vec{k}_\|$. For the one-band model described in Section 7.3.1, however, this dependence arises only if the effective mass m^* varies across the device structure, and even when the effective mass does vary, the dependence of $T(E_\perp, \vec{k}_\|)$ on $\vec{k}_\|$ is small[29]. Thus, for the one-band model we have $T(E_\perp, \vec{k}_\|) \approx T(E_\perp)$, and the current density (7.67) can be written

$$J = \frac{e}{4\pi^3\hbar}\left(\int T(E_\perp)[f(E) - f(E+eV)]dE_\perp 2\pi k_\| dk_\| \right. \tag{7.68}$$

$$= \frac{ek_BT}{2\pi^2\hbar^3}\int_{E_c}^{\infty} T(E_\perp)\Big[m^*_{z=0}\ln\left(1+e^{-(E_\perp-\mu)/k_BT}\right) - m^*_{z=L}\ln\left(1+e^{-(E_\perp+eV-\mu)/k_BT}\right)\Big]dE_\perp, \tag{7.69}$$

where m^* is the conduction-band effective mass for the one-band model, and E_c is the position of the conduction-band edge at $z = 0$. This simplification in the one-band model leads to a significant decrease in the amount of computation required to obtain a current-voltage characteristic, since it is necessary to calculate only the one-dimensional integral in Eq. (7.69), rather than a multidimensional integral as given in Eq. (7.67).

For the more elaborate band-structure models described in Section 7.3, the expression for the current given by Eq. (7.69) does not apply, and one must calculate the multidimensional integral of Eq. (7.67). In the two-band models discussed in Section 7.3.2, the band structure is assumed to be isotropic in $\vec{k}_\|$, and Eq. (7.67) can be simplified to a two-dimensional integral,

$$J = \frac{e}{2\pi^2\hbar}\int T(E_\perp, k_\|)[f(E) - f(E+eV)]dE_\perp k_\| dk_\|. \tag{7.70}$$

For the eight-band model discussed in Section 7.3.3, the band structure is anisotropic and the current density must be calculated using the full three-dimensional integral in Eq. (7.67).

7.5 III-V/II-VI Resonant Tunneling Structures

To illustrate the calculation of current-voltage characteristics in semiconductor heterostructures using the techniques discussed in this chapter, we present in this section calculations, using the two-band model described in Section 7.3.2, of current-voltage characteristics for double-barrier resonant-tunneling structures realized in two lattice-matched III-V/II-VI material systems, GaAs/ZnSe and InAs/ZnTe[29]. Such structures could be of interest for a variety of reasons. ZnSe is a potentially important II-VI material because its lattice parameter is very close to that of GaAs ($\sim$0.27% lattice mismatch), and because its wide band gap (2.67 eV) would make possible emission of blue light. Recently developed low-temperature growth techniques such as migration-enhanced epitaxy[30, 31] allow the growth of GaAs and possibly other III-V materials at substrate temperatures compatible with II-VI material growth, making feasible the experimental realization of these structures. GaAs/ZnSe and InAs/ZnTe tunnel structures might in fact provide a novel way to study mixed III-V/II-VI material systems and growth techniques, since structures of fairly high quality are required for fabrication of functional double-barrier resonant-tunneling structures.

For actual device applications, one advantage that a GaAs/ZnSe structure might have over a GaAs/$Al_xGa_{1-x}As$ device is speed. One of the parameters that will ultimately limit the speed of a double-barrier resonant-tunneling device is the RC time constant for charging the capacitor formed by the barriers. This parameter can be estimated as $\tau \sim \hbar/\Delta E$, where ΔE is the width of the transmission resonance for a given quasi-bound state in the double barrier; typically, τ in a double-barrier structure is on the order of 1 ps. Since the capacitance is

proportional to the dielectric constant in the barrier, and since ZnSe has a lower dielectric constant than $Al_xGa_{1-x}As$ (9.1 compared to ~ 12), the capacitance, and therefore the *RC* time constant, should be reduced by replacing $Al_xGa_{1-x}As$ by ZnSe.

InAs/ZnTe tunnel structures should exhibit an even greater advantage in speed. The dielectric constant for ZnTe is 10.4, which again is smaller than that in $Al_xGa_{1-x}As$. More importantly, InAs has a much higher mobility than GaAs (33 000 $cm^2/V{\cdot}s$ compared to 8500 $cm^2/V{\cdot}s$ at 300 K). The resistivity in InAs will therefore be much lower than in GaAs, leading to a substantial reduction in the *RC* time constant. The low resistivity in InAs will also permit a greater fraction of the voltage drop across the structure to occur in the active region of the device, so that a smaller bias voltage will be required to reach the resonance peak.

The material parameter that is most critical, however, in determining the electrical properties of a double-barrier tunnel structure is the conduction-band offset. The valence-band offset for the GaAs/ZnSe (110) heterojunction has been measured by x-ray photoelectron spectroscopy[32] and found to be, depending on growth conditions, between 0.96 and 1.10 eV at 300 K. The corresponding conduction-band offset is between 0.15 and 0.29 eV, which is comparable to the conduction-band offset in the GaAs/$Al_xGa_{1-x}As$ material system (~ 0.25 eV for $x = 0.33$). In the InAs/ZnTe material system, the conduction-band offset is probably very large, which is another advantage of this system over GaAs/-$Al_xGa_{1-x}As$. The value of the InAs/ZnTe band offset has not been measured directly, but we can obtain some idea of its value if we assume transitivity of band offsets. We will do this in spite of the evidence presented in Chapter 5 that band offsets in III-V/II-VI material systems often violate the transitivity rule[33]; the deviations from transitivity measured in our experiments were $\sim$0.2 eV, which is

sufficiently small that the arguments presented here will not be strongly affected.

For GaAs/ZnSe, we use the valence-band offset measured by Kowalczyk et al.[32], $\Delta E_v = 1.10$ eV. For the InAs/GaAs heterojunction, a valence-band offset of 0.17 eV has been measured[34]. However, the InAs/GaAs heterojunction system has a large lattice mismatch ($\sim 7\%$), and the strain configuration in the heterojunctions grown for the band offset measurements was unknown; the uncertainty in the measured InAs/GaAs valence-band offset may therefore be quite large. For the ZnSe/ZnTe material system, which also has a large lattice mismatch ($\sim 7\%$), a value of 0.98 eV has been obtained[35]. Using these values, we deduce a valence-band offset for InAs/ZnTe of ~ 0.30 eV, corresponding to $\Delta E_c \approx 1.6$ eV. The large conduction-band offset will reduce thermionic currents through higher resonances and over the barrier, facilitating device operation at room temperature.

Fig. 7.4(a) shows an energy-band diagram for an InAs/ZnTe/InAs/ZnTe/InAs double-barrier tunnel structure, and Fig. 7.4(b) shows calculated current-voltage characteristics for an InAs/ZnTe double barrier with 20 Å ZnTe barriers and a 50 Å InAs quantum well. The InAs electrodes were assumed to be doped n-type with a carrier concentration $n = 1 \times 10^{18}$ cm^{-3}. As seen in the figure, the current-voltage characteristics are very similar at 300 K and 77 K. This similarity is a consequence of the extreme height ($\Delta E_c = 1.6$ eV) of the ZnTe barriers and of the relatively large (compared to $k_B T$) energy width of the Fermi sea in the emitter. Although the valley current, at approximately 0.6 V applied bias, is unrealistically low in these calculations because of the neglect of scattering processes, the negligible difference between the valley currents calculated at 300 K and at 77 K indicates that thermionic currents in actual devices should be effectively suppressed by the ZnTe barriers. The calculated current-voltage characteristics also show a slight decrease in the peak current density at 300 K compared to

that at 77 K. This result is a consequence of the broader Fermi distribution in the emitter at higher temperatures. The resonance in the InAs quantum well acts as an energy filter for incoming electrons — only electrons with $E_\perp$ in a narrow energy window centered about the resonance energy E_0 will be able to tunnel through the double-barrier structure. For a given total carrier concentration, the broader Fermi distribution at higher temperatures reduces, for $E < E_f$, the number of carriers with $E_\perp = E_0$, and therefore reduces the resonant current in the device. As can be seen from Eq. (7.69), however, the peak resonant current occurs near $E_\perp = 0$ in the emitter; the size of this effect will therefore decrease as the energy width of the Fermi sea increases. Finally, the calculated current-voltage characteristic at 300 K exhibits a more rapid initial increase in current than the characteristic at 77 K. This is also due to the broader Fermi distribution at higher temperatures. For applied bias well below the peak, the resonance is at energies $E_\perp > E_f$; the number of carriers with energy greater than the Fermi energy E_f increases with temperature, resulting in larger currents at low bias for higher temperatures.

Fig. 7.5(a) shows an energy-band diagram for a GaAs/ZnSe/GaAs/ZnSe/-GaAs double-barrier tunnel structure, and Fig. 7.5(b) shows calculated current-voltage characteristics for a GaAs/ZnSe double barrier with 30 Å ZnSe barriers and a 50 Å InAs quantum well. The GaAs electrodes were assumed to be doped n-type with a carrier concentration $n = 1 \times 10^{18}$ cm^{-3}. Because the height of the ZnSe barriers is relatively small ($\Delta E_c = 0.29$ eV, compared to $\Delta E_c = 1.6$ eV for the InAs/ZnTe structure), the current-voltage characteristics at 77 K and 300 K are quite different. As with the InAs/ZnTe double-barrier structure, the broader Fermi distribution at higher temperature causes the peak current density to be somewhat lower at 300 K than at 77 K; this effect is slightly more pronounced for the GaAs/ZnSe structure because of the smaller energy width of the Fermi sea in

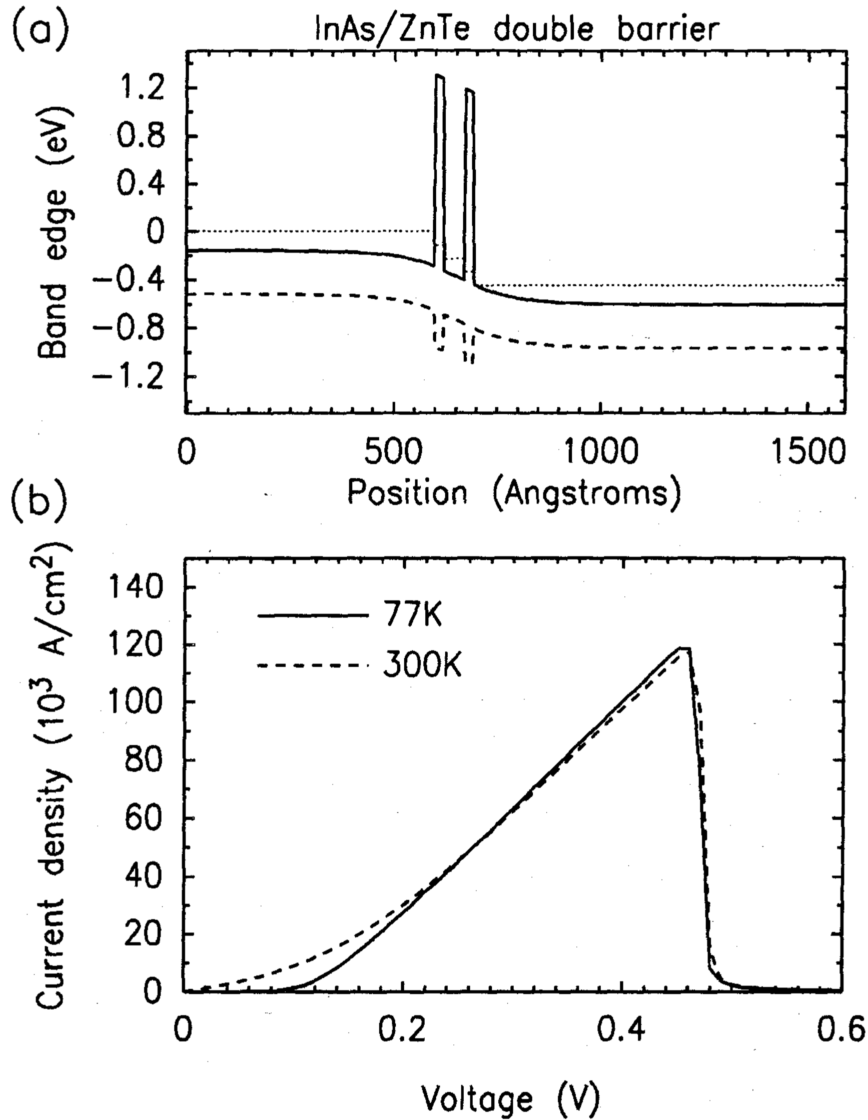

Figure 7.4: (a) Energy-band diagram for the InAs/ZnTe/InAs/ZnTe/InAs double-barrier tunnel structure, calculated for $V = 0.45$ V. The conduction-band edge is represented by a solid line, the valence-band edge by the heavy dashed line, and the quasi-Fermi level in each layer by the dotted line. (b) Current-voltage (J–V) characteristics calculated for this device structure at 77 K and 300 K.

the GaAs emitter compared to that in the InAs emitter. The faster initial increase in current density at 300 K compared to 77 K arises from the same mechanism as in the InAs/ZnTe double-barrier structure. In addition, the current-voltage characteristic at 300 K exhibits a much lower peak-to-valley current ratio and a much more rapidly rising current density at high bias than at 77 K; these features are both a result of the low barrier height presented by the ZnSe layers. At 300 K, the Fermi distribution in the emitter yields a substantial number of electrons with energies near or above the top of the ZnSe barriers; these electrons are transmitted across the device structure with very little attenuation, leading to a relatively large thermionic current independent of the position in energy of the tunneling resonance produced by the double barrier. As the voltage bias is increased, the height of the ZnSe barriers with respect to the Fermi level in the emitter is reduced, leading to the observed increase in current density for high bias.

7.6 Conclusions

In this chapter we have presented a discussion of some of the theoretical techniques we have employed to simulate the electrical behavior of a wide variety of semiconductor heterostructure devices. The starting point for these simulations is a calculation of the conduction- and valence-band-edge profiles in a device, incorporating electrostatic band bending due to material sequence, doping profiles, and voltage applied to the structure. Band bending is calculated by solving Poisson's equation in one dimension for the device, using the Thomas-Fermi approximation to relate the local carrier concentration to the band-edge positions at each point, and enforcing an overall charge-neutrality condition across the device structure. Our experiences indicate that the use of relaxation algorithms to

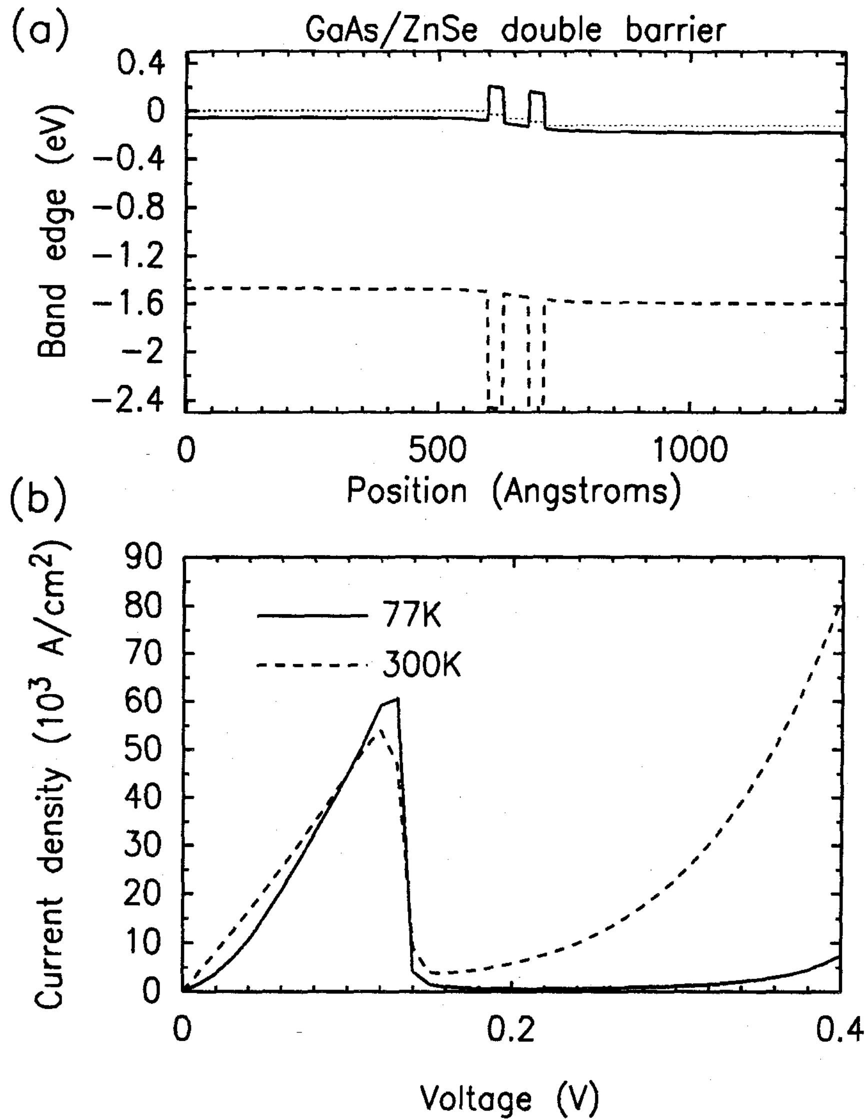

Figure 7.5: (a) Energy-band diagram for the GaAs/ZnSe/GaAs/ZnSe/GaAs double-barrier tunnel structure, calculated for $V = 0.12$ V. The conduction-band edge is represented by a solid line, the valence-band edge by the heavy dashed line, and the quasi-Fermi level in each layer by the dotted line. Because of the large energy separation between the conduction- and valence-band edges throughout this device structure, the role of the valence band is negligible. (b) Current-voltage characteristics calculated for this device structure at 77 K and 300 K.

solve Poisson's equation is highly preferable to numerical integration from a single point in the device structure, because of various numerical instabilities that can arise in using the latter method.

Once the energy-band profiles have been calculated for a device structure, transport properties are studied by calculating transmission coefficients that give the probability for carriers with given energy E and parallel wave vector $\vec{k}_{\|}$ to be transmitted across the device structure. We have employed a variety of band-structure models to calculate transmission coefficients. For devices in which transport involves only conduction-band states throughout the structure, a simple one-band model, described in Section 7.3.1, is sufficient. For structures in which conduction-band and valence-band states interact, more complicated band-structure models are required; in Section 7.3.2 we presented a two-band model that accounts for the most important interactions between conduction-band and valence-band states, and in Section 7.3.3 we described briefly a model developed by Ting, Yu, and McGill[10] to describe the full range of interactions between the conduction-band and valence-band states. Because increasing complexity in the band-structure model used to calculate transmission coefficients exacts an extremely high price in computational efficiency, it is generally desirable to employ the simplest possible model that adequately describes the phenomena one wishes to investigate.

In many cases, calculation of transmission coefficients is sufficient to yield a useful description of device behavior. Often, however, one wishes to calculate actual current-voltage characteristics for a device. Current-voltage characteristics can be obtained by integrating calculated transmission coefficients over the incident carrier distribution, as we have described in Section 7.4. Our calculations of current-voltage characteristics yield a semiquantitative description of the electrical behavior of heterostructure devices. Peak current densities and often

peak voltages for tunnel structures can be calculated semiquantitatively; however, nonresonant currents, such as valley currents in double-barrier structures, are not calculated accurately because of our neglect of scattering processes.

Finally, we have illustrated the use of the techniques described in this chapter by calculating current-voltage characteristics for double-barrier tunnel structures realized in two III-V/II-VI material systems, InAs/ZnTe and GaAs/ZnSe. Such devices could be of interest because of the possibility of operation at higher speeds than might be obtainable in conventional GaAs/$Al_xGa_{1-x}As$ double-barrier structures, and could also provide a useful way to study epitaxial growth of III-V/II-VI material systems. Our studies indicate that double-barrier structures in the InAs/ZnTe and GaAs/ZnSe material systems should be viable device concepts, and also demonstrate some of the possible advantages and disadvantages of each device.

References

[1] L. Esaki, *Phys. Rev.* **109**, 603 (1958).

[2] R. Tsu and L. Esaki, *Appl. Phys. Lett.* **22**, 562 (1973).

[3] L. L. Chang, L. Esaki, and R. Tsu, *Appl. Phys. Lett.* **24**, 593 (1974).

[4] T. C. L. G. Sollner, W. D. Goodhue, P. E. Tannenwald, C. D. Parker, and D. D. Peck, *Appl. Phys. Lett.* **43**, 588 (1983).

[5] B. Ricco and M. Ya. Azbel, *Phys. Rev. B* **29**, 1970 (1984).

[6] W. R. Frensley, *J. Vac. Sci. Technol. B* **3**, 1261 (1985).

[7] S. Luryi, *Appl. Phys. Lett.* **47**, 490 (1985).

[8] J. R. Söderström, E. T. Yu, M. K. Jackson, Y. Rajakarunanayake, and T. C. McGill, *J. Appl. Phys.* **68**, 1372 (1990).

[9] D. Z.-Y. Ting, E. T. Yu, D. A. Collins, D. H. Chow, and T. C. McGill, *J. Vac. Sci. Technol. B* **8**, 810 (1990).

[10] D. Z.-Y. Ting, E. T. Yu, and T. C. McGill, to be published in *Appl. Phys. Lett.* (1990).

[11] M. Sweeny and J. Xu, *Appl. Phys. Lett.* **54**, 546 (1989).

[12] J. R. Söderström, D. H. Chow, and T. C. McGill, *Appl. Phys. Lett.* **55**, 1094 (1989).

[13] L. F. Luo, R. Beresford, and W. I. Wang, *Appl. Phys. Lett.* **55**, 2023 (1989).

[14] D. A. Collins, D. H. Chow, E. T. Yu, D. Z.-Y. Ting, J. R. Söderström, Y. Rajakarunanayake, and T. C. McGill, presented at the 1990 NATO Workshop on Resonant Tunneling, El Escorial, Spain (1990).

[15] E. T. Yu, D. A. Collins, D. Z.-Y. Ting, D. H. Chow, and T. C. McGill, *Appl. Phys. Lett.* **57** 2675 (1990).

[16] E. O. Kane, in *Tunneling Phenomena in Solids*, E. Burstein and S. Lundqvist, eds. (Plenum Press, New York, 1969), p. 1.

[17] N. W. Ashcroft and N. D. Mermin, *Solid State Physics* (Saunders College, Philadelphia, PA, 1976), pp. 45-46.

[18] A. R. Bonnefoi, *Electronic Properties and Device Applications of $GaAs/Al_xGa_{1-x}As$ Quantum Barrier and Quantum Well Heterostructures*, Ph.D. thesis, California Institute of Technology, Pasadena, CA (1987).

[19] W. H. Press, B. P. Flannery, S. A. Teukolsky, and W. T. Vetterling, *Numerical Recipes: The Art of Scientific Computing* (Cambridge University Press, Cambridge, 1986), pp. 578-614.

[20] G. Bastard, *Phys. Rev. B* **24**, 5693 (1981).

[21] G. Bastard, *Phys. Rev. B* **25**, 7584 (1982).

[22] D. Z.-Y. Ting, E. T. Yu, and T. C. McGill, *Appl. Phys. Lett.* **58**, 292 (1991).

[23] Y. C. Chang, *Phys. Rev. B* **37**, 8215 (1988).

[24] G. T. Einevoll and Y. C. Chang, *Phys. Rev. B* **40**, 9683 (1990).

[25] E. O. Kane, *Semiconductors and Semimetals*, Vol. 1, R. K. Willardson and A. C. Beer, eds. (Academic Press, New York, 1966), p. 75.

[26] C. Mailhiot and D. L. Smith, *Phys. Rev. B* **33**, 8360 (1986).

[27] C. S. Lent and D. J. Kirkner, *J. Appl. Phys.* **67**, 6353 (1990).

[28] A. Messiah, *Quantum Mechanics*, Vol. II, (John Wiley & Sons, New York, 1958), pp. 807-9, 829-31, 867-8.

[29] E. T. Yu and T. C. McGill, *Appl. Phys. Lett.* **53**, 60 (1988).

[30] Y. Horikoshi, M. Kawashima, and H. Yamaguchi, *Jpn. J. Appl. Phys.* **25**, L868 (1986).

[31] S. Ramesh, N. Kobayashi, and Y. Horikoshi, *Appl. Phys. Lett.* **57**, 1102 (1990).

[32] S. P. Kowalczyk, E. A. Kraut, J. R. Waldrop, and R. W. Grant, *J. Vac. Sci. Technol.* **21**, 481 (1982).

[33] E. T. Yu, M. C. Phillips, D. H. Chow, D. A. Collins, and T. C. McGill, *Bull. Am. Phys. Soc.* **35**, 416 (1990).

[34] S. P. Kowalczyk, W. J. Schaffer, E. A. Kraut, and R. W. Grant, *J. Vac. Sci. Technol.* **20**, 705 (1982).

[35] Y. Rajakarunanayake, R. H. Miles, G. Y. Wu, and T. C. McGill, *Phys. Rev. B* **37**, 10212 (1988).

Chapter 8

Carrier Transport in Two-Terminal Interband Tunnel Structures

8.1 Introduction

8.1.1 Background and Motivation

Until quite recently, investigations of resonant tunneling had been confined primarily to studies of the standard double-barrier resonant-tunneling structure discussed by Tsu and Esaki[1] and first demonstrated by Chang, Esaki, and Tsu[2], with efforts focused primarily on the GaAs/$Al_xGa_{1-x}As$ and InGaAs/-InAlAs material systems. Advances in epitaxial growth techniques for the InAs/-GaSb/AlSb material system, however, have led to considerable interest in tunneling devices involving coupling between the conduction and valence bands of different materials across heterointerfaces. The first devices of this type to be proposed[3] and demonstrated[4, 5, 6, 7] were single-barrier structures in

which negative differential resistance (NDR) arose from the enhanced tunneling probability for electrons tunneling near the valence band edge of the barrier. More recently, resonant interband tunneling structures have been proposed[8] and demonstrated[9, 10]; in these devices, NDR arises from conduction-band electrons in an InAs emitter tunneling through AlSb barriers into quasi-bound valence-band states in a GaSb quantum well. NDR in interband tunneling devices is also enhanced because of blocking of current through the device structure by the GaSb band gap for voltages beyond resonance. Devices with peak-to-valley current ratios as high as 20:1 at 300 K, and as high as 88:1 at 77 K, have been realized[9], and NDR has been demonstrated in other device structures with peak current densities of over 1×10^5 A/cm^2 and corresponding peak-to-valley current ratios of 1.2–1.8 at 300 K[11, 12].

The novel transport properties of interband tunneling devices arise from the unusual energy band alignments found in the InAs/GaSb/AlSb material system. Fig. 8.1 shows the relative positions of the conduction- and valence-band edges for InAs, GaSb, and AlSb. Valence-band offsets for the InAs/GaSb[13] and GaSb/AlSb[14] heterojunctions have been measured by x-ray photoelectron spectroscopy; we have assumed that the value of the InAs/AlSb valence-band offset is given by the transitivity rule. As shown in the figure, the conduction-band edge of InAs lies below the valence-band edge of GaSb, allowing conduction-band states in InAs to interact with valence-band states in GaSb in heterostructures containing both materials. The InAs/AlSb and GaSb/AlSb band offset values are such that AlSb acts as a barrier for transport of carriers between InAs conduction-band states and GaSb valence-band states.

In addition to the unusual electronic properties that arise in heterostructures realized in the InAs/GaSb/AlSb material system, InAs and GaSb possess a number of electrical properties that make them particularly attractive materials for

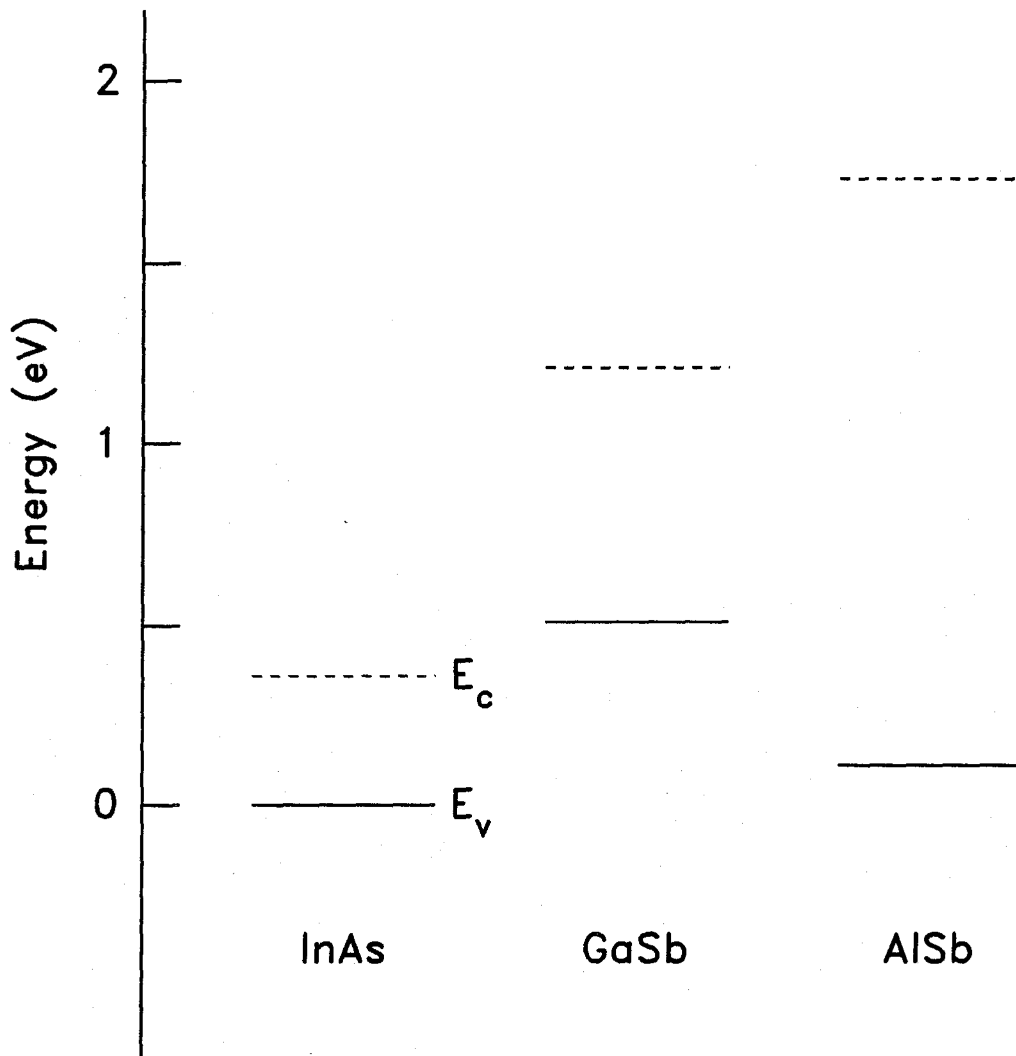

Figure 8.1: Relative positions of the conduction-band edges (dashed lines) and valence-band edges (solid lines) for InAs, GaSb, and AlSb, as determined from the InAs/GaSb and GaSb/AlSb valence-band offsets measured by x-ray photoelectron spectroscopy[13, 14] and assuming transitivity of band offsets. The conduction-band edge shown for AlSb is the indirect minimum, in the Δ direction in the Brillouin zone.

quantum-effect devices, such as tunnel structures. InAs is easily doped n-type, has very high electron mobility ($\sim$ 33 000 $cm^2/V{\cdot}s$ at 300 K), and naturally forms n-type ohmic contacts. GaSb can be doped p-type[15] and has a small p-type Schottky barrier, facilitating the formation of p-type ohmic contacts. These properties reduce parasitic series resistance for metal contacts to n-type InAs and p-type GaSb, and make possible contact to relatively thin layers of InAs or GaSb, because of the lack of surface depletion. An additional advantage of InAs is its small effective mass compared to that of GaAs ($m^*_{\mathrm{InAs}} = 0.023m_e$ compared to $m^*_{\mathrm{GaAs}} = 0.067m_e$), which enhances quantum effects so that subband spacings in quantum-confined structures such as quantum wells, wires, and dots will be larger for given feature sizes in InAs than in GaAs; thus, technological limitations such as lithographic resolution should be less restrictive for InAs than for GaAs.

8.1.2 Summary of Results

In this chapter we discuss some results obtained in theoretical and experimental studies of interband transport in the InAs/GaSb/AlSb material system. A wide variety of interband transport devices exhibiting negative differential resistance have been grown, fabricated, and characterized in the McGill group laboratories. A brief overview of this work is presented in this chapter. In addition, we describe a more detailed theoretical and experimental study of current-voltage characteristics in the InAs/GaSb/InAs device structure that demonstrated the resonant nature of transport through the GaSb quantum well, despite the absence of classically forbidden barrier regions. By studying theoretically calculated and experimentally observed peak current densities in these devices as a function of GaSb layer width, we have demonstrated that transmission resonances are formed that are due solely to the imperfect matching of wave functions at the InAs/GaSb

interfaces. Our results also suggest that coupling between InAs conduction-band and GaSb heavy-hole states has little influence on the current-voltage characteristics of these devices.

8.1.3 Outline of Chapter

Section 8.2 presents an overview of recent developments in two-terminal interband transport devices. Several device structures that have been demonstrated in the McGill group, and their respective advantages, disadvantages, and novel properties of interest are briefly discussed. In Section 8.3 we focus on the InAs/-GaSb/InAs device structure, which is, in some sense, the most elementary of the devices exhibiting resonant interband transport. We present a theoretical and experimental study of the dependence of the resonant current density on the GaSb layer width in the InAs/GaSb/InAs device that demonstrated the existence of resonances in the GaSb quantum-well layers, despite the absence of classically forbidden barrier layers surrounding the GaSb layer; the resonances are formed solely by the imperfect coupling of the InAs conduction band and GaSb valence band wave functions at the InAs/GaSb interfaces. Conclusions are presented in Section 8.4.

8.2 Overview of Two-Terminal Interband Transport Structures

The variety of band alignments available in the InAs/GaSb/AlSb material system allows the realization of a large number of device structures exhibiting NDR. Table 8.1 summarizes some of the interband transport device structures that have been grown, fabricated, and characterized in the McGill group

laboratories[9, 11, 12, 16, 17, 18], and lists the key performance characteristics of these devices. As shown in the table, an extremely wide variety of device structures can be devised that exhibit NDR, with either very high peak-to-valley current ratios and relatively low peak current densities, very high peak current densities and relatively low peak-to-valley current ratios, or intermediate values for both parameters.

The key feature that allows the realization of such a wide range of device structures exhibiting NDR is the Type II broken-gap band alignment for the InAs/GaSb heterojunction. Because the conduction-band edge of InAs is lower in energy than the valence-band edge of GaSb, transport processes in heterostructures containing InAs and GaSb involve interactions between conduction-band states in InAs and valence-band states in GaSb. The combination of these interactions, the superior electrical properties of InAs and GaSb, and the blocking effect of the InAs or GaSb energy band gaps for transport in structures biased beyond resonance leads to markedly superior performance in many interband transport devices compared to that of more conventional structures.

The first device of this type to be demonstrated was the n-InAs/AlSb/GaSb/-AlSb/n-InAs resonant interband tunnel (RIT) structure[9]; a schematic energy-band diagram for this device is shown in Fig. 8.2(a). Söderström et al.[9] reported peak-to-valley current ratios as high as 20:1 and 88:1 at 300 K and 77 K, respectively, for RIT devices. The operation of the device is based on transport of electrons in the InAs electrodes through quasi-bound valence-band states in the GaSb quantum well. At low bias, resonant tunneling of electrons occurs via the quasi-bound valence-band state in the GaSb quantum well. For voltages beyond resonance, the electrons must tunnel not only through the AlSb barriers, but also through the forbidden energy gap of the GaSb quantum well. This leads to very strong suppression of the valley current beyond resonance, resulting in extremely

Material Sequence	Temperature (K)	Peak-to-Valley Current Ratio	Peak Current Density (A/cm^2)
n-InAs/AlSb/InAs/AlSb/n-InAs	300	4.0	3.7×10^5
	300	13.0	4.0×10^3
n-InAs/AlSb/GaSb/AlSb/n-InAs	300	12	950
	77	60	1.7×10^3
	300	21	50
	77	88	90
p-GaSb/AlSb/InAs/AlSb/p-GaSb	300	8.0–10.0	450–500
	77	16	450–500
n-InAs/GaSb/n-InAs	300	2.2	5.1×10^3
	300	1.2	1.2×10^5
n-InAs/GaSb/InAs/GaSb/n-InAs	300	2.2	1.2×10^4
n-InAs/GaSb/AlSb/GaSb/n-InAs	300	3.5	1.4×10^4
n-InAs/p-GaSb	300	1.7	4.2×10^4
n-InAs/GaSb/AlSb/p-GaSb	300	1.5–1.8	1.6×10^5
n-InAs/AlSb/InAs/p-GaSb	300	1.5–1.7	3.1×10^3
n-InAs/AlSb/GaSb/n-InAs	300	15.0–18.0$^{(a)}$	$2.7 \times 10^{3(a)}$
		1.6–2.2$^{(b)}$	$1.5 \times 10^{4(b)}$

$^{(a)}$**Reverse bias, i.e., negative voltage applied to electrode next to AlSb barrier.**

$^{(b)}$Forward bias, i.e., positive voltage applied to electrode next to AlSb barrier.

Table 8.1: A summary of some of the interband transport device structures grown, fabricated, and characterized in the McGill group laboratories[9, 11, 12, 16, 17, 18], and a list of their key performance characteristics.

high peak-to-valley current ratios.

The RIT device concept can also be extended to a structure in which there are no classically forbidden barrier regions, i.e., the n-InAs/GaSb/n-InAs device; Fig. 8.2(b) shows a schematic energy-band diagram for this structure. Because of the absence of the AlSb barrier regions in this device, the peak current densities are much larger than in the original RIT structure — (few)$\times 10^2$ A/cm^2 for a typical RIT compared to (few)$\times 10^4$ A/cm^2 or more for an InAs/GaSb/InAs device. Transmission resonances in the InAs/GaSb/InAs devices are also very broad, with widths corresponding to quasi-bound-state lifetimes of a few tens of femtoseconds[19], compared to typical quasi-bound-state lifetimes of picoseconds or longer for typical double-barrier structures. The short resonant-state lifetimes in these structures suggest that limitations on device speed arising from quantum-well charging effects should be much less stringent than for conventional double-barrier structures. However, the absence of the AlSb barriers also induces a severe deterioration in the valley current, with typical InAs/GaSb/InAs structures exhibiting peak-to-valley ratios of 1.2–2.2 at 300 K.

Current-voltage characteristics for the InAs/GaSb/InAs structure also exhibit a number of interesting features. Because the InAs conduction-band states and GaSb valence-band states interact directly at the InAs/GaSb interfaces, the nature of this interaction is more apparent in these devices than in structures with AlSb barriers separating the InAs and GaSb layers. Section 8.3 describes a study of the resonant current density as a function of GaSb layer width in the InAs/-GaSb/InAs device structure that demonstrates the existence of resonances in the GaSb quantum well that are due solely to confinement induced by the imperfect matching of InAs conduction-band and GaSb valence-band wave functions at the InAs/GaSb interfaces. This confinement is quite different from the quantum confinement induced by classically forbidden barrier regions in conventional

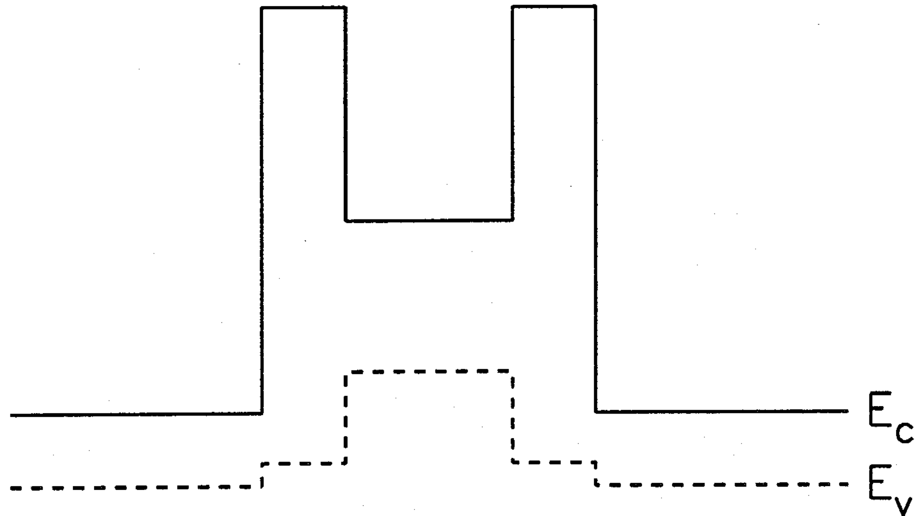

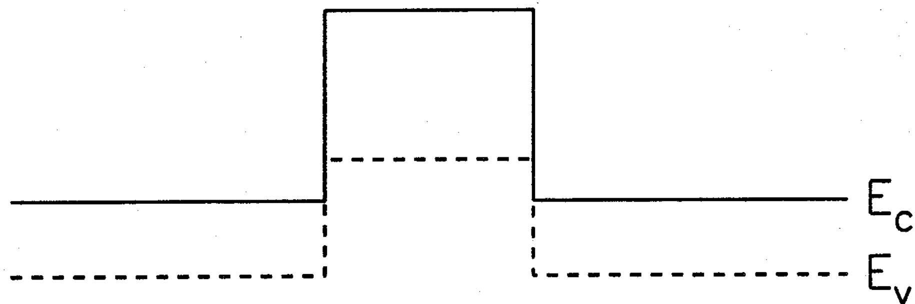

Figure 8.2: Schematic energy-band diagrams for (a) the InAs/AlSb/GaSb/AlSb/-InAs (RIT) and (b) the InAs/GaSb/InAs device structures. In each diagram, the conduction-band edge is represented by a solid line and the valence-band edge by a dashed line.

double-barrier structures.

Large peak current densities have also been observed from a class of interband transport devices based on carrier transport from InAs conduction-band states into GaSb valence-band states. Schematic energy-band diagrams for three devices of this type are shown in Fig. 8.3. Fig. 8.3(a) shows an n-InAs/p-GaSb device, Fig. 8.3(b) an n-InAs/GaSb/AlSb/p-GaSb device, and Fig. 8.3(c) an n-InAs/-AlSb/InAs/p-GaSb device. In each of these three devices, the peak current occurs for low positive bias (positive voltage applied to the GaSb layer), with electrons traveling from InAs conduction-band states into unoccupied GaSb valence-band states. For higher applied bias, transport of electrons from the InAs electrode is blocked by the GaSb band gap, resulting in NDR. Current densities in these devices are relatively high — $\sim 4 \times 10^4$ A/cm^2 for the InAs/GaSb structure and up to 1.6×10^5 A/cm^2 for the InAs/GaSb/AlSb/GaSb structure, with peak-to-valley current ratios in both cases of 1.5–1.8 at room temperature.

An interesting feature observed in the latter device structure is that the insertion of the AlSb barrier in the GaSb electrode layer yields an increase in the peak current density, rather than reducing the current, as one might expect. This somewhat counterintuitive result occurs because the insertion of the AlSb barrier induces the formation of a resonant quasi-bound state that is due to confinement of carriers in the middle GaSb layer by the AlSb barrier and the InAs/GaSb interface. This resonance enhances the probability for transport between the InAs conduction-band states and the GaSb valence-band states, resulting in an increased peak current density. A similar argument should hold for the effect of the AlSb barrier in the InAs/AlSb/InAs/GaSb structure. However, it is also expected that the peak current density in these devices should depend quite sensitively on the separation between the AlSb barrier layer and the InAs/GaSb interface. In order for the peak current density to be enhanced by the resonance,

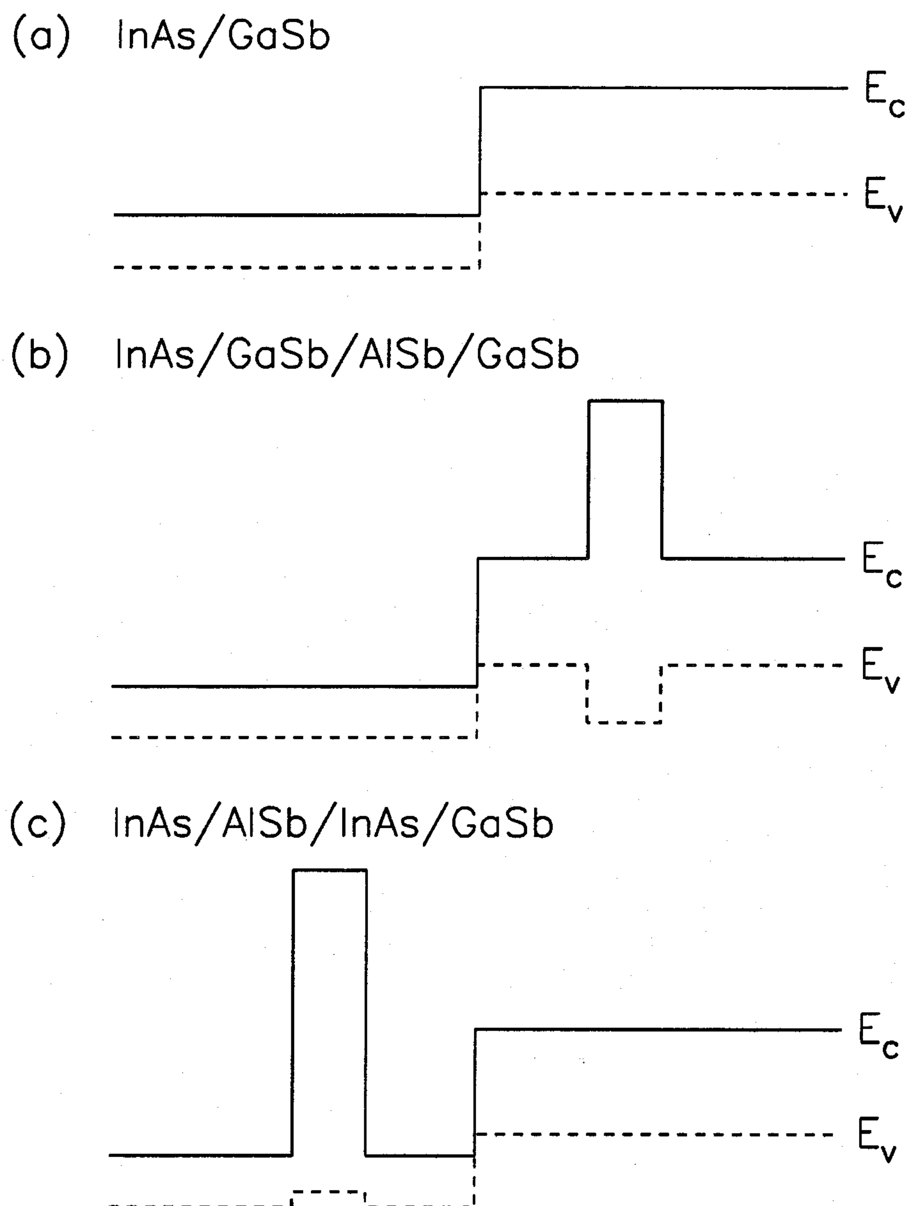

Figure 8.3: Schematic energy-band diagrams for (a) an n-InAs/p-GaSb structure, (b) an n-InAs/GaSb/AlSb/p-GaSb structure, and (c) an n-InAs/AlSb/InAs/-p-GaSb structure. The conduction-band edges are represented by solid lines, and the valence-band edges by dashed lines.

it is necessary for the occupied states in the InAs electrode, the quasi-bound state in the middle InAs or GaSb layer, and the unoccupied states in the GaSb electrode to be aligned in energy; this will occur only for fairly specific values of the confinement energy of the quasi-bound state resonance, which is determined primarily by the separation between the AlSb barrier and the InAs/GaSb interface. Theoretical calculations of peak current density as a function of the width of the middle GaSb layer in the device structure shown in Fig. 8.3(b) and of the middle InAs layer in the device structure shown in Fig. 8.3(c) indicate that this should be a very pronounced effect[11]. The resonances formed in structures of the type shown in Fig. 8.3(b) and (c) are also very broad, with a resonance width corresponding to a lifetime of $\sim$25 fs for an InAs/GaSb/AlSb/InAs structure with a 51 Å GaSb quantum well and a 12 Å AlSb barrier. This extremely short intrinsic lifetime and the high peak current densities observed in these devices make structures of this type very promising as possible components in high-frequency oscillators.

A number of other device structures in the InAs/GaSb/AlSb material system have been demonstrated to exhibit NDR in their current-voltage characteristics. A more detailed description of this work and of some other possible device applications in the InAs/GaSb/AlSb material system has been given by Collins et al.[18].

8.3 Interband Transport in InAs/GaSb/InAs Structures

As discussed very briefly in Section 8.2, the InAs conduction-band states interact directly with the GaSb valence-band states at the InAs/GaSb interfaces

in the InAs/GaSb/InAs device structure, and the nature of this interaction has direct consequences for the current-voltage characteristics of these devices. The current transport mechanism in the InAs/GaSb/InAs structure has been claimed by some investigators[20] to be simply ohmic conduction from one InAs electrode to the other through the GaSb valence-band states. However, studies we have performed of the peak current density in InAs/GaSb/InAs devices as a function of GaSb layer width provide convincing evidence refuting this explanation and demonstrating that despite the absence of classically forbidden barrier regions in these structures, transmission resonances still exist because of the imperfect coupling between the InAs conduction-band states and the GaSb valence-band states. Our results also suggest that the coupling between conduction-band and heavy-hole states produces a relatively small contribution to the peak resonant current density in these structures.

8.3.1 Device Structures

The samples for this study were grown in a Perkin-Elmer 430 molecular-beam epitaxy system using GaAs (100) substrates. Functional devices were routinely obtained despite the large lattice mismatch between GaAs and the lattice-matched InAs/GaSb/AlSb material system; our technique for obtaining high-quality InAs, GaSb, and AlSb grown on GaAs substrates has been described elsewhere[21]. The device structures consisted of InAs electrode layers, doped n-type with Si to an estimated carrier concentration of $n \approx 2 \times 10^{17}$ cm^{-3}, surrounding a nominally undoped GaSb quantum-well layer ranging from 60 to 300 Å in thickness. The GaSb wells were separated from the InAs electrode layers by nominally undoped InAs spacer layers ranging in thickness from 50 to 75 Å. A schematic energy-band diagram for the InAs/GaSb/InAs device structure is

shown in Fig. 8.2(b). Circular device mesas 6 μm in diameter were fabricated using standard photolithography and a wet etch. Ohmic contacts to the InAs were formed by evaporation of Au/Ge, and devices were probed at 300 K and 77 K using a thin gold wire.

Fig. 8.4 shows current-voltage characteristics measured at 77 K and 300 K for an InAs/GaSb/InAs device with a GaSb layer width of 74 Å. We obtained a peak current density at 300 K of $\sim 1 \times 10^5$ A/cm^2, significantly higher than previously reported results for this device structure[20]; peak-to-valley current ratios for these devices were approximately 1.5:1.

8.3.2 Calculation of Transmission Coefficients

A theoretical analysis of these devices reveals a number of interesting features. Because interband tunneling devices involve both conduction and valence band states, any theoretical model for these structures must include both the conduction and the valence bands, and must also correctly account for the interactions between these bands. We have implemented a simple two-band, tight-binding model[22], incorporating the conduction and light-hole bands, that satisfies these requirements. As discussed in Section 7.3.2, the heavy-hole valence band has been neglected, based on the small coupling between the conduction and heavy-hole bands. This model, in conjunction with realistic band-bending calculations as described in Section 7.2, allows us to simulate semiquantitatively the current-voltage behavior of a wide variety of interband tunneling devices.

The two-band, tight-binding model employed here is very similar to the two-band $\vec{k} \cdot \vec{p}$ model described in Section 7.3.2, but has proven to be more efficient computationally, since the transfer matrices contain only rational functions, rather than the trigonometric functions present in the transfer matrices for the

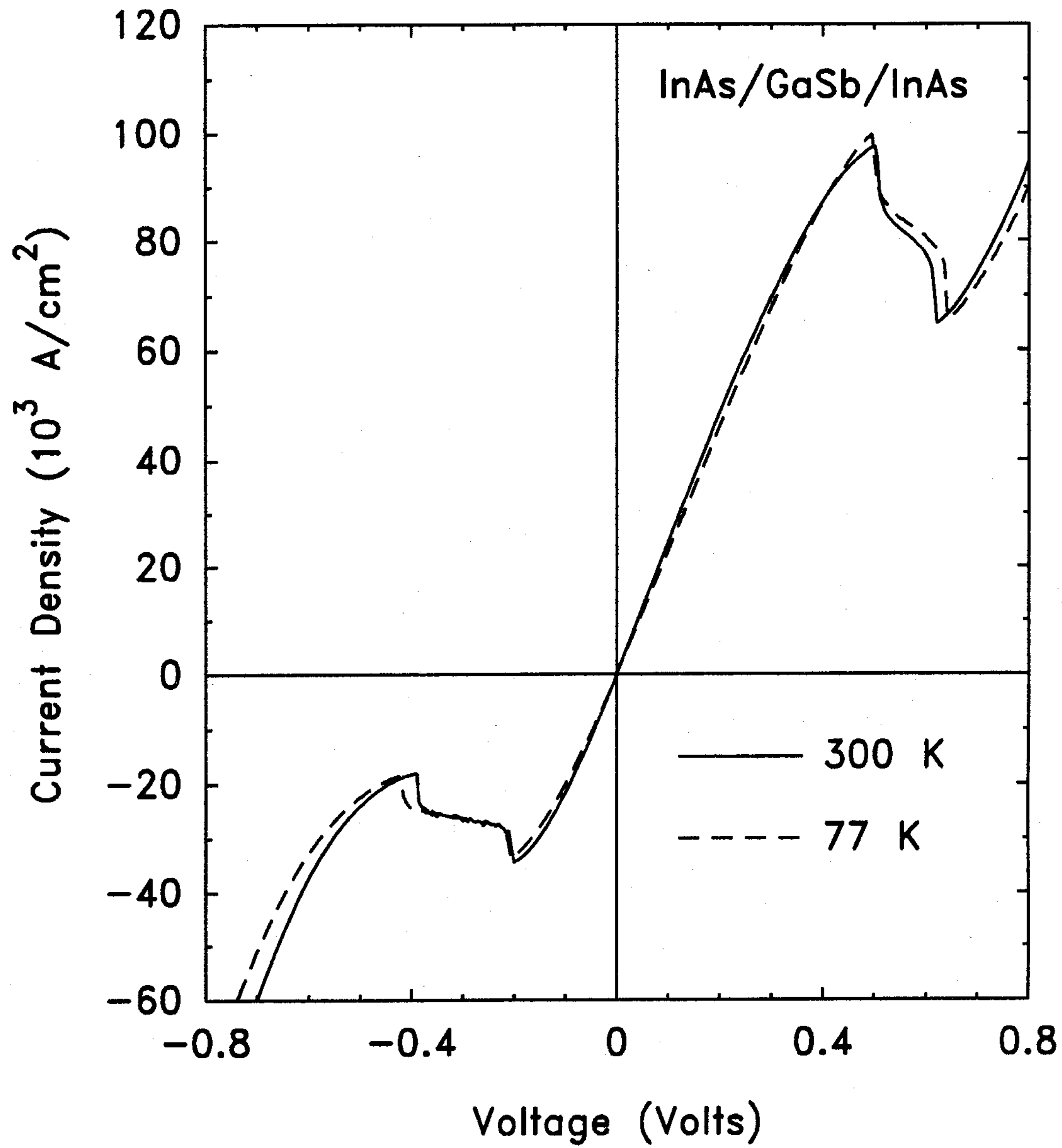

Figure 8.4: Current-voltage characteristics at 300 K (solid line) and 77 K (dashed line) for an InAs/GaSb/InAs interband tunneling device with a GaSb layer width of 74 Å.

two-band $\vec{k} \cdot \vec{p}$ model. The two-band, tight-binding model is constructed from a linear chain of alternating s and p orbitals, with on-site energies E_s and E_p, respectively. The on-site energies E_s and E_p in the tight-binding model are analogous to the band-edge energies E_c and E_v, respectively, in the two-band $\vec{k} \cdot \vec{p}$ model. The nearest-neighbor interaction t between adjacent s and p orbitals is determined from the effective mass m^* according to[22]

$$t^2 = \frac{\hbar^2}{2m^* d^2}(E_s - E_p), \tag{8.1}$$

where d is the spacing between unit cells. The band structure in the tight-binding model is then given by the secular equation

$$(E - E_s)(E - E_p) - 4t^2 \sin^2\left(\frac{kd}{2}\right) = 0. \tag{8.2}$$

The interaction term t is analogous to the matrix element p in the $\vec{k} \cdot \vec{p}$ model, as can be seen by comparing Eq. (8.1) with Eq. (7.49) and Eq. (8.2) with Eq. (7.46).

The physics of the tight-binding model is therefore reassuringly similar to that of the $\vec{k} \cdot \vec{p}$ model. However, in the tight-binding framework wave-function amplitudes at adjacent lattice sites are related very naturally by the hopping term t, so that transfer matrices in the tight-binding formalism contain only rational functions of the energy and the material parameters. In the $\vec{k} \cdot \vec{p}$ framework, the wave functions are plane waves with wavelengths that are not simply related to any lattice spacing; computation of the transfer-matrix elements is therefore more complicated than in the tight-binding framework, resulting in a loss of computational efficiency. We have therefore used the tight-binding model to calculate transmission coefficients in the InAs/GaSb/InAs device and in other interband tunnel structures. Once the transmission coefficients have been calculated, current-voltage characteristics are obtained using the methods described in Section 7.4.

Simulations of the InAs/GaSb/InAs structure for varying GaSb layer widths and subsequent experimental measurements for these devices have provided strong evidence that the mechanism for current transport through the GaSb layer is indeed resonant. Fig. 8.5 shows transmission coefficients in the energy range between the InAs conduction band edge ($E = 0$ eV) and the GaSb valence band edge ($E = 0.15$ eV) calculated for devices with three different GaSb layer widths. The main feature of interest is that despite the absence of any classically forbidden barrier regions in the energy range of interest, transmission resonances are formed that are due solely to the imperfect matching of InAs conduction-band and GaSb valence-band wave functions at the InAs/GaSb interfaces. For the 45 Å GaSb well (Fig. 8.5(a)), the quantum confinement energy places the quasi-bound state below the InAs conduction band edge; in this case, resonant transport cannot occur. For the 90 Å GaSb well (Fig. 8.5(b)), a single, broad resonance is present in the transmission coefficient, and for the 300 Å GaSb well (Fig. 8.5(c)), a large number of resonances occur in the energy range between the InAs conduction band edge and the GaSb valence band edge. This variation in the transmission coefficient leads to a strong dependence of the peak current density on the GaSb layer width. The absence of a resonance should lead to a very small resonant current for a device with a thin GaSb layer; devices with intermediate GaSb layer widths should exhibit much higher resonant current densities, because of the presence of the single broad resonance. For wide GaSb layers, however, the peak current density should decrease; the resonances, although more numerous, are significantly narrower than for GaSb layers of intermediate width and therefore allow less of the incoming electron distribution to be transmitted across the GaSb layer.

A somewhat curious feature of the calculated transmission coefficients is that the width of the transmission resonance is not related in a straightforward way

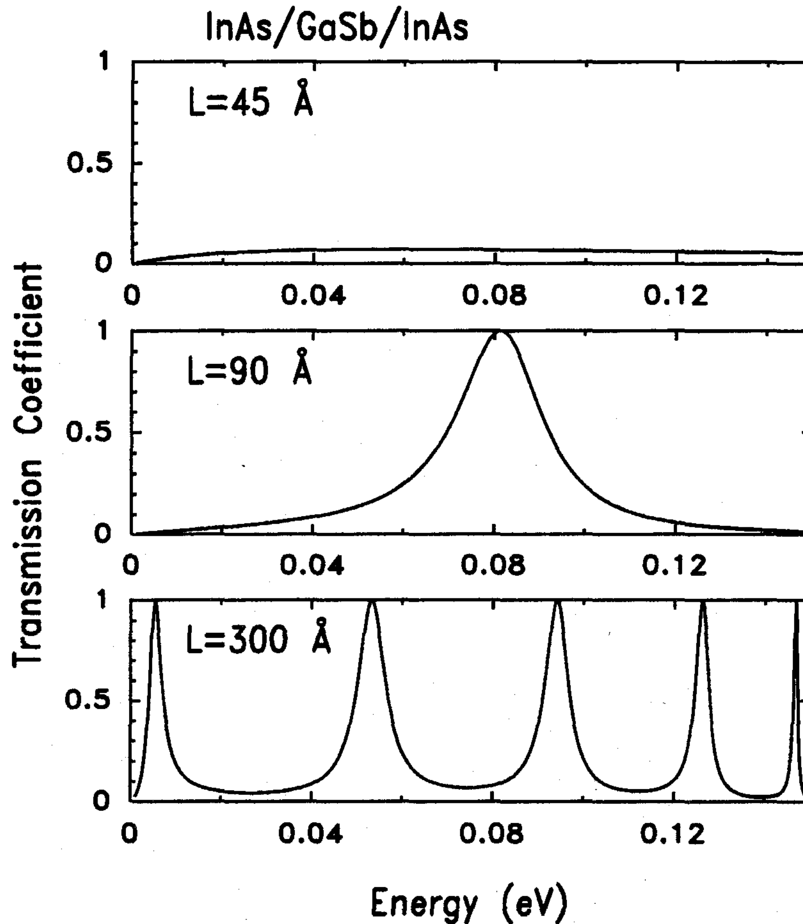

Figure 8.5: Theoretical transmission coefficients for InAs/GaSb/InAs interband transmission devices for GaSb layer widths of (a) 45 Å, (b) 90 Å, and (c) 300 Å. On the energy scale shown, the InAs conduction-band edge is at 0 eV, and the GaSb valence-band edge is at 0.15 eV. These calculations demonstrate that quasi-bound states should be formed in the GaSb quantum-well layer, despite the absence of classically forbidden barrier regions, simply from the imperfect matching of InAs conduction-band and GaSb valence-band wave functions at the InAs/GaSb interfaces.

to the strength of the coupling of InAs and GaSb wave functions at the resonance energy. In a typical double-barrier tunnel structure, the width of the transmission resonance, and therefore the quasi-bound-state lifetime, is determined primarily by the attenuation of the wave function in the barrier layers; this dependence yields, for example, an exponential dependence of resonance width on barrier thickness in a double-barrier structure[23]. One might, therefore, expect resonance widths in the InAs/GaSb/InAs structure to be determined primarily by the strength of the coupling between the InAs and GaSb wave functions at the resonance energy. In the InAs/GaSb/InAs structure, however, resonances at similar energies can have very different energy widths, as seen in Figs. 8.5(b) and (c).

That this should indeed be the case may be seen by deriving an analytical expression for the transmission coefficient for an InAs/GaSb/InAs structure with no applied bias. The transfer matrix for the entire device is given simply by the transfer matrix for propagation across the GaSb layer:

$$\mathbf{T}(0,L) = \begin{pmatrix} \cos k'L & \left(\frac{E - E_v^{\mathrm{GaSb}}}{pk'}\right) \sin k'L \\ -\left(\frac{pk'}{E - E_v^{\mathrm{GaSb}}}\right) \sin k'L & \cos k'L \end{pmatrix}, \tag{8.3}$$

where we have used the expression given in Eq. (7.57) for the transfer matrix in the two-band $\vec{k} \cdot \vec{p}$ model; E is the energy, $k' = (m/\hbar p_{\mathrm{GaSb}})\sqrt{(E - E_c^{\mathrm{GaSb}})(E - E_v^{\mathrm{GaSb}})}$ is the wave vector in the GaSb layer, and L is the width of the GaSb layer. Using Eq. (7.64), we obtain the transmission coefficient for the InAs/GaSb/InAs structure,

$$T = \frac{4}{(2\cos k'L)^2 + \left(\frac{p_{\mathrm{InAs}} k(E - E_v^{\mathrm{GaSb}})}{p_{\mathrm{GaSb}} k'(E_v^{\mathrm{InAs}} - E)} \sin k'L + \frac{p_{\mathrm{GaSb}} k'(E_v^{\mathrm{InAs}} - E)}{p_{\mathrm{InAs}} k(E - E_v^{\mathrm{GaSb}})} \sin k'L\right)^2}, \tag{8.4}$$

where $k = (m/\hbar p_{\mathrm{InAs}})\sqrt{(E - E_c^{\mathrm{InAs}})(E - E_v^{\mathrm{InAs}})}$ is the wave vector in the InAs

electrodes. Defining

$$\alpha(E) = \frac{p_{\mathrm{InAs}} k(E - E_v^{\mathrm{GaSb}})}{p_{\mathrm{GaSb}} k'(E_v^{\mathrm{InAs}} - E)} \tag{8.5}$$

$$= \sqrt{\frac{(E_c^{\mathrm{InAs}} - E)(E_v^{\mathrm{GaSb}} - E)}{(E_c^{\mathrm{GaSb}} - E)(E_v^{\mathrm{InAs}} - E)}}, \tag{8.6}$$

we can rewrite Eq. (8.4) in the form

$$T = \frac{4}{4\cos^2 k'L + \left(\alpha(E) + \frac{1}{\alpha(E)}\right)^2 \sin^2 k'L} \tag{8.7}$$

$$= \frac{4}{4 + \left(\alpha(E) - \frac{1}{\alpha(E)}\right)^2 \sin^2 k'L}. \tag{8.8}$$

From Eq. (8.8) we see that resonances occur for $\sin k'L = 0$, or $k' = n\pi/L$. Performing a Taylor series expansion of Eq. (8.8) about the resonance energy E_n, where $k' = (m/\hbar p_{\mathrm{GaSb}})\sqrt{(E_n - E_c^{\mathrm{GaSb}})(E_n - E_v^{\mathrm{GaSb}})} = n\pi/L$, and recognizing that, near a resonance, the transmission coefficient should be of the form $T = 1/(1 + (E - E_n)^2/\Gamma^2)$, we can obtain an expression for the resonance width Γ:

$$\Gamma = 4\pi \left(\alpha(E_n) - \frac{1}{\alpha(E_n)}\right)^{-1/2} \left(\frac{\hbar p_{\mathrm{GaSb}}}{m}\right)^2 \left(2E_n - \left(E_c^{\mathrm{GaSb}} + E_v^{\mathrm{GaSb}}\right)\right) \frac{n}{L^2} \tag{8.9}$$

$$\propto \frac{n}{L^2}. \tag{8.10}$$

From Eq. (8.10) we see that the width of a resonance should vary approximately inversely with the square of the GaSb layer width, and directly with the resonance index n. An examination of Fig. 8.5 shows that this does indeed appear to be the case.

8.3.3 Current-Voltage Characteristics: Theory and Experiment

Using the transmission coefficients calculated for the InAs/GaSb/InAs device structures, we have computed current-voltage characteristics as a function of GaSb layer width. Fig. 8.6(a) shows the theoretically calculated difference between the peak and valley current densities as a function of GaSb layer width; calculated valley currents are extremely small compared to the peak currents, because of the neglect of scattering processes. Fig. 8.6(b) shows the difference between the peak and valley current densities measured experimentally for devices with varying GaSb layer widths. The difference between the peak and valley current densities, rather than simply the peak current density, has been used in order to eliminate contributions to the peak current density from inelastic transport mechanisms, which have not been included in our calculations; as seen in Fig. 8.4, the thermionic contribution to the nonresonant current is relatively small.

As shown in Fig. 8.6, both the experimental and the theoretical curves exhibit the qualitative dependence on GaSb layer width expected from our analysis of the transmission coefficients for these structures. In particular, the sharp drop in the resonant current for narrow GaSb layers is strong evidence that the current flow in these devices is due to transport through a resonance in the GaSb layer, rather than to simple ohmic conduction through the GaSb valence band that is eventually blocked by the GaSb band gap; if the transport mechanism were simply ohmic conduction, the current would not be expected to decrease in devices with narrow GaSb layers. The quantitative discrepancy between the theoretical and experimental values for the resonant current could arise from a number of factors. The calculated peak current densities are quite sensitive to the

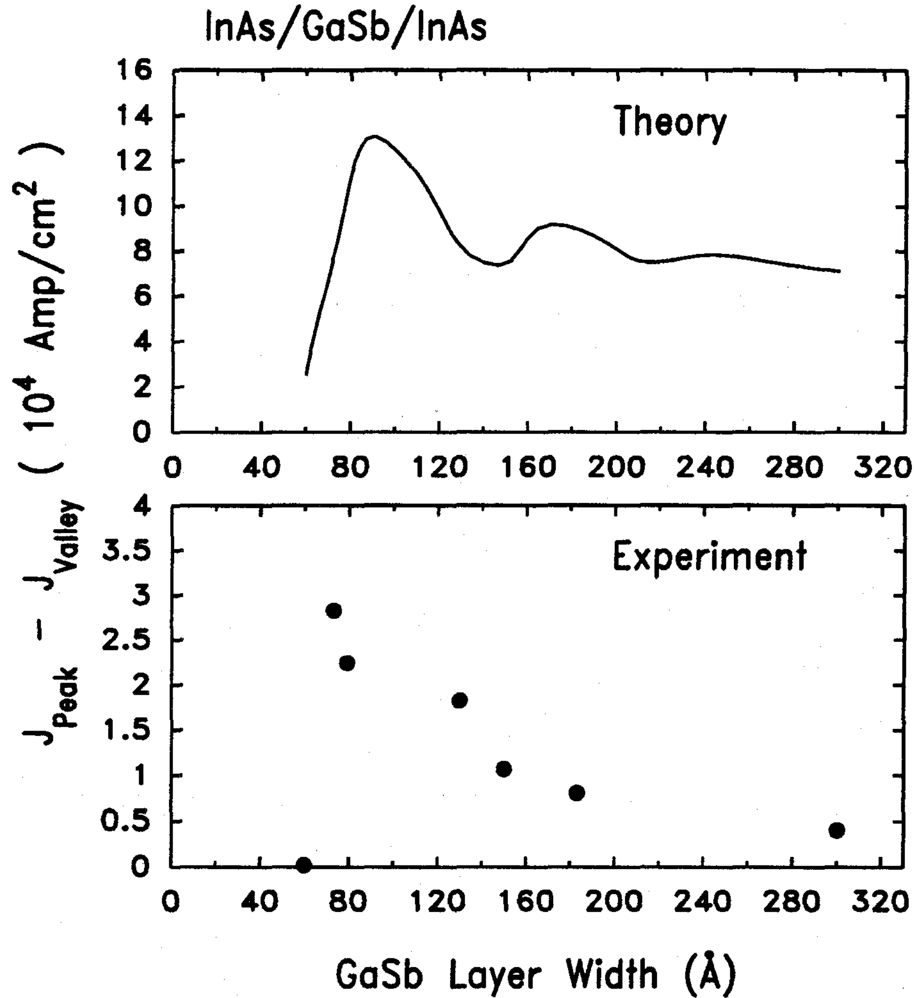

Figure 8.6: (a) Theoretical calculations and (b) experimental values for the difference between the peak and valley current density for the InAs/GaSb/InAs interband transport device as a function of GaSb layer width. The sharp drop in current density for narrow GaSb layer widths is a result of the light-holelike quasi-bound state in the GaSb layer moving below the InAs conduction-band edge in energy, and demonstrates the resonant nature of the current transport mechanism in this structure.

separation between the InAs conduction-band edge and the GaSb valence-band edge, meaning that uncertainties of a few hundredths of an eV in the InAs/GaSb valence-band offset, or small amounts of As incorporated into the GaSb layers, could significantly affect the quantitative agreement between theory and experiment. The qualitative behavior that we observe, however, should not be affected by these uncertainties.

The drop in resonant current at a GaSb layer width of 60 Å also suggests that transport through heavy-holelike states in the GaSb layer is relatively unimportant. The lowest heavy-holelike quasi-bound state should remain above the InAs conduction-band edge for GaSb layer widths of approximately 27 Å or more; if resonant transport through heavy-holelike quasi-bound states were important, NDR in these devices should persist for GaSb layer widths well below 60 Å.

8.4 Conclusions

Interband transport structures are a general class of semiconductor heterostructure devices realized in the lattice-matched InAs/GaSb/AlSb material system and involving carrier transport between conduction-band states in InAs and valence-band states in GaSb. The unusual conduction- and valence-band alignments in this material system, in which the conduction-band edge of InAs is lower in energy than the valence-band edge of GaSb, permit considerable flexibility in the design of heterostructure devices and allow the realization of new device concepts that are not possible in more conventional material systems such as GaAs/$Al_xGa_{1-x}As$.

In this chapter we have presented an overview of experimental and theoretical studies of transport in two-terminal interband transport structures, and have described a detailed study of transport in InAs/GaSb/InAs device structures as

a function of GaSb layer width that helped to clarify a basic issue regarding the nature of carrier transport across the InAs/GaSb interface. A wide variety of interband transport structures exhibiting negative differential resistance have been grown, fabricated, and characterized in the McGill group laboratories. Various device structures have been found to yield extremely high peak current densities or high peak-to-valley current ratios, making them of considerable interest for high-frequency oscillators or various logic applications.

A particularly simple device, the InAs/GaSb/InAs structure, was found to exhibit behavior that helped elucidate the basic nature of interband transport across the InAs/GaSb interface. We performed a theoretical and experimental analysis of the dependence of the current-voltage behavior of InAs/GaSb/InAs interband transport devices on GaSb layer width. Our results demonstrated that transport in these devices occurs primarily via light-holelike transmission resonances in the GaSb quantum wells formed because of the imperfect matching of InAs conduction-band and GaSb valence-band wave functions at the InAs/GaSb interfaces, rather than through simple ohmic conduction, as had been previously proposed. Our results also suggested that coupling between the InAs conduction-band states and GaSb heavy-hole valence band states is relatively unimportant in these devices. In addition, this study allowed us to determine the GaSb layer width that yielded optimum device performance. For a GaSb layer width of 74 Å, we obtained peak current densities of 1×10^5 A/cm^2, significantly higher than any other reported results for this device structure.

References

[1] R. Tsu and L. Esaki, *Appl. Phys. Lett.* **22**, 562 (1973).

[2] L. L. Chang, L. Esaki, and R. Tsu, *Appl. Phys. Lett.* **24**, 593 (1974).

[3] G. A. Sai-Halasz, R. Tsu, and L. Esaki, *Appl. Phys. Lett.* **30**, 651 (1977).

[4] D. H. Chow, T. C. McGill, I. K. Sou, J.–P. Faurie, and C. W. Nieh, *Appl. Phys. Lett.* **52**, 54 (1988).

[5] R. Beresford, L. F. Luo, and W. I. Wang, *Appl. Phys. Lett.* **54**, 1899 (1988).

[6] J. R. Söderström, D. H. Chow, and T. C. McGill, *Appl. Phys. Lett.* **55**, 1348 (1989).

[7] H. Munekata, T. P. Smith, III, and L. L. Chang, *J. Vac. Sci. Technol.* **B7**, 324 (1989).

[8] M. Sweeny and J. Xu, *Appl. Phys. Lett.* **53**, 60 (1989).

[9] J. R. Söderström, D. H. Chow, and T. C. McGill, *Appl. Phys. Lett.* **55**, 1094 (1989).

[10] L. F. Luo, R. Beresford, and W. I. Wang, *Appl. Phys. Lett.* **55**, 2023 (1989).

[11] D. Z.-Y. Ting, D. A. Collins, E. T. Yu, D. H. Chow, and T. C. McGill, *Appl. Phys. Lett.* **57**, 1257 (1990).

[12] E. T. Yu, D. A. Collins, D. Z.-Y. Ting, D. H. Chow, and T. C. McGill, *Appl. Phys. Lett.* **57** 2675 (1990).

[13] G. J. Gualtieri, G. P. Schwartz, R. G. Nuzzo, R. J. Malik, and J. F. Walker, *J. Appl. Phys.* **61**, 5337 (1987).

[14] G. J. Gualtieri, G. P. Schwartz, R. G. Nuzzo, and W. A. Sunder, *Appl. Phys. Lett.* **49**, 1037 (1986).

[15] T. M. Rossi, D. A. Collins, D. H. Chow, and T. C. McGill, *Appl. Phys. Lett.* **57**, 2256 (1990).

[16] D. H. Chow, E. T. Yu, J. R. Söderström, D. A. Collins, D. Z.-Y. Ting, and T. C. McGill, *J. Appl. Phys.* **68** 3744 (1990).

[17] D. A. Collins, E. T. Yu, Y. Rajakarunanayake, J. R. Söderström, D. Z.-Y. Ting, D. H. Chow, and T. C. McGill, *Appl. Phys. Lett.* **57**, 683 (1990).

[18] D. A. Collins, D. H. Chow, E. T. Yu, D. Z.-Y. Ting, J. R. Söderström, Y. Rajakarunanayake, and T. C. McGill, presented at the 1990 NATO Workshop on Resonant Tunneling, El Escorial, Spain (1990).

[19] J. R. Söderström, E. T. Yu, M. K. Jackson, Y. Rajakarunanayake, and T. C. McGill, *J. Appl. Phys.* **68**, 1372 (1990).

[20] K. Taira, I. Hase, and H. Kawai, *Electronics Letters* **25**, 1708 (1990).

[21] J. R. Söderström, D. H. Chow, and T. C. McGill, *Mat. Res. Soc. Symp. Proc.* **145**, 409 (1989).

[22] D. Z.-Y. Ting, E. T. Yu, D. A. Collins, D. H. Chow, and T. C. McGill, *J. Vac. Sci. Technol. B* **8**, 810 (1990).

[23] M. K. Jackson, M. B. Johnson, D. H. Chow, T. C. McGill, and C. W. Nieh, *Appl. Phys. Lett.* **54**, 552 (1989).

Chapter 9

Calculation of Hole Tunneling Times in GaAs/AlAs Double-Barrier Structures

9.1 Introduction

9.1.1 Background and Motivation

The high-frequency behavior of the double-barrier heterostructure proposed by Tsu and Esaki[1] has been a subject of intense study because of interest in high-speed devices, such as oscillators[2, 3, 4] and switching elements[5, 6], based on the double-barrier structure. Several experimental[7, 8, 9] and theoretical[10, 11, 12, 13, 14] studies have focused on the characteristic time scale for electron tunneling processes, an issue of both practical and fundamental physical importance. In one study, Jackson et al.[7] used photoluminescence excitation correlation spectroscopy[15, 16, 17] to study the decay of photoexcited electron and hole populations in undoped GaAs/AlAs/GaAs/AlAs/GaAs double-barrier

heterostructures. An unexpected result in this experiment was that electrons and holes were observed to have very similar tunneling times; if all the photoexcited holes in the quantum well are assumed to relax to the lowest subband, which corresponds to a heavy-hole state at the Brillouin zone center, a simple model of hole tunneling would suggest that the holes should be characterized by a much longer tunneling time than the electrons, because of the large effective mass of the heavy holes. Fig. 9.1 shows the tunneling times measured experimentally by Jackson et al.[7], along with electron, heavy-hole, and light-hole tunneling times calculated from theoretical transmission-resonance widths for GaAs/AlAs double-barrier structures. As seen in the figure, the calculated electron tunneling times agree reasonably well with the experimental times; however, the heavy-hole tunneling times are orders of magnitude larger than the measured times.

This observation of unexpectedly short hole tunneling times in GaAs/AlAs double-barrier heterostructures could influence the interpretation of other experiments in which tunneling escape of photoexcited carriers from a quasi-bound state has been studied. Tsuchiya et al.[8] studied time-resolved photoluminescence spectra from photoexcited carriers in the quantum well of a GaAs/AlAs double-barrier heterostructure, and claimed to measure the electron tunneling escape time by assuming escape of photoexcited holes to be negligible. However, the results of Jackson et al. indicate that this assumption is not valid, and that in the experiment of Tsuchiya et al., both electron and hole tunneling times must be included. A theoretical understanding of the origin of these unexpectedly short hole tunneling times is needed to develop a correct interpretation of tunneling-time measurements in which both electrons and holes are present. In addition, such an understanding would be of importance in the design and study of device structures involving tunneling transport of holes, and would also be of considerable fundamental physical interest.

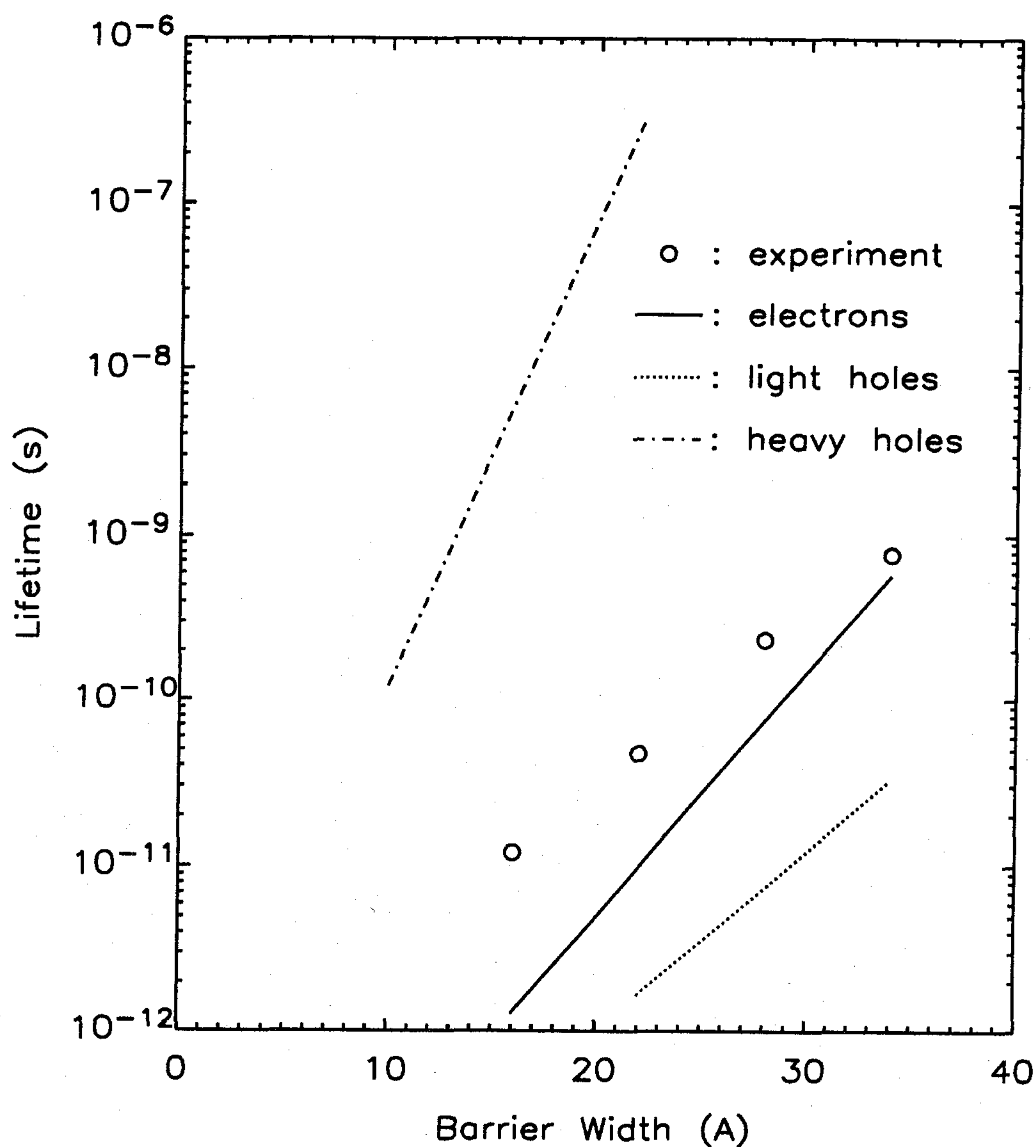

Figure 9.1: Tunneling times measured as a function of barrier thickness in GaAs/-AlAs double-barrier structures. Also shown are tunneling times for electrons, heavy holes, and light holes calculated from theoretical transmission-resonance widths for GaAs/AlAs double barriers. The electron tunneling times are in reasonable agreement with the experimental times, but the calculated heavy-hole times are orders of magnitude larger than the measured times.

In this chapter we propose an explanation for these anomalously short hole tunneling times. By including quantum-well band-mixing effects in our calculations of hole tunneling times, we have found that, for sufficiently high hole temperatures and concentrations, average hole tunneling times are obtained that are comparable to electron tunneling times in the same structure. Our calculated electron and hole tunneling times are thus in good agreement with the previously reported experimental results of Ref. [7].

9.1.2 Summary of Results

We have developed a model for calculating tunneling escape times for holes in a double-barrier heterostructure that explains the anomalously short hole tunneling times measured by Jackson et al.[7] using photoluminescence excitation correlation spectroscopy. Because of band-mixing effects, tunneling times for holes are found to be much shorter than the calculated heavy-hole tunneling time. At the Brillouin zone center ($\vec{k}_{\|} \equiv (k_x, k_y) = 0$), the quantum-well valence subbands can each be characterized as being entirely heavy-holelike or light-holelike; for $\vec{k}_{\|} \neq 0$, however, each subband is composed of a mixture of heavy-hole and light-hole components. By including this effect in a phenomenological model for calculating average tunneling times for a population of holes in the lowest quantum-well valence subband, we obtain average hole tunneling times that are comparable to electron tunneling times. Our calculations are in good agreement with the experimental results of Ref. [7]. The average hole tunneling time is a function of the distribution of holes in the lowest subband, and therefore depends on both the carrier concentration and the carrier temperature. Our results suggest that, for low carrier concentrations and temperatures, an increase in the average hole tunneling time might be observable. More recent calculations using

the effective-bond-orbital model[18, 19] to compute transmission coefficients for valence-band states in a GaAs/AlAs double-barrier heterostructure demonstrate the basic validity of our earlier phenomenological model for calculating average hole tunneling times.

9.1.3 Outline of Chapter

The 4×4 Luttinger-Kohn Hamiltonian used to calculate the quantum-well valence band structure is described in Section 9.2; actual calculations of quantum-well band structure are also presented in this section. Section 9.3 describes the model we have used to calculate average hole tunneling times for a distribution of holes in the lowest valence subband. In Section 9.4 we present calculated average hole tunneling times and compare these times to calculated electron tunneling times and experimentally measured tunneling times from Ref. [7]. It is shown that the average hole tunneling times calculated using our model, theoretically calculated electron tunneling times, and experimentally measured carrier escape times are all within an order of magnitude of each other, contrary to what one would expect on the basis of a simple calculation of heavy-hole tunneling times. Section 9.5 contains a brief description of more recent calculations of average hole tunneling times derived from transmission coefficients computed using the eight-band effective-bond-orbital model[18, 19]. Conclusions are presented in Section 9.6.

9.2 Luttinger-Kohn Valence-Band Hamiltonian

We begin by calculating the valence-band structure in a GaAs quantum well with AlAs barriers; we assume that in the double-barrier structure, the finite barrier thickness has a negligible effect on the quantum well band structure, and merely broadens the quantum-well bound states because of the finite lifetime for tunneling escape through the barriers. Calculations of quantum-well bound-state energies and of energies of transmission resonances in double-barrier structures indicate that this approximation should be valid. Based on the relatively large spin-orbit splitting in GaAs and AlAs ($\Delta_0^{\rm GaAs} = 0.34$ eV and $\Delta_0^{\rm AlAs} = 0.29$ eV), we have neglected spin-orbit coupling in these calculations. With these approximations, the valence bands can be described by the 4×4 Luttinger-Kohn Hamiltonian[20],

$$H = \begin{pmatrix} P+Q+V(z) & L & M & 0 \\ L^* & P-Q+V(z) & 0 & M \\ M^* & 0 & P-Q+V(z) & -L \\ 0 & M^* & -L^* & P+Q+V(z) \end{pmatrix}, \tag{9.1}$$

where

$$P = \frac{\hbar^2}{2m_e}\gamma_1\left(k_x^2 + k_y^2 - \frac{d^2}{dz^2}\right), \tag{9.2}$$

$$Q = \frac{\hbar^2}{2m_e}\gamma_2\left(k_x^2 + k_y^2 + 2\frac{d^2}{dz^2}\right), \tag{9.3}$$

$$L = \frac{\hbar^2}{2m_e}\sqrt{12}\gamma_3(k_x - ik_y)\frac{d}{dz}, \tag{9.4}$$

$$M = -\frac{\hbar^2}{2m_e}\sqrt{3}\left[\gamma_2\left(k_x^2 - k_y^2\right) + 2i\gamma_3 k_x k_y\right]; \tag{9.5}$$

m_e is the free-electron mass, and $V(z)$ is the quantum-well potential produced by the AlAs barriers. The Hamiltonian (9.1) is written in the angular-momentum ba-

sis set, with basis elements $\{|j,m\rangle\}$ ($j = 3/2$ and $m = \pm 3/2, \pm 1/2$); $|3/2, \pm 3/2\rangle$ are zone-center heavy-hole states, and $|3/2, \pm 1/2\rangle$ are zone-center light-hole states. γ_1, γ_2, and γ_3 are the Luttinger parameters; for simplicity, we employ the spherical approximation[21] and set $\gamma_2 = \gamma_3 \equiv \bar{\gamma}$, with the values of γ_1 and $\bar{\gamma}$ determined by the known heavy- and light-hole effective masses for GaAs and AlAs[22]. We have assumed a valence-band offset of 0.55 eV between GaAs and AlAs[23], and a direct band gap of 3.13 eV in AlAs at 80 K.

The quantum-well subband structure is obtained by substituting the Hamiltonian (9.1) for fixed k_x, k_y into the time-independent Schrödinger equation,

$$\sum_{j=1}^{4} H_{ij}\psi_j(z) = E\psi_i(z), \qquad i = 1, ..., 4 \tag{9.6}$$

and solving for the eigenvalues E. We impose the following boundary conditions on the problem: (a) all wave functions should decay exponentially as $z \rightarrow \pm\infty$, (b) the wave function components $\psi_i(z)$ should be continuous at the GaAs/AlAs interfaces, and (c) the probability current density should be continuous at the interfaces[24].

To derive the condition for current continuity, we define parameters $D_{jk}^{\alpha\beta}$ such that

$$H_{jk} = D_{jk}^{zz}\frac{d^2}{dz^2} + iD_{jk}^{z\alpha}k_\alpha\frac{d}{dz} + D_{jk}^{\alpha\beta}k_\alpha k_\beta, \tag{9.7}$$

where the indices α and β can be x or y. An expression for the probability current can be derived from the continuity equation

$$\frac{d}{dt}\int |\psi(z)|^2 dz - \int \frac{dJ}{dz}dz = 0; \tag{9.8}$$

the resulting expression for the probability current density is

$$\begin{aligned} J &= \frac{1}{i\hbar}\left\{\left[\frac{i}{2}D_{jk}^{z\alpha}k_\alpha\psi_k + D_{jk}^{zz}\frac{d\psi_k}{dz}\right]\psi_j^* + \left[\frac{i}{2}D_{kj}^{z\alpha}k_\alpha\psi_k^* - D_{kj}^{zz}\frac{d\psi_k^*}{dz}\right]\psi_j\right\} && (9.9) \\ &= \frac{1}{i\hbar}\left\{\left[\frac{i}{2}D_{jk}^{z\alpha}k_\alpha\psi_k + D_{jk}^{zz}\frac{d\psi_k}{dz}\right]\psi_j^* - \left[\frac{i}{2}D_{jk}^{z\alpha}k_\alpha\psi_k + D_{jk}^{zz}\frac{d\psi_k^*}{dz}\right]^*\psi_j\right\}. && (9.10) \end{aligned}$$

From Eq. (9.10) we see that the appropriate boundary conditions to impose are that ψ_i and $\left[\frac{i}{2}D_{ij}^{z\alpha}k_\alpha + D_{ij}^{zz}\frac{d}{dz}\right]\psi_j$ be continuous at each interface.

For $k_x = k_y = 0$, the Hamiltonian (9.1) is diagonal, and there is no mixing between the heavy- and light-hole states; each valence subband can therefore be identified unambiguously as either heavy-holelike ($|3/2, \pm 3/2\rangle$) or light-holelike ($|3/2, \pm 1/2\rangle$) in character. For $\vec{k}_{\|} \equiv (k_x, k_y) \neq 0$, however, the Hamiltonian is no longer diagonal, and interactions occur between the light-hole and heavy-hole states; each valence subband is therefore composed of a superposition of the zone-center heavy-hole and light-hole components. The lowest valence subbands calculated for a 58 Å GaAs quantum well surrounded by AlAs barriers are shown in Fig. 9.2.

Figs. 9.3(a) and (b) show light-hole and heavy-hole probability densities in the lowest subband for $\vec{k}_{\|} = 0$ and $\vec{k}_{\|} \neq 0$, respectively. As shown in the figure, the lowest subband has purely heavy-hole character for $\vec{k}_{\|} = 0$; for $\vec{k}_{\|} \neq 0$, the band is primarily heavy-holelike but also contains a small component from the lowest light-hole subband; smaller contributions from higher subbands can also be seen. For the calculated probability densities shown in Fig. 9.3, we have taken the GaAs quantum well to be centered at $z = 0$, with the AlAs barriers located at $z = \pm 29$ Å.

The total probability density for each basis component $|j, m\rangle$ at a given energy, $P_{|j,m\rangle}(E)$, is obtained by integrating the spatial probability density across the entire structure. Fig. 9.4 shows the decomposition of the lowest quantum well subband into the individual zone-center basis components. As seen in the figure, the lowest subband is entirely heavy-hole in character for $k_{\|} = 0$, but, as $k_{\|}$ increases, contains an increasing contribution from the zone-center light-hole state.

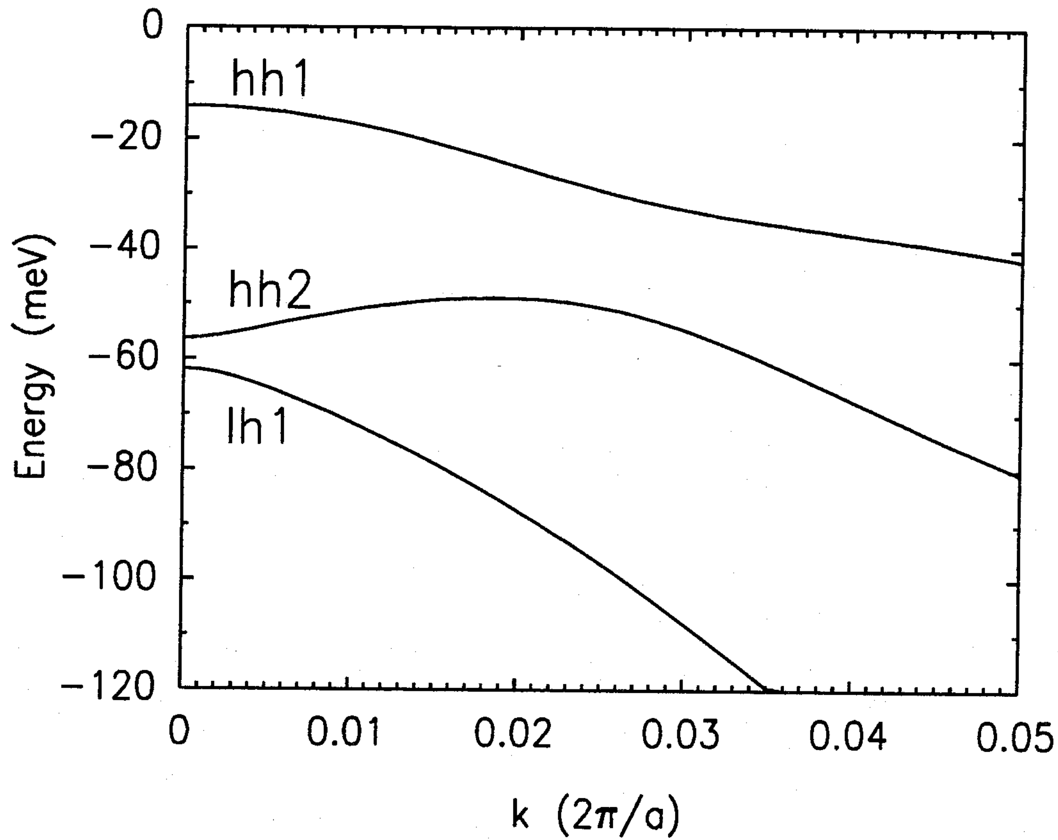

Figure 9.2: Valence subband structure for a 58 Å GaAs quantum well surrounded by AlAs barriers. The quantum-well subband structure was calculated using the 4×4 Luttinger-Kohn Hamiltonian in the spherical approximation. The two lowest subbands (labeled $hh1$ and $hh2$) correspond to pure heavy-hole states at $k = 0$. The third subband (labeled $lh1$) corresponds to a pure light-hole state at $k = 0$.

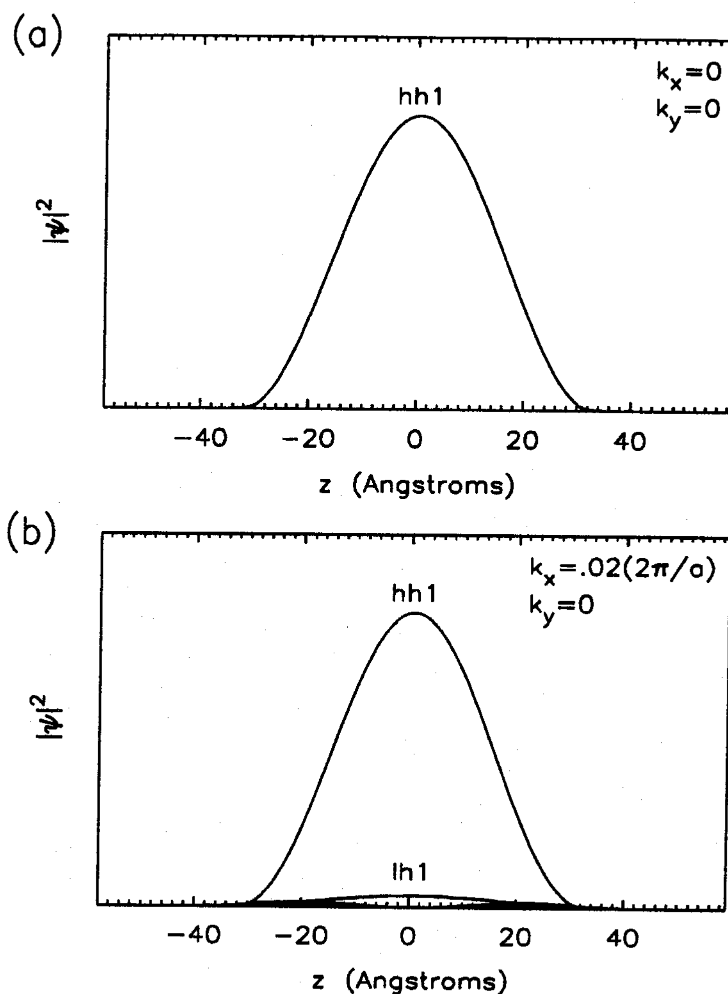

Figure 9.3: Individual components of the quantum-well wave function in the lowest valence subband for (a) $\vec{k}_{||} = 0$, and (b) $\vec{k}_{||} \neq 0$; the components corresponding to the lowest heavy-hole and lowest light-hole states are labeled $hh1$ and $lh1$, respectively. The GaAs quantum well is taken to be centered at $z = 0$, with the AlAs barriers located at $z = \pm 29$ Å. For $\vec{k}_{||} = 0$, the band is purely heavy-hole in character. For $\vec{k}_{||} \neq 0$, the band is primarily heavy-hole in character with a small component from the lowest light-hole subband; smaller contributions from higher subbands (unlabeled) can also be seen in (b).

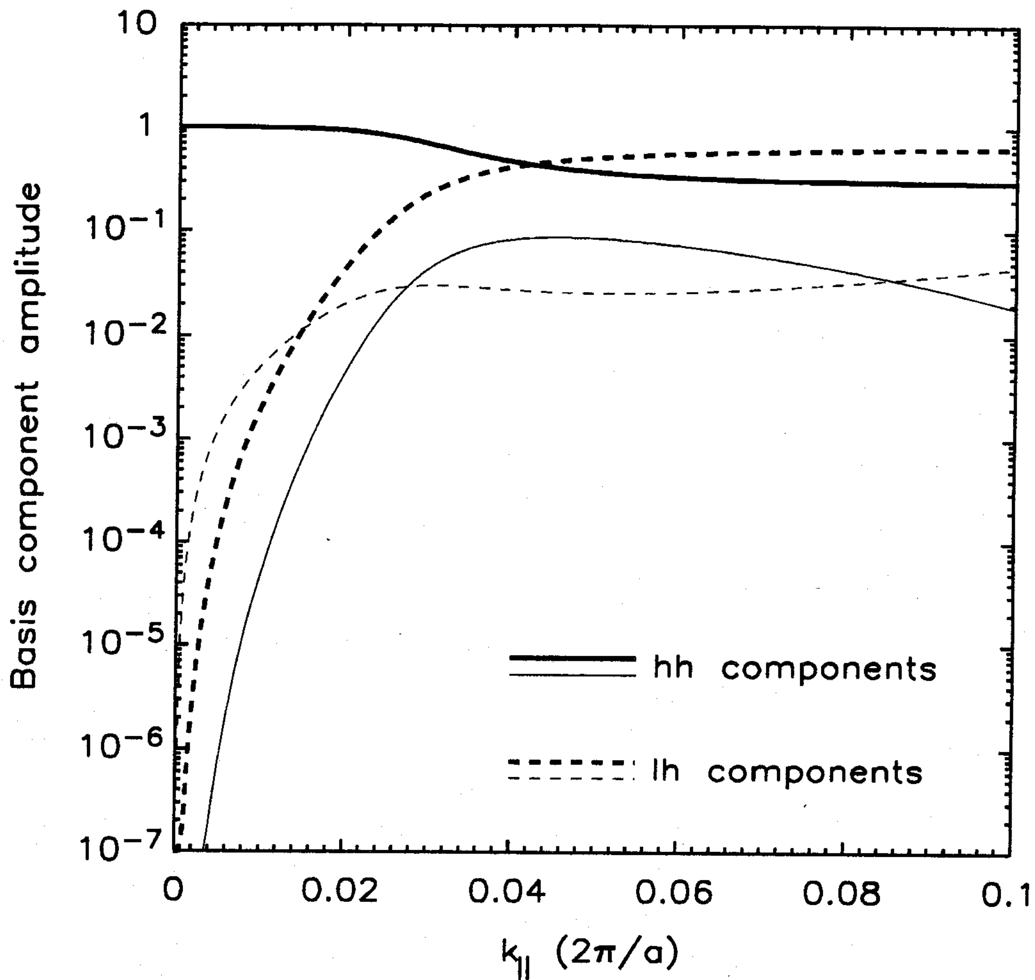

Figure 9.4: Decomposition of the lowest quantum-well subband (labeled $hh1$ in Fig. 9.2) into the zone-center heavy-hole and light-hole basis components. The solid lines represent heavy-hole components, and the dashed lines represent light-hole components. Thick lines represent the lowest heavy-hole and light-hole zone-center states; the thin lines represent higher subbands. As shown, the $hh1$ subband is entirely heavy-hole in character at the Brillouin zone center ($k_{||} = 0$), but develops increasing light-hole character away from the zone center, as $k_{||}$ increases.

9.3 Phenomenological Model for Average Hole Tunneling Times

Tunneling escape times for holes in the quantum-well layer of a double-barrier heterostructure are calculated assuming that all the holes in the quantum well have relaxed to the lowest valence subband, and that the hole distribution is characterized by a carrier temperature T_c. Measurements for GaAs/$Al_xGa_{1-x}As$ multiple-quantum-well structures indicate that intersubband relaxation times for electrons are less than 200 fs[25], and studies of carrier thermalization in optically excited GaAs quantum wells yield electron thermalization times of less than 10 fs and hole thermalization times of approximately 60 fs[26]. However, Shum et al.[27] have found that although carrier thermalization occurs very rapidly (within less than 1 ps), the carrier temperature T_c remains well above the lattice temperature for a considerably longer time, because of the creation of a nonequilibrium phonon population by the initial rapid cooling of carriers; the characteristic decay time for the electrons and nonequilibrium phonons was found to be $\sim$30 ps for photoexcited carriers in a GaAs multiple-quantum-well structure. Because the photoexcitation energy in the experiment of Jackson et al.[7] was, at 2 eV, considerably higher than the quantum-well transition energy of $1.6 - 1.8$ eV, the relevant carrier temperature T_c during the measurement of tunneling escape times could have been considerably higher than the lattice temperature.

Given the carrier temperature T_c, a chemical potential μ for the holes in the lowest quantum-well subband can be determined from the condition

$$p = \int_0^\infty \mathcal{D}(E) f(\mu, E, T_c) dE, \tag{9.11}$$

where $\mathcal{D}(E)$ is the density of states in the quantum well, $f(\mu, E, T_c)$ is the Fermi distribution function, and p is the total hole population. The probability density

for each basis component averaged over the entire hole distribution is then given by

$$\bar{P}_{|j,m\rangle}(p,T_c) = \frac{1}{p}\int_0^\infty \mathcal{D}(E)f(\mu,E,T_c)P_{|j,m\rangle}(E)dE. \tag{9.12}$$

To obtain an average hole tunneling rate $1/\tau_h$, we simply take an average of the tunneling rates for the individual light- and heavy-hole components, weighted by the probability density for each basis component given by Eq. (9.12), i.e.,

$$\frac{1}{\tau_h} = \sum_{|j,m\rangle} \bar{P}_{|j,m\rangle}(p,T_c)\frac{1}{\tau_{|j,m\rangle}}. \tag{9.13}$$

The heavy- and light-hole tunneling times are calculated from the full widths at half maximum (FWHM) of the transmission probability resonances in the double-barrier structure using the relation $\tau \sim \hbar/\Delta E_{FWHM}$. Transmission probabilities were calculated using the transfer-matrix method of Kane[28], modified to account for the different hole effective masses in GaAs and AlAs. Wave vectors in the AlAs barriers were estimated using a two-band $\vec{k}\cdot\vec{p}$ model[29] for the light-hole components and a one-band model for the heavy-hole components. For GaAs/AlAs double-barrier structures, tunneling times for light holes were found to be somewhat shorter than for electrons and several orders of magnitude shorter than for heavy holes; thus, even a small amount of band mixing can have a large effect on the average hole tunneling time.

It is also instructive to examine the hole tunneling time as a function of energy E, or equivalently, of $k_{||}$. Eq. (9.13) may be rewritten using Eq. (9.12) as

$$\frac{1}{\tau_h} = \sum_{|j,m\rangle}\left(\frac{1}{p}\int_0^\infty \mathcal{D}(E)f(\mu,E,T_c)P_{|j,m\rangle}(E)dE\right)\frac{1}{\tau_{|j,m\rangle}} \tag{9.14}$$

$$= \frac{1}{p}\int_0^\infty \mathcal{D}(E)f(\mu,E,T_c)\left(\sum_{|j,m\rangle} P_{|j,m\rangle}(E)\frac{1}{\tau_{|j,m\rangle}}\right)dE \tag{9.15}$$

$$\equiv \frac{1}{p}\int_0^\infty \mathcal{D}(E)f(\mu,E,T_c)\frac{1}{\tau_h(k_{||})}dE, \tag{9.16}$$

where

$$\frac{1}{\tau_h(k_{||})} \equiv \sum_{|j,m\rangle} P_{|j,m\rangle}(E(k_{||}))\frac{1}{\tau_{|j,m\rangle}}. \tag{9.17}$$

Fig. 9.5 shows the hole tunneling time $\tau_h(k_{||})$ given by Eq. (9.17) plotted as a function of $k_{||}$ for the lowest quantum-well valence subband, labeled $hh1$ in Fig. 9.2. As shown in the figure, the hole tunneling time at $k_{||} = 0$ is given by the pure heavy-hole value. For $k_{||} \neq 0$, the hole tunneling time decreases rapidly because of the increasing contribution to the $hh1$ valence subband wave function from the zone-center light-hole state, as shown in Fig. 9.4.

9.4 Comparison with Experimental Results

Our results indicate that valence-band mixing can play an important role in determining tunneling times for holes. In Fig. 9.6 we have plotted, for $T_c = 80$ K, theoretical average hole tunneling times calculated using Eq. (9.13) as a function of hole population and barrier thickness; also plotted are theoretical electron tunneling times and experimental carrier population-decay times measured at $T = 80$ K[7]. Electron and hole densities for these measurements were estimated to be approximately 10^{11} cm^{-2}. At the estimated experimental carrier concentrations, the calculated hole and electron tunneling times are in good agreement with these experiments. Jackson et al.[7, 30] have discussed other effects, such as diffusion and quantum-well charging, that may conspire to make the electron and hole tunneling escape times exactly equal, but these effects will be small compared to the reduction in hole tunneling times caused by mixing of the valence subbands.

In Fig. 9.7 we have plotted the hole tunneling time as a function of hole concentration and hole temperature for a barrier width of 28 Å. These results indicate that for sufficiently low hole temperatures and concentrations, band-mixing

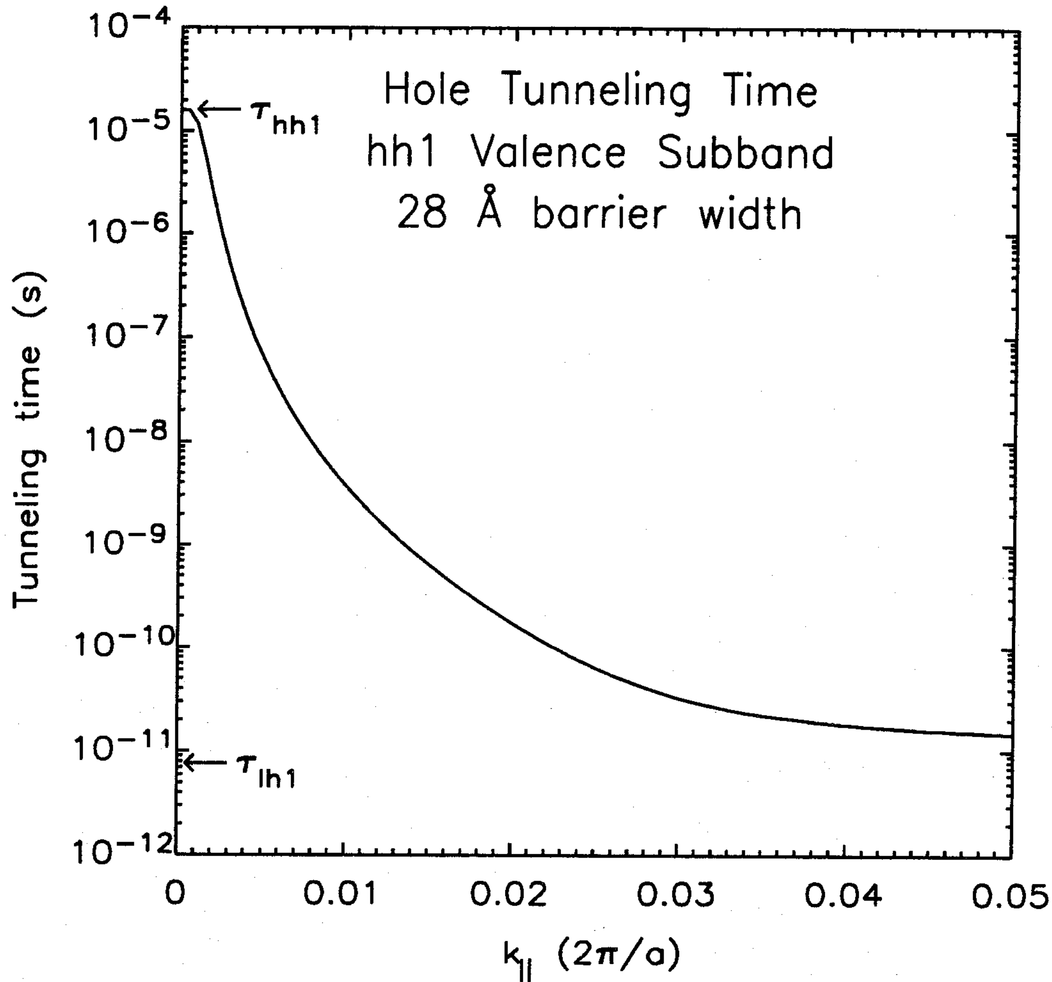

Figure 9.5: Hole tunneling time $\tau_h(k_{||})$ plotted as a function of $k_{||}$ for the lowest quantum-well valence subband, labeled $hh1$ in Fig. 9.2, for a double-barrier heterostructure with a 28 Å barrier width. At $k_{||} = 0$, $\tau_h(k_{||})$ is given by the pure heavy-hole value. For $k_{||} \neq 0$ the hole tunneling time decreases rapidly because of the increasing contribution to the valence subband wavefunction from the zone-center light-hole state, as shown in Fig. 9.4.

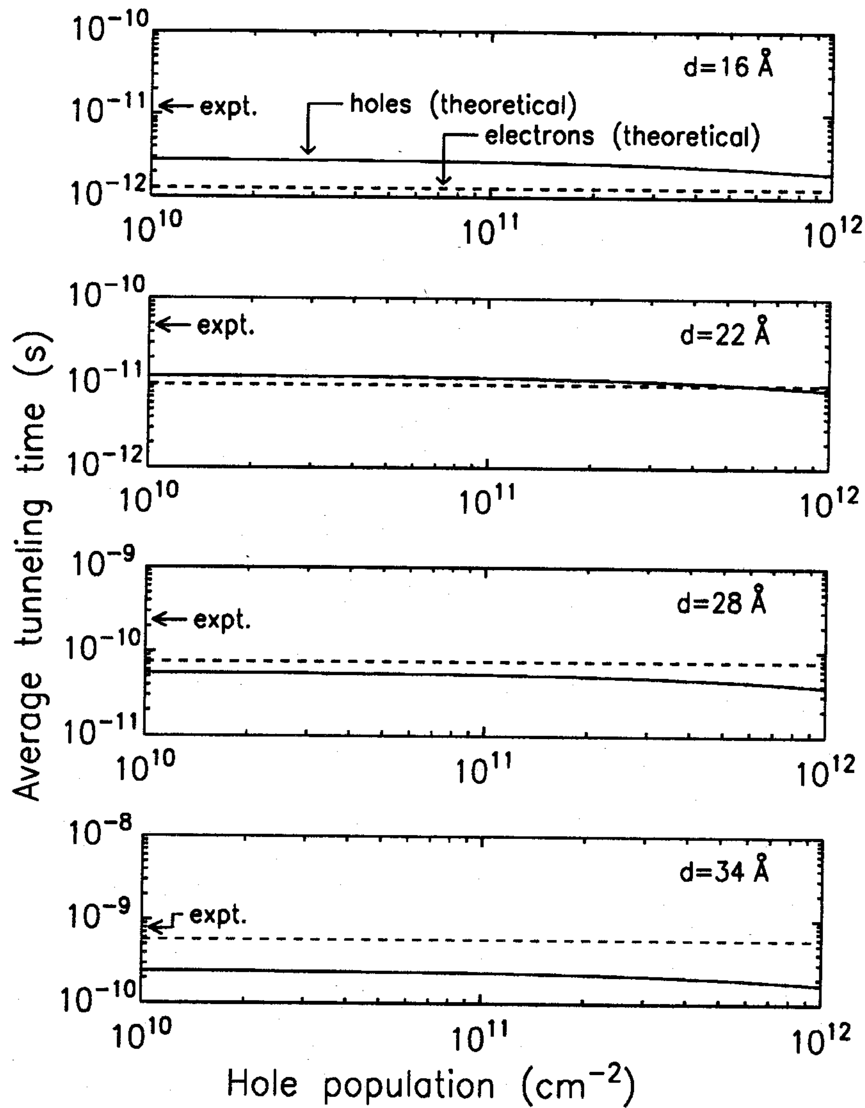

Figure 9.6: Calculated average hole tunneling times (solid lines) and electron tunneling times (dashed lines), and experimentally measured tunneling times for barrier widths of 16, 22, 28, and 34 Å. Experimental carrier concentrations in the work of Ref. [7] were estimated to be approximately 10^{11} cm^{-2}. For each structure, calculated electron and hole tunneling times are comparable in magnitude, and at the estimated experimental carrier concentrations are in good agreement with experimental measurements.

effects are diminished and the average hole tunneling time increases, asymptotically approaching the pure heavy-hole value. This is exactly the result one would expect, since for low carrier temperatures and concentrations, the holes are very close to the bottom of the band ($k_{||} = 0$), where the band is almost entirely heavy-hole in character. For higher carrier temperatures and concentrations, however, calculated hole tunneling times rapidly drop to values comparable to electron tunneling times, since even a small light-hole component in the hole population causes a very significant reduction in the average hole tunneling time. It is possible that much longer hole tunneling times might be observed in experiments similar to that of Jackson et al.[7] but in which lower photoexcitation intensities, yielding a lower hole concentration, and lower photoexcitation energies, yielding a lower carrier temperature, were used.

9.5 Transmission Resonances Calculated in the Effective-Bond-Orbital Model

More recently, Ting, Yu, and McGill[31] have performed calculations of transmission coefficients for hole states in GaAs/AlAs/GaAs/AlAs/GaAs double-barrier tunnel structures using the eight-band effective-bond-orbital model[18, 19] discussed in Chapter 7, and have used these calculated transmission coefficients to deduce tunneling times for hole states in these structures. These calculations confirm the validity of the more heuristic model discussed in Sections 9.3 and 9.4.

To obtain average tunneling times using the effective-bond-orbital model, transmission coefficients were calculated as a function of energy E and wave vector parallel to the direction of confinement, $\vec{k}_{||}$. The energies of the transmission resonances for the double-barrier structure as a function of $\vec{k}_{||}$ corresponded

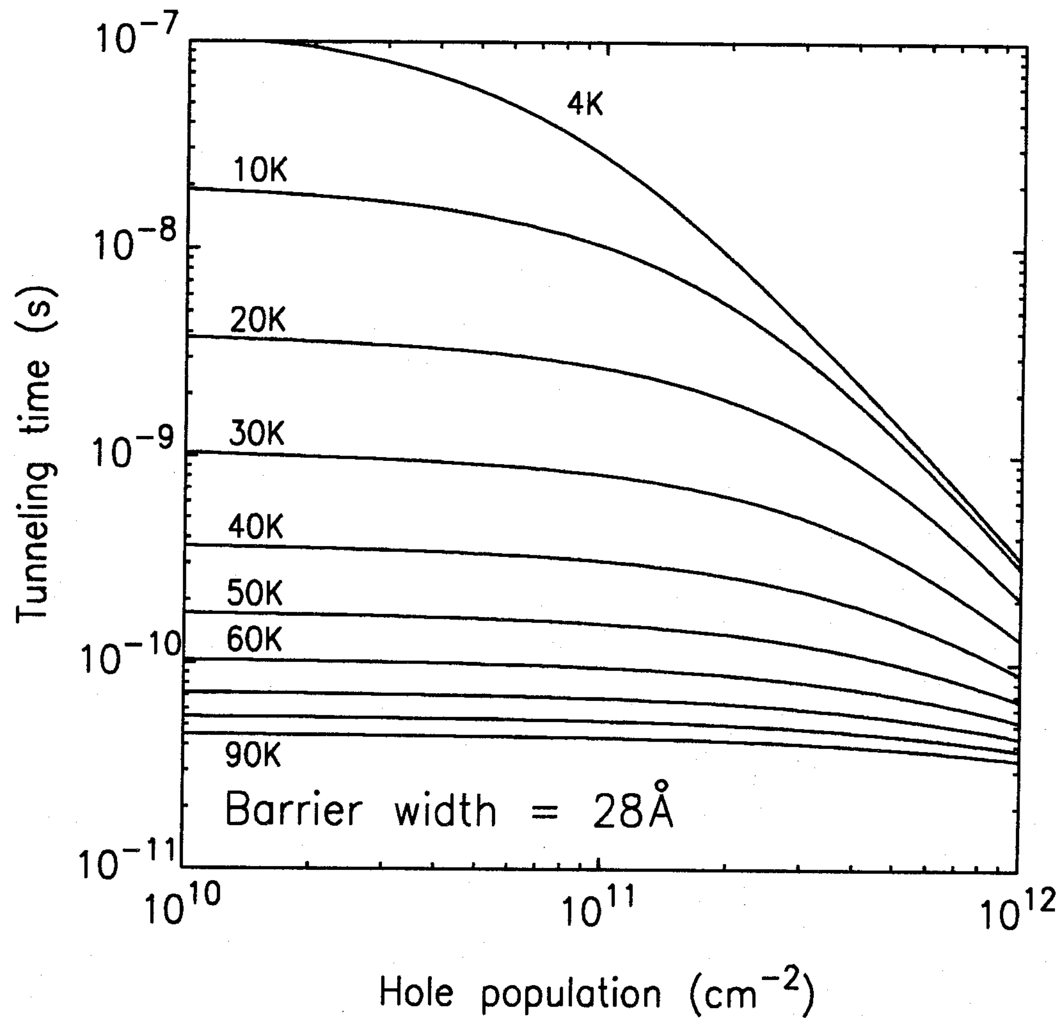

Figure 9.7: Calculated average hole tunneling times as a function of hole concentration and temperature for a barrier width of 28 Å. For low hole temperatures and hole concentrations, the average tunneling time increases significantly, and should asymptotically approach the pure heavy-hole tunneling time.

to the valence subband structure in the GaAs quantum well, and the widths of these resonances yielded tunneling times $\tau_h(\vec{k}_{||})$ for each point in each subband via the usual relationship $\tau \sim \hbar/\Delta E_{FWHM}$. Tunneling times for electrons in the GaAs/AlAs double-barrier structure were also calculated using the effective-bond-orbital model.

Fig. 9.8 shows the hole tunneling time for the lowest ($hh1$) valence subband calculated as a function of $\vec{k}_{||} = (k_x, 0)$ using the effective-bond-orbital model. The hole tunneling times were found to be essentially isotropic in the Brillouin zone, so that $\tau_h(\vec{k}_{||}) \approx \tau_h(k_{||})$. The pure light-hole and heavy-hole tunneling times in this model are somewhat different from those obtained using the 4×4 Luttinger-Kohn Hamiltonian, but the dependence of the hole tunneling time on $k_{||}$ for small $k_{||}$ is seen to be very similar to that obtained using the earlier phenomenological model. For larger values of $k_{||}$, the tunneling time calculated from transmission-resonance widths actually increases, rather than approaching a fixed multiple of the light-hole value, as occurs in the phenomenological model. This effect is due to the mixing of the zone-center light-hole and heavy-hole states that occurs for $\vec{k}_{||} \neq 0$ even in bulk material; this mixing has not been included in the calculation of tunneling times in the phenomenological model, but turns out to have a relatively small effect on the average tunneling time.

Fig. 9.9 shows average hole tunneling times and average electron tunneling times calculated using the effective-bond-orbital model, and experimental carrier decay times observed in Ref. [7]. As shown in the figure, the average hole and electron tunneling times and the experimentally observed carrier decay times are all within approximately an order of magnitude of each other, in agreement with the basic conclusions drawn from the calculations using the phenomenological model for hole tunneling times. The actual times calculated using the phenomenological model and using the resonance widths obtained from the effective bond

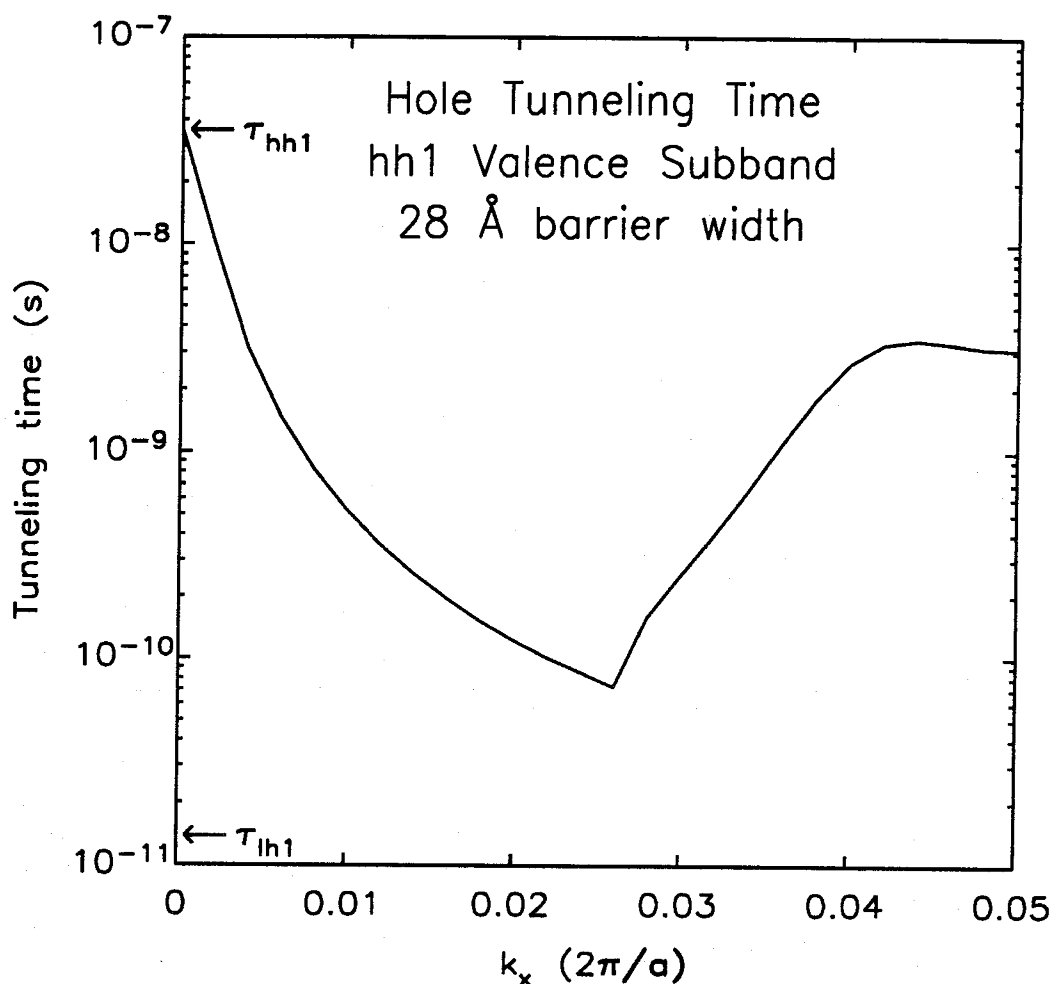

Figure 9.8: Hole tunneling time as a function of $k_{||}$ for the $hh1$ valence subband, for a double-barrier heterostructure with a 28 Å barrier width. The hole tunneling time in the effective-bond-orbital model was found to be essentially isotropic, so that $\tau_h(\vec{k}_{||}) \approx \tau_h(k_{||})$. At $k_{||} = 0$, τ_h is given by the pure heavy-hole value. The tunneling time initially decreases with increasing $k_{||}$, then increases because of the mixing of the zone-center light-hole and heavy-hole states that occurs even in bulk material. However, this increase has little effect on average tunneling times calculated for hole population distributions in a quantum well.

orbital model differ somewhat, partly because of the neglect of bulk mixing of the zone-center light-hole and heavy-hole states in the phenomenological model, but primarily because of the different pure light-hole and pure heavy-hole tunneling times obtained from the 4×4 Luttinger-Kohn Hamiltonian and from the effective-bond-orbital model for band structure.

In Fig. 9.10 are shown calculated average hole tunneling times as a function of hole concentration and hole temperature for a barrier width of 28 Å. As in the calculations using the phenomenological model, the average hole tunneling times asymptotically approach the pure heavy-hole tunneling time for low hole concentrations and hole temperatures, and rapidly decrease for higher concentrations and carrier temperatures. The average tunneling times calculated using resonance widths from the effective-bond-orbital model actually increase slightly for very large hole concentrations and high carrier temperatures, because of the increase in $\tau_h(k_{||})$ with $k_{||}$, as shown in Fig. 9.8. However, this effect is quite small compared to the reduction in tunneling time from the pure heavy-hole value that occurs due to mixing in the quantum well of the pure heavy-hole and light-hole states to form each individual quantum-well valence subband.

9.6 Conclusions

In this chapter we have presented some theoretical studies of tunneling times for holes in GaAs/AlAs double-barrier tunnel structures. Prior to this work, it was often assumed[8] that tunneling times for photoexcited holes in the quantum well of a GaAs/AlAs double-barrier tunnel structure would be extremely long, because of the large effective mass for the heavy-hole valence band in GaAs and AlAs. However, we have found that band-mixing effects in the lowest valence subband in the GaAs quantum well induce a sharp reduction in hole tunneling

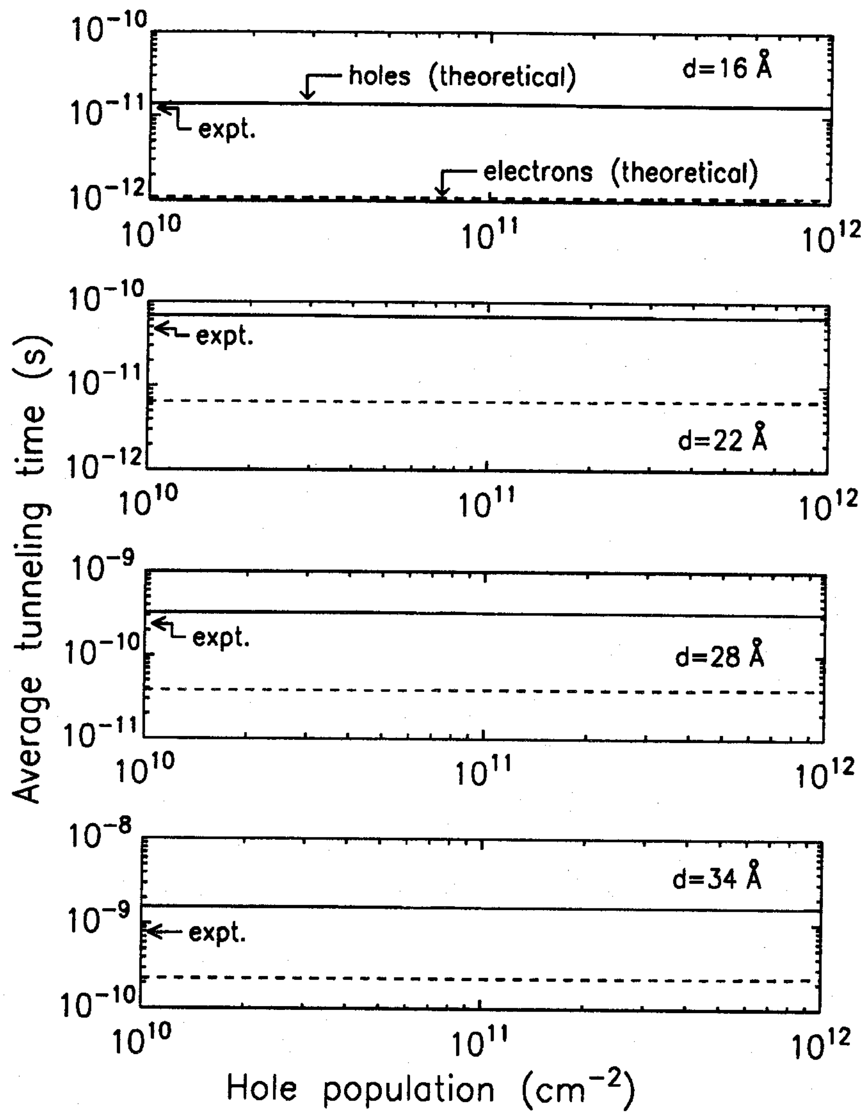

Figure 9.9: Calculated average hole tunneling times (solid lines) and average electron tunneling times (dashed lines), and experimentally measured tunneling times for barrier widths of 16, 22, 28, and 34 Å obtained from Ref. [7]. For each structure, all three times are within approximately an order of magnitude of each other, confirming the basic conclusions obtained from calculations using our earlier phenomenological model.

10^{-8}

4K

10K

10^{-9}

20K

30K

40K

100K

Barrier width = 28Å

10^{-10}

Tunneling time (s)

10^{10} 10^{11} 10^{12}

Hole population (cm^{-2})

Figure 9.10: Average hole tunneling times as a function of hole concentration and hole temperature calculated from transmission resonance widths obtained using the effective-bond-orbital model. As in the phenomenological model, the average hole tunneling time asymptotically approaches the pure heavy-hole value for low hole concentrations and hole temperatures, and decreases rapidly for higher concentrations and carrier temperatures. These calculations also yield an increase in the average hole tunneling time for very high hole concentrations and temperatures, arising from the increase in $\tau_h(k_{||})$ that occurs for large $k_{||}$ in this model, as shown in Fig. 9.8. However, this effect is small compared to the reduction in tunneling time from the pure heavy-hole value that occurs because of mixing in the quantum well of the pure heavy-hole and light-hole states to form each individual quantum-well subband.

times; this occurs because of the admixture, for $\vec{k}_{\|} \neq 0$, of light-hole character in the lowest valence subband, which has entirely heavy-hole character at the zone center ($\vec{k}_{\|} = 0$). We have performed calculations of average hole tunneling times using a phenomenological model in which the hole tunneling rate as a function of $k_{\|}$ is obtained by adding the tunneling rates for heavy holes and light holes weighted by the relative heavy-hole and light-hole components in the valence subband at each $k_{\|}$. Our results demonstrate that band-mixing effects can reduce hole tunneling times, averaged over an entire hole population distribution, to values comparable to light-hole and electron tunneling times. More recent results obtained by calculating transmission coefficients for GaAs/AlAs double-barrier structures using the effective-bond-orbital model for band structure and relating the transmission resonance widths ΔE_{FWHM} to the tunneling time, using the standard relationship $\tau_h(\vec{k}_{\|}) \sim \hbar/\Delta E_{FWHM}(\vec{k}_{\|})$, confirm the basic validity of the earlier, more heuristic approach.

Our results provide an explanation for experimental observations[7] that under certain conditions, tunneling times for holes were much shorter than expected for the lowest heavy-holelike valence subband, and comparable in fact to electron tunneling times. Specifically, we have found that for sufficiently high hole temperatures and concentrations, band-mixing effects lower the average hole tunneling times to values comparable to electron tunneling times, whereas for very low hole temperatures and concentrations, band mixing becomes less important and the hole tunneling times asymptotically approach the pure heavy-hole value. It might be possible to observe much longer hole tunneling times in experiments similar to that of Jackson et al.[7], modified to investigate hole tunneling times using lower photoexcitation energies and intensities to yield hole distributions characterized by very low concentrations and carrier temperatures. Finally, these results could

have relevance for device concepts involving tunneling transport of holes, since tunneling times for holes could be much shorter than expected on the basis of a simple model of heavy-hole tunneling, and might impose a much less severe limitation on device speed than one would first assume.

References

[1] R. Tsu and L. Esaki, *Appl. Phys. Lett.* **22**, 562 (1973).

[2] T. C. L. G. Sollner, W. D. Goodhue, P. E. Tannenwald, C. D. Parker, and D. D. Peck, *Appl. Phys. Lett.* **43**, 588 (1983).

[3] E. R. Brown, T. C. L. G. Sollner, C. D. Parker, W. D. Goodhue, and C. L. Chen, *Appl. Phys. Lett.* **55**, 1777 (1989).

[4] E. R. Brown, C. D. Parker, L. J. Mahoney, J. R. Söderström, and T. C. McGill, presented at the 48th Annual Device Research Conference, Santa Barbara, CA (1990).

[5] T. K. Woodward, T. C. McGill, H. F. Chung, and R. D. Burnham, *IEEE Electron Device Lett.* **9**, 122 (1988).

[6] F. Capasso, K. Mohammed, and A. Y. Cho, *IEEE J. Quantum Electron.* **QE-22**, 1853 (1986).

[7] M. K. Jackson, M. B. Johnson, D. H. Chow, T. C. McGill, and C. W. Nieh, *Appl. Phys. Lett.* **54**, 552 (1989).

[8] M. Tsuchiya, T. Matsusue, and H. Sakaki, *Phys. Rev. Lett.* **59**, 2356 (1987).

[9] J. F. Whitaker, G. A. Mourou, T. C. L. G. Sollner, and W. D. Goodhue, *Appl. Phys. Lett.* **53**, 385 (1988).

[10] K. K. Thornber, T. C. McGill, and C. A. Mead, *J. Appl. Phys.* **38**, 2384 (1967).

[11] M. Büttiker and R. Landauer, *Phys. Rev. Lett.* **49**, 1739 (1982).

[12] N. Harada and S. Kuroda, *Jpn. J. Appl. Phys. Pt. 2* **25**, L871 (1986).

[13] S. Collins, D. Lowe, and J. R. Barker, *J. Phys. C* **20**, 6213 (1987).

[14] H. Guo, K. Diff, G. Neofotistos, and J. D. Gunton, *Appl. Phys. Lett.* **53**, 131 (1988).

[15] D. Rosen, A. G. Doukas, Y. Budansky, A. Katz, and R. R. Alfano, *Appl. Phys. Lett.* **39**, 935 (1981).

[16] D. von der Linde, J. Kuhl, and E. Rosengart, *J. Lumin.* **24/25**, 675 (1981).

[17] M. B. Johnson, T. C. McGill, and A. T. Hunter, *J. Appl. Phys.* **63**, 2077 (1988).

[18] Y. C. Chang, *Phys. Rev. B* **37**, 8215 (1988).

[19] G. T. Einevoll and Y. C. Chang, *Phys. Rev. B* **40**, 9683 (1989).

[20] J. M. Luttinger and W. Kohn, *Phys. Rev.* **97**, 869 (1955).

[21] A. Fasolino and M. Altarelli, in *Two-Dimensional Systems, Heterostructures, and Superlattices*, G. Bauer, F. Kuchar, and H. Heinrich, eds. (Springer, New York, 1984), p. 176.

[22] S. Adachi, *J. Appl. Phys.* **58**, R1 (1985).

[23] J. Batey and S. L. Wright, *J. Appl. Phys.* **59**, 200 (1986).

[24] M. Altarelli, *Phys. Rev. B* **28**, 842 (1983).

[25] K. K. Choi, B. F. Levine, C. G. Bethea, J. Walker, and R. J. Malik, *Appl. Phys. Lett.* **50**, 1814 (1987).

[26] W. H. Knox, D. S. Chemla, G. Livescu, J. E. Cunningham, and J. E. Henry, *Phys. Rev. Lett.* **61**, 1290 (1988).

[27] K. Shum, M. R. Junnarkar, H. S. Chao, R. R. Alfano, and H. Morkoç, *Phys. Rev. B* **37**, 8923 (1988).

[28] E. O. Kane, in *Tunneling Phenomena in Solids*, E. Burstein and S. Lundqvist, eds. (Plenum Press, New York, 1969), p. 1.

[29] E. O. Kane, *Semiconductors and Semimetals*, Vol. 1, R. K. Willardson and A. C. Beer, eds. (Academic Press, New York, 1966), p. 75.

[30] M. K. Jackson, *Optical Studies of Semiconductor Heterostructures: Measurements of Tunneling Times, and Studies of Strained Superlattices*, Ph.D. thesis, California Institute of Technology, Pasadena, CA (1990).

[31] D. Z.-Y. Ting, E. T. Yu, and T. C. McGill, submitted to *Phys. Rev. B* (1991).